Extended Bree-like diagrams for high-temperature structures

A thesis in fulfilment of the requirements for the degree of Doctor of Philosophy

By

Zhiyuan Ma

Department of Mechanical and Aerospace Engineering
University of Strathclyde
Glasgow
UK

2022

Declaration of Authenticity and Author's Rights

This thesis is the result of the author's original research. It has been composed by the author and has not been previously submitted for examination which has led to the award of a degree.

Zhiyuan Ma

September 26, 2022

Acknowledgements

Firstly, I would like to thank my supervisor, Dr Haofeng Chen, for his guidance during my PhD study. A deep relationship has been established between us since I did the individual projects with him in my 4th year of undergraduate study. He has taught me the basics of solid mechanics, inspired me on my research topics, and showed me the way to become a proper researcher and engineer. Without his firm endorsement, I could hardly proceed and complete the thesis and PhD research.

Also, I would like to thank all my colleagues and visiting researchers from the SILA group. We have had a wonderful time working together and discussing research problems. They have helped me solve several tricky issues and find the right path. I hope the best for their life and career.

I would like to express my special gratitude to Professor A.R.S Ponter from the University of Leicester for his help at the beginning of my PhD research. With his inspiration and assistance, I was able to publish my first journal paper during my 2nd year of PhD study.

Finally, I would like to sincerely thank my parents for their generous support and encouragement along the way. The writing of this thesis would not be possible without their strength and love.

Abstract

With the development of nuclear engineering, there is an increasing demand for structural integrity assessment for the design and life extension of nuclear reactors. The high operating temperature and cyclic loading conditions could significantly affect the longevity of nuclear components, causing creep and fatigue damage. The Bree diagram has been proposed for the quick determination of structural response and cyclic plasticity behaviours. As a series of direct methods, the Linear Matching Method (LMM) framework has also been proposed to provide a complete solution for high-temperature structural integrity assessment.

In this work, the Bree-like diagrams are extended for structural design and assessment. At lower temperatures, the shakedown limit is extended by considering kinematic hardening materials. Constant low cycle fatigue life curves are also added to the Bree-like diagram. At higher temperatures, the creep rupture limit can be plotted considering cyclic loads. Constant creep-fatigue life curves are also added to the Bree-like diagram. Meanwhile, the LMM framework is further developed for the evaluation of extended Bree-like diagrams. In the LMM shakedown algorithm, a two-surface kinematic hardening model is implemented. In the LMM creep rupture algorithm, a Unified Creep Rupture Equation (UCRE) is implemented for the interpolation of creep rupture curves. Based on the LMM DSCA algorithm, a Unified Procedure for Fatigue and Ratchet Analysis (UPFRA) is developed to evaluate the constant fatigue life curves and ratchet limit. Based on the LMM eDSCA algorithm, an extended UPFRA is developed to evaluate the constant creep-fatigue life curves. In addition, several engineering examples are presented in this work and the mechanisms of creep and cyclic plasticity behaviours of high-temperature structures have been investigated and discussed.

Therefore, the capability and functionality of the existing LMM framework have been improved by implementing multiple numerical procedures for different aspects of structural integrity assessment. The Bree-like diagram has also been enhanced in various ways to provide a reliable engineering tool for high-temperature design and assessment.

Publications

Shen, J.[1], **Ma, Z.[1]**, & Chen, H. Shakedown and ratcheting analysis of Printed Circuit Heat Exchangers under multiple cyclic mechanical and thermal loads. International Journal of Pressure Vessels and Piping, 2022, accepted for publication.

Ma, Z., Wang, X., Chen, H., Xuan, F. Z., & Liu, Y. A unified direct method for ratchet and fatigue analysis of structures subjected to arbitrary cyclic thermal-mechanical load histories. International Journal of Mechanical Sciences, Volume 194, March 2021, 106190.

Ma, Z., Chen, H., Liu, Y., & Xuan, F. Z. A direct approach to the evaluation of structural shakedown limit considering limited kinematic hardening and non-isothermal effect. European Journal of Mechanics-A/Solids, Volume 79, February 2020, 103877.

Cho, N. K., Wang, R. Z., **Ma, Z.**, Chen, H., & Xuan, F. Z. Creep-fatigue endurance of a superheater tube plate under non-isothermal loading and multi-dwell condition. International Journal of Mechanical Sciences, Volumes 161–162, October 2019, 105048.

Ma, Z., Wang, X., Chen, H., & Xuan, F. Creep fatigue life assessment of hydrogenation reactor manufactured of 2.25 Cr-1Mo steel using the linear matching method framework. ESIA15 & ISSI-2019 Joint Conference on Engineering Structural Integrity, May 2019.

Zheng, X., Chen, H., **Ma, Z.**, & Xuan, F. A novel fatigue assessment approach by Direct Steady Cycle Analysis (DSCA) considering the temperature-dependent strain hardening effect. International Journal of Pressure Vessels and Piping, Volume 170, February 2019, Pages 66-72.

Zheng, X., Chen, H., & **Ma, Z.** Shakedown boundaries of multilayered thermal barrier systems considering interface imperfections. International Journal of Mechanical Sciences, Volume 144, August 2018, Pages 33-40.

Contents

List of figures

List of tables

Nomenclature

α	Thermal expansion coefficient
$\Delta\varepsilon_e$	Elastic strain range
$\Delta\varepsilon_p$	Plastic strain range
$\Delta\varepsilon_t$	Total strain range
Δt	Creep dwell time
ΔT	Temperature difference
$\dot{\varepsilon}$	Strain rate
$\bar{\varepsilon}$	Effective strain
ε_c	Creep strain
ε_p	Plastic strain
ε_R	Ratchet strain
ε_T^R	Target ratchet strain
θ	Thermal load
λ	Load multiplier
λ_R	Creep rupture limit multiplier
λ_{KH}	Kinematic hardening shakedown limit multiplier
λ_{LB}	Lower bound load multiplier
λ_{UB}	Upper bound load multiplier
λ_{UH}	Unlimited hardening shakedown limit multiplier
$\bar{\mu}$	Modified shear modulus
ν	Poisson's ratio
ρ_{ij}	Residual stress field
$\bar{\rho}_{ij}$	Constant residual stress field
ρ_{ij}^r	Varying residual stress field
σ	Stress

$\bar{\sigma}$	Effective stress
σ_1	Maximum principal stress
σ_a	Stress amplitude
σ_{ac}	Average stress during creep dwell
σ_c	Stress at the end of creep dwell
σ_m	Mean stress
σ_R	Creep rupture strength
σ_s	Stress at the start of creep dwell
σ_U	Ultimate strength
σ_Y	Yield strength
$\hat{\sigma}_{ij}$	Linear elastic solution
ω_C	Creep damage accumulated per cycle
ω_F	Fatigue damage accumulated per cycle
ω_T	Total damage accumulated per cycle
A	Creep coefficient
A^*	Frequency factor for *A*
A_{ij}	Back stress
C	Stiffness matrix
C_p	Specific heat capacity
D	Total damage
D_C	Creep damage
D_F	Fatigue damage
E	Elastic modulus
$\bar{E}$	Effective elastic modulus
F	Force
J	Jacobian matrix
i	Iteration number in the UPFRA algorithm

k	Iteration number in the LMM algorithm
K	Kinematic hardening factor
m	Time exponent for creep power law
M	Mechanical load
n	Stress exponent for Norton's creep law
N	Number of cycles to failure
N_T	Target number of cycles to failure
N_{tot}	Total number of cycles to failure
P	Pressure
P_0	Normalization pressure
P_{LM}	Larson-Miller parameter
P_{MH}	Manson-Haferd parameter
P_{OSD}	Ordd-Sherby-Dorn parameter
Q	Activation energy
R	Global gas constant
S	Body surface
t	Time
t^*	Time to creep rupture
T	Temperature
T_0	Normalization temperature
V	Body volume
x	Integration point position
Z	Elastic follow up factor

Acronyms

ASME BPVC	American Society of Mechanical Engineers Boiler and Pressure Vessel Code
CAE	Computer Aided Engineering
CEGB	Central Electricity Generating Board
CPU	Central Processing Unit
CRDA	Creep Rupture Data Assessment
CSV	Comma-Separated Values
DCA	Direct Cycle Analysis
DE	Ductility Exhaustion
DSCA	Direct Steady Cycle Analysis
eDSCA	extended Direct Steady Cycle Analysis
ECCC	European Creep Collaborative Committee
ECM	Elastic Compensation Method
EDF	Électricité de France
EPP	Elastic Perfectly Plastic
E-N	Strain-life
FE	Finite Element
GLOSS	Generalised Local Stress-Strain
GUI	Graphic User Interface
HCF	High Cycle Fatigue
HTGR	Hgh-Temperature Gas-cooled Reactor
LCF	Low Cycle Fatigue
LDS	Linear Damage Summation
LMM	Linear Matching Method
MDF	Multiaxial Ductility Factor
MECM	Modified Elastic Compensation Method

MUSM	Modified Universal Slopes Method
PAT	Post Assessment Testing
PCHE	Printed Circuit Heat Exchangers
PEEQ	Equivalent Plastic Strain
PEMAG	Plastic Strain Magnitude
RCC-MRx	Design and Construction Rules for Mechanical Components in high-temperature structures, experimental reactors and fusion reactors
RSG	Really Simple GUI
R5	Assessment procedure for the high temperature response of structure
R-O	Ramberg-Osgood
SBS	Step-by-Step
SCM	Stress Compensation Method
SEDE	Energy Based Ductility Exhaustion
SILA	Structural Integrity and Life Assessment
SMDE	Stress Modified Ductility Exhaustion
SRP	Strain Range Partitioning
S-N	Stress-life
TF	Time Fraction
UCRE	Unified Creep Rupture Equation
UK	United Kingdom
UMAT	User subroutine to define a material's mechanical behaviour
UPFRA	Unified Procedure for Fatigue and Ratchet Analysis
USM	Universal Slope Method
UTS	Ultimate Tensile Strength

This page intentionally left blank

1. Introduction

1.1 Research background

With the economic growth and increasing demand for electric energy, supercritical and ultra-supercritical water reactors have been widely constructed and deployed worldwide. Compared to fossil fuel power plants which burn natural gas and coal, nuclear power plants have less greenhouse gas emissions and environmental pollution. Also, nuclear fuels produce millions of times of more energy density than fossil fuels which significantly reduces the transportation cost and the effect on the international economic situation. In the UK, around 21% of the electricity is generated by 15 nuclear power plants across the country. However, by 2025, almost half of reactors are expected to be retired. Therefore, there is an increasing demand for high-temperature structural integrity assessment of key components in the reactors to extend the service life of existing reactors and design a new generation of reactors. As a new generation of design of nuclear reactors, the Generation IV reactors have been developed with two main types: the fast reactors and the thermal reactors with three systems each [1, 2]. Generally, the efficiency of nuclear power plants can be significantly improved by increasing operating temperature [3]. The Very High Temperature Reactor (VHTR) is a typical thermal reactor whose primary outlet temperature can reach 1000 °C during the operation process.

The tsunami in Japan and the following Fukushima Daiichi nuclear accident have raised the alarm of the danger of nuclear meltdown and radiation leaks [4]. Therefore, the safety of nuclear reactors has become a high priority, while a robust standard is needed to regulate the design and assessment procedures. Popular international design codes for high-temperature structures include the ASME Boiler and Pressure Vessel Code (NH) [5] from the American Society of Mechanical Engineers in the USA, the RCC-MR Code [6] in France, and the R5 procedure for Assessing the High Temperature Response of Structure [7] in the UK. These rule-based codes provide comprehensive procedures to standardize the design and assessment of pressure vessels based on elastic Finite Element (FE) analyses. For safety concerns, the results obtained with the rule-based methods are highly conservative to allow margins of error and extreme loading conditions. Also, due to the limitation of standardized procedures, high-temperature design codes are only applicable for typical

engineering components and specific materials. For complicated geometry and loading condition, inelastic FE analyses are suggested to consider sophisticated constitutive equations and damage models. The nonlinear FE analyses are highly accuracy and less conservative, but they can be computational consuming and difficult to converge. Therefore, an alternative method is widely demanded among industries which can perform structural integrity assessment with high accuracy and efficiency.

The traditional FE analyses and alternative methods can be used for physical characterization and evaluation of the cyclic response of structures at high temperatures. They can be further used to evaluate the creep, fatigue and thermal fatigue damage which could greatly affect the lifespan of nuclear components [8]. Creep behaviour can cause a change in dimension, which leads to distortion, leakage and cavitation at critical locations, such as steam pipes, boiler headers, superheated reactor tubes, turbine serrations and blades [9]. The load-bearing capacity of steel may also degrade at high temperatures while the structure would rupture at a relatively low stress level. Fatigue behaviour is another common failure mechanism induced by cyclic loading conditions, which can interact with creep behaviour in various ways. Fatigue induces transgranular cracks at the surface of components, while creep induces intergranular cracks within the body. The interaction between creep and fatigue can cause significant damage to the component leading to many failure cases [10]. Depending on the stress type in the load cycle, the failure mechanism can be dominated by either creep or fatigue. Cyclic thermal stress is common and dominant in rotor grooves and blades, which is often caused by thermal gradient and thermal expansion differences [9]. For components operating in relatively low temperatures, the creep effect can be neglected, but low cycle fatigue becomes the major concern where the number of cycles to failure is lower than 5×10^4 [11]. An interaction diagram has been introduced by Bree [12] so that the structural response can be determined directly for various combinations of thermal-mechanical loads. Several cyclic behaviours are differentiated by the shakedown and ratchet boundaries in the Bree diagram: elastic shakedown behaviour, plastic shakedown behaviour leading to low cycle fatigue damage, and ratchetting behaviour leading to incremental collapse. Therefore, the Bree diagram has become a useful tool for structural integrity assessment.

To calculate Bree-like diagrams and provide an alternative method for structural integrity assessment, the Linear Matching Method (LMM) framework has been proposed by previous researchers [13] based on a series of direct methods. The original LMM framework consists of several modules for different types of industrial problems, including shakedown analysis, creep rupture analysis, ratchet analysis, low cycle fatigue analysis and creep-fatigue analysis. Several algorithms have been adopted to support the various modules within the LMM framework, including the Linear Matching Method (LMM) algorithm [14], the extended LMM algorithm [15], the Direct Steady Cycle Analysis (DSCA) algorithm [16-18] and the extended Direct Steady Cycle Analysis (eDSCA) [19, 20]. The LMM framework has also been implemented in the commercial FE software ABAQUS/CAE [21] as a plug-in for better usability and adopted to solve a number of academic and industrial problems. It can also be coupled with the rule-based codes mentioned above to reduce the requirement of inelastic FE analyses. In this thesis, the LMM framework is further extended and improved in various ways to assist in solving a broader range of engineering problems.

1.2 Key issues to be solved

Although the existing LMM framework has covered several aspects of structural integrity assessment, it can still be improved in several ways. The classical Bree diagram can also be extended for better functionality. Four different issues are listed below which need a deep investigation on solid mechanisms and computer algorithms to be solved:

1) The Bauschinger effect [22] is often observed in materials under cyclic loads, which is caused by kinematic hardening. The shakedown analysis module in the current LMM framework only considers the Elastic Perfectly Plastic (EPP) model to describe the stress-strain relationship, which can be over-conservative and inaccurate when the material hardening effect is significant. Sophisticated constitutive models have been proposed based on experimental results to describe the hardening effect. However, they are only suitable for cycle-by-cycle inelastic analysis and are not applicable for direct methods. Therefore, it is necessary to develop an extended shakedown theorem within the LMM framework to consider the kinematic hardening materials.

2) Based on an extended shakedown algorithm, the creep rupture analysis module has been developed by previous researchers in the LMM framework. To achieve the structural creep rupture boundary for a specific rupture time, the module adopts the temperature-dependent rupture strength of material to replace the yield stress in the LMM shakedown algorithm. However, the current rupture analysis module only adopts linear interpolation and extrapolation techniques to calculate the rupture stress based on input data points, which is considered inaccurate to describe the curved relationship between rupture stress, time, and temperature. Thus, a uniform creep rupture equation suitable for various materials is required to be implemented in the LMM framework.
3) The constant life diagrams have been widely used for fatigue design among industries, but they are limited to the material level. Based on the concept of the Bree diagram, it is meaningful to extend the constant life diagrams to the structural level, on which the low cycle fatigue (LCF) or creep-fatigue life is constant. The DSCA subroutine has been adopted in the fatigue analysis module, and the eDSCA subroutine has been adopted in the creep-fatigue analysis module for the current LMM framework. Further development on the DSCA and eDSCA is required for the evaluation of the constant structural life boundary.
4) The DSCA is combined with the shakedown algorithm to evaluate the structural ratchet boundary in the current LMM framework. However, the current ratchet analysis module is limited to solving Bree-like problems with a constant mechanical load and a cyclic thermal load. Thus, it is not suitable for complex loading conditions where both thermal and mechanical loads are cyclic. Therefore, it becomes crucial to develop a numerical procedure to fully utilize the DSCA subroutine to calculate the ratchet boundaries for structures subjected to arbitrary cyclic thermal-mechanical loading histories.

1.3 Objectives and research methods

The general goal of the study is to extend the Bree-like diagrams and solve the key issues mentioned above. A series of computational methods are to be developed to evaluate cyclic plasticity and creep behaviours of high-temperature structures. The computational methods are then programmed and implemented in engineering tools

based on ABAQUS for structural design and integrity assessment. To accomplish the goal, four main objectives and corresponding research methods are given as follows:

1) Develop and implement an extended LMM algorithm for shakedown analysis considering the limited kinematic hardening effect. To achieve this objective, a two-stage numerical procedure is proposed. Melan's static shakedown theorem is extended using a two-surface hardening model to evaluate the shakedown limit considering the unlimited hardening effect. Then the original LMM algorithm is adopted to evaluate the ultimate bounding shakedown limit. After the convergence of both stages, the shakedown limit considering the limited kinematic hardening effect is evaluated, which is bounded by the results from both stages. The numerical procedure is verified by comparing the calculated shakedown boundaries with results from the literature.
2) Create a uniform creep rupture equation for the interpolation and extrapolation of experimental data for various materials. The equation can be implemented in the existing LMM creep rupture analysis module to evaluate the rupture limit. To achieve this objective, a Unified Creep Rupture Equation (UCRE) is developed based on the experiment results from the ECCC data sheet. The numerical model is verified by comparing the predicted creep rupture curves with ones from the literature.
3) Develop a numerical procedure for the evaluation of the structural constant life diagram. To achieve this objective, a three-stage procedure is proposed. Bounded by the shakedown limit and limit load, the constant life diagram is evaluated using the Unified Procedure for Fatigue and Ratchet Analysis (UPFRA). The UPFRA is further extended to support the eDSCA module for creep-fatigue interaction. Both fatigue and creep-fatigue problems can be solved by iteratively running the existing DSCA and eDSCA modules, respectively. The numerical procedure is verified by the ABAQUS step-by-step (SBS) inelastic FE analysis.
4) Develop an alternate procedure for the evaluation of the ratchet limit of structures subjected to arbitrary thermal-mechanical loading histories. Based on previous works [23, 24], a small and consistent value of ratchet strain is found alongside the structural ratchet boundary. Therefore, this objective is achieved by utilizing the UPFRA to scale the thermal-mechanical loads and call the DSCA module iteratively. The ratchet limit is determined when the

ratchet strain induced by the load point converges to the specified value. The numerical procedure is also verified by the SBS inelastic analysis.

A technology roadmap of the study is presented in Figure 1.1 for an intuitive illustration of the methodology of this thesis. The Bree-like diagrams are extended in four different ways, including the shakedown limit, creep rupture limit, the constant low cycle fatigue (LCF) life curves and the constant creep-fatigue life curves. This work is based on four different modules in the original platform of the LMM framework. A two-surface model is implemented in the LMM shakedown analysis module to calculate the shakedown limit considering kinematic hardening materials. Temperature-dependent material properties are considered. The UCRE has been developed and implemented in the LMM creep rupture analysis module. A general equation for the description of creep rupture curves of various types of steel is proposed. The UPFRA has been developed and implemented in the LMM fatigue analysis module. The extended UPFRA has been developed and implemented in the LMM creep-fatigue analysis module. A unified numerical procedure for fatigue, creep-fatigue and ratchet analyses is proposed for the evaluation of structural constant life diagram and ratchet limit. All the numerical methods stated above have been applied in several numerical examples, including benchmark cases and engineering cases. For benchmark cases, simple numerical examples are considered and the results are justified by comparing with either literature results or ABAQUS SBS analysis. For engineering cases, complicated numerical examples are considered and the structural cyclic plasticity and creep behaviours at high temperatures are illustrated and investigated.

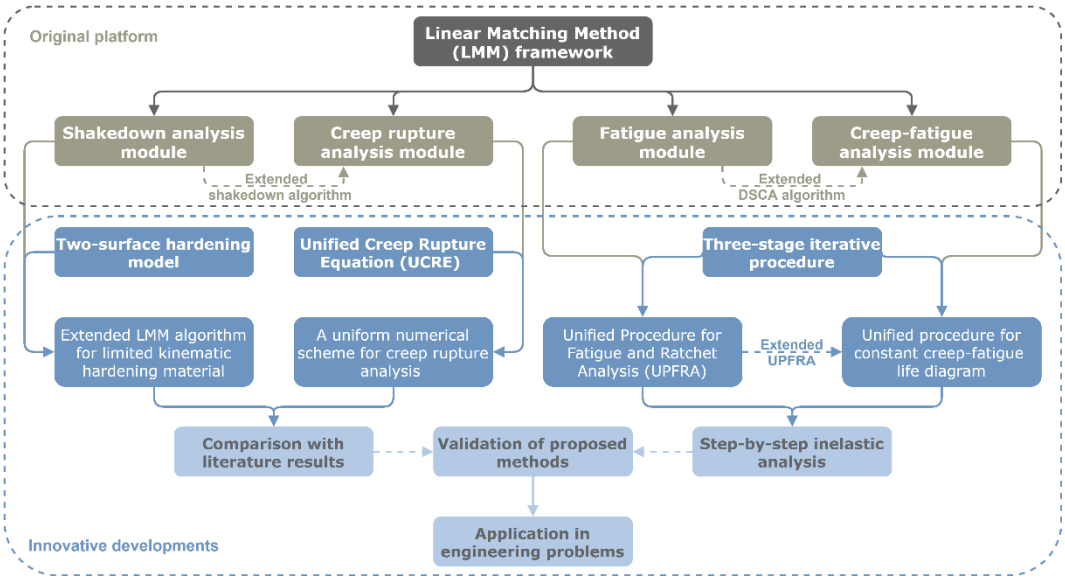

Figure 1.1: Technology roadmap of the study

1.4 Outline of the thesis

This thesis is composed of seven chapters as given below:

Chapter 2 presents a general review of high-temperature design and assessment methods. The theoretical backgrounds of the research are briefly introduced, including high-temperature structural cyclic response, R5 procedure and the current LMM framework.

Chapter 3 proposes a limited kinematic hardening algorithm for shakedown analysis, including the introduction of the two-surface model, Melan's extended shakedown algorithm and the implementation of the proposed method in the current LMM shakedown analysis module. Two numerical examples are presented.

Chapter 4 proposes a mathematical equation for creep rupture analysis. A Unified Creep Rupture Equation (UCRE) is introduced and implemented in the current LMM creep rupture analysis module. The equation is used to fit the rupture curves of various materials and is utilized in the parametric study of an industrial component. The corresponding creep rupture limit diagrams are presented.

Chapter 5 proposes a numerical procedure for fatigue and ratchet analysis. The Unified Procedure for Fatigue and Ratchet Analysis (UPFRA) is introduced to evaluate both the constant low cycle fatigue life curves and the ratchet boundary in the Bree-like diagrams considering arbitrary thermal-mechanical load histories. The procedure is integrated with the DSCA algorithm and implemented in the current LMM fatigue and ratchet analysis modules. Two numerical examples are presented.

Chapter 6 proposes a numerical procedure for creep-fatigue analysis, which is extended from the UPFRA and used to evaluate the structural constant creep-fatigue life curves. The procedure is integrated with the eDSCA algorithm and implemented in the current LMM creep-fatigue analysis modules. Constant LCF life curves are included in the existing Bree-like diagram. Two numerical examples are presented.

Chapter 7 concludes the outputs of the research and provides recommendations for future works.

2. Review of high-temperature analysis and assessment methods

2.1 Introduction

The topics of creep and cyclic plasticity have been intensely studied by numerous researchers in the past decades. The cyclic response of structures at high temperatures is introduced and reviewed in this chapter to give insight into the basic concept and fundamentals of this work. Cyclic plasticity response and corresponding failure mechanisms are briefly discussed with consideration of the creep effect. In addition, rule-based methods such as ASME NH and the R5 procedure have been introduced for the structural integrity assessment at high temperatures. Inelastic FE analysis is suggested for complicated cases that are not suitable to be designed by rules. For these complicated industrial problems, the Linear Matching Method (LMM) is one of the most advanced direct methods proposed to replace the inelastic FE analysis. With years of development, the LMM framework has included several modules for different steps in the R5 procedure. Since most works in this thesis are based on the LMM framework, the development history, advantages, and numerical procedures of the LMM are fully reviewed.

2.2 Cyclic response of structures at high temperature

2.2.1 The Bree diagram

When monotonic loads are applied within a structure, the load-bearing capacity of the structure is represented by the limit load. If the stress level reaches the limit load, the structure would fail by instantaneous collapse. However, the structural response becomes complicated when the loads applied are cyclic. An interaction diagram has been introduced by Bree [12] so that the structural response can be determined directly for various loading conditions. In Figure 2.1, a typical Bree diagram is presented for a cylinder subjected to constant pressure and cyclic thermal load. Both the mechanical and thermal stress has been normalised by the yield stress of material as the coordinate axes of the diagram. With different combinations of thermal and mechanical loads, four different structural responses are predicted in various regions separated by the Bree diagram.

When the applied stress is lower than the yield stress, the whole structure would remain elastic with limitless service life. When the applied stress goes beyond the yield stress but within the shakedown and ratchet limit, the elastic shakedown behaviour is expected. The stress-strain relationship becomes elastic after a few cycles, and the plastic strain remains constant. The lifespan of components operating in this region is often considered very long at more than 10000 cycles. When the cyclic thermal stress increases above twice the yield stress, the structural response of plastic shakedown would appear, and a closed hysteresis loop would form in local areas of the structure. In this case, the structural life highly depends on the strain range of the hysteresis loop with consideration of low cycle fatigue (LCF) damage. When the stress level increases over the ratchet limit, the ratchetting behaviour is observed where plastic strain accumulates at each cycle. The structure would fail by the mechanism of incremental collapse after a limited number of cycles. For most engineering problems, the component is usually designed to operate in the elastic or the elastic shakedown region for safety concerns.

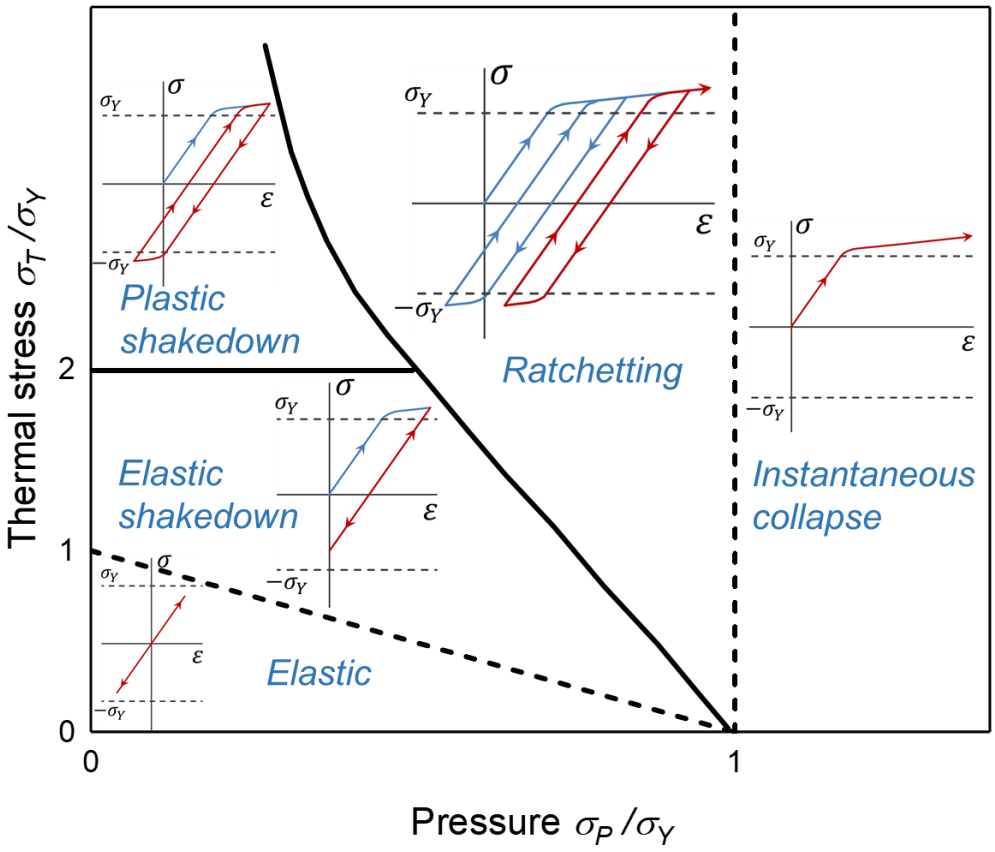

Figure 2.1: Typical Bree diagram [12] and cyclic response of structures

2.2.1.1 Elastic shakedown

The elastic shakedown region in the Bree diagram is delimited by the shakedown limit. For the evaluation of the shakedown limit, Melan's [25] and Koiter's [26] theories have been widely adopted for structural analysis. Considering elastic-perfectly plastic material, Melan's static shakedown theorem is given by:

"For given cyclic loads, the structure will shakedown if a constant self-equilibrium residual stress field is found while the yield condition is satisfied for any composition of cyclic stress and residual stress."

Koiter's kinematic shakedown theorem is defined by:

"For given cyclic loads $P(t)$ *over time period* t*, the structure will shakedown if the kinematically admissible strain rate is found while the strain field is compatible with the displacement field* u *satisfying specified boundary conditions and* $\int_0^t \sum P\dot{u} \geq \int_0^t \int_V \dot{D}dVdt$*, where* $\dot{D}$ *is the plastic dissipation rate corresponding to the admissible strain rate* $\dot{\varepsilon}$*."*

Melan's theorem produces a lower bound shakedown limit which is lower than the actual elastic shakedown limit. It is thus considered conservative and highly affected by the local stress concentration in the structure. Koiter's theorem provides an upper bound shakedown limit that is higher than the actual elastic shakedown limit. It is based on the global energy match between the internal and external work and is considered more reliable and accurate than Melan's theory. However, Koiter's theorem is also less conservative so that the actual elastic shakedown limit can be predicted between the upper and lower bound limits.

2.2.1.2 Plastic shakedown

The plastic shakedown region in the Bree diagram is delimited by both the reverse plasticity limit and the ratchet limit. For load cases inside the plastic shakedown region in the Bree diagram, the failure mechanism of low cycle fatigue (LCF) is observed, which significantly affects the predicted life of structures. LCF induces local failure in high-stress areas and crack initiation. Unlike high cycle fatigue (HCF), which is estimated using the stress amplitude σ_a and stress-life (S-N) curves, LCF considers the total strain range $\Delta\varepsilon_t$ as the main factor of damage evaluation. The total strain

range $\Delta\varepsilon$ is considered to be made up of two parts, the elastic strain range $\Delta\varepsilon_e$ and the plastic strain range $\Delta\varepsilon_p$:

$$\Delta\varepsilon_e N_f^{\alpha_1} = C_1 \tag{2.1}$$

$$\Delta\varepsilon_p N_f^{\alpha_2} = C_2 \tag{2.2}$$

where α_1, α_2, C_1, and C_2 are material constants corresponding to fatigue ductility. The Coffin-Manson [27, 28] relationship has been proposed to describe the relationship between the total strain range $\Delta\varepsilon_t$ and the number of cycles to failure N_f:

$$\frac{\Delta\varepsilon_t}{2} = \frac{\sigma_f'(2N_f)^b}{E} + \varepsilon_f'(2N_f)^c \tag{2.3}$$

where σ_f' denotes the fatigue strength and ε_f' is the fatigue ductility strength of the material. However, the Coffin-Manson model is based on several assumptions and lacks consideration of acceleration effects caused by stress relaxation and creep behaviour [29]. Based on the Coffin-Manson relationship, Manson has worked with other researchers and proposed a number of improved methods, including the Universal Slope Method (USM) [30] and the Modified Universal Slopes Method (MUSM) [31]. In addition, some other numerical methods have also been proposed for a better description of experiment curves, including the modified four-point correlation method [32], Mitchell's method [33], the Modified Mitchell's method [34], the Uniform material law [35], and the Medians method [36].

2.2.1.3 Ratchetting

The ratchetting region in the Bree diagram is delimited by both the ratchet limit and the limit load. When the load level is large enough to reach beyond the ratchet limit, the failure mechanism becomes incremental collapse where the plastic strain accumulates cycle by cycle. Ratchetting is a global behaviour and can be observed in multiple regions of the structure. It is considered dangerous for structures to operate in the ratchetting zone as the component's lifespan becomes extremely short after a few cycles. Therefore, ratchetting behaviour is usually avoided during the design process as recommended by design codes and assessment procedures.

There are several differences between the ratchetting behaviour observed at the material and structure level. At the material level, ratchetting is found in open

hysteresis loops caused by non-zero mean stress or zero mean stress with tension-compression asymmetry [37]. It is investigated in the bar experiment with cyclic tension loads, which creates a homogeneous cyclic stress field without residual stress. Material ratchetting involves a variable accumulation rate, and various complicated constitutive models have been proposed to describe the behaviour [38]. On the contrary, at the structure level, ratchetting can be detected in part of a component when the structural ratchet limit is reached. In this case, the cyclic stress field becomes inhomogeneous with complex residual stress. For the sake of simplicity, a constant accumulation is assumed for steady-state stress-strain behaviour. Also, the Elastic Perfectly Plastic (EPP) model is often used for the evaluation of the ratchet limit in engineering design and structural integrity assessment [39]. A two-bar experiment is presented in [40, 41] to further explain the structural ratchetting behaviour.

2.2.2 Material hardening under cyclic loads

2.2.2.1 Isotropic hardening

Plastic deformation can cause metals to harden under cyclic loads. In this case, the strength of the material would increase, which is related to the accumulated plastic strain p:

$$p = \int d\boldsymbol{\varepsilon}_p = \int \dot{\boldsymbol{\varepsilon}}_p dt \tag{2.4}$$

where $\dot{\boldsymbol{\varepsilon}}_p$ is the plastic strain rate and $d\boldsymbol{\varepsilon}_p$ is the effective plastic strain increment. In the 2D stress space, as shown in Figure 2.2, the yield surface expands when the stress level goes above the initial yield stress. The reverse yield stress also increases so that the material behaves elastically during the unloading stage while the overall strength grows. Since the yield surface expands uniformly in all directions, the hardening behaviour is considered isotropic [42]. The yield function is given by:

$$f(\boldsymbol{\sigma}, p) = \bar{\sigma} - \sigma_Y(p) = 0 \tag{2.5}$$

where the effective stress $\bar{\sigma} = \sqrt{\frac{3}{2}\boldsymbol{\sigma}' : \boldsymbol{\sigma}'}$. $\sigma_Y(p)$ is also given by:

$$\sigma_Y(p) = \sigma_{Y_0} + r(p) \tag{2.6}$$

where σ_{Y_0} denotes the initial yield stress and $r(p)$ represents an isotropic hardening function. To simulate an exponential stress-strain curve that gradually approaches a constant value, one of the most common forms of $r(p)$ is given by:

$$\dot{r}(p) = b(Q - r)\dot{p} \tag{2.7}$$

where Q and b are material parameters. Integrating equation (2.7) with $r(0) = 0$:

$$r(p) = Q\left(1 - e^{-bp}\right) \tag{2.8}$$

where the mathematical constant $e \approx 2.718$. The maximum size of the expended yield stress is determined by Q while the growth rate of the yield stress is dependent on b.

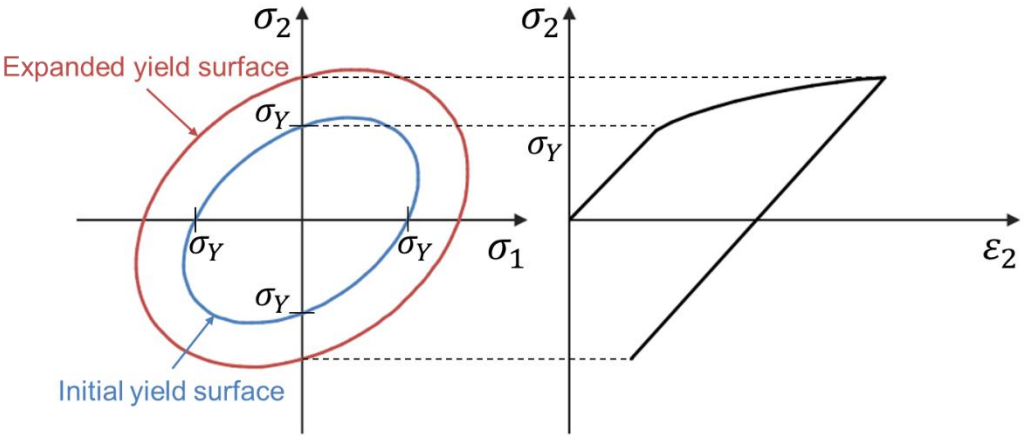

Figure 2.2: The yield surface and stress-strain curve of isotropic hardening behaviour

2.2.2.2 Kinematic hardening

For monotonic loading, isotropic hardening models can be considered reasonable to describe the stress-strain behaviour. However, for reversed loading cases, the isotropic hardening models would predict a large elastic region during the unloading stage. Thus, another type of hardening model – the kinematic hardening is introduced for cyclic loading cases, which produces smaller elastic regions. Instead of expansion, a translation of the yield surface is assumed in the stress space, which is also named the Bauschinger effect [22]. As shown in Figure 2.3, the yield surface translates upward by a back stress $|\boldsymbol{A}|$ when the stress reaches beyond the yield strength. The reversed yield stress also increases so that the elastic region during the unloading stage is twice the yield stress $2\sigma_Y$, while for isotropic hardening, the elastic region is $2(\sigma_Y + r)$. The consistency and normality conditions are still satisfied regarding the

plastic flow, so that the load point lies on the yield surface and the plastic strain is in the direction normal to the tangent line of the yield surface [42]. The yield function considering kinematic hardening then becomes:

$$f = \sqrt{\frac{3}{2}(\boldsymbol{\sigma}' - \boldsymbol{A}'):(\boldsymbol{\sigma}' - \boldsymbol{A}')} - \sigma_Y \tag{2.9}$$

A general form is considered to describe the back stress $\boldsymbol{A}$ in non-linear kinematic hardening:

$$d\boldsymbol{A} = \frac{2}{3}cd\boldsymbol{\varepsilon}_p - \gamma \boldsymbol{A}dp \tag{2.10}$$

where c and γ are material constants.

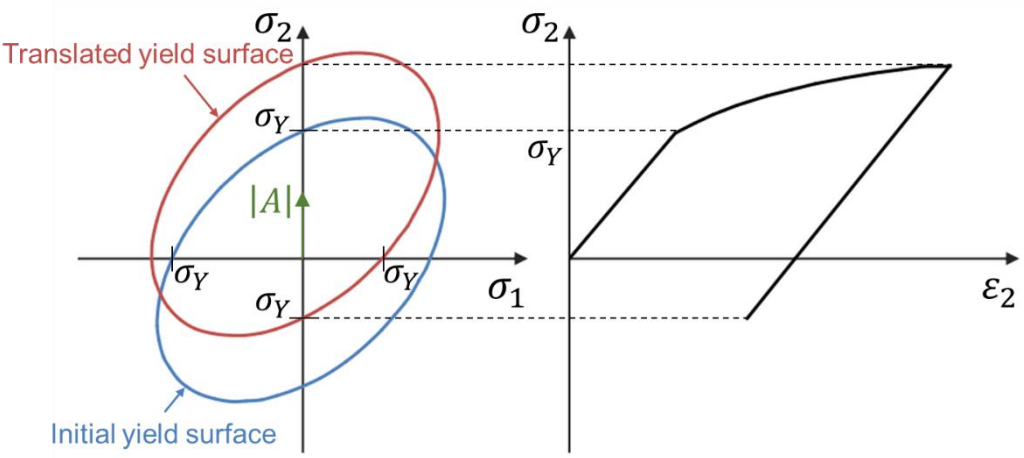

Figure 2.3: The yield surface and stress-strain curve of kinematic hardening behaviour

Over the years, many constitutive models have been proposed [43-45] to describe the cyclic hardening behaviour based on experiment results. Nevertheless, these models usually require a specific loading spectrum and evaluate the explicit back stress evolution, which can be complex and unrealistic to be implemented in direct methods. A two-surface model has thus been proposed [46] to simplify the problem by assuming the movement of the yield surface is constrained by an ultimate bounding surface.

2.2.2.3 Combined isotropic and kinematic hardening

For a component subjected to cyclic loading conditions, the isotropic and kinematic hardening behaviour can be observed simultaneously. The kinematic hardening

process is prominent as observed in each individual cycle, while the isotropic hardening process also accumulates cycle by cycle until saturation is achieved. The hysteresis loop is then formed when plotting the stress-strain relationship over the cycles. The increase of peak stress and strain in the hysteresis loop caused by the accumulated isotropic hardening is also called cyclic hardening [42]. By combining equations (2.8) and (2.9), the yield function considering combined hardening is then given by:

$$f = \sqrt{\frac{3}{2}(\boldsymbol{\sigma}' - \boldsymbol{A}'):(\boldsymbol{\sigma}' - \boldsymbol{A}')} - r(p) - \sigma_Y \tag{2.11}$$

The consistency condition is also given by:

$$\frac{\partial f}{\partial \boldsymbol{\sigma}} \cdot d\boldsymbol{\sigma} + \frac{\partial f}{\partial \boldsymbol{A}} \cdot d\boldsymbol{A} + \frac{\partial f}{\partial p} dp = 0 \tag{2.12}$$

Considering Hooke's law and equations (2.7) and (2.10), the consistency condition becomes:

$$\frac{\partial f}{\partial \boldsymbol{\sigma}} \cdot \boldsymbol{C}\left(d\boldsymbol{\varepsilon} - d\boldsymbol{\varepsilon}_p\right) + \frac{\partial f}{\partial \boldsymbol{A}} \cdot \left(\frac{2}{3} c d\boldsymbol{\varepsilon}_p - \gamma \boldsymbol{A} dp\right) - b\left(Q - r(p)\right) dp = 0 \tag{2.13}$$

where $\boldsymbol{C}$ is the elastic stiffness matrix. According to the normality hypothesis of plasticity:

$$d\boldsymbol{\varepsilon}_p = dp \frac{\partial f}{\partial \boldsymbol{\sigma}} \tag{2.14}$$

The effective plastic strain increment dp can then be calculated by rearranging equation (2.13) and substituting equation (2.14):

$$dp = \frac{\frac{\partial f}{\partial \boldsymbol{\sigma}} \cdot \boldsymbol{C} d\boldsymbol{\varepsilon}}{\frac{\partial f}{\partial \boldsymbol{\sigma}} \cdot \boldsymbol{C} \frac{\partial f}{\partial \boldsymbol{\sigma}} - \gamma \frac{\partial f}{\partial \boldsymbol{\sigma}} \cdot \boldsymbol{A} + \frac{2}{3} c \frac{\partial f}{\partial \boldsymbol{\sigma}} \cdot \frac{\partial f}{\partial \boldsymbol{\sigma}} + b\left(Q - r(p)\right)} \tag{2.15}$$

The effective plastic strain increment dp can also be determined by the increment of stress:

$$dp = \frac{\frac{\partial f}{\partial \boldsymbol{\sigma}} \partial \boldsymbol{\sigma}}{\frac{2}{3} c \frac{\partial f}{\partial \boldsymbol{\sigma}} \cdot \frac{\partial f}{\partial \boldsymbol{\sigma}} - \gamma \frac{\partial f}{\partial \boldsymbol{\sigma}} \cdot \boldsymbol{A} + b\left(Q - r(p)\right)} \tag{2.16}$$

2.2.3 Creep mechanism in structures subjected to monotonic load

Creep is a mechanism that affects the load-bearing capacity of materials at high temperatures. Influenced by time, pressure and temperature, the creep behaviour can be expressed in a creep strain versus time plot, as shown in Figure 2.4. There are three distinct stages in a tensile creep test curve: primary stage, secondary stage and tertiary stage. For the primary stage, the creep strain rate gradually reduces due to the hardening effect. For the secondary stage, the creep strain rate remains constant at a relatively low level. Intergranular damage can be observed during this stage. After that, the tertiary stage is reached while the creep strain rate progressively increases until creep rupture occurs. For some materials, the tertiary stage has a short period of time, which can be dangerous since the material would fail quickly. The microstructural mechanism of creep failure includes dislocation slipping, grain boundary sliding and diffusion of vacancies [47].

2.2.3.1 Primary and secondary creep

For the description of primary and secondary stages of creep, a Norton-Bailey law is proposed in the form of:

$$\dot{\bar{\varepsilon}}^c = A\bar{\sigma}^n t^m \tag{2.17}$$

where $\dot{\bar{\varepsilon}}^c$ denotes the effective creep strain rate, $\bar{\sigma}$ denotes the effective von-Mises stress, t denotes the dwell time, and A, n, and m are power-law parameters. As shown in Figure 2.4, the first two stages predicted by the Norton-Bailey law agree well with experimental curves. The total strain is then the sum of elastic, plastic and creep strain. For some materials, the primary stage of creep has a relatively short time period so that it can be neglected. The Norton law can then be adopted by setting $m = 0$ in equation (2.17) so that the equation becomes time-independent. Considering the non-isothermal effect, creep parameter A is temperature-dependent with application of the Arrhenius law:

$$A = A^* \exp\left(-\frac{Q}{RT}\right) \tag{2.18}$$

where A^* denotes the frequency factor, Q denotes the activation energy, R is the global gas constant, and T denotes the local temperature.

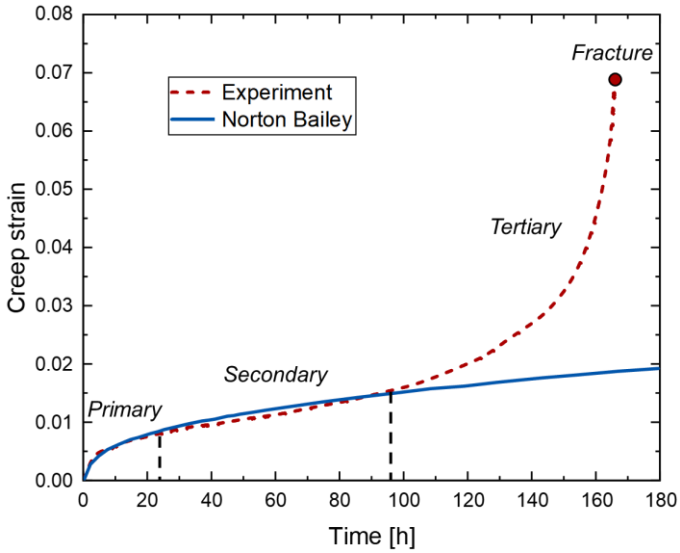

Figure 2.4: A tensile creep test curve interpolated by the Norton-Bailey law

2.2.3.2 Tertiary creep and creep rupture

At the end of the tertiary stage of creep, the creep rupture behaviour would occur due to the development and coalescence of micro voids in the structure. The fracture is initiated by three main factors. The first factor is the reduction of cross-section caused by the deformation of the whole component. The second factor is the recrystallization and the precipitation behaviours in the material caused by high operating temperature. The third factor is the stress concentration and intergranular cracking induced by the growth of original defects. Therefore, it is vital to study the relationship between creep rupture stress, temperature, and time to rupture in order to avoid the occurrence of creep rupture during the design stage.

The European Creep Collaborative Committee (ECCC) was established in 1991 to create systematic standards and design codes on creep rupture assessment for Europe. A “guidance for the assessment of full size creep rupture datasets” was published by the ECCC in 1996 to provide recommendations on the approaches for Creep Rupture Data Assessment (CRDA) [48]. A vast amount of creep rupture experiments have been performed by various members of ECCC, and the results have been collated and included in the ECCC data sheets [49]. Since many creep rupture tests are conducted in a short period of time at higher stress levels and temperatures, several extrapolation methods have been proposed for the prediction of long-term rupture data. The linear interpolation and extrapolation techniques are widely used due to their simplicity of implementation. However, these techniques are

often considered inaccurate to simulate curves with significant nonlinearity. The concept of temperature-dependent parameters is then proposed to combine rupture curves at different temperatures into one curve. The combined curve can be easily described with polynomial or exponential equations. One of the methods using this concept is the Larson-Miller parameter [50] with the form of:

$$P_{LM} = (T + 273.15) \cdot (\log(t_R) + C) \tag{2.19}$$

The Larson-Miller parameter assumes the presence of coincidence for all the iso-stress curves which is controlled by the material parameter C. For most steel, C is usually considered between 20 and 22. However, the Larson-Miller parameter may produce unreliable results for cases involving high temperature and low stress [51]. To solve this problem, the Manson-Haferd model [52] is then proposed, which contains two material parameters:

$$P_{MH} = \frac{\log(t_R) - \log(t_a)}{T - T_a} \tag{2.20}$$

In addition, the Ordd-Sherby-Dorn parameter [53] is proposed considering the physical and thermal behaviours of the material:

$$P_{OSD} = \log(t_R) - \frac{Q}{RT} \tag{2.21}$$

The Ordd-Sherby-Dorn parameter includes the activation energy Q and the universal gas constant R. Compared to models mentioned before, the Ordd-Sherby-Dorn parameter is capable of considering a wider range of temperatures. In decades, many other models [53-55] have also been proposed to improve and optimize the fitting process of creep rupture curves. However, most models mentioned above are only suitable to be applied for specific types of steel. They are not applicable for a wide range of materials and can be difficult to be implemented in direct methods. A numerical scheme has been developed in the Stress Compensation Method (SCM) [56, 57] for creep rupture assessment. However, this direct method is not considered user-friendly and its computational efficiency could be further improved.

2.2.4 Creep mechanism in structures subjected to cyclic load

Creep and fatigue are different structural mechanisms, but they interact with each other in various ways. On the micro level, the creep mechanism induces intergranular

damage with the growth of cavities, while the fatigue mechanism induces transgranular damage with the propagation of cracks [58]. Four different scenarios of interaction between creep and fatigue have been introduced in [59, 60]. The first scenario is pure fatigue behaviour, and surface crack is the primary failure mechanism. The second scenario is transgranular competing, where the cavity growth starts during creep dwell with the presence of transgranular cracks. The third scenario is mixed interaction, where intergranular damage gradually becomes dominant over transgranular damage. The fourth scenario is pure creep behaviour, where the creep dwell period is so long that the load cycle can be simplified to monotonic loads. Different creep mechanisms have various impact on the cyclic plasticity behaviour. A thermodynamically based model [61] has also been proposed to describe the interaction between creep and plasticity behaviours.

The effect of creep dwell on the stress-strain behaviour of typical cyclic responses has been presented in Figure 2.5. A simplified load cycle is considered with three stages: loading, creep dwell and unloading. A reduction of stress is often found in high-stress regions with the structure during the creep dwell stage. The phenomenon is called stress relaxation, which is caused by the conversion of elastic strain to creep strain. The reduction of elastic strain results in the decrease of stress under certain boundary conditions. When the overall stress is lower than the yield stress, the stress relaxation is observed with no plasticity in the structure, as shown in Figure 2.5(a). With the increase of stress level, the cyclic response becomes elastic shakedown with plasticity in the first few cycles, as shown in Figure 2.5(b). It can be observed that the curves at stress dwell follow the relaxation curve under monotonic load marked in red dashed lines. In Figure 2.5(c), a longer creep dwell time is applied in the load cycle, and a larger amount of stress relaxation is thus observed, which induces a higher level of residual stress at the unloading stage. Therefore, additional reverse plasticity is enhanced by creep dwell, and the stress-strain behaviour forms a closed loop. Figure 2.5(d) shows the plastic shakedown behaviour due to the high level of cyclic stress in the structure. The reverse plasticity is further enhanced by creep dwell and is observed at both loading and unloading stages. Both Figure 2.5(c) and Figure 2.5(d) show closed hysteresis loops, and the creep behaviour is also affected by cyclic plasticity. For each cycle, the creep strain and accumulated creep damage are enlarged due to the higher stress level at the start of the creep dwell stage compared to the monotonic load case. Therefore, this phenomenon is called “cyclically enhanced creep” [47].

The presence of creep dwell can also cause an open hysteresis loop which is known as the creep ratchetting behaviour. Ratchetting can be driven by the high level of either mechanical or thermal load while the plastic strain accumulates in each cycle [62, 63]. Although the cyclic behaviour without creep is elastic or plastic shakedown, structural ratcheting behaviour is still possible with the inclusion of the creep dwell period. Therefore, the creep ratchetting is a complex mechanism controlled by dwell time, load type, stress level and material properties. Two typical hysteresis loops of creep ratchetting are shown in Figure 2.5(e) and Figure 2.5(f). When the creep strain is relatively large, but the stress relaxation is small, the creep strain dominates and the hysteresis loop shifts toward the direction of creep strain (right), as shown in Figure 2.5(e). When the creep strain is relatively small but the stress relaxation is large, the reverse plastic strain dominates, and the hysteresis loop shifts toward the opposite direction (left), as shown in Figure 2.5(f). The enlarged amount of reverse plasticity is caused by the residual stress field after the stress relaxation behaviour. This phenomenon of creep-fatigue interaction is called “creep enhanced plasticity” [47]. Similar to regular ratchetting behaviour, the creep ratchetting can induce large creep-fatigue damage and should be avoided as possible during the design stage.

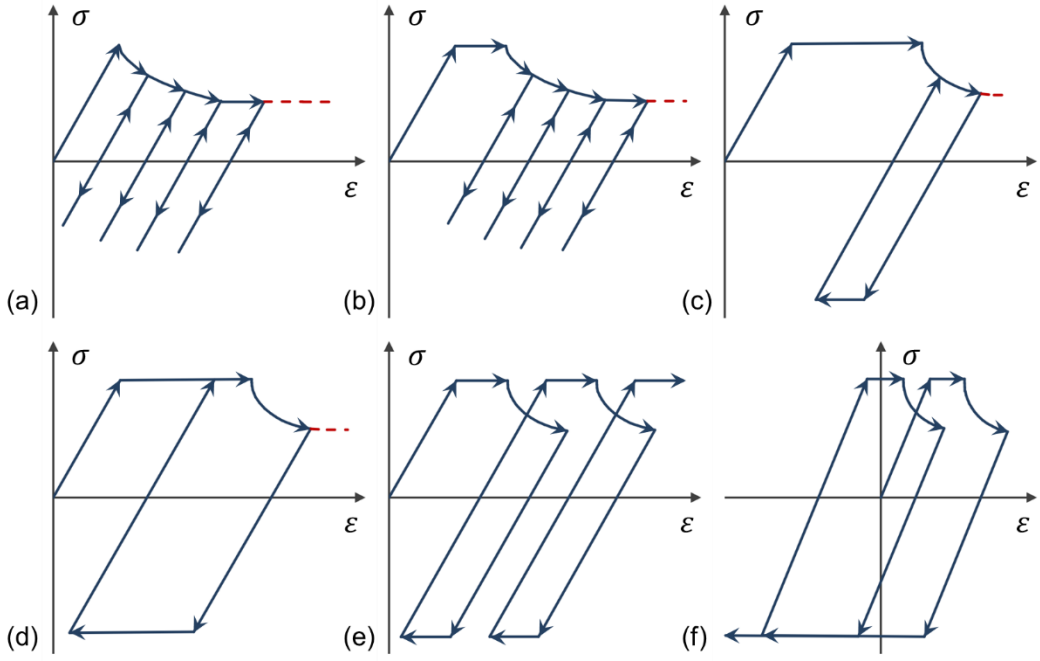

Figure 2.5: Effect of creep dwell on cyclic responses of (a) pure elastic (b) elastic shakedown (c) creep enhanced reverse plasticity (d) creep enhanced plastic shakedown (e) creep ratchetting dominated by creep strain (f) creep ratchetting dominated by plastic strain

2.2.5 The evaluation of creep-fatigue damage

2.2.5.1 The saturated hysteresis loops

To evaluate the creep and fatigue damage, it is important to plot the hysteresis loop at steady-state cycles. An example saturated hysteresis loop is presented in Figure 2.6(a). The nonlinear cyclic stress-strain relationship can be described by the Ramberg-Osgood (R-O) relationship by:

$$\Delta\varepsilon = \Delta\varepsilon_e + \Delta\varepsilon_p \tag{2.22}$$

$$\Delta\varepsilon_e = \frac{\Delta\sigma}{E} \tag{2.23}$$

$$\Delta\varepsilon_p = \left(\frac{\Delta\sigma}{A}\right)^{\frac{1}{\beta}} \tag{2.24}$$

where A and β are material parameters. Several parameters obtained from the hysteresis loop are crucial, including the start of dwell stress σ_s, the elastic follow up factor Z and the effective total strain range $\Delta\bar{\varepsilon}$. The elastic follow up factor Z is calculated by dividing the effective creep strain $\bar{\varepsilon}_c$ by the decrease of elastic strain during creep dwell:

$$Z = \frac{\bar{E}\bar{\varepsilon}_c}{\bar{\sigma}_s - \bar{\sigma}_c} \tag{2.25}$$

where $\bar{\sigma}_c$ denotes the effective stress at the end of dwell the effective elastic modulus $\bar{E} = \frac{3E}{2(1+\nu)}$. The value of Z highly depends on the boundary conditions. For extreme cases observed in experiments, $Z \to \infty$ when the specimen is stress-controlled or the load applied is primary, while $Z = 1$ when the specimen is strain-controlled or the load applied is secondary. With Z and σ_s available, the stress relaxation curve can be plotted and the average stress $\bar{\sigma}_{ac}$ during creep dwell can also be evaluated, as shown in Figure 2.6(b).

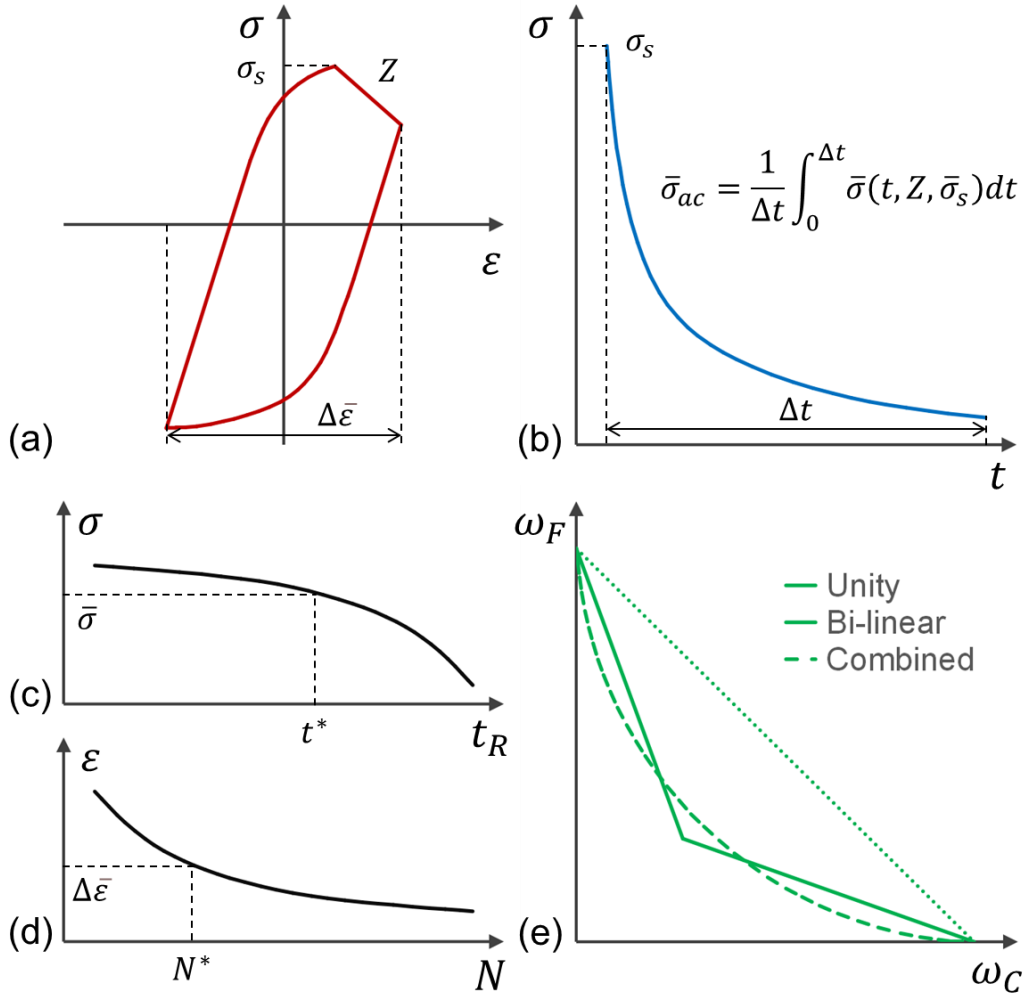

Figure 2.6: (a) Saturated hysteresis loop (b) stress relaxation curve (c) creep rupture curve (d) strain-life (E-N) curve (e) creep-fatigue interaction diagram

2.2.5.2 The evaluation of creep damage

With the assumption that the creep damage is unrelated to the loading sequence of stress, a linear damage accumulation rule has been proposed which is known as the Time Fraction rule (TF) rule [64]. The creep damage is determined by the limited creep life:

$$\omega_C^{TF} = \frac{\Delta t}{t^*(\bar{\sigma}_{ac}, T)} \tag{2.26}$$

where ω_C denotes the creep damage accumulated per cycle, Δt denotes the time of creep dwell, and t^* denotes the time to creep rupture. t^* can be evaluated by substituting the $\bar{\sigma}_{ac}$ and the temperature T in the creep rupture curve shown in Figure 2.6(c). The TF rule has also been adopted in ASME BPVC Section III Subsection NH

[5] for the evaluation of creep damage of structures subjected to varying tension loads. The TF rule is simple to use but lacks prediction accuracy [65].

With similar assumptions, another linear accumulation rule has been proposed which is known as the creep Ductility Exhaustion (DE) rule [66, 67]. The creep damage is determined by the limited creep strain:

$$\omega_C^{DE} = \frac{\dot{\bar{\varepsilon}}_c \Delta t}{\bar{\varepsilon}_c(\dot{\bar{\varepsilon}}_c, T)} \tag{2.27}$$

where $\dot{\bar{\varepsilon}}_c$ denotes the creep strain rate and $\bar{\varepsilon}_c$ is the uniaxial creep ductility calculated from the creep strain rate and temperature T. The DE rule has been adopted in the R5 procedure [7]. The DE rule provides better prediction accuracy but lacks consideration of creep-fatigue interaction [65]. In addition, some improved methods have been proposed based on the DE method, such as the Stress Modified Ductility Exhaustion (SMDE) method [68-70]. The effect of stress has been taken into account in the function $\bar{\varepsilon}_c$ by:

$$\omega_C^{SMDE} = \frac{\dot{\bar{\varepsilon}}_c \Delta t}{\bar{\varepsilon}_c(\dot{\bar{\varepsilon}}_c, \sigma, T)} \tag{2.28}$$

To improve the systematic prediction of creep-fatigue life considering multiple materials, the energy-based ductility exhaustion method (SEDE) has been proposed [71]. The creep damage at a saturated cycle ω_C^{SEDE} is given by:

$$\omega_C^{SEDE} = \int_0^{\Delta t} \frac{\dot{w}_{in}}{w_f(\dot{w}_{in}, T)} dt \tag{2.29}$$

where $\dot{w}_{in}$ denotes the energy density rate of inelastic strain, w_f denotes the failure strain energy density. The SEDE rule has both physical meaning and good prediction accuracy [65]. To consider the influence of multiaxial ductility, the multiaxial ductility factor (MDF) can also be multiplied in the denominator of creep ductility exhaustion rules described above. The MDF from the R5 procedure is given by:

$$MDF = \exp\left[p\left(1 - \frac{\sigma_1}{\bar{\sigma}}\right) + q\left(\frac{1}{2} - \frac{3\sigma_m}{2\bar{\sigma}}\right)\right] \tag{2.30}$$

where σ_1 denotes the maximum principal stress, σ_m denotes the mean stress, p and q are material constants.

2.2.5.3 The evaluation of fatigue damage

The fatigue life of materials can be described in three different forms: stress-life, strain-life, and energy-life [72]. The high cycle fatigue (HCF) damage can be determined by the stress amplitude σ_a and stress-life (S-N) curves, while the low cycle fatigue (LCF) damage can be evaluated based on the strain-life (E-N) diagram of the material and the effective total strain range $\Delta\bar{\varepsilon}$, as shown in Figure 2.6(d). The S-N curves are not suitable for the evaluation of LCF life for EPP models when the stress is unable to rise above the yield stress. Other methods for the LCF damage calculation have been mentioned in Section 2.2.1.2.

A linear accumulation rule known as the Palmgren-Miner rule [73, 74] has been proposed for the evaluation of fatigue damage. With the number of cycles to fatigue failure N^* available, the fatigue damage per cycle ω_F is given by:

$$\omega_F = \frac{1}{N^*} \tag{2.31}$$

The total fatigue damage D_F is then determined by the number of cycles n:

$$D_F = \sum \omega_F = \frac{n}{N^*} \tag{2.32}$$

The failure of material occurs at $D_F = 1$ when the capacity of fatigue life is exhausted.

2.2.5.4 The evaluation of creep-fatigue damage

After the calculation of creep and fatigue damage separately, the total damage can then be evaluated using the creep-fatigue interaction diagram, as shown in Figure 2.6(e). R5 procedure introduces the linear damage summation (LDS) rule as follows:

$$\omega_T = \omega_C + \omega_F \tag{2.33}$$

where ω_T denotes the total damage. The structure is considered safe without issues of crack initiation when $\omega_T < 1$. ASME NH and RCC-MR [6] suggest the use of a bi-linear relationship for the evaluation of total damage:

$$D_C + D_F \leq D \tag{2.34}$$

where D_C and D_F are accumulated creep and fatigue damage, and D denotes the creep-fatigue damage factor for the material. In addition, a nonlinear model has been

proposed in [75] to evaluate the combined creep-fatigue damage. When the total damage is smaller than 1, the concave failure locus is given by:

$$\frac{D_C}{1-D_F}+\frac{D_F}{1-D_C}\leq 1 \tag{2.35}$$

The LDS rule is simple to use but is unable to describe the creep-fatigue interaction properly. The strain range partitioning (SRP) model [76] is then proposed to address this issue. Based on the tensile or compressive portion of the cycle, the SRP divides the inelastic strain into three parts: ε_{pp}, ε_{cc}, and ε_{pc}. Each part is described by a power-law relationship:

$$\varepsilon_{jk}=C_{jk}N_{jk}^{-\beta_{jk}} \tag{2.36}$$

The accumulative damage is calculated by:

$$D_{jk}=\sum_i n_i\left(\frac{\varepsilon_{jk(i)}}{C_{jk}}\right)^{\frac{1}{\beta_{jk}}} \tag{2.37}$$

The creep-fatigue failure occurs when $D_{pp}+D_{cc}+D_{pc}=1$. The SRP model can predict the creep-fatigue interaction better than the LDS rule, but it can be highly difficult to separate the strain components in the hysteresis loop. Therefore, several numerical models have been proposed based on the mechanics of creep-fatigue interaction. A crack growth model [77] has been introduced based on the creep fracture mechanics:

$$\left.\frac{da}{dN}\right|_{cycle}=\left.\frac{da}{dN}\right|_{creep}+\left.\frac{da}{dN}\right|_{fatigue} \tag{2.38}$$

$$\left.\frac{da}{dN}\right|_{fatigue}=C_1\Delta J_{eff}^{\frac{n}{2}} \tag{2.39}$$

$$\left.\frac{da}{dN}\right|_{creep}=C_2C^{*n'} \tag{2.40}$$

where ΔJ_{eff} denotes the effective range of J-integral and C^* denotes the time-dependent path integral. Both creep fracture parameters are dependent on the crack size of the structure. Assuming the fatigue damage is determined by the crack size a while the creep damage is determined by the cavity size c, another mechanism-based model [78] has been proposed as follows:

$$\frac{1}{a}\frac{da}{dt} = \binom{T}{C}\left(1 + \alpha \ln\frac{c}{c_0}\right)|\varepsilon_{in}^{m}|\left|\dot{\varepsilon}_{in}^{k}\right| \tag{2.41}$$

$$\frac{1}{c}\frac{dc}{dt} = \binom{G_T}{-G_c}|\varepsilon_{in}^{m}|\left|\dot{\varepsilon}_{in}^{k}\right| \tag{2.42}$$

where c_0 denotes a threshold cavity size for the evaluation of the interaction between the growth of crack size and creep cavity. Based on the Kachanov's damage model [79], a unified damage model [80] is further proposed by:

$$\dot{\omega}|_{creep} = \frac{\dot{\omega}_{0,c}}{(1-\omega)^r} \tag{2.43}$$

$$\left.\frac{d\omega}{dN}\right|_{fatigue} = \frac{\dot{\omega}_{0,f}}{(1-\omega)^q} \tag{2.44}$$

$$\dot{\omega}_{0,c} = B_1\sigma^k \tag{2.45}$$

$$\dot{\omega}_{0,f} = B_2\Delta\sigma^s \tag{2.46}$$

where $\dot{\omega}_{0,c}$ and $\dot{\omega}_{0,f}$ are the growth rate of creep and fatigue damage when $\omega = 0$, B_1 and B_2 are temperature-dependent parameters, k, s, r and q are positive parameters, and ω is the common damage parameter for the description of creep-fatigue interaction damage. For a clear and intuitive demonstration of the proposed numerical methods in this thesis, the TF rule is adopted for the creep damage evaluation, the E-N diagram is adopted for the fatigue damage evaluation, and the LDS rule is adopted for creep-fatigue damage evaluation, as presented in Figure 2.6.

2.3 The R5 high-temperature assessment procedure

A preliminary version of the high-temperature assessment procedure was firstly proposed by the UK Central Electricity Generating Board (CEGB). The procedure is further developed by EDF Energy to include sections of defect, weldment, etc. Hence the R5 procedure has been proposed and widely adopted in nuclear industries in the UK. The R5 procedure provides a series of step-by-step instructions for engineers to assess the failure mechanism, crack initiation, crack propagation and life prediction for high-temperature components subjected to cyclic loads. In this section, the "volume 2/3: Creep-fatigue initiation procedure for defect-free structures" of the R5 procedure is introduced. This volume provides comprehensive step-by-step procedures to assess the number of cycles to crack initiation and the total creep-

fatigue damage. The last two steps have been neglected here since they are considered irrelevant to the scope of this study. The other 16 steps in the R5 volume 2/3 are briefly described below.

Step 1: resolve load history into cycle types.

The realistic loading history is simplified to reduce the number of service cycles for following fatigue assessment procedures. Standard techniques for the simplification process include the rainflow method or the reservoir method.

Step 2: perform elastic stress analysis.

The elastic analyses can be performed with Finite Element analysis or analytical solutions. The critical locations are selected where the maximum stress level or temperature is observed. Then the von Mises equivalent stress and strain ranges can be computed before the calculation of key equivalent stress values P_m, P_L, P_B, Q and F through the thickness of the structure.

Step 3: demonstrate sufficient margins against plastic collapse.

It is ensured that the plastic collapse does not occur upon the first loading process before the steady cyclic state is reached. The following conditions should be satisfied:

$$P_m \leq 0.67 S_y' \tag{2.47}$$

$$P_L + P_B \leq S_y' \tag{2.48}$$

$$\Delta(P_L + P_B + Q) \leq 2.0 S_y' \text{ for ferritic steels} \tag{2.49}$$

$$\Delta(P_L + P_B + Q) \leq 2.7 S_y' \text{ for austenitic steels} \tag{2.50}$$

where $S_y' = S_y = \sigma_Y$ for typical ferritic and austenitic steels. The satisfaction of equations (2.49) and (2.50) means the steady cyclic state operates within the global shakedown region. If the above conditions are not satisfied, further inelastic analyses may be required for the demonstration of margins.

Step 4: determine whether creep is significant.

The significance of creep strain depends on the type of loading cycle and temperature. The creep effect can be neglected when the following condition is satisfied:

$$\sum_j N_j \left[\frac{t}{t_m(T_{ref})}\right]_j \leq 1 \tag{2.51}$$

where N_j denotes the total number of cycles of each type of cycle j, t denotes the creep dwell time and t_m denotes the allowable time at the reference temperature T_{ref}. The insignificant creep curves have also been provided for the evaluation of t_m for different materials.

Step 5: demonstrate that creep rupture endurance is satisfactory.

Creep rupture is caused by primary loads on the structure so that the primary load reference stress is required. Together with Step 3, the primary loads are limited to prevent plastic collapse and creep rupture failure. For a simple geometry with a rectangular cross-section, the primary load reference stress σ_{ref} is given by:

$$\sigma_{ref} = \frac{P_B}{3} + \sqrt{\left(\frac{P_B}{3}\right)^2 + P_L^2} \tag{2.52}$$

Then the rupture reference stress σ_{ref}^R is calculated by:

$$\sigma_{ref}^R = [1 + 0.13(\chi - 1)]\sigma_{ref} \text{ for creep ductile materials} \tag{2.53}$$

$$\sigma_{ref}^R = \left[1 + \frac{1}{n}(\chi - 1)\right]\sigma_{ref} \text{ for other materials} \tag{2.54}$$

where n is the parameter from the Norton law and the stress concentration factor $\chi = \bar{\sigma}_{el,max}/\sigma_{ref}$. Here $\bar{\sigma}_{el,max}$ denotes the maximum equivalent stress that is evaluated elastically. For the above equations, it is acceptable to use $\chi \leq 4.0$. Otherwise, it is suggested to consider existing defects in the structure using the R5 volume 4/5. The creep usage factor U is evaluated by:

$$U = \sum_j N_j \left[\frac{t}{t_f\left(\sigma_{ref}^R, T_{ref}\right)}\right]_j \leq 1 \tag{2.55}$$

where t_f denotes the allowable time before rupture, which is derived from the creep rupture curves based on σ_{ref}^R and T_{ref}.

Step 6: perform simple test for shakedown and check for insignificant cyclic loading.

With the satisfaction of global shakedown conditions in Step 3, a test for the shakedown state can be conducted by assuming a zero residual stress field. The linearised equivalent elastic stress $\bar{\sigma}_{el,lin}$ at every location x in the structure over the time period t is limited by the modified yield stress:

$$\bar{\sigma}_{el,lin}(x,t) \leq K_s S_y \tag{2.56}$$

where K_s is a material constant. Also, the region of cyclic plasticity should satisfy the following condition:

$$\left(r_p\right)_i + \left(r_p\right)_o \leq 0.2w \tag{2.57}$$

where w denotes the section thickness. When the equations (2.56) and (2.57) are both satisfied, Step 7 can be skipped. In addition, it may be possible to determine the insignificant cyclic loading where the fatigue and creep behaviours are not affected by the cyclic loads applied. In this case, Steps 8 to 14 can be skipped. The insignificant cyclic loading is determined by the following criteria:

a) The load cycle operates within the elastic limit of the material.
b) The total fatigue damage is less than 0.05.
c) The creep behaviour is not affected by cyclic loading.

Step 7: perform global shakedown check and calculate cyclic plastic zone size.

For a detailed check on the shakedown status of the structure, both primary and secondary loads are considered. A constant residual stress field $\hat{\rho}(x)$ should be evaluated manually or achieved by post-processing the elastic analysis results. When checking the shakedown state manually, the stress at steady-state $\hat{\sigma}_s(x,t)$ is given by:

$$\hat{\sigma}_s(x,t) = \hat{\sigma}_{el}(x,t) + \hat{\rho}(x) \tag{2.58}$$

where $\hat{\sigma}_{el}(x,t)$ denotes the elastic stress field. The equivalent stress at steady-state $\bar{\sigma}_s(x,t)$ should satisfy the following shakedown criterion:

$$\bar{\sigma}_s(x,t) \leq K_s S_y \tag{2.59}$$

where K_s is a material constant. When using the post-processing technique, it is essential to present contours that distinguish shakedown and non-shakedown regions.

If the shakedown criterion is satisfied at over 80% of the thickness of each section, the whole structure may be considered to operate in the shakedown state.

Step 8: calculate shakedown reference stress, reference temperature and the start of dwell stress.

The steady-state equivalent stress from Step 7 is adopted to calculate the shakedown reference stress σ_{ref}^{S} at the reference temperature T_{ref}^{S}. The overall creep deformation and the creep rupture life can be further evaluated based on σ_{ref}^{S} and T_{ref}^{S}. When the structural response is global shakedown, a conservative creep usage is predicted. When the structural response is elastic shakedown, the start of dwell stress is considered identical to the primary load reference stress σ_{ref}. Therefore, the start of dwell stress σ_0 is given by:

$$\sigma_0 = \Delta\bar{\sigma}_{el,max} - \left(K_s S_y\right)_{nc} \tag{2.60}$$

For load points outside the shakedown limit, the predicted σ_0 may go above yield stress. In this case, a realistic value of σ_0 can be achieved by evaluating the steady-state hysteresis loop with cyclic stress-strain curves.

Step 9: estimate elastic follow-up factor and associated stress drop during creep dwell.

For components subjected to relatively large thermal stress and small mechanical loads, the stress relaxation and increase of strain may be observed during the creep dwell period. To describe the stress relaxation behaviour, the elastic follow up factor Z is given by:

$$Z = -\frac{\Delta\bar{\varepsilon}^{c}}{\Delta\bar{\varepsilon}^{e}} \tag{2.61}$$

where $\Delta\bar{\varepsilon}^{c}$ denotes the equivalent creep strain increment and $\Delta\bar{\varepsilon}^{e}$ denotes the equivalent elastic strain increment. Three simplified methods have been provided to evaluate the elastic follow up factor for different types of load cycles:

a) The stress relaxation is neglected by assuming $Z \to \infty$. This will lead to a conservative estimation of creep damage.

b) If the maximum variation of temperature in the structure is lower than 10 °C and the primary loads are much smaller than the secondary loads, it is conservatively assumed that $Z = 3$ when the following inequality is satisfied:

$$P_L + P_B < 0.2\sigma_{ref}^S \tag{2.62}$$

c) An inelastic elastic-creep computation is required with monotonic loading conditions applied. The alternation plasticity and creep behaviours are not considered to simplify the procedure. In this case, the elastic follow up factor is given by:

$$Z = \frac{\Delta\bar{\varepsilon}_{tot} + \frac{\Delta\sigma_{rD}}{\bar{E}}}{\frac{\Delta\sigma_{rD}}{\bar{E}}} \tag{2.63}$$

where $\Delta\bar{\varepsilon}_{tot}$ denotes the total strain increment, $\bar{E} = 3E/2(1+\nu)$ denotes the effective Young's modulus and $\Delta\sigma_{rD}$ denotes the drop in stress. If $Z \leq 1$, $\Delta\sigma_{rD}$ is taken from experiment results; if $Z > 1$, $\Delta\sigma_{rD}$ is replaced by $\Delta\sigma'$ which is a constant value from the cyclic relaxation data.

Step 10: calculate the total strain range.

To determine the strain range for fatigue assessment, the elastic stress history $\hat{\sigma}_{el}(x,t)$ from Step 2 is used. A simplified method considering the enhancement of plasticity and creep is then given to estimate the maximum equivalent fatigue strain range $\Delta\bar{\varepsilon}_t$ for each loading cycle type. The elastic stress range is enhanced by the stress relaxation value $\Delta\sigma_{rD}$ to compute the increased elastic stress range $\Delta\bar{\sigma}_{el,r}$:

$$\Delta\bar{\sigma}_{el,r} = \Delta\bar{\sigma}_{el} + \Delta\sigma_{rD} \tag{2.64}$$

The corresponding elastic strain range $\Delta\bar{\varepsilon}_{el,r}$ is given by:

$$\Delta\bar{\varepsilon}_{el,r} = \frac{\Delta\bar{\sigma}_{el,r}}{\bar{E}} \tag{2.65}$$

The steady-state cyclic stress-strain curves can be described by the Ramberg-Osgood (R-O) model by:

$$\Delta\varepsilon = \frac{\Delta\sigma}{E} + \left(\frac{\Delta\sigma}{A}\right)^{\frac{1}{\beta}} \tag{2.66}$$

where A and β are material parameters. The equivalent total strain range $\Delta\bar{\sigma}$ is achieved by solving the following equation:

$$\Delta\bar{\sigma}_{el,r}\Delta\bar{\varepsilon}_{el,r} = \frac{(\Delta\bar{\sigma}_{el}+\Delta\sigma_{rD})^2}{\bar{E}} = \Delta\bar{\sigma}\left[\frac{\Delta\bar{\sigma}}{\bar{E}} + \left(\frac{\Delta\bar{\sigma}}{A}\right)^{\frac{1}{\beta}}\right] \tag{2.67}$$

The total strain range $\Delta\bar{\varepsilon}_t$ is then given by:

$$\Delta\bar{\varepsilon}_t = \left[\frac{\Delta\bar{\sigma}}{\bar{E}} + \left(\frac{\Delta\bar{\sigma}}{A}\right)^{\frac{1}{\beta}}\right] + \Delta\bar{\varepsilon}_{vol} \tag{2.68}$$

where $\Delta\bar{\varepsilon}_{vol}$ denotes the enhancement caused by constant volume deformation, which is defined by:

$$\Delta\bar{\varepsilon}_{vol} = (K_\nu - 1)\Delta\bar{\varepsilon}_{el,r} \tag{2.69}$$

where

$$K_\nu = \left(\frac{1+\bar{\nu}}{1+\nu}\right)\left(\frac{1-\nu}{1-\bar{\nu}}\right) \tag{2.70}$$

$$\bar{\nu} = \frac{\nu E_s}{\bar{E}} + 0.5\left(1 - \frac{E_s}{\bar{E}}\right) \tag{2.71}$$

$$E_s = \frac{\Delta\bar{\sigma}}{\frac{\Delta\bar{\sigma}}{\bar{E}}+\left(\frac{\Delta\bar{\sigma}}{A}\right)^{\frac{1}{\beta}}} \tag{2.72}$$

where E_s denotes the secant modulus.

Step 11: check limits on cyclically enhanced creep and calculate creep usage factor.

The shakedown reference stress σ_{ref}^S and the reference temperature T_{ref}^S from Step 8 can be used here to check the enhancement of creep strain induced by cyclic thermal stress. To consider the effect of stress controlling deformation, the core stress is proposed which represents the stress level within the cross-section. For components subjected to constant primary loads and cyclic secondary loads, the load parameters X and Y are first calculated by:

$$X = \frac{\sigma_{ref}}{S_y} \tag{2.73}$$

$$Y = \frac{\Delta Q}{S_y} \tag{2.74}$$

where σ_{ref} denotes the reference stress from Step 5, and ΔQ denotes the maximum elastic thermal stress range within the structure. The core stress σ_{core} is then given by:

$$\sigma_{core} = \left[Y - 2\sqrt{Y(1-X)} + 1\right] S_y \qquad Y(1-X) < 1 \tag{2.75}$$

$$\sigma_{core} = XYS_y \qquad Y(1-X) \geq 1 \tag{2.76}$$

The core stress σ_{core} is considered to be less conservative to replace σ_{ref}^{s} in the following calculation. The limit on the creep usage factor W is given by:

$$W = \sum_j n_j \left[\frac{t}{t_f\left(\sigma_{ref}^{s}, T_{ref}^{s}\right)}\right]_j < 1.0 \tag{2.77}$$

where n_j denotes the total number of cycles for cycle type j, t denotes the time period when creep is significant, and t_f denotes the allowable time from the creep rupture curves.

Step 12: summarise assessment parameters.

A number of important parameters are summarised in this section to be used for the evaluation of creep-fatigue damage in Steps 14 and 15. The parameters required are listed as follows:

r_p: The size of the cyclic plastic zone is given in Step 7. It is further adopted in Step 14 for the estimation of initiation crack size.

T_{ref}^{s} and σ_0: The shakedown reference temperature and stress at the start of creep dwell are given in Step 8. They are both used in Step 15 for creep damage evaluation.

Z and $\Delta\bar{\sigma}'$: The elastic follow up factor and the drop of stress during creep dwell are given in Step 9. They are both used in Step 10 for the evaluation of the total strain range and in Step 15 for creep damage evaluation.

$\Delta\bar{\varepsilon}_t$: The total strain range is given in Step 10 and is used in Step 14 for the evaluation of fatigue damage.

W: The creep usage factor is given in Step 11. It is essential to ensure that $W < 1.0$ during the lifetime of the structure, but the value of W is not necessarily used for the evaluation of creep damage in Step 15.

Step 13: treatment of weldments.

For welded structures, the weldments are normally treated similarly to the parent material with several exceptions:

a) Differences in material properties between parent and weldment materials.
b) Welding defects introduced during the welding procedure.
c) Large residual stress introduced during the cooling process.
d) Differences in surface finish between “dressed” and “undressed” weldments.

With the presence of conditions listed above, it becomes necessary to treat the weldments differently from the parent material. The detailed procedure is not described here since it is out of the scope of this review.

Step 14: calculate fatigue damage per cycle.

The fatigue damage per cycle ω_F is calculated by:

$$\omega_F = \frac{1}{N_0} \tag{2.78}$$

where N_0 denotes the number of cycles to crack initiation with a crack size of a_0. It can be computed by the procedure given below:

a) The fatigue endurance data is acquired as well as the fatigue strength reduction factor for the consideration of ageing and environment.
b) The fatigue endurance data is divided into curves that show the relationship between the number of cycles to failure and the total strain range. The number of cycles to crack nucleation N_i and crack growth N_g are given by:

$$\ln(N_i) = \ln(N_l) - 8.06N_l^{-0.28} \tag{2.79}$$

$$N_g = N_l - N_i \tag{2.80}$$

c) Assume the initial crack size a_i grows to size a_0 and the number of cycles $N_g' = MN_g$. The value M is given by:

$$M = \frac{a_{min}\ln\left(\frac{a_0}{a_{min}}\right)+(a_{min}-a_i)}{a_{min}\ln\left(\frac{a_l}{a_{min}}\right)+(a_{min}-a_i)} \qquad \text{for } a_0 > a_{min} \tag{2.81}$$

$$M = \frac{a_0-a_i}{a_{min}\ln\left(\frac{a_l}{a_{min}}\right)+(a_{min}-a_i)} \qquad \text{for } a_0 < a_{min} \tag{2.82}$$

where $a_{min} = 0.2\ \text{mm}$. The fatigue endurance N_0 for crack size a_0 is then given by:

$$N_0 = N_i + N_g' \tag{2.83}$$

Step 15: calculate creep damage per cycle.

If the insignificant cyclic loading criteria in Step 6 are satisfied, the creep damage per cycle ω_C is calculated by:

$$\omega_C = \frac{t_h}{t_r\left(\sigma_{ref}^R\right)} \tag{2.84}$$

where t_h denotes the creep dwell time and $t_r\left(\sigma_{ref}^R\right)$ denotes the creep rupture time of the material at the rupture reference stress σ_{ref}^R from equation (2.54). For cases with significant cyclic loading, the ductility exhaustion method is adopted to evaluate creep damage ω_C:

$$\omega_C = \int_0^{t_h} \frac{\dot{\bar{\varepsilon}}_c}{\bar{\varepsilon}_f(\dot{\bar{\varepsilon}}_c)}\,dt \tag{2.85}$$

where $\dot{\bar{\varepsilon}}_c$ denotes the equivalent creep strain rate and $\bar{\varepsilon}_f(\dot{\bar{\varepsilon}}_c)$ denotes the corresponding creep ductility.

Step 16: calculate total damage.

The total damage D is evaluated by the sum of total fatigue damage D_F and total creep damage D_C over the cyclic history:

$$D = D_F + D_C \tag{2.86}$$

$$D_F = \sum_j \frac{n_j}{N_{0j}} = \sum_j n_j d_{Fj} \tag{2.87}$$

$$D_C = \sum_j n_j d_{Cj} \tag{2.88}$$

where n_j denotes the number of cycles of type j and N_{0j}, d_{Fj} and d_{Cj} denote the corresponding values of N_0, d_F and d_C of type j. A crack initiation envelope can then be plotted on which $D_F + D_C = 1$. For an assessment point (D_F, D_C) located inside the envelope, $D < 1$ and the crack initiation does not occur. For the assessment point outside the envelope, $D \geq 1$ and crack initiation occurs. A further creep-fatigue crack growth assessment is then required, which is given in the R5 volume 4/5.

2.4 The Linear Matching Method (LMM) framework

In the R5 procedure and ASME codes, the incremental Finite Element (FE) analysis is recommended as the primary approach during the design by analysis process. The incremental FE analysis can be performed on complicated engineering structures subjected to cyclic thermal-mechanical loads. Also, sophisticated constitutive models can be applied to describe the inelastic stress-strain relationship of realistic engineering materials. However, it is often considered time-consuming and difficult to converge. In addition, a large number of repetitive simulations are required when plotting the structural response boundaries, such as the Bree diagram. Therefore, numerical direct methods have been developed to replace the incremental FE analysis gradually. Based on a few assumptions, the direct methods can provide results with similar accuracy but also with better efficiency compared to the incremental FE analysis.

Over the past decades, many direct methods have been proposed, including the mathematical programming methods [81-86] and a number of modified elastic modulus methods [14, 87-90], including the Reduced Modulus Method [87], the Generalised Local Stress-Strain (GLOSS) Method [88, 91], the Elastic Compensation Method (ECM) [89, 92], the Modified Elastic Compensation Method (MECM) [93], the Non-linear Superposition Method [94], the Stress Compensation Method (SCM) [95] [96], and the Linear Matching Method (LMM) [14, 90]. Among them, the LMM framework is one of the most advanced and versatile tools for structural integrity assessment.

2.4.1 The general numerical procedure of the current LMM

Consider a body with volume V and surface S. It is subjected to cyclic temperature $\lambda_\theta \theta(x,t)$ in V and cyclic pressure $\lambda_P P(x,t)$ on the part of the surface S_T. The

remainder part of the surface S is restricted to have zero displacements. Here x denotes the location in the body, and t is constrained by the time cycle $0 \leq t \leq \Delta t$. Assume the body is constructed with an elastic-perfectly plastic (EPP) material. The linear elastic stress history in the structure is then given by:

$$\hat{\sigma}_{ij}(x,t) = \lambda_\theta \hat{\sigma}_{ij}^{\theta}(x,t) + \lambda_P \hat{\sigma}_{ij}^{P}(x,t) \tag{2.89}$$

where $\hat{\sigma}_{ij}^{\theta}$ and $\hat{\sigma}_{ij}^{P}$ are the linear elastic solution calculated with $\theta(x,t)$ and $P(x,t)$, λ_θ and λ_P are the thermal and mechanical multipliers which are used to construct arbitrary combinations of loading history. The general stress field is then given by:

$$\sigma_{ij}(x,t) = \hat{\sigma}_{ij}(x,t) + \bar{\rho}_{ij}(x) + \rho_{ij}^{r}(x,t) \tag{2.90}$$

where $\bar{\rho}_{ij}(x)$ denotes a constant residual stress field that is self-equilibrium and independent of time, ρ_{ij}^{r} denotes a varying residual stress field that is dependent on time. For elastic shakedown problems, the varying residual stress field is ignored so that $\rho_{ij}^{r} = 0$. Considering a kinematically admissible strain rate history $\dot{\varepsilon}_{ij}^{c}$, a minimization procedure has been proposed to evaluate various structural limits and cyclic responses. The simplified minimization function is given by:

$$I\left(\dot{\varepsilon}_{ij}^{c}, \lambda\right) = \sum_{n=1}^{N} I^{n} \tag{2.91}$$

$$I^{n}\left(\Delta\varepsilon_{ij}^{n}, \lambda\right) = \int_{V} \left(\sigma_{ij}^{n}\Delta\varepsilon_{ij}^{n} - \sigma_{ij}(x,t)\Delta\varepsilon_{ij}^{n}\right) dV \tag{2.92}$$

$$\rho_{ij}^{r}(x,t) = \sum_{n=1}^{N} \Delta\rho_{ij}(t_n) \tag{2.93}$$

where N denotes the number of load instances in a load cycle, t_n denotes the current load instance, λ denotes a general load multiplier which is applied on all loads in the structure, $\Delta\rho_{ij}$ denotes the varying residual tress increment and $\Delta\varepsilon_{ij}^{n}$ denotes the strain increment. To iteratively solve the minimization problem, a series of linear equations are defined by:

$$\Delta\varepsilon_{ij,k+1}(t_n)' = \frac{1}{2\bar{\mu}_k(t_n)}\left[\hat{\sigma}_{ij}(t_n) + \rho_{ij,k+1}(t_{n-1}) + \Delta\rho_{ij,k+1}(t_n)\right]' \tag{2.94}$$

$$\Delta\varepsilon_{kk,k+1}(t_n)' = 0 \tag{2.95}$$

where symbol $'$ denotes the deviatoric stress component, k is the iteration number and $\bar{\mu}_k$ denotes the iterative shear modulus, which is constantly revised to match the yield condition. At iteration $k+1$, the shear modulus is updated by:

$$\bar{\mu}_{k+1}(x,t_n) = \frac{\bar{\mu}_k(x,t_n)\sigma_Y(x,t_n)_k}{\bar{\sigma}\left[\hat{\sigma}_{ij}(x,t_n)+\rho_{ij}^r(x,t_n)_k\right]} \tag{2.96}$$

where $\rho_{ij}^r(x,t_n)_k$ denotes the summation of constant and varying residual stress fields at different load instances. $\sigma_Y(x,t_n)_k$ denotes the iterative yield stress. It can be a constant value for the EPP model or a strain-dependent value based on the Ramberg-Osgood (R-O) model to consider cyclic hardening behaviour. For evaluation of creep rupture limit, the yield stress is revised by the rupture strength of the material. For load cycles with creep dwell, the yield stress is revised by the creep flow stress. The original LMM algorithm for shakedown analysis is shown below. All the other modules in the LMM framework are based on the concept of the original LMM algorithm. A detailed introduction of the numerical procedures for different modules in the LMM framework is given in the following chapters.

2.4.2 The original LMM algorithm for shakedown analysis

2.4.2.1 Melan's static shakedown theorem

For the computation of the lower bound shakedown limit, Melan's static shakedown theorem [97] has been adopted. The total linear elastic stress field is first calculated by:

$$\lambda\hat{\sigma}_{ij} = \lambda\hat{\sigma}_{ij}^{\theta} + \lambda\hat{\sigma}_{ij}^{P} \tag{2.97}$$

where $\hat{\sigma}_{ij}^{\theta}$ and $\hat{\sigma}_{ij}^{P}$ are linear elastic stress fields generated by $\theta(x_i,t)$ and $P_i(x_i,t)$.

A residual stress field is observed in the structure when steady-state is reached during the time cycle $0 \le t \le \Delta t$:

$$\sigma_{ij}(x_i,t) = \lambda\hat{\sigma}_{ij}(x_i,t) + \bar{\rho}_{ij}(x_i) + \rho_{ij}^r(x_i,t) \tag{2.98}$$

where $\bar{\rho}_{ij}(x_i)$ denotes a self-equilibrium constant residual stress field, while $\rho_{ij}^r(x_i,t)$ denotes a varying residual stress field. For shakedown problems, $\rho_{ij}^r(x_i,t) = 0$. Melan's static shakedown theorem is then given by:

The structure will shake down, when a constant residual stress field can be found so that the steady-state stress field satisfies the von Mises yield condition for arbitrary load paths from a specific loading domain:

$$f_Y\left[\lambda\hat{\sigma}_{ij}(x_i,t)+\bar{\rho}_{ij}(x_i),\sigma_Y(x_i)\right]\leq 0,\forall x\in V,\forall t \tag{2.99}$$

2.4.2.2 The LMM theorem

The LMM method considers a kinematically admissible strain rate history $\dot{\varepsilon}_{ij}^{c}$, which matches a compatible strain increment $\Delta\varepsilon_{ij}^{c}$:

$$\int_0^{\Delta t}\dot{\varepsilon}_{ij}^{c}dt=\Delta\varepsilon_{ij}^{c} \tag{2.100}$$

which is also compatible with a displacement increment field:

$$\Delta\varepsilon_{ij}^{c}=\frac{1}{2}\left(\frac{\partial\Delta u_i^{c}}{\partial x_j}+\frac{\partial\Delta u_j^{c}}{\partial x_i}\right) \tag{2.101}$$

The upper bound shakedown limit is calculated by:

$$\lambda_{UB}\int_V\int_0^{\Delta t}\left(\hat{\sigma}_{ij}\dot{\varepsilon}_{ij}^{c}\right)dtdV=\int_V\int_0^{\Delta t}\left(\sigma_{ij}^{c}\dot{\varepsilon}_{ij}^{c}\right)dtdV \tag{2.102}$$

where σ_{ij}^{c} is the stress at yield state, $\hat{\sigma}_{ij}$ is the elastic linear solution from equation (2.97). Adopting the corresponding flow rule, equation (2.102) can be further simplified by:

$$\lambda_{UB}=\frac{\int_V\int_0^{\Delta t}\sigma_Y\bar{\dot{\varepsilon}}\left(\dot{\varepsilon}_{ij}^{c}\right)dtdV}{\int_V\int_0^{\Delta t}\left(\hat{\sigma}_{ij}\dot{\varepsilon}_{ij}^{c}\right)dtdV} \tag{2.103}$$

where $\bar{\dot{\varepsilon}}=\sqrt{\frac{2}{3}\dot{\varepsilon}_{ij}\dot{\varepsilon}_{ij}}$ denotes the effective strain rate.

A series of linear equations is then defined using the general programming skill given in [98]. The final plastic strain rate history $\dot{\varepsilon}_{ij}^{f}$ is derived from an initial kinematically admissible strain rate history $\dot{\varepsilon}_{ij}^{i}$:

$$\dot{\varepsilon}_{ij}^{f\prime}=\frac{1}{\mu}\left(\lambda_{UB}^{i}\hat{\sigma}_{ij}+\bar{\rho}_{ij}^{f}\right)' \tag{2.104}$$

$$\dot{\varepsilon}_{kk}^{i}=0 \tag{2.105}$$

$$\mu = \frac{\sigma_Y}{\bar{\dot{\varepsilon}}^i} \tag{2.106}$$

where $\bar{\rho}_{ij}^f$ is a constant residual stress field defined in equation (2.98). The symbol $'$ denotes the deviatoric component of a tensor. The shear modulus μ is defined by matching the stress state to elastic perfectly plastic material at the start of each iteration. Over the time cycle, equation (2.104) can be integrated so that:

$$\Delta\varepsilon_{ij}^{f\,\prime} = \frac{1}{\bar{\mu}}\left(\bar{\rho}_{ij}^{f\,\prime} + \sigma_{ij}^{in\,\prime}\right) \tag{2.107}$$

$$\sigma_{ij}^{in\,\prime} = \bar{\mu}\left\{\int_0^{\Delta t} \frac{1}{\mu(t)} \lambda_{UB}^i \hat{\sigma}_{ij}'(t)dt\right\} \tag{2.108}$$

$$\frac{1}{\bar{\mu}} = \int_0^{\Delta t} \frac{1}{\mu_n} dt \tag{2.109}$$

The linear problem described above would produce a monotonically decreasing shakedown multiplier which becomes a converged minimum upper bound eventually using equation (2.103):

$$\lambda_{ij}^f \leq \lambda_{ij}^i \tag{2.110}$$

2.4.2.3 Implementation of numerical procedures in ABAQUS

For the convex yield condition, the load history is described by straight loading paths in load space. Plastic strains are only observed at the vertices of the loading space. The vertices are expressed by individual load instances, which simplified the problem proposed above. The integration process of the strain rate history is then replaced by the sum of values at load instances:

$$\Delta\varepsilon_{ij}^c = \sum_{n=1}^r \Delta\varepsilon_{ij}^n \tag{2.111}$$

An initial stress field is then defined to solve the linear problem in equation (2.104):

$$\sigma_{ij}^{in\,\prime} = \bar{\mu}\left\{\sum_{n=1}^r \frac{1}{\mu_n} \lambda \hat{\sigma}_{ij}'(t_n)\right\} \tag{2.112}$$

$$\frac{1}{\bar{\mu}} = \sum_{n=1}^r \frac{1}{\mu_n} \tag{2.113}$$

where

$$\mu_n = \frac{\sigma_Y}{\bar{\varepsilon}(\Delta\varepsilon_{ij}^{ni})} \tag{2.114}$$

To implement the procedure described above in ABAQUS, an iterative process is proposed using the user subroutine UMAT and URDFIL [99]. At the first iteration $k = 1$, $\bar{\mu}^1 = 1$. $\hat{\sigma}_{ij}(t_n)$ is calculated with external loads without scaling. At the $(k+1)^{\text{th}}$ iteration,

$$\lambda^{k+1} = \lambda_{UB}^k \tag{2.115}$$

$$\mu_n^{k+1} = \frac{\sigma_Y}{\bar{\varepsilon}_n^k} \tag{2.116}$$

where

$$\bar{\varepsilon}_n^k = \bar{\varepsilon}\left(\Delta\varepsilon_{ij}^{nk}\right) \tag{2.117}$$

$$\frac{1}{\bar{\mu}^{k+1}} = \sum_{n=1}^{r} \frac{1}{\mu_n^{k+1}} \tag{2.118}$$

Then the Jacobian matrix $[J]^{k+1}$ is defined with updated shear modulus $\bar{\mu}^{k+1}$ in UMAT, which describes the relationship between stress and strain. The initial stress field is then given by:

$$\sigma_{ij}^{in\,k+1} = \bar{\mu}^{k+1}\left(\sum_{n=1}^{r} \frac{\lambda^{k+1}\hat{\sigma}_{ij}(t_n)}{\mu_n^{k+1}}\right) \tag{2.119}$$

The constant residual stress field is computed by:

$$\bar{\rho}_{ij}^{k+1} = [J]^{k+1}\Delta\varepsilon_{ij}^{k+1} - \sigma_{ij}^{in\,k+1} \tag{2.120}$$

The strain rate at the vertices of load space is calculated by:

$$\Delta\varepsilon_{ij}^{n(k+1)} = [C]_n^{k+1}\left(\bar{\rho}_{ij}^{k+1} + \hat{\sigma}_{ij}^{k+1}(t_n)\right) \tag{2.121}$$

where $[C]_n^{k+1}$ denotes the stiffness matrix calculated with $\bar{\mu}_n^{k+1}$. Using the energy output function in ABAQUS, the volume integration $\int_V \left(\sigma_Y \sum_{n=1}^{r} \bar{\varepsilon}_n^{k+1}\right) dV$ and $\int_V \left(\sum_{n=1}^{r} \Delta\varepsilon_{ij}^{n(k+1)}\hat{\sigma}_{ij}(t_n)\right) dV$ are then calculated. The shakedown multiplier is determined by:

$$\lambda_{UB}^{k+1} = \frac{\int_V \left(\sigma_Y \sum_{n=1}^{r} \bar{\varepsilon}_n^{k+1}\right) dV}{\int_V \left(\sum_{n=1}^{r} \dot{\varepsilon}_{ij}^{n(k+1)} \hat{\sigma}_{ij}(t_n)\right) dV} \tag{2.122}$$

2.4.3 The development of the current LMM plug-in

As one of the most advanced Finite Element software, ABAQUS/CAE provides a comprehensive solution for FE modelling, visualization and process automation. Based on the ABAQUS platform, Abaqus/Standard is a generalised FE analysis programme with a powerful nonlinear solver, a user-friendly graphic interface and a versatile development platform [21]. ABAQUS plug-in is a tool located in the ABAQUS/CAE interface, which provides a programming environment for user customization. As shown in Figure 2.7(a), there are two main types of ABAQUS plug-in: kernel plug-in and GUI plug-in. Kernel plug-in directly issues commands to the kernel to accomplish simple tasks such as setting viewport and display options. For more complicated tasks, the GUI plug-in is user-friendly and can be constructed using the GUI toolkit or the RSG dialog builder. The RSG dialog builder is a built-in plug-in in ABAQUS and contains basic widgets for the execution of kernel commands. The GUI toolkit is an advanced option for the creation of a GUI plug-in. It provides over 500 Python classes to control the pre-processing, modelling and post-processing stages during the simulation process. It can also work with user-subroutines based on FORTRAN to describe material constitutive equations and configure user-defined elements. A complete GUI plug-in typically consists of several elements, including start-up script, application object, main window, GUI modules, modes, dialogs, and widgets. As shown in Figure 2.7(b), the ABAQUS GUI plug-in is based on Abaqus, Python and GUI, which are also mutually connected. Firstly, the kernel of ABAQUS/CAE is scripted by Python, which is an open-source, object-oriented programming language. Python has become one the most popular language in the world with high efficiency, high compatibility and short development periods. Also, ABAQUS/CAE provides a GUI toolkit for the creation of a user-defined interface. In addition, GUI commands include both basic Python modules and Abaqus kernel scripts. The GUI plug-in interacts with the kernel by a series of procedures, including post dialog box, process query, execute commands and handle exceptions [21].

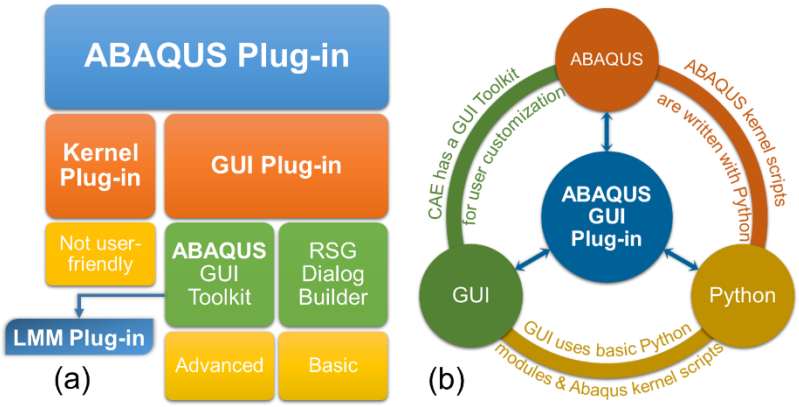

Figure 2.7: (a) The main types of ABAQUS plug-ins (b) The composition of the ABAQUS GUI plug-in

At the early stage of development, the LMM is written in FORTRAN as ABAQUS user subroutines. Since the use of subroutines requires sufficient knowledge of FORTRAN programming and LMM algorithms, it becomes difficult for engineers to learn and use the LMM subroutine. Users are prone to make mistakes due to the large number of modifications needed when employing the LMM in industrial cases. Therefore, the LMM subroutines are gradually updated to the version of an ABAQUS GUI plug-in. The LMM plug-in is capable of gathering information in a graphic interface, modifying the FE model for LMM computation, and updating keywords for LMM outputs. Users can firstly configure the FE model for elastic analysis in ABAQUS/CAE, before running the LMM plug-in and filling in the material properties and load cycles. The LMM job is then created for submission. The whole process is straightforward and user-friendly, while the chance of encountering errors is minimized. In addition, the LMM plug-in enables the use of multiple processors when submitting the job, which dramatically improves the overall computational efficiency. The main progression during the developing history of the LMM is given in Figure 2.8(a). In 2001, the LMM subroutine for shakedown and limit analyses for 3D structures was created [14]. In 2003, the LMM subroutine for creep rupture analysis was developed based on the extended shakedown algorithm [15]. Then in 2010, the Direct Steady Cycle Analysis (DSCA) subroutine was proposed for ratchet and fatigue analysis [16]. In 2014, the LMM plug-in was developed with LMM and DSCA subroutines included [17, 18]. In the same year, the extended Direct Steady Cycle Analysis (eDSCA) subroutine was developed for creep-fatigue analysis based on the DSCA subroutine [19]. In 2017, the LMM plug-in was further extended by including the eDSCA subroutine [20]. Therefore, the original version of the LMM plug-in is comprised of 5 different modules for different

types of industrial problems, as shown in Figure 2.8(b). An LMM framework has been established with the implementation of shakedown, creep rupture, ratchet, low-cycle fatigue and creep-fatigue modules, which provides a complete solution to structural integrity assessment problems.

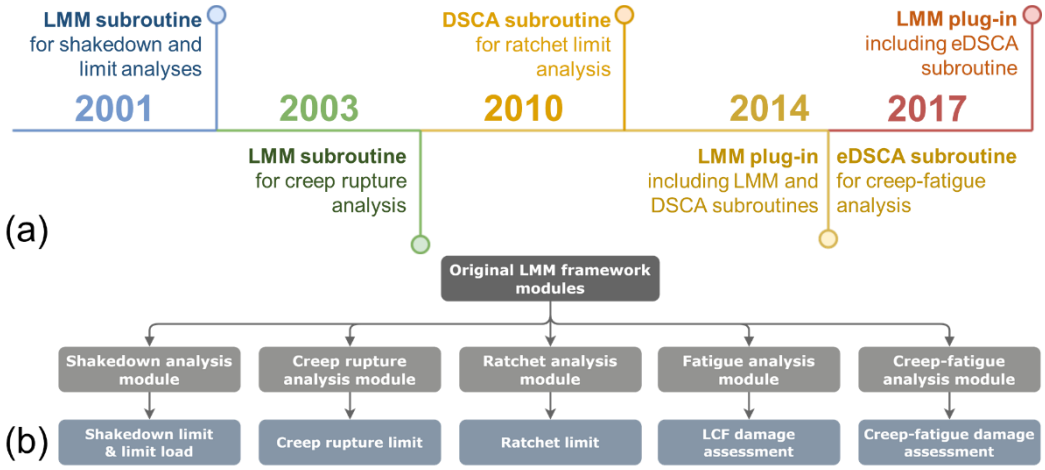

Figure 2.8: (a) The history of the development of the LMM (b) Original modules in the LMM framework

As presented in Figure 2.9, there are several main features of the LMM framework. Firstly, the LMM plug-in is based on ABAQUS/CAE, which is a popular commercial FE software with a large user base. Secondly, as a direct method, the LMM calculates much faster than the inelastic step-by-step FE analysis but with similar accuracy. The LMM procedure is also easier to converge, especially for complicated geometry and loading spectrum. Thirdly, the LMM framework has been successfully adopted in many industrial and research projects and produced satisfactory results. Fourthly, as an Abaqus plug-in, the LMM is designed to be easy to install and simple to use for engineers among industries. Fifthly, the LMM framework is continuously being developed and updated with new features added and bugs fixed by the Structural Integrity and Life Assessment (SILA) group based at the University of Strathclyde. Lastly, the LMM framework has been developed to be an alternative method for international codes and procedures, such as ASME, R5 and RCC-MRx.

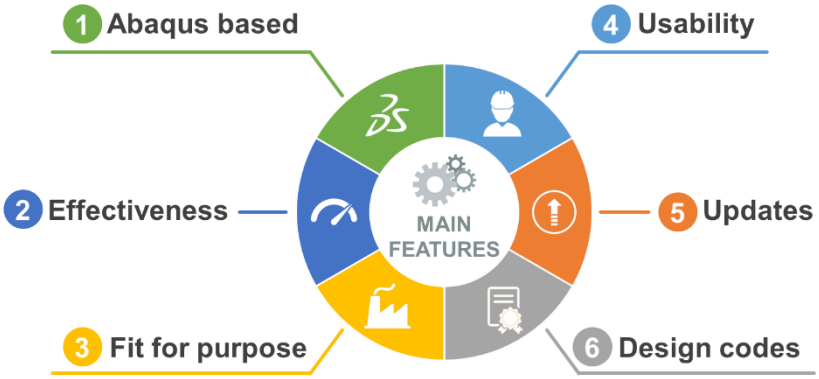

Figure 2.9: Main features of the LMM framework

The LMM framework can be used to support the computation of several main steps of the R5 volume 2/3 introduced in Section 2.3, as shown in Figure 2.10. For some steps, full inelastic analyses are suggested by R5 for the evaluation of some key parameters. Since full inelastic analyses require a lot of computational resources and detailed constitutive equations, they are often not viable and efficient enough for engineering problems. The LMM framework is thus developed to solve the main steps in the R5 procedure with high efficiency and reliability. The R5 procedure starts by defining the load, temperature and material properties. The linear elastic FE analysis is then performed for both thermal and mechanical loads. This process is also performed in the pre-processing module in the LMM framework. Then in R5, the safe margins against plastic collapse are assessed, as well as the rupture limit if creep is significant. The limit analysis is done using a special case in the LMM shakedown module, and the creep rupture analysis is done using the LMM extended shakedown module. After that, the shakedown analysis is recommended by R5 by considering the residual stress field. This part is performed by the LMM shakedown module, which provides both upper and lower bound solutions. The LMM can also produce the ratchet limit of the structure to prevent incremental collapse using a combined shakedown and DSCA module. If reverse plasticity is significant, R5 recommends a low cycle fatigue assessment by evaluating the total strain range. This part is conducted in the LMM DSCA module, which produces the hysteresis loop and fatigue damage per cycle. When the creep is considered significant during the load cycle, R5 suggests the creep-fatigue analysis, where the creep and fatigue damage is evaluated separately. This part can be accomplished in the LMM eDSCA module, which calculates the saturated hysteresis loop with creep dwell and creep-fatigue interaction damage. Therefore, the LMM framework provides a viable solution for nearly every step in the R5 volume 2/3 for a complete structural integrity assessment.

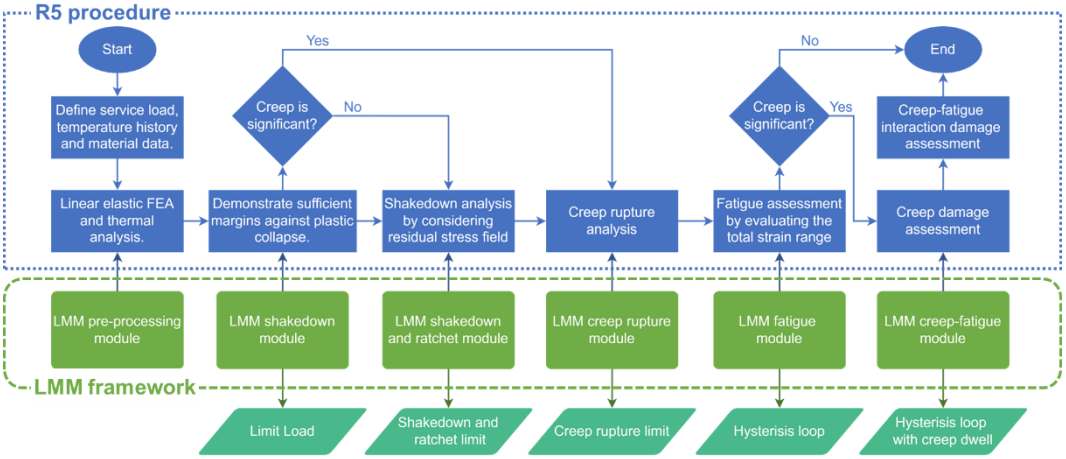

Figure 2.10: The use of the LMM framework in support of the R5 procedure

2.5 Summary

In this chapter, the cyclic response of structures at high temperatures is comprehensively reviewed. The Bree diagram and corresponding failure mechanisms have been introduced for the time-independent cyclic response. The differences between HCF and LCF, structural ratchetting and material ratchetting, have been discussed. The material hardening under cyclic loads and numerical models have also been introduced, including isotropic hardening, kinematic hardening and combined hardening. In addition, the creep mechanism in structures subjected to monotonic load has been reviewed, including the introduction of primary, secondary and tertiary creep stages. The creep rupture behaviour is also reviewed, as well as popular numerical models to describe the relationship between rupture stress, time to rupture and temperature. Finally, the creep mechanism in structures subjected to cyclic load has been introduced where the creep and fatigue behaviours interact with each other. The creep ratchetting behaviour is also discussed, as well as creep-fatigue interaction phenomena such as “cyclically enhanced creep” and “creep enhanced plasticity”. The evaluation of creep-fatigue damage is further introduced based on several international design codes such as ASME NH, R5 procedure and RCC-MR.

The main steps in volume 2/3 of the R5 procedure have been reviewed in detail due to their correlation with the scope of the thesis. Some key concepts in R5 have been introduced, as well as the rule-based procedures for complete structural integrity assessment. For complicated cases where rules are not suitable to comply with,

inelastic FE analysis is suggested for the evaluation of specific parameters. As a replacement for the inelastic FE analysis, the LMM framework is proposed by previous researchers as one of the most advanced direct methods. The LMM consists of several modules to support each step in the R5 volume 2/3, including the shakedown, fatigue, ratchet, creep rupture and creep-fatigue modules based on different algorithms. With decades of development by the SILA group, the LMM plug-in has become a versatile, efficient and reliable engineering tool for structural integrity assessment.

3. The evaluation of the shakedown limit considering limited kinematic hardening material

3.1 Introduction

To evaluate the load-bearing capacity of structures undergoing cyclic thermal-mechanical loads, the shakedown analysis is often performed as part of the structural integrity assessment. By allowing a relatively small amount of plastic strain, the shakedown limit has been considered as an essential indicator when the total plastic dissipation is bounded in the structure [100]. The shakedown factor is then proposed, which scales the external loads proportionally to the limit of structural failure. Two failure mechanisms are often observed when the loads exceed the shakedown limit: low-cycle fatigue and incremental collapse [101]. Many approaches have been proposed to evaluate the shakedown factor, as introduced in Chapter 2. The Linear Matching Method (LMM) is one of the direct methods that calculate the shakedown limit considering elastic-perfectly plastic (EPP) material. The LMM theorem is based on a small deformation assumption without considering any creep effect. It consists of Koiter's kinematic theorem [26] for the upper bound shakedown solution, as well as Melan's static theorem [97] for the lower bound shakedown limit calculation.

However, for materials subjected to cyclic loading with reverse plasticity, the Bauschinger effect [22] may be observed so that the yield strength would be different from the one with monotonic loading. Due to the kinematic hardening effect of materials, the shakedown limit computed using the EPP constitutive model may be over-conservative and inaccurate. A two-surface model [46] is adopted in this work to describe the translation of yield surface. This model has been combined with Melan's static theorem [97] and adopted in many direct methods [46, 100, 102-109] to consider the influence of kinematic hardening on the shakedown limit. Unlike unlimited kinematic hardening where the yield surface translation is unrestricted [110, 111], limited nonlinear kinematic hardening is considered in this work where the back stress is implicitly restricted by the ultimate bounding surface [100]. Some researchers have also considered linear hardening laws for the bounding of back stress known as

limited linear kinematic hardening [104, 109], but it is only applicable for specific types of material.

Although many researchers have considered thermal stress in their research [108, 109, 112, 113], few have investigated the effect of temperature-dependent material properties. It is widely acknowledged that the yield strength of some materials greatly varies due to the non-isothermal effect in a component. The corresponding shakedown limit also significantly differs from the case when constant material parameters are applied throughout the structure. In this work, the LMM algorithm has been extended to include limited nonlinear kinematic hardening for general materials using the two-surface model [114]. Temperature-dependent material parameters have also been considered and applied in the computation of shakedown boundaries for complex engineering structures. The LMM subroutines have been newly updated so that the shakedown boundaries considering EPP materials, unlimited hardening, and limited kinematic hardening can be calculated simultaneously. In addition, since the LMM framework uses the concept of the shakedown theorem in the ratchet analysis module [16, 24], the ratchet limit considering kinematic hardening has also been realized.

In this study, the Bree-like diagram is extended by including the shakedown limit considering limited kinematic hardening material. The description of the extended LMM algorithm considering limited kinematic hardening material in Section 3.2. Two numerical examples are given in Section 3.3 to demonstrate the reliability and usability of the proposed method.

3.2 Extended LMM algorithm considering limited kinematic hardening material

3.2.1 Extended Melan's static shakedown theorem

Considering an isotropic material with limited kinematic hardening, which satisfies the two-surface hardening model. The yield surface is bounded by an initial yield stress σ_Y and an ultimate strength σ_U.

A two-surface model proposed by [46] has been considered here to simulate the limited kinematic hardening behaviour. The yield surface can freely move inside the bounding surface, where the size of both surfaces is fixed, as shown in Figure 3.1.

The back stress is denoted by $A_{ij}(x_i)$ which is the translation tensor of the yield surface centre. The stress at yield is denoted by $\sigma_{ij}^{'c}$, where $\sigma_{ij}^{'c}(x_i,t) = \lambda\hat{\sigma}_{ij}(x_i,t) + \bar{\rho}_{ij}(x_i)$. Within the original yield stress, the reduced stress is denoted by $\nu_{ij}'(x_i,t)$, so that:

$$f_Y\left[\,\sigma_{ij}^{'c}(x_i,t) - A_{ij}(x_i), \sigma_Y(x_i)\right] \leq 0 \tag{3.1}$$

The stress at yield $\sigma_{ij}^{'c}(x_i,t)$ is also bounded by the outer bounding surface:

$$f_U\left[\sigma_{ij}^{'c}(x_i,t), \sigma_U(x_i)\right] \leq 0 \tag{3.2}$$

Since the stress at yield can be expressed as $\sigma_{ij}^{'c}(x_i,t) = \lambda\hat{\sigma}_{ij}(x_i,t) + \bar{\rho}_{ij}(x_i)$, the extended Melan's static shakedown theorem is given as follows:

The structure will shake down, when a constant residual stress field and a constant back stress field can be found so that both the von Mises yield condition and the bounding condition are satisfied for arbitrary load paths from a specific loading domain:

$$f_Y\left[\lambda\hat{\sigma}_{ij}(x_i,t) + \bar{\rho}_{ij}(x_i) - A_{ij}(x_i), \sigma_Y(x_i)\right] \leq 0 \tag{3.3}$$

$$f_U\left[\lambda\hat{\sigma}_{ij}(x_i,t) + \bar{\rho}_{ij}(x_i), \sigma_U(x_i)\right] \leq 0 \tag{3.4}$$

The theorem has been explained in [108], where no particular hardening rules are adopted. It has also been implemented in several direct methods as a general nonlinear kinematic hardening law. No explicit back stress field is calculated during the iteration process, so the extended shakedown theory has been greatly simplified with only two parameters: the yield stress and the ultimate stress. However, it is worth mentioning that there are a number of assumptions in the theorem as stated in [115], such as the maximal dissipation hypothesis, the positive hysteresis postulate, the multiaxial Bauschinger hypothesis, and the strictly-stable hardening hypothesis.

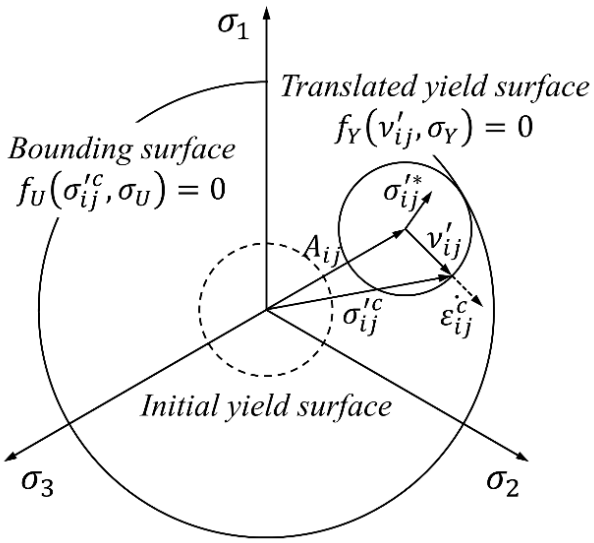

Figure 3.1: A two-surface model for the description of limited kinematic hardening behaviour in the deviatoric plane

3.2.2 The effect of temperature-dependent material properties

Since the performance of material can significantly degrade with increasing temperature, it is vital to consider the non-isothermal effect during FE analysis. In this work, both the yield stress σ_Y and the ultimate stress σ_U in the two-surface model are defined to be temperature-dependent. Linear interpolation and extrapolation techniques are adopted when evaluating parameters at integration points in the structure. The ultimate stress is often defined as follows:

$$\sigma_U = K\sigma_Y \tag{3.5}$$

where K is a constant hardening factor. Due to the consideration of the non-isothermal effect, the hardening factor also becomes a dynamic ratio between the ultimate stress and the yield stress:

$$K(T) = \frac{\sigma_U(T)}{\sigma_Y(T)} \tag{3.6}$$

For the selection of material parameters mentioned above, it is recommended in [116] to take the “fatigue limit for arbitrary high-cycle loading” for σ_Y and the “high-cycle ratchetting” for σ_U. However, these material properties are rarely mentioned in other literature and corresponding experimental data are also limited. Thus in this work, 0.2% proof stress $\sigma_s(T)$ and the ultimate tensile strength $\mathrm{UTS}(T)$ are selected for the numerical examples in Section 3.3, so that:

$$\mathrm{UTS}(T) = K(T)\sigma_s(T) \tag{3.7}$$

3.2.3 A two-stage numerical procedure

The proposed numerical procedure of the extended shakedown algorithm consists of two stages. Two stages are operated in the UMAT subroutine simultaneously to satisfy equations (3.3) and (3.4). Based on the maximum work principle:

$$\left(\sigma_{ij}^{\prime c} - A_{ij}\right)\dot{\varepsilon}_{ij}^{c} \geq \left(\sigma_{ij}^{\prime *} - A_{ij}\right)\dot{\varepsilon}_{ij}^{c} \tag{3.8}$$

The strain increment $\Delta\varepsilon_{ij}^{c}$ is compatible and is the integration of the kinematically admissible strain rate history $\dot{\varepsilon}_{ij}^{c}$:

$$\int_0^{\Delta t} \dot{\varepsilon}_{ij}^{c} dt = \Delta\varepsilon_{ij}^{c} \tag{3.9}$$

A displacement increment field Δu_i^c is also given by,

$$\Delta\varepsilon_{ij}^{c} = \frac{1}{2}\left(\frac{\partial \Delta u_i^c}{\partial x_j} + \frac{\partial \Delta u_j^c}{\partial x_i}\right) \tag{3.10}$$

Stage 1 evaluates the shakedown limit considering unlimited hardening, which satisfies equation (3.3). The corresponding shakedown factor λ_{UH} is defined by:

$$\lambda_{UH} = \min\left\{\frac{\sigma_Y(T)}{\bar{\sigma}\left(\widehat{\sigma}_{ij}(t_n) + \overline{\rho}_{ijUH} - A_{ij}\right)}\right\} \tag{3.11}$$

where $\bar{\sigma}$ denotes the effective von Mises stress. Stage 2 utilizes the original LMM shakedown subroutine to evaluate the shakedown multiplier λ which satisfies equation (3.4):

$$\lambda = \frac{\int_V \int_0^{\Delta t} \sigma_{U(T)} \bar{\dot{\varepsilon}}\left(\dot{\varepsilon}_{ij}^{c}\right) dt dV}{\int_V \int_0^{\Delta t} \widehat{\sigma}_{ij}\dot{\varepsilon}_{ij}^{c} dt dV} \tag{3.12}$$

where the effective strain rate $\bar{\dot{\varepsilon}} = \sqrt{(2/3)\dot{\varepsilon}_{ij}\dot{\varepsilon}_{ij}}$. The shakedown factor considering kinematic hardening λ_{KH} is then calculated after the completion of both stages:

$$\lambda_{KH} = \min\{\lambda_{UH}, \lambda\} \tag{3.13}$$

A series of linear equations are then given to solve the numerical problem described above. The shear modulus is updated iteratively at every gauss point in the structure

to match the von Mises yield condition, as shown in Figure 3.2. For stage 1, the linear problem is:

$$\dot{\varepsilon}_{ijUH}^{f'} = \frac{1}{\mu_{UH}(t)}\left\{\lambda_{UH}^{i}\hat{\sigma}_{ij}(t) + \left(\bar{\rho}_{ijUH} - A_{ij}\right)^{f}\right\}' \tag{3.14}$$

where the shear modulus $\mu_{UH}(t) = \sigma_Y(T)/\bar{\dot{\varepsilon}}(\dot{\varepsilon}_{ij}^{i})$. The symbol $'$ denotes the deviatoric component of tensors. $\dot{\varepsilon}_{ijUH}^{f}$ denotes a kinematically admissible strain rate history. $\bar{\rho}_{ijUH}$ denotes a constant residual stress field. A_{ij} denotes the back stress. Equation (3.14) is further integrated over the time cycle:

$$\Delta\varepsilon_{ijUH}^{f'} = \left\{\int_0^{\Delta t}\frac{1}{\mu_{UH}}\lambda_{UH}^{i}\hat{\sigma}_{ij}dt\right\} + \left\{\int_0^{\Delta t}\frac{1}{\mu_{UH}}dt\right\}\left(\bar{\rho}_{ijUH} - A_{ij}\right)^{f'} \tag{3.15}$$

For unlimited hardening limit, $\Delta\varepsilon_{ijUH}^{f'} = 0$. $\left(\bar{\rho}_{ijUH} - A_{ij}\right)^{f'}$ can then be solved by:

$$\left(\bar{\rho}_{ijUH} - A_{ij}\right)^{f'} = -\frac{\int_0^{\Delta t}\frac{1}{\mu_{UH}}\lambda_{UH}^{i}\hat{\sigma}_{ij}dt}{\int_0^{\Delta t}\frac{1}{\mu_{UH}}dt} \tag{3.16}$$

Equation (3.16) is then substituted into Equation (3.14) for the evaluation of $\dot{\varepsilon}_{ijUH}^{f'}$. The unlimited hardening limit multiplier λ_{UH} is finally calculated with Equation (3.11).

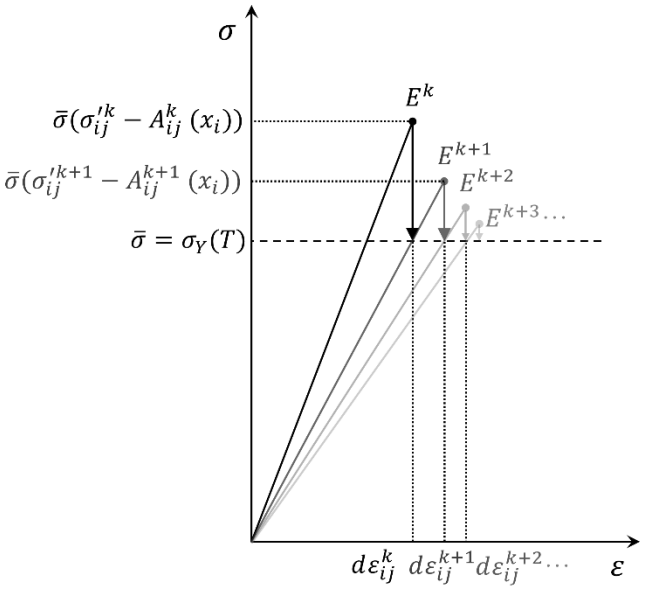

Figure 3.2: The matching procedure of the LMM considering kinematic hardening behaviour

For stage 2, the original LMM shakedown algorithm is adopted as given in Section 2.4.2.2. Instead of using the yield stress σ_Y, the ultimate strength σ_U is adopted here when evaluating the shear modulus. The linear problem is given as:

$$\dot{\varepsilon}_{ij}^{f'} = \frac{1}{\mu}\left(\lambda^i \hat{\sigma}_{ij} + \bar{\rho}_{ij}^{f}\right)' \tag{3.17}$$

where $\mu = \sigma_U(T)/\bar{\dot{\varepsilon}}$. Equation (3.17) is then integrated over the time cycle:

$$\Delta\varepsilon_{ij}^{f'} = \frac{1}{\bar{\mu}}\left(\bar{\rho}_{ij}^{f\,\prime} + \sigma_{ij}^{in'}\right) \tag{3.18}$$

where $\sigma_{ij}^{in'} = \bar{\mu}\{\int_0^{\Delta t} \frac{1}{\mu(t)} \lambda^i \hat{\sigma}_{ij}'(t)dt\}$ and $\frac{1}{\bar{\mu}} = \int_0^{\Delta t} \frac{1}{\mu_n} dt$. A monotonically decreasing upper bound multiplier λ is finally evaluated with Equation (3.12).

3.2.4 Implementation of numerical procedures in ABAQUS

The numerical procedure described above has been fully implemented in ABAQUS using the FORTRAN subroutine. Similar to Section 2.4.2.3, the integration function over the time cycle has been simplified to the sum operator at each load instance. The iteration process is presented in a flowchart, as shown in Figure 3.3.

1) For iteration number $k = 1$, the initialization procedure is firstly performed:

$$\mu^1 = \mu_{UH}^1 = \frac{E}{2(1+v)}, \lambda^1 = \lambda_{UH}^1 = 1 \tag{3.19}$$

where μ denotes the shear modulus, E denotes Young's modulus, v denotes the Poisson's ratio, λ denotes the shakedown multiplier. The elastic stress history $\hat{\sigma}_{ij}(t_n)$ is also calculated during the first iteration.

2) For the $(k+1)^{\text{th}}$ iteration, stage 1 given in Section 3.2.3 is conducted by:

$$\lambda_{UH}^{k+1} = \lambda_{UH}^{k} \tag{3.20}$$

$$\mu_{nUH}^{k+1} = \frac{\sigma_Y(T)}{\bar{\varepsilon}\left(\Delta\varepsilon_{ijUH}^{nk}\right)} \tag{3.21}$$

The equations (3.14) – (3.16) have been simplified by:

$$d\varepsilon_{ijUH}^{n(k+1)} = \frac{1}{\lambda_{UH}^{k+1}(t_n)}\left\{\lambda_{UH}^{k+1}\hat{\sigma}_{ij}(t_n) + \left(\bar{\rho}_{ijUH} - A_{ij}\right)^{k+1}\right\} \tag{3.22}$$

$$\left(\bar{\rho}_{ijUH} - A_{ij}\right)^{k+1} = -\frac{\sum_{n=1}^{r} \frac{1}{\mu_{nUH}^{k+1}} \lambda_{UH}^{k+1} \hat{\sigma}_{ij}(t_n)}{\sum_{n=1}^{r} \frac{1}{\mu_{nUH}^{k+1}(t_n)}} \tag{3.23}$$

Meanwhile, stage 2 from Section 3.2.3 is performed in parallel:

$$\lambda^{k+1} = \lambda^{k} \tag{3.24}$$

$$\mu_n^{k+1} = \frac{\sigma_U(T)}{\bar{\varepsilon}\left(\Delta\varepsilon_{ij}^{nk}\right)} \tag{3.25}$$

$$\frac{1}{\bar{\mu}^{k+1}} = \sum_{n=1}^{r} \frac{1}{\mu_n^{k+1}} \tag{3.26}$$

$$\sigma_{ij}^{in(k+1)} = \bar{\mu}^{k+1} \left(\sum_{n=1}^{r} \frac{\lambda^{k+1} \hat{\sigma}_{ij}(t_n)}{\mu_n^{k+1}} \right) \tag{3.27}$$

Then a Jacobian matrix $[J]^{k+1}$ is built based on the updated shear modulus $\bar{\mu}^{k+1}$. The constant residual stress field $\bar{\rho}_{ij}^{k+1}$ is given by:

$$\bar{\rho}_{ij}^{k+1} = [J]^{k+1} \Delta\varepsilon_{ij}^{k+1} - \sigma_{ij}^{in(k+1)} \tag{3.28}$$

After that, the compliance matrix $[C]_n^{k+1}$ is constructed as an inverse matrix of $[J]^{k+1}$. The strain rate at load instances $\Delta\varepsilon_{ij}^{n(k+1)}$ is computed by:

$$\Delta\varepsilon_{ij}^{n(k+1)} = [C]_n^{k+1} \left(\bar{\rho}_{ij}^{k+1} + \hat{\sigma}_{ij}^{k+1}(t_n) \right) \tag{3.29}$$

3) At the end of $(k+1)^{\text{th}}$ iteration, the user subroutine URDFIL is called for post-processing. The unlimited hardening multiplier λ_{UH}^{k+1} is calculated by:

$$\lambda_{UH}^{k+1} = \min \left\{ \frac{\sigma_Y(T)}{\bar{\sigma}\left(\hat{\sigma}_{ij}(t_n) + \left(\bar{\rho}_{ijUH} - A_{ij}\right)^{k+1}\right)} \right\} \tag{3.30}$$

The shakedown multiplier bounded by the ultimate stress σ_U is also calculated by:

$$\lambda^{k+1} = \frac{\int_V \left(\sigma_U(T) \sum_{n=1}^{r} \bar{\varepsilon}_n^{k+1}\right) dV}{\int_V \left(\sum_{n=1}^{r} \dot{\varepsilon}_{ij}^{n(k+1)} \hat{\sigma}_{ij}(t_n)\right) dV} \tag{3.31}$$

After the load multiplier at both stages has satisfied the corresponding convergence criteria, the shakedown multiplier considering limited kinematic hardening λ_{KH} is computed with equation (3.13).

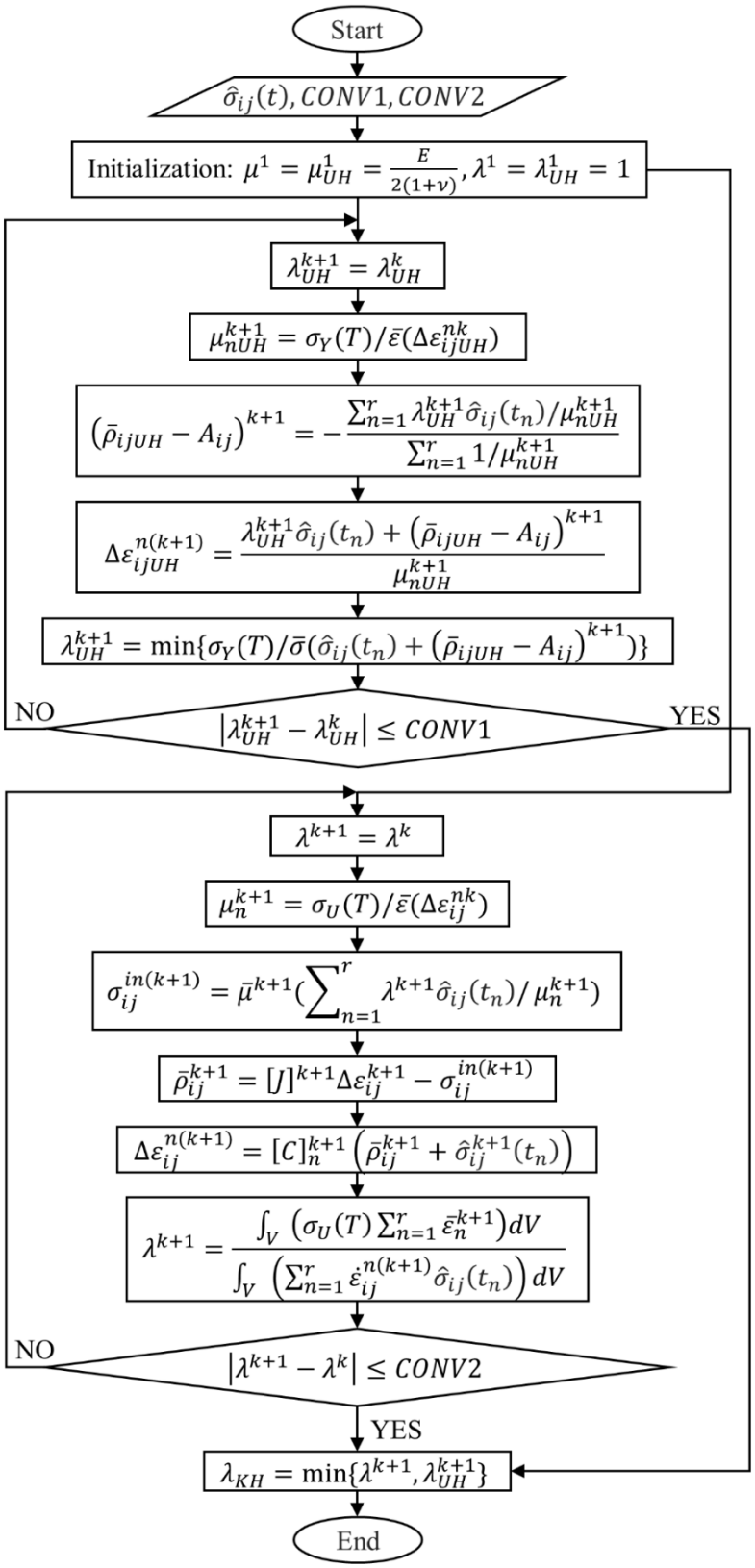

Figure 3.3: Flowchart of the extended LMM algorithm for shakedown analysis considering limited kinematic hardening material

3.3 Numerical examples

3.3.1 A thin cylindrical pipe

3.3.1.1 FE model and material parameters

As a typical benchmark problem, the thin cylindrical pipe has been used by several researchers [108, 109, 112, 113] for shakedown analysis considering kinematic hardening material. The geometry from [109] has been adopted in this work, which is a 2D axisymmetric model with the radius R and the thickness $d = 0.1R$, as shown in Figure 3.4(a). A reference pressure $P = 1$ MPa and a temperature of 204.38 ºC are subjected to the inner surface, while a temperature of 0 ºC is applied on the outer surface. A thermal difference ΔT is created and the steady-state temperature field is presented in Figure 3.4(b). The FE model is further meshed into 500 CAX8R elements in Abaqus/CAE. The loading domain for shakedown analysis consists of four load vertices: $V(1) = (P, 0); V(2) = (0, \Delta T); V(3) = (P, \Delta T); V(4) = (0,0)$, as shown in Figure 3.4(c). The corresponding loading spectrum is presented in Figure 3.5.

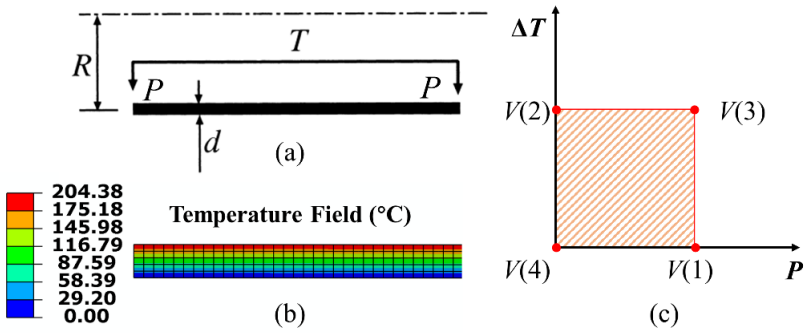

Figure 3.4: (a) The geometry of a typical thin pipe [109] (b) FE mesh and temperature distribution (c) The loading domain for shakedown analysis

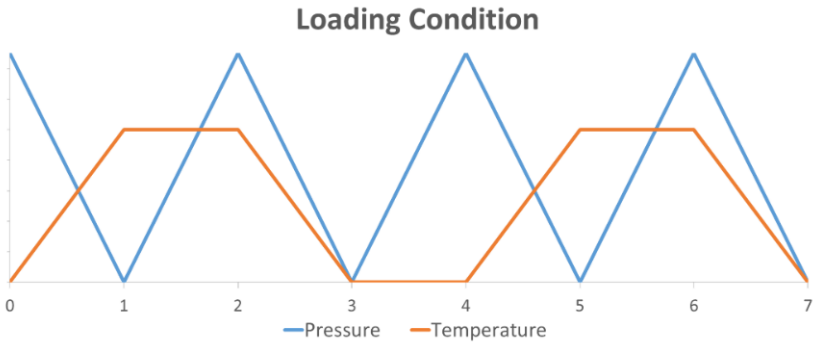

Figure 3.5: The loading condition for shakedown analysis

3.3.1.2 Results and discussions

The shakedown and ratchet analyses on the cylindrical pipe considering kinematic hardening material have been performed, as shown in Figure 3.6. The extended shakedown algorithm described in Section 3.2 has been adopted for the shakedown analysis, while the LMM DSCA module has been used for the ratchet analysis. The inner pressure P and temperature ΔT have been normalised by the limit load P_0 and the reverse plasticity limit ΔT_0, respectively. A number of fictitious hardening factors K have been chosen, ranging from 1.2 to 1.5.

It can be observed in Figure 3.6 that the ratchet boundaries enlarge proportionally with increasing K. Since the ratchet limit is controlled by the failure mechanism of incremental collapse, it is greatly influenced by the ultimate bounding stress σ_U. In addition to incremental collapse, the shakedown boundaries are controlled by another failure mechanism – reverse plasticity. This mechanism can be demonstrated by the unlimited hardening limit [110]. The unlimited hardening limit is only determined by the yield stress σ_Y. Therefore, the lower part of shakedown limit is bounded by ratchet limit, which intersects with the X-axis at $P/P_0 = 1, 1.2, 1.35, 1.5$. Meanwhile, the upper part of the shakedown limit is bounded by a uniform unlimited hardening limit, which is unaffected by the hardening factor K.

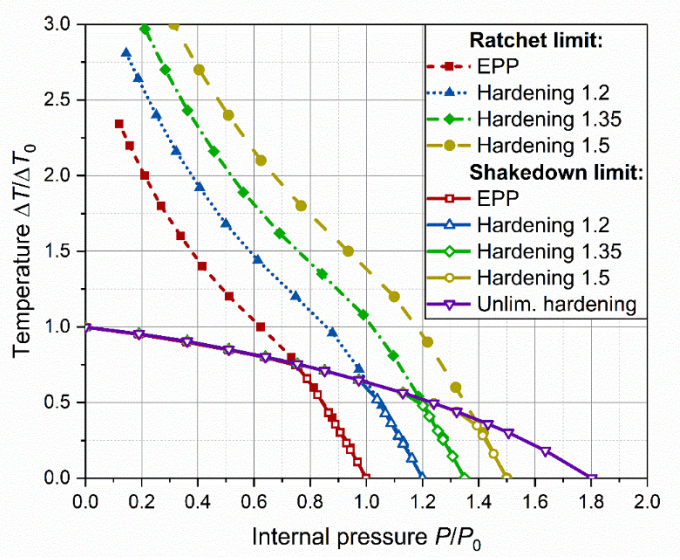

Figure 3.6: Ratchet and shakedown limit of the thin pipe with various fictitious hardening factors

3.3.1.3 Verification of results

To validate the calculated boundaries, the results from the extended LMM algorithm have been compared with ones from the literature. As shown in Figure 3.7, the shakedown limit with a hardening factor of 1.35 generally agrees well with the results from Heitzer [109] using the modified basis reduction method. As shown in Figure 3.8, the shakedown limit with various hardening factors also matches well with the results from Simon [108] using the interior-point algorithm. Some minor deviations can be observed when compared with the literature, which are mainly caused by model processing and numerical errors. To further verify the accuracy of the proposed method, the shakedown multipliers λ are selected in radial directions to compare with the corresponding data points provided in the literature [108, 109, 113]. As shown in Figure 3.9, all the comparison data points can fit in the region with a deviation factor of 0.7, with a coefficient of determination $R^2 = 0.98$. Therefore, the reliability of the extended LMM method has been proved for shakedown analyses considering limited kinematic hardening material.

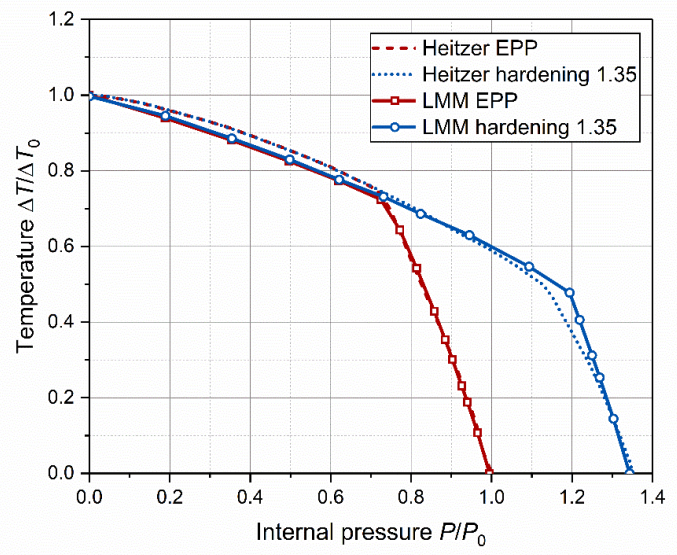

Figure 3.7: Comparison of shakedown boundaries with results from Heitzer [109]

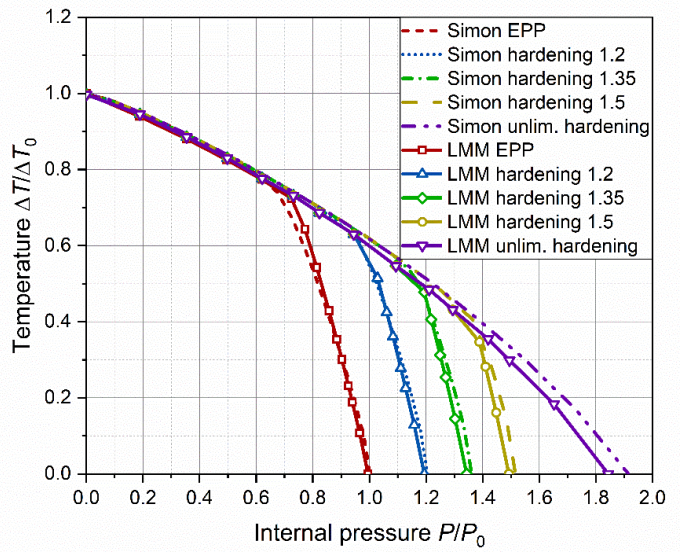

Figure 3.8: Comparison of shakedown boundaries with results from Simon [108]

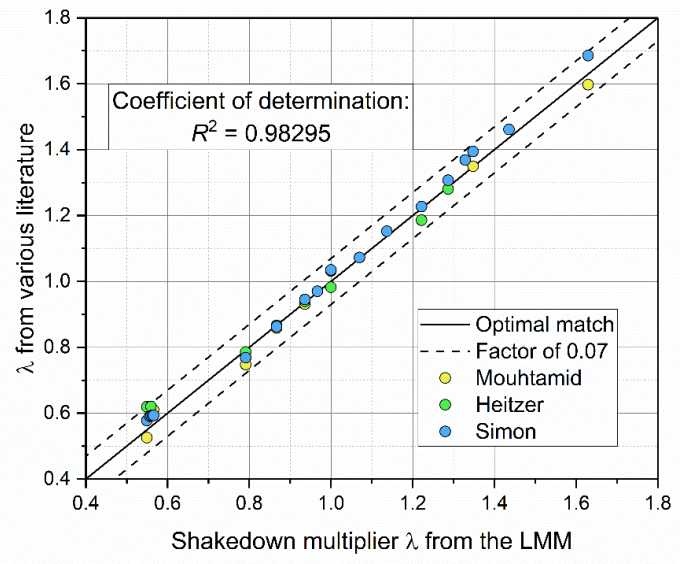

Figure 3.9: Comparison of the shakedown multiplier λ from the LMM and literature

3.3.2 An aero-engine turbine disk

3.3.2.1 FE model and material parameters

In the field of the aerospace industry, turbine disks are significant components for the generation of thrust power in an aero-engine. Since they are operated at high speed in a high-temperature environment, cyclic thermal-mechanical loads are often subjected to turbine disks for typical loading conditions. The structural integrity analysis is crucial for the reliability and lifespan of the engine [117], so the shakedown

analysis has been conducted considering limited kinematic hardening material for improved accuracy and usability in engineering problems.

An axisymmetric FE model has been created to simulate a rotating turbine disk, with its dimensions given in Figure 3.10. It should be noticed that the mounting parts and tiny bores in the structure have been neglected for the sake of simplicity. The model has been meshed into 1975 elements of type CAX8R, as shown in Figure 3.11. For a typical loading condition, the turbine disk is subjected to the centrifugal force F due to the rotating speed $\omega = 1780.24\ \mathrm{rad/s}$, the equivalent pressure $P_{eq} = 148.835\ \mathrm{MPa}$ at the end of the disk due to the reaction force caused by connected turbine blades. The cyclic thermal stress is also considered in the body caused by the temperature difference ΔT. Beside the axisymmetric boundary condition, the normal displacement at the bottom edge of the disk has been restricted to prevent rigid movement in the axial direction.

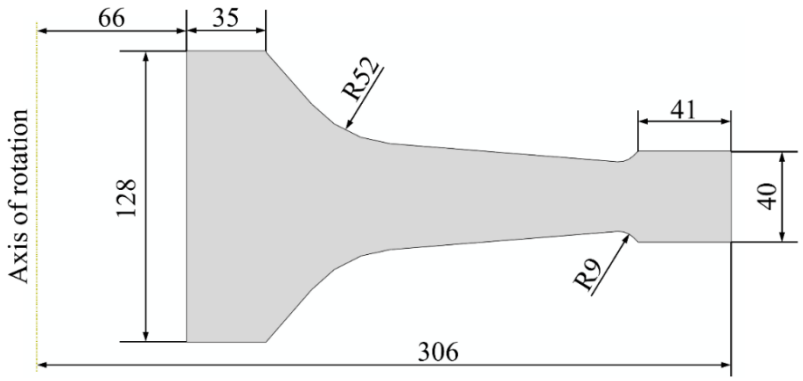

Figure 3.10: The geometry of a typical turbine disk (dimensions in millimetres)

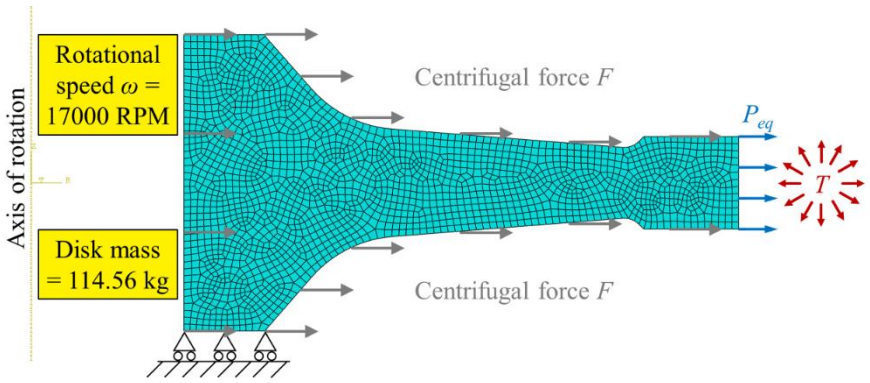

Figure 3.11: The FE mesh and a typical operating condition

A simplified load spectrum and the corresponding loading domains have been presented in Figure 3.12. Some fluctuations in the loading spectrum have been neglected due to the path-independency of the extended LMM algorithm. Two different loading conditions are considered here for comparison. Loading domain I consists of cyclic thermal loads and cyclic mechanical loads with two load instances $V(1) = (0,0),\ V(2) = (M, \Delta\theta)$. Loading domain II consists of cyclic thermal loads and constant mechanical loads with two load instances $V(2) = (M, \Delta\theta),\ V(3) = (M, 0)$, where M indicates mechanical loads while $\Delta\theta$ indicates temperature difference.

The turbine disk is manufactured from a nickel-based superalloy GH4169. The material is widely used in the aerospace industry due to its superior high-temperature performance, weldability and formability. Temperature-independent and temperature-dependent material parameters of GH4169 are given in Table 3.1 and Table 3.2, respectively. The non-isothermal effect on the material performance is considered by using a dynamic parameter $K(T) = \mathrm{UTS}(T)/\sigma_s(T)$ based on temperature dependent yield stress and tensile strength from [118].

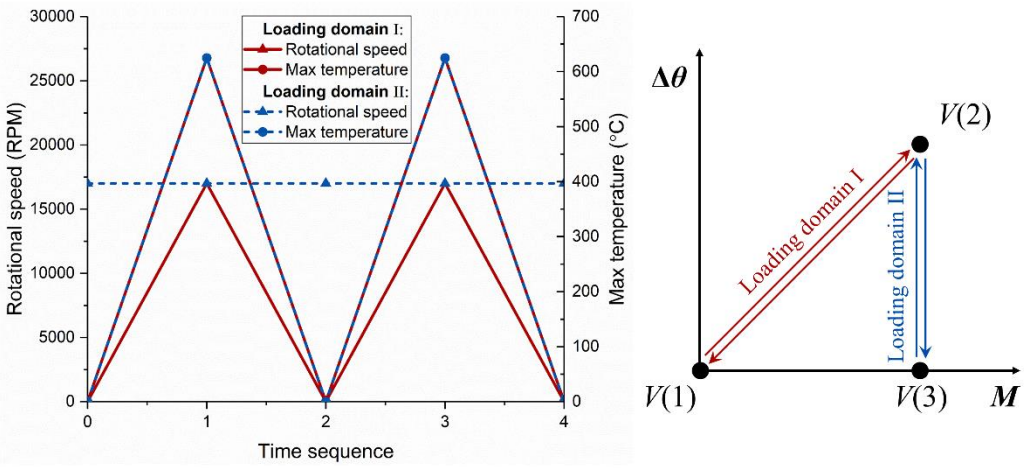

Figure 3.12: Simplified load spectrums and the corresponding loading domains

Table 3.1: Temperature-independent material parameters of superalloy GH4169

Conductivity, *k* [W/(m·ºC)]	23.6
Density, *ρ* [g/cm^3]	8.24
Young's modulus, *E* [GPa]	177
Poisson's ratio, *v*	0.3
Thermal expansion coefficient, *α* [10^{-6}/ºC]	17
Specific heat capacity, *c* [J/(kg·ºC)]	573.4

Table 3.2: Temperature-dependent material parameters of superalloy GH4169

Temperature, T (ºC)	σ_s (MPa)	UTS (MPa)	K
0	1177	1377	1.170
350	1156	1294	1.119
450	1088	1196	1.099
550	1117	1215	1.088
600	1078	1215	1.127
650	1000	1166	1.166
700	951	1039	1.093
750	764	862	1.128

3.3.2.2 Results and discussions

The elastic analysis is first performed to generate the von Mises stress filed $\hat{\sigma}_{ij}$ for the shakedown analysis. Steady-state thermal analysis is also conducted to compute the temperature field at the loading stage, as shown in Figure 3.13(a). The heat is conducted from the high-temperature turbine blade to the connected turbine disk. A temperature gradient is thus formed with the highest temperature of 624.1 ºC at the outer edge of the turbine disk, as well as the lowest temperature of 252.9 ºC at the inner part of the disk. The thermal stress is then calculated by importing the predefined temperature field into an elastic analysis, as shown in Figure 3.13(b). With the centrifugal force F and the equivalent pressure P_{eq} applied, the mechanical stress field can also be evaluated, as shown in Figure 3.13(c). It is worth mentioning that the stress concentration in the mechanical stress field can be found at the inner edge of the disk, while thermal stress concentrates at the outer edge of the disk.

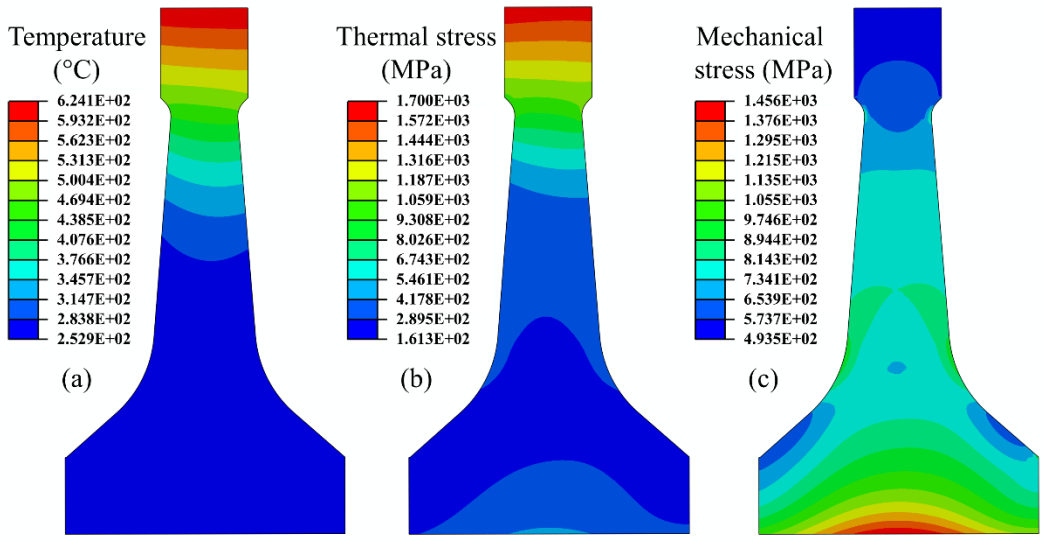

Figure 3.13: Elastic analysis contours of (a) temperature field (b) thermal von Mises stress (c) mechanical von Mises stress

Based on the elastic analysis results, the shakedown analysis considering kinematic hardening with loading domain I has been performed, as presented in Figure 3.14. In the diagram, both mechanical and thermal loads are normalised by the reference value given in Figure 3.12. For normal operating conditions, the load point $(M/M_0, \Delta\theta/\Delta\theta_0) = (1, 1)$ is found inside the shakedown envelope, so the structure would not shake down during the standard operation process. Unlike a typical Bree-like diagram [119], the reverse plasticity limit is not horizontal for load domain I with cyclic thermal-mechanical loads. It is due to the counteraction effect between the thermal and mechanical loads, where the stress concentration is cancelled out with the application of both loads.

The shakedown boundary is plotted by scaling the loads proportionally with various fixed ratios between mechanical and thermal load: $\eta = M/\Delta\theta$. The diagram can be divided into two sections by the load ratio $\eta = 0.8$, as shown in Figure 3.14. Two distinct failure mechanisms are observed for load points in each region. For $\eta < 0.8$, the thermal load is dominant, and the failure mode is low cycle fatigue in local areas of the structure. It can be observed that the reverse plasticity limits are identical for the EPP model and limited kinematic hardening model, which are both bounded by the unlimited hardening limit. For $\eta > 0.8$, the mechanical load becomes dominant, and the failure mode is incremental collapse which is a global structural behaviour. After load point $(1.12, 1.40)$, the unlimited kinematic hardening limit separates from the EPP shakedown limit. The shakedown limit considering limited hardening is then bounded by both the unlimited hardening limit and the ratchet limit controlled by the temperature-dependent UTS. Two load points beside the separation point have been chosen for further clarification of the failure mechanism, as presented in Figure 3.15. The coordinate for load point (1) is $(0.96, 1.38)$ and the local failure location caused by the dominant thermal load is spotted at the corner of the outer edge of the disk. The coordinate for load point (2) is $(1.28, 1.28)$ which is mechanical load dominant. The corresponding failure mechanism is global, initiated from the inner edge of the turbine disk.

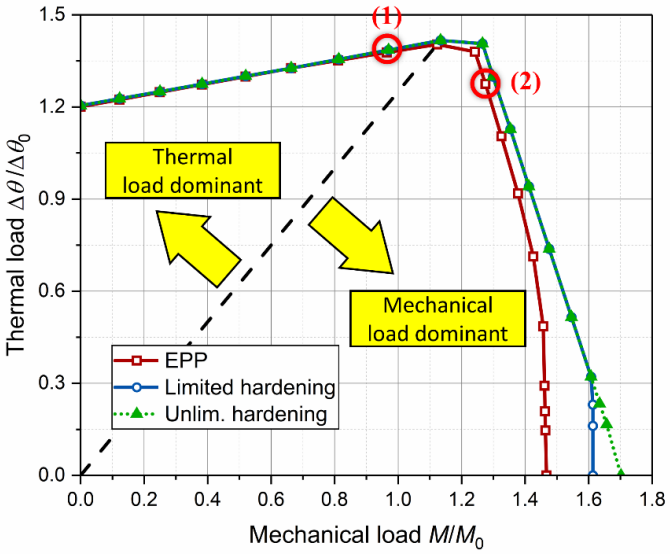

Figure 3.14: Shakedown analysis considering kinematic hardening and temperature-dependent material properties for loading domain I

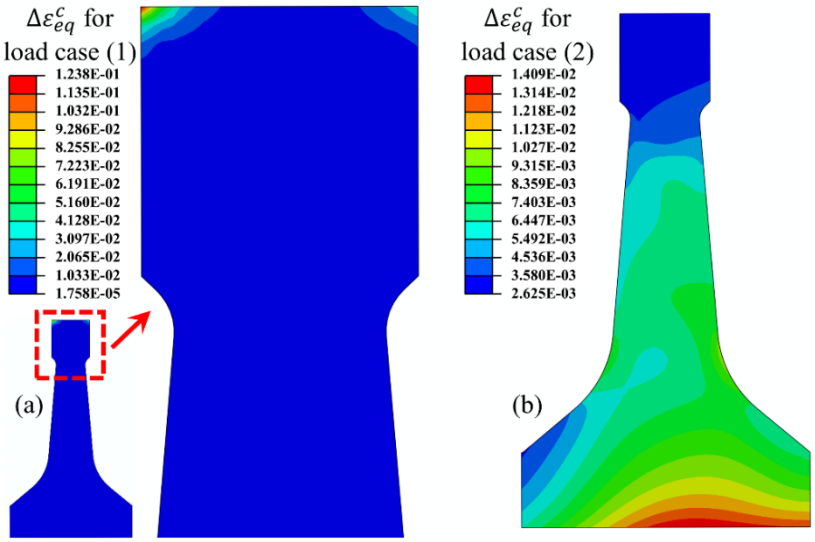

Figure 3.15: The failure mechanism for two different load cases

3.3.2.3 The effect of temperature-dependent material parameters

To further investigate the importance of using temperature-dependent material properties, the shakedown analysis has been performed again using temperature-independent yield stress and UTS, as presented in Figure 3.16. The loading domain I from Figure 3.12 is considered with a cyclic thermal-mechanical load. Constant material properties are selected from Table 3.2 with the temperature at 0 ºC. It can be observed that when the temperature level is low, the shakedown boundaries calculated with both temperature-dependent material parameters and constant

parameters are nearly identical. With the increase of thermal load, the shakedown limit obtained with temperature-dependent material parameters become more conservative, which is also found in [120]. The largest difference between the shakedown envelopes is found at the transition point when the thermal and mechanical stress counteracts with each other.

The parametric study has also been performed considering load domain II with constant mechanical load and cyclic thermal load, as shown in Figure 3.17. A typical Bree-like diagram [119] is obtained with a horizontal reverse plasticity limit on which the scaled thermal stress is twice the yield stress. With the increase of temperature, the influence of using the temperature-dependent material properties becomes more substantial. It can also be observed that the adoption of non-isothermal parameters has a more significant effect on the shakedown boundary considering limited kinematic hardening at lower temperature levels, suggesting that the shakedown analysis with hardening material could be more sensitive to temperature-dependent parameters. Therefore, it is essential to implement non-isothermal material parameters as part of the proposed extended LMM method for more accurate and conservative results.

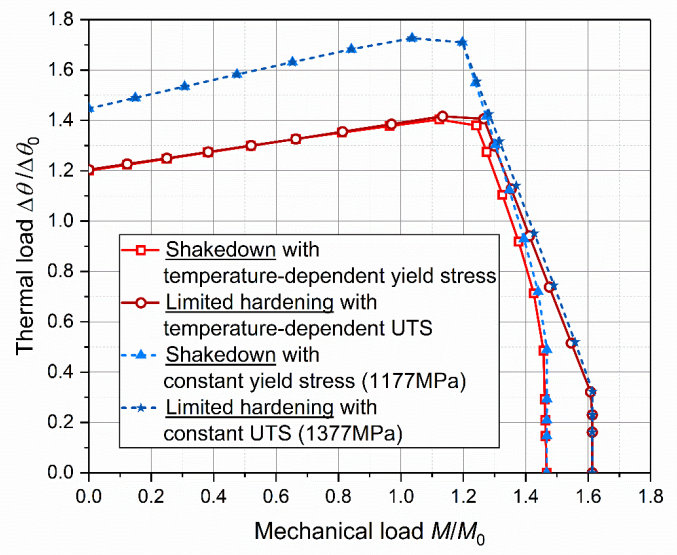

Figure 3.16: Comparison of shakedown boundaries considering temperature-dependent and constant material properties for loading domain I

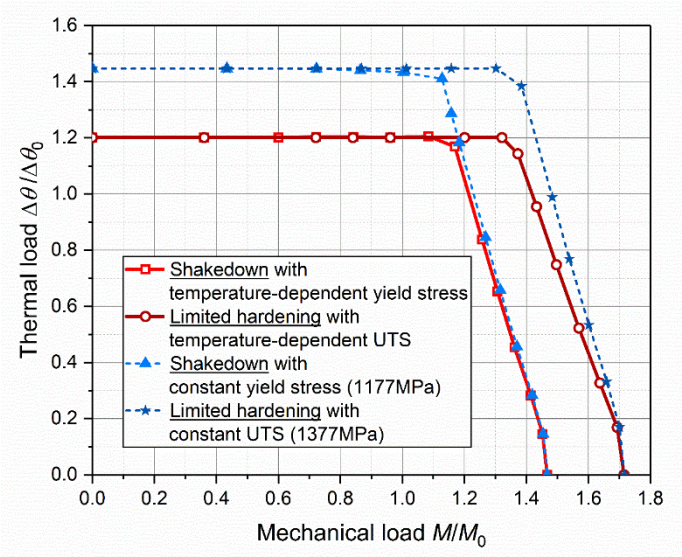

Figure 3.17: Comparison of shakedown boundaries considering temperature-dependent and constant material properties for loading domain II

3.4 Summary

In this chapter, a shakedown algorithm considering limited kinematic hardening material is introduced and implemented in the extended LMM shakedown module. The material properties considering the non-isothermal effect are adopted using the proposed direct method. Based on the two-surface hardening model, the method uses fictitious hardening factors calculated from temperature-dependent yield stress and UTS. A thin cylindrical pipe has been modelled and analysed with the extended LMM shakedown module. The result shakedown boundaries match well with ones from literature with a deviation factor of 0.07, where the reliability and accuracy of the proposed method are successfully validated.

A case study on an aero-engine turbine disk has also been conducted to show the versatility of the extended LMM shakedown algorithm for generic industrial problems. Two distinct failure mechanisms have been observed in the structure, which are caused by different loading combinations with dominant thermal or mechanical loads. Due to the counteracting effect between thermal and mechanical loads, a transition point in the shakedown boundaries has been spotted. Two failure modes are separated by the transition point. The shape of the shakedown envelope is affected by the choice of loading domain. The size of the shakedown envelope is affected by the use of temperature-dependent material parameters. Compared to constant material properties, the shakedown limit considering temperature-dependent material

parameters would be much more conservative at high temperatures. Therefore, the benchmark example of the thin cylindrical pipe indicates that the results from the extended LMM shakedown module agree well with the ones from literature. The engineering example of the aero-engine turbine disk illustrate the versatility of the proposed method. In addition, an extended Bree-like diagram considering limited kinematic hardening and non-isothermal effect has also been plotted and discussed.

4. The evaluation of the creep rupture limit using a unified creep rupture equation

4.1 Introduction

With superior heat transfer efficiency and compactness, the Printed Circuit Heat Exchangers (PCHE) have become increasingly popular in the nuclear industry. Due to the large surface area inside the channels, they are highly suitable for gaseous heat transfer in high-temperature gas-cooled reactors (HTGRs) [121]. Helium loops are often used as coolants, and the temperature in the channels could reach over 950 °C [122]. Time-dependent behaviours such as creep are often found in such engineering structures when the operating temperature reaches the material's creep range. In the circumstances when the components are affected by both plasticity and creep behaviour, the load-bearing capacity of structures would be significantly reduced. Therefore, creep rupture analysis has been introduced to study the load-carrying limit of a component before reaching the creep rupture state [15]. The creep rupture analysis has thus become highly important as part of the structural integrity assessment of a PCHE core. Although the creep effect on the PCHE has been considered by some researchers with experiments and Finite Element (FE) analysis [123, 124], the structural creep rupture limits and the creep rupture mechanisms have been rarely discussed in the literature.

The R5 procedure [7] has been widely adopted for comprehensive structural integrity assessment, including shakedown, ratchet, creep, and fatigue analyses. A series of simplified inelastic methods have been introduced in R5 to replace inaccurate elastic analyses or costly cycle-by-cycle plastic analyses. Regarding the creep rupture endurance, R5 defined a rupture reference stress σ_{ref}^{R} for the evaluation of structural creep rupture life based on rupture data of the material. The reference stress of a constant primary load is used to calculate σ_{ref}^{R}, with further correction of the stress concentration factor χ. The bounding limit can then be predicted based on the creep rupture data conservatively. According to the R5 procedure, the shakedown boundary would reduce correspondingly when the structures experience creep behaviour during high-temperature operation. Some modifications can be made to evaluate the creep rupture boundaries based on traditional shakedown theory. For locations in a structure where the temperature is below the creep range, a temperature-dependent

yield stress $\sigma_y(T)$ can be applied. While for areas with higher temperature above the creep range, the yield stress is substituted by the rupture stress $\sigma_R(t_R, T)$ which is based on both temperature T and time to rupture t_R. Therefore, existing shakedown theorem can be directly used to solve creep rupture problems with provision of the creep rupture strength.

As introduced in Section 2.4, the Linear Matching Method (LMM) framework has been integrated with ABAQUS [21] for comprehensive structural integrity assessment. An extended shakedown algorithm has also been implemented in the LMM framework for creep rupture analysis. The creep rupture module was developed in [15] and has successfully solved many engineering problems [13, 20, 125-129]. The main technique used in the LMM for evaluating the temperature-dependent rupture stress $\sigma_R(t_R, T)$ is linear interpolation and extrapolation. The linear technique is simple to implement but sometimes difficult and unreliable to use. For instance, a large number of data points for various rupture times need to be entered in the LMM plug-in to simulate nonlinear rupture curves. Also, linear extrapolation may produce inaccurate results for some materials due to the nonlinearity of creep rupture curves. In addition, it can be time-consuming to input all the data manually when conducting parametric studies with different materials. Therefore, it is crucial to develop a numerical scheme for rupture strength evaluation with better usability and reliability.

To generate the master equations to describe the relationship between rupture stress, temperature and time to rupture, several numerical models have been adopted by the European Creep Collaborative Committee (ECCC), including the Larson-Miller parameter [50], standard ISO 6303 method [130], and Manson-Haferd model [52]. These models have been proved to be more accurate and reliable than linear interpolation and extrapolation, but they are often limited to being used for specific materials. This actively demonstrates that the form of equations heavily depends on the type of material, so it is challenging to implement them respectively in the LMM framework by including a uniform material database. To solve this problem, a Unified Creep Rupture Equation (UCRE) has been proposed to simulate the creep rupture curves for a broader range of materials. The UCRE refers to the format of the traditional Larson-Miller parameter method with the advantages of fitting the rupture curves for most steels included in the ECCC data sheets [49] with good efficiency and reliability. A Matlab script [131] has been developed to extract and fit the curves automatically, and fitted parameters have been exported into a database. A

modification has also been made in the LMM creep rupture module to implement the UCRE equations. Therefore, it becomes more practical and efficient to use the LMM creep rupture module to determine the most suitable material for engineering structures by performing parametric studies.

In this study, the Bree-like diagram is extended by including the creep rupture limit and a unified mathematical equation is introduced for the evaluation of rupture strength. The current LMM algorithm for creep rupture analysis is briefly introduced in Section 4.2. Then the UCRE is proposed and compared with other numerical schemes for the description of creep rupture curves in Section 4.3, followed by a comprehensive validation of the proposed mathematical equation using the ECCC guidelines in Section 4.4. Finally, a numerical example of creep rupture analysis on a PCHE core is presented in Section 4.5. Several parametric studies have been further conducted by changing the material, channel shape and channel dimensions to show the usability and reliability of the proposed mathematical equation.

4.2 The current LMM algorithm for creep rupture analysis

According to the R5 procedure [7], the shakedown boundary of the structure would reduce when the thermal loads are significant, and the creep effect is involved. The creep effect can be represented by applying a temperature-dependent revised yield stress $\sigma_y^R(T)$ for each integration point in the component. The creep rupture limit for constant a rupture time can then be calculated with an extended LMM shakedown analysis. In the original LMM subroutine, this problem is addressed by introducing functions R and g [15]. The revised yield stress for a point in the body at time t is given by:

$$\sigma_y^R(x,t) = \min\{\sigma_y(T), \sigma_R\big(t_R, T(x,t)\big)\} \tag{4.1}$$

where the creep rupture stress $\sigma_R(t_R, T)$ is calculated by:

$$\sigma_R(t_R, T) = R(\frac{t_R}{t_0})g(\frac{T}{T_0}) \tag{4.2}$$

where R is a function of the ratio of creep rupture time t_R to reference time t_0, and g is a function of the ratio of local temperature T to reference temperature T_0.

However, it becomes difficult to define these functions for many realistic engineering problems. A simplified numerical scheme to describe the revised yield stress has been

proposed in [126]. The LMM subroutine has been modified by including both linear and the Larson-Miller parameter [50] for the calculation of creep rupture stress σ_R for given rupture time. The revised yield stress σ_y^R can then be computed with Equation (4.1) by comparing σ_R with the yield stress σ_y of the material. The field of σ_y^R is updated iteratively at every integration point based on a scaled temperature field. The general procedure of the extended shakedown algorithm for creep rupture analysis in the LMM is presented as follows.

Considering an isotropic, EPP material that forms a body with volume V and surface S. The body is subjected to cyclic mechanical stress $\lambda_R\hat{\sigma}_{ij}^P$ on the part of surface S_T and thermal stress $\lambda_R\hat{\sigma}_{ij}^\theta$ in V. On the remaining part of surface S_u, the displacement rate $\dot{u}_i = 0$. The linear elastic stress field is then given by:

$$\lambda_R\hat{\sigma}_{ij} = \lambda_R\hat{\sigma}_{ij}^P + \lambda_R\hat{\sigma}_{ij}^\theta \tag{4.3}$$

where λ_R denotes the load multiplier for creep rupture analysis. The strain rate history $\dot{\varepsilon}_{ij}^c$ is considered to be incompressible and kinematically admissible, forming a compatible strain increment $\Delta\varepsilon_{ij}^c$:

$$\int_0^{\Delta t} \dot{\varepsilon}_{ij}^c dt = \Delta\varepsilon_{ij}^c \tag{4.4}$$

The displacement increment is also related to the strain increment:

$$\Delta\varepsilon_{ij}^c = \frac{1}{2}\left(\frac{\partial\Delta u_i^c}{\partial x_j} + \frac{\partial\Delta u_j^c}{\partial x_i}\right) \tag{4.5}$$

Combined with the flow rule, the upper bound creep rupture limit multiplier is given by:

$$\lambda_R = \frac{\int_V \int_0^{\Delta t} \sigma_y^R(t)\bar{\dot{\varepsilon}}(\dot{\varepsilon}_{ij}^c)dtdV}{\int_V \int_0^{\Delta t} (\hat{\sigma}_{ij}\dot{\varepsilon}_{ij}^c)dtdV} \tag{4.6}$$

where the effective strain rate $\bar{\dot{\varepsilon}} = \sqrt{\frac{2}{3}\dot{\varepsilon}_{ij}\dot{\varepsilon}_{ij}}$ and the revised yield stress σ_y^R is calculated by Equation (4.1). An iterative linear process has been developed in [98] to solve the creep rupture multiplier. The process begins with an initial kinematically admissible plastic strain rate history $\dot{\varepsilon}_{ij}^i$ to derive a final kinematically admissible strain rate history $\dot{\varepsilon}_{ij}^f$:

$$\dot{\varepsilon}_{ij}^{f\,\prime} = \frac{1}{\mu}\left(\lambda_R^i \hat{\sigma}_{ij} + \bar{\rho}_{ij}^f\right)' \tag{4.7}$$

$$\dot{\varepsilon}_{kk}^f = 0 \tag{4.8}$$

$$\mu = \frac{\sigma_y^R}{\bar{\dot{\varepsilon}}^i} \tag{4.9}$$

where $(')$ denotes the deviatoric component of stress or strain, $\bar{\rho}_{ij}^f$ is a constant residual stress field. The shear stress μ is modified linearly to match the perfectly plastic material. Equation (4.7) is further integrated over the time cycle:

$$\Delta\varepsilon_{ij}^{f\,\prime} = \frac{1}{\bar{\mu}}\left(\bar{\rho}_{ij}^f + \hat{\sigma}_{ij}^{in}\right)' \tag{4.10}$$

where

$$\sigma'^{in}_{ij} = \bar{\mu}\{\int_0^{\Delta t} \frac{1}{\mu(t)} \lambda_R^i \hat{\sigma}'_{ij}(t)dt\} \tag{4.11}$$

$$\frac{1}{\bar{\mu}} = \int_0^{\Delta t} \frac{1}{\mu_n} dt \tag{4.12}$$

where σ'^{in}_{ij} is the scaled linear stress over the time cycle, $\Delta\varepsilon_{ij}^f$ is the plastic strain increment. A final creep rupture multiplier λ_R^f is then found by substituting $\dot{\varepsilon}_{ij}^f$ into Equation (4.6). By repeating the process described above, a monotonically reducing λ_R is computed iteratively so that:

$$\lambda_R^f \leq \lambda_R^i \tag{4.13}$$

When the difference between λ_R^f and λ_R^i becomes considerably small, the scaled stress at every integration point is lower or equal to σ_y^R while the convergence is achieved. The process can be further simplified for a convex yield surface, where load histories are described by connecting vertices in the load space with straight lines. Thus, the plastic strain can only be observed at the vertices of a loading history. The strain rate history can then be evaluated as follows:

$$\Delta\varepsilon_{ij}^c = \sum_{n=1}^r \Delta\varepsilon_{ij}^n \tag{4.14}$$

where n is the number of load instances. Equation (4.11) then becomes:

$$\sigma'^{in}_{ij} = \bar{\mu}\{\sum_{n=1}^{r} \frac{1}{\mu_n} \lambda_R \hat{\sigma}'_{ij}(t_n)\} \tag{4.15}$$

where

$$\frac{1}{\bar{\mu}} = \sum_{n=1}^{r} \frac{1}{\mu_n} \tag{4.16}$$

$$\mu_n = \frac{\sigma_y^R(t)}{\bar{\varepsilon}(\Delta\varepsilon_{ij}^{ni})} \tag{4.17}$$

The simplified procedure reduces the use of the integration function, which benefits the implementation process in commercial FE software. Based on user subroutines and Python scripts in ABAQUS [21], the LMM algorithm for creep rupture analysis has been implemented as an individual module in the LMM plug-in [20].

4.3 Numerical schemes for the evaluation of creep rupture strength

To evaluate the creep rupture strength in Equation (4.1), many numerical schemes have been adopted, including different interpolation and extrapolation techniques that can predict the creep rupture properties of materials based on limited data points from experiments. Creep rupture experiments can be highly time-consuming when the stress or temperature applied to the specimen is relatively low, so it is crucial to develop a reliable and unsophisticated mathematical model to describe the creep rupture behaviour.

One of the most commonly used techniques is linear interpolation or extrapolation. Being simple and mostly conservative, this technique has been implemented in the LMM plug-in to calculate the temperature-dependent revised yield stress based on the input data points [18]. However, the accuracy of linear interpolation heavily relies on the number of data points provided. If the database is small, the non-linear material behaviour would not be adequately described. Also, linear extrapolation is often considered unreliable when the temperature is scaled beyond the range of input values, which is a common scenario during the operation of the LMM algorithm given in Section 4.2.

Another method used to fit creep rupture data is the Larson-Miller parameter [50]. It has been widely used in industries to predict long term rupture data based on short

term experimental data. The Larson-Miller parameter has also been adopted to generate master equations for a number of materials to demonstrate the relationship between rupture stress, temperature, and rupture time. The form is defined by:

$$P_{LM} = \frac{T(\log(t_R)+C)}{1000} \tag{4.18}$$

where P_{LM} is the Larson-Miller parameter, T is the absolute temperature, C is a constant, generally between 20 and 22, and t_R is the creep rupture time in hours. After processing the rupture data using this technique, the creep rupture curves would ideally become a single curve of P_{LM} versus $\log(\sigma)$. Then a third-order polynomial form can be used to fit this curve using the least square method:

$$\log(\sigma) = B_1\big(P_{LM}(T)\big)^3 + B_2\big(P_{LM}(T)\big)^2 + B_3 P_{LM}(T) + B_4 \tag{4.19}$$

The Larson-Miller equation has been proved to be robust and accurate while fitting the creep rupture data for some materials. It has also been included in the LMM algorithm as a tool to interpolate and extrapolate creep rupture stress [126]. The Larson-Miller parameter relies on the assumption that all the iso-stress curves would coincide at one single point. However, for many ferritic steels and nickel base alloys, such assumption may not be fully satisfied as the experiment data points are unable to converge to a single curve after applying the Larson-Miller relationship.

Based on the concept of the Larson-Miller parameter and other similar models, a Unified Creep Rupture Equation (UCRE) has been proposed to fit the creep rupture data for a broader range of steel types. It combines the form of logarithm and polynomial by:

$$\sigma_R = f_1(T)\ln(t_R) + f_2(T) \tag{4.20}$$

$$f_1(T) = a_1T^3 + a_2T^2 + a_3T + a_4 \tag{4.21}$$

$$f_2(T) = b_1T^3 + b_2T^2 + b_3T + b_4 \tag{4.22}$$

where T is the absolute temperature and t_R is the creep rupture time in hours. Instead of fitting a 3D surface equation with variables of σ_R, T, and t_R, the procedure is simplified by fitting two 2D curves with the least square method. Thus, the fitting process becomes both efficient and accurate, which can produce material parameters within the 95% confidence bounds of the 3D surface fitting. To show the capability of

the proposed method, the UCRE has been used to fit the creep rupture curves for different types of steels from the ECCC data sheets [49], including carbon-manganese steels, low alloy ferritic steels, high alloy ferritic steels, austenitic steels, nickel-base alloys, and high temperature bolting steels. A Matlab script [131] has also been developed to read and process the rupture data from the ECCC data sheets. In this way, the UCRE parameters for various materials can be fitted automatically so that the fitting process becomes highly efficient. The UCRE parameters for the materials to be mentioned in the following sections are provided in Table 4.1.

Table 4.1: The UCRE parameters fitted for several materials

Material	a_1	a_2	a_3	a_4	b_1	b_2	b_3	b_4
5CrMo	-3.20E-05	7.58E-02	-59.69	15605.03	2.44E-04	-5.66E-01	434.09	-109799.51
2.25Cr1Mo	4.66E-06	-1.24E-02	11.05	-3299.84	-7.03E-05	1.88E-01	-169.16	51018.72
11CrMoVNb	1.37E-05	-3.14E-02	23.87	-6084.54	-7.94E-05	1.78E-01	-135.54	35828.53
18Cr11Ni	2.94E-06	-8.61E-03	8.39	-2739.02	-3.26E-05	9.66E-02	-95.97	32090.30
31Ni20CrAlTi	7.80E-08	-4.08E-04	0.65	-329.76	-3.96E-06	1.54E-02	-19.99	8679.64
Alloy 617	-5.10E-07	1.45E-03	-1.25	297.31	-9.68E-07	7.72E-03	-14.68	8232.79
Alloy 800H	7.42E-07	-2.51E-03	2.86	-1096.63	-1.21E-05	4.10E-02	-46.61	17881.59

To compare the accuracy and performance of the numerical schemes mentioned above, they have been adopted to fit the data points of the carbon-manganese steel – 5CrMo (normalised and tempered), as shown in Figure 4.1. During the fitting process, instead of using the realistic data points, only 13 of them are used to demonstrate the potential ability to interpolate and extrapolate experimental creep rupture data. Equations (4.18) and (4.19) are used for the Larson-Miller fitting process. The fitted parameters are given as follows: $B_1 = -0.00107, B_2 = 0.0633, B_3 = -1.516, B_4 = 15.417, C = 20$. In practice, this material is not suitable to be fitted by the Larson-Miller parameter as the curves for various creep rupture times are poorly superimposed after being processed by Equation (4.18). Thus in Figure 4.1, it can be observed that “LM 3rd order” curves deviate heavily from the real data points for rupture time $t_R = 10\,\mathrm{kh}$ and $t_R = 200\,\mathrm{kh}$. For rupture time $t_R = 100\,\mathrm{kh}$, the Larson-Miller method is also slightly conservative when the temperature is lower than 763K or higher than 803K.

In terms of the linear technique, linear interpolation can provide acceptable results but predicted curves are still not able to pass all the realistic data points. Extrapolated results from the linear technique are generally too conservative, so the predicted curves fail to pass the actual data points at the end of the curves. Therefore, the linear technique is unable to predict non-linear curves correctly when the amount of available points is low. On the other hand, the curves fitted by the Unified Creep Rupture Equation (UCRE) can almost pass through all the real data points, showing the best performance of all three methods. The UCRE is better than the linear technique when describing the nonlinearity of creep rupture curves and more reliable than the Larson-Miller technique when predicting the curves for different creep rupture times. The accuracy and reliability of the proposed mathematical equation will be further justified in the next section.

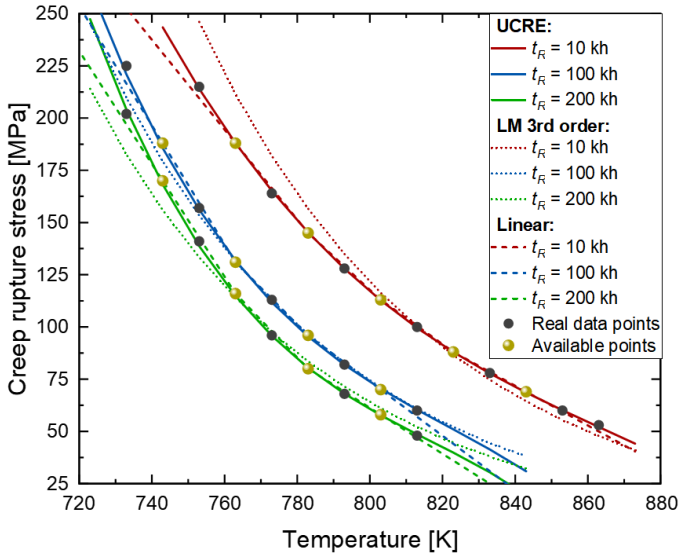

Figure 4.1: Interpolation and extrapolation of experimental creep rupture data using three different methods

4.4 Validation of the proposed mathematical equation

Since a large number of numerical models have been proposed for Creep Rupture Data Assessment (CRDA) on various materials, a general procedure has been provided by the ECCC to give guidance on model development and select appropriate models as shortlisted ones in the ECCC guidelines. Four main steps are involved in the procedure, including data pre-assessment, model fitting, Post Assessment Testing (PAT), and comparison of independent models to finally determine the models adopted by the ECCC. Although it is recommended by ECCC PATs to use different

models for various materials, the UCRE is developed to describe the creep rupture behaviour of a broader range of steels in a simple but effective form. So that the UCRE can be easily implemented in the LMM framework, and a linked database can also be created for the storage of the material parameters.

Four different types of steel have been considered to verify the credibility of UCRE, including low alloy ferritic steel (2.25Cr1Mo), high alloy martensitic steel (11CrMoVNb), and austenitic steel (18Cr11Ni and 31Ni20CrAlTi). The creep rupture strengths at the main temperatures generated by nine individual models are presented in Table 4.2. Eight of them have been adopted by ECCC PATs [132] due to their high effectiveness and credibility. For each material, the creep rupture strengths with rupture times of 100,000 hours and 300,000 hours from two ECCC shortlisted models are given and compared with the values from UCRE. It can be observed that for 2.25Cr1Mo and 18Cr11Ni, the UCRE is more conservative than other models, while for 11CrMoVNb and 31Ni20CrAlTi, the UCRE is less conservative than other models. The overall rupture strengths predicted by UCRE are comparable to other models, with a maximum margin of error of $\pm 10\%$. The most considerable difference can be found when comparing the rupture stress of austenitic stainless steel. It is suggested by ECCC that to pass the PATs, the 100,000-hour rupture strengths at main temperatures should be within 10% of two different models, and the 300,000-hour rupture strengths should be within 20% [132]. Therefore, the numerical errors between the UCRE and other models are within the acceptable range given by the ECCC PATs.

Table 4.2: Creep rupture strength for various materials at the main temperatures predicted by several numerical models

Material	T [°C]	Rupture time [kh]	MC_mod	MB3	SM_mod	OSD	SM_M	SM_P	SM	SM_D	UCRE
2.25Cr1Mo	550	100kh	62.9	64.6	–	–	–	–	–	–	61.4
		300kh	48.9	48.5	–	–	–	–	–	–	45.8
11CrMoVNb	550	100kh	–	–	154	153	–	–	–	–	154.5
		300kh	–	–	100	98.5	–	–	–	–	105.8
18Cr11Ni	650	100kh	–	–	–	–	56.3	54.4	–	–	55.0
		300kh	–	–	–	–	45.0	42.0	–	–	40.4
31Ni20CrAlTi	700	100kh	–	–	–	–	–	–	41.6	40.0	44.4
		300kh	–	–	–	–	–	–	32.9	31.2	32.9

The creep rupture curves simulated by UCRE and ECCC shortlisted models have been further compared in Figure 4.2. The material properties for both steel types can be found in Table 4.1. It can be observed that for 2.25Cr1Mo at 550 °C, the UCRE

produces overall lower rupture strengths compared to the other two models. For 11CrMoVNb at 550 °C, the creep rupture strengths predicted by UCRE are slightly higher than other models when the rupture time is shorter than 700,000 hours, and then the curve gradually becomes lower than the other models when the rupture time is longer than 700,000 hours. Nevertheless, the deviation of curves is potentially caused by the form of equations and regression techniques adopted by different models. It can be concluded that the UCRE is capable of fitting the creep rupture curves for four different types of steel mentioned above precisely and versatilely.

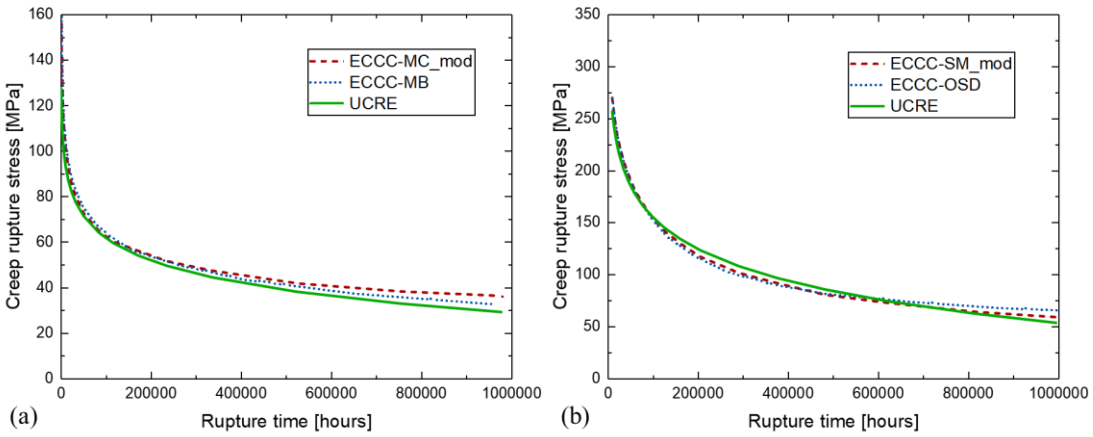

Figure 4.2: Comparisons of creep rupture strength predicted by UCRE and ECCC shortlisted models for (a) 2.25Cr1Mo at 550°C (b) 11CrMoVNb at 550°C

To further validate the proposed model, the creep rupture curves of more than 40 different materials from the ECCC data sheets [49] have been fitted by UCRE, as given in Appendix A. The comparisons of predicted creep rupture strengths using UCRE with the observed ones from ECCC data sheets have been presented in Figure 4.3. Three different creep rupture times (10000, 100000 and 200000 hours) have been chosen and grouped by various colours. The data points are collected by comparing the calculated creep rupture stress with the original database at equivalent temperature and rupture time. It can be seen that all the data points are situated alongside the mean line, within the boundaries of a deviation factor of 0.55. The predicted creep rupture strengths particularly agree well with the observed ones when the rupture stress is high, and the temperature is low. While at the higher temperature, the rupture stress becomes lower, and some predicted creep rupture strengths deviate from the observed ones. Most deviations are considered to be conservative as the predicted values are lower than the observed ones. In addition, more minor deviations can be found when the creep rupture time is longer and the overall

coefficient of determination $R^2 = 0.99927$. Therefore, despite a few materials that are not compatible with the numerical scheme proposed, the UCRE is capable of predicting the creep curves for most of the steels listed in the ECCC data sheets correctly, with minor conservativeness at high temperatures for several materials.

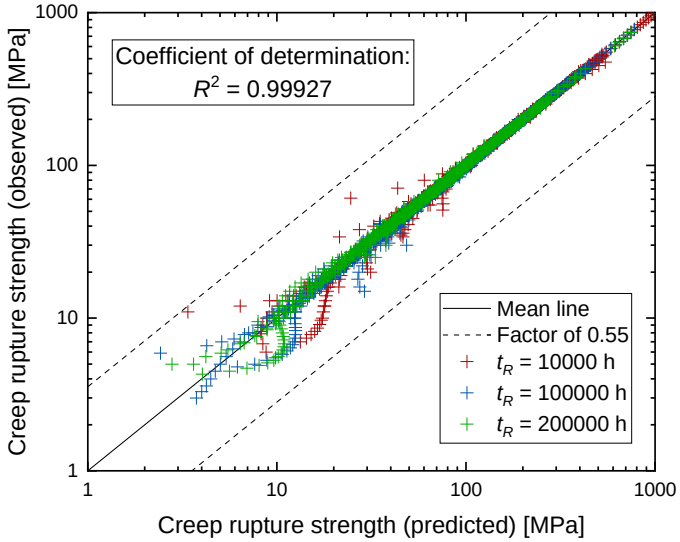

Figure 4.3: Comparisons of predicted creep rupture strength using UCRE with the observed rupture strength from the ECCC data sheets

4.5 Numerical examples

4.5.1 Creep rupture analysis on a PCHE core

To demonstrate the usability of the proposed mathematical equation, a comprehensive creep rupture analysis has been performed on a typical PCHE core and a series of creep rupture boundaries have been derived considering variable materials, geometry shape and dimensions. The PCHE channels are manufactured by photochemical etching on a number of metal plates before stacking them together, as shown in Figure 4.4(a). Instead of conventional welding, the diffusion bonding technique is used to merge the plates into a single component [133]. Thus numerous semi-circular channels are formed in the component without having weld joints, filler materials and heat-affected zones. To simplify the problem, a 2D unitary cell model has been considered by a few researchers [134, 135], as given in Figure 4.4(b). The plane strain condition has been applied to simulate the sufficiently long body for the sake of conservativeness. Also, a quarter model is created by applying symmetry boundary conditions on the right and bottom edges while any rigid body movements have been prevented in the meantime. The normal displacements on the top and left

edges have been coupled to consider the repetition of the unitary model along these edges, which simulates the pattern of channels on the cross-section surface of a PCHE core. The hot channels, marked in red, are subjected to relatively high pressure P_H and high temperature T_H; while the cold channels, marked in blue, are subjected to relatively low pressure P_C and low temperature T_C. To avoid numerical singularity during FE analysis, a fillet radius *r* is applied at the corner of each channel. The FE model is then meshed into 5357 quadratic elements of type CPE8R in Abaqus/CAE.

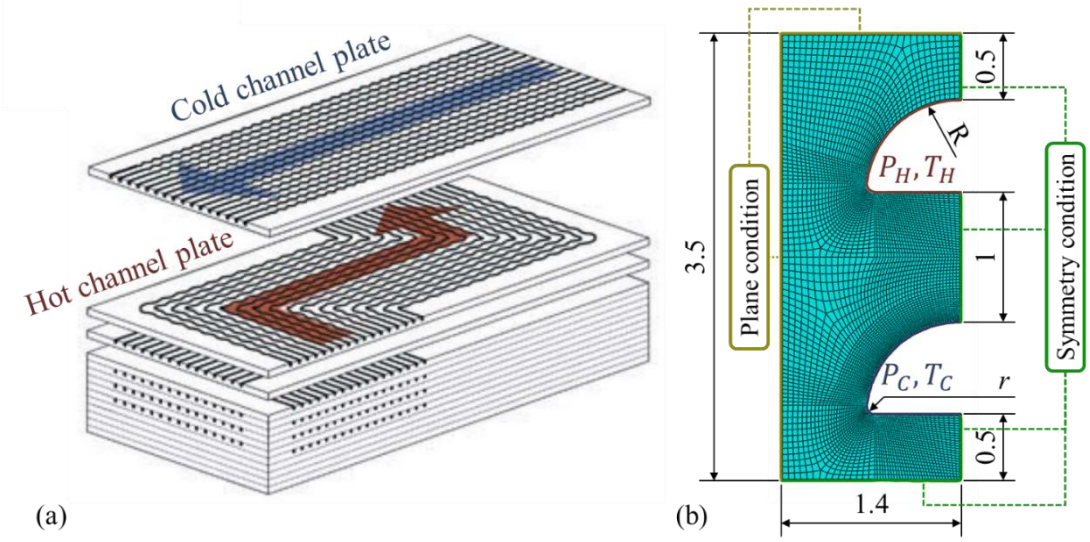

Figure 4.4: (a) Plate stacking of a PCHE core (b) The geometry, mesh and boundary conditions of a unitary cell model (dimensions in millimetres)

For loading conditions, the PCHE channels are subjected to constant inner pressure and cyclic temperature gradient, as shown in Figure 4.5. For hot channels, the initial pressure $P_H = 250\ \mathrm{MPa}$ and the initial temperature $T_H = T_0 + \Delta T_C(t)$ with extreme temperatures of 0 °C and 100 °C; for cold channels, the initial pressure $P_C = 100\ \mathrm{MPa}$ and the initial temperature $T_C = T_0 + \Delta T_C(t)$ with extreme temperatures of 0 °C and 90 °C. The temperature field is then evaluated by a steady-state thermal analysis, and the thermal stress θ is caused by the temperature difference between the hot and cold channels. After the linear elastic analysis with both the initial pressure and temperature, an extended shakedown algorithm is employed to scale the loads by a multiplier to reach the creep rupture boundary for a given rupture time.

Operated at high temperature and high pressure, the preferred materials for Intermediate Heat Exchangers (IHX) are alloy 617 and alloy 800H [133]. As described in Section 4.2, the revised yield strength is determined by the smaller value between the yield stress of the material and the creep rupture stress calculated by the UCRE,

as shown in Figure 4.6. The temperature-dependent yield stress is obtained from ASME BPVC Section II [136], and the parameters for creep rupture stress evaluation are given in Table 4.1. Two different creep rupture times T_R are also considered for both materials: 10000 hours and 100000 hours. It can be seen in Figure 4.6 that yield stress is dominant for lower temperature and the creep effect dominate for higher temperature. For alloy 617, the transition temperature is around 700 °C ($t_R = 10000$ h) and 650 °C ($t_R = 100000$ h); for alloy 800H, the transition temperature is around 650 °C ($t_R = 10000$ h) and 575 °C ($t_R = 100000$ h). The overall allowable stress of alloy 617 is higher than alloy 800H. Other material properties used in this work are temperature-independent for the sake of simplicity. For alloy 617, the Young's modulus $E_1 = 211$ GPa and the thermal expansion coefficient $\alpha_1 = 1.58 \times 10^{-5}$ °C^{-1}; for alloy 800H, the Young's modulus $E_1 = 196.5$ GPa and the thermal expansion coefficient $\alpha_1 = 1.44 \times 10^{-5}$ °C^{-1}.

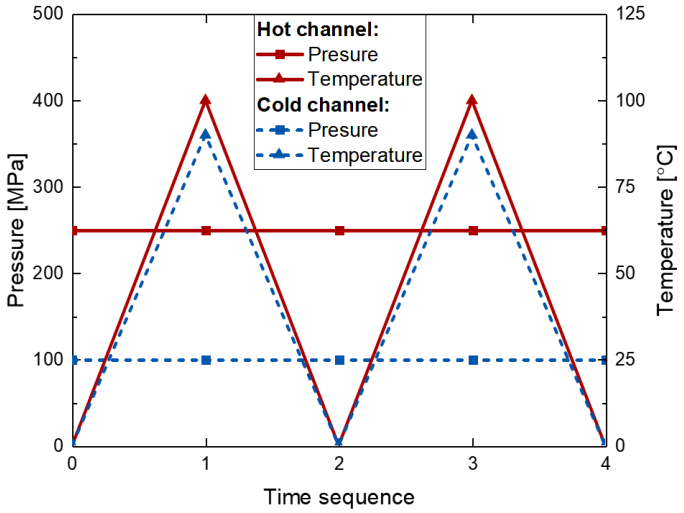

Figure 4.5: The loading history considered for the creep rupture assessment of the PCHE core

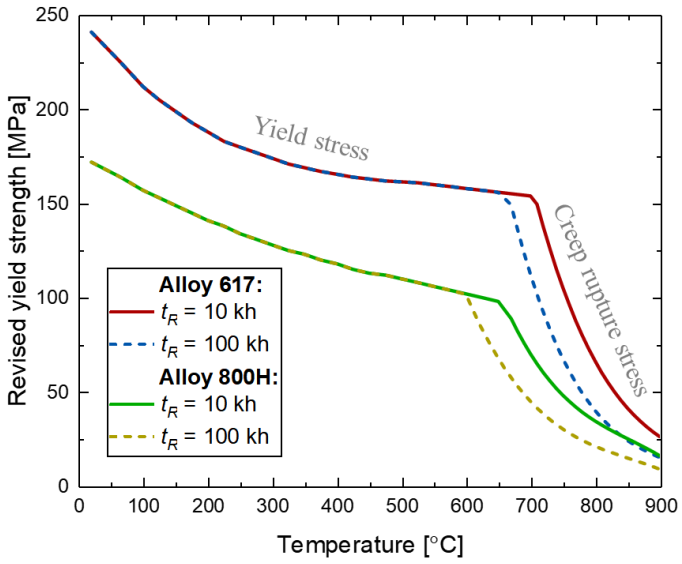

Figure 4.6: The revised yield strength with various rupture times for alloy 617 and alloy 800H

The shakedown and creep rupture limits of the PCHE core manufactured of alloy 617 with creep rupture time $t_R = 100000\ \mathrm{h}$ are firstly evaluated and presented in Figure 4.7. The pressure difference ΔP between the hot and cold channels is presented in megapascal [MPa], and the temperature difference ΔT between the hot and cold channels is shown in degrees Celsius [°C]. The creep rupture limit denotes an envelope on which the time to rupture is constant for any load case applied. It is calculated by specifying the ratio $\varphi = \Delta P/\theta$ between thermal and mechanical loads, before scaling both loads to the rupture boundary by the extended shakedown algorithm. Compared to the shakedown boundary, the effect of creep becomes significant with the increase of temperature. When $\Delta T \leq 66\ ^{\circ}\mathrm{C}$, the creep rupture boundary is controlled by original yield stress only; when $\Delta T \geq 66\ ^{\circ}\mathrm{C}$, the boundary is controlled by the creep rupture strength instead. The contours of the temperature field and corresponding revised yield stress for load point (B) are shown in Figure 4.8. It can be observed that the upper part of the component is affected by the creep rupture strength due to high temperature while the lower part is not.

Unlike Bree-like diagrams, which contain reverse plasticity limit segment and ratchet limit segment, the creep rupture limit comprises three distinct segments divided by the grey dashed line in Figure 4.7. Similar phenomena have also been reported in [56, 126]. To further study the difference in failure mechanisms, three cyclic load points have been chosen from various segments in the diagram with their effective strain increment $\Delta\varepsilon_{eq}^{c}$ given in Figure 4.9. For load point (A) (10.5, 81), the failure mechanism is local creep rupture with maximum $\Delta\varepsilon_{eq}^{c}$ appears at the corner of the

cold channels caused by dominant thermal stress. For load point (B) (50.8, 72), the failure mechanism is global creep rupture with a strain zone across the body starting from the corner of the hot channel. Similarly, for load point (C) (97.2, 25), the failure mechanism is global plastic rupture with a strain zone at the upper part of the structure. There are slight differences between Figure 4.9(b) and Figure 4.9(c), which are caused by the interaction between creep and plasticity, proving the distinction between the global creep rupture and global ratchetting. A similar contour of failure mechanisms of PCHE cores can also be found in [135], proving the accuracy of the proposed direct method.

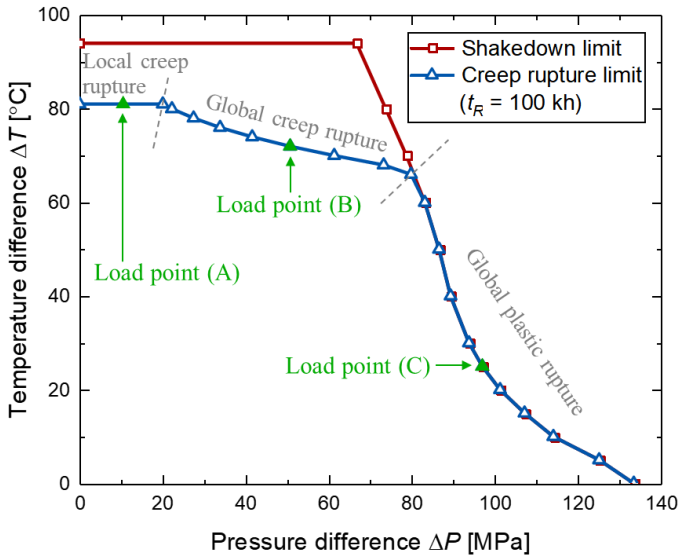

Figure 4.7: The shakedown and creep rupture limit of the PCHE core manufactured of alloy 617

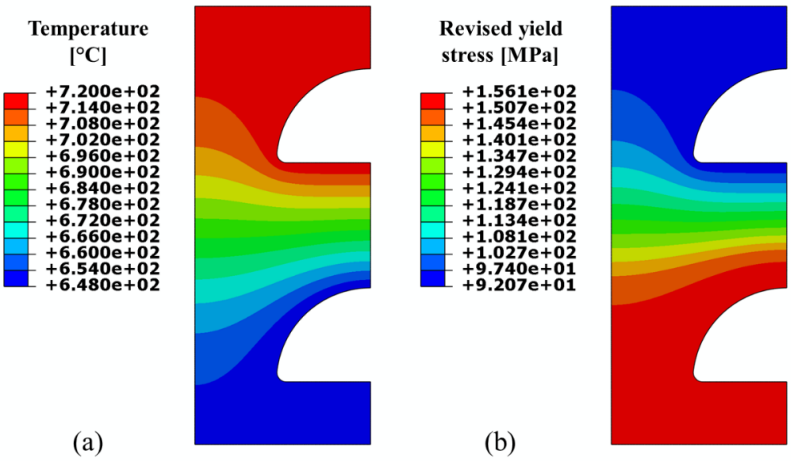

Figure 4.8: The temperature field and corresponding revised yield stress for load point (B)

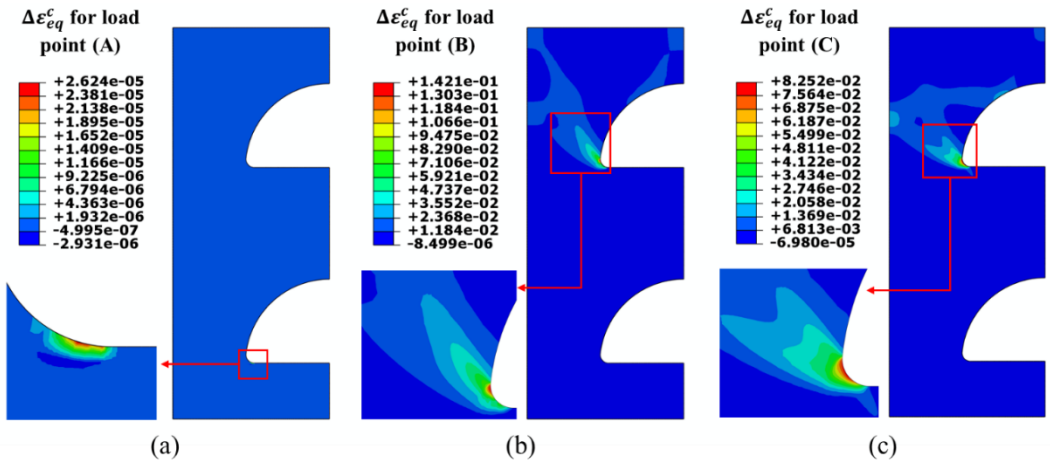

Figure 4.9: The failure mechanisms for three different load points

4.5.2 Effect of changing material

The shakedown and creep rupture analyses have also been performed on the PCHE core manufactured of alloy 800H considering identical boundary and loading conditions compared to previous analyses. The comparisons of the shakedown and creep rupture boundaries of the PCHE core manufactured of both materials are given in Figure 4.10. Although similar patterns of shakedown and creep rupture boundaries can be found for 800H, the overall boundaries are smaller than the structure made from 617 because the overall revised yield stress of 800H is lower than 617, as shown in Figure 4.6. For alloy 800H, the creep effect becomes significant when the temperature reaches 64 °C ($t_R = 10000$ h) and 62 °C ($t_R = 100000$ h). It is worth noting that there is a minor difference in reverse plasticity limits on shakedown and creep rupture boundaries for alloy 800H at $t_R = 10$ kh. The reason is that the failure mechanism at that load point is local creep rupture and the damage concentrates at the corner of the bottom channels, similarly in Figure 4.9(a). However, after scaling the thermal stress to the reverse plasticity limit, the revised yield stress at the corner of cold channels is not affected by the creep rupture stress since the temperature is around 675 °C. With the increase of pressure, the failure location shifted to the hot channels, making the creep rupture limit deviate from the horizontal reverse plasticity limit. Another notable difference of the boundaries between 617 and 800H lines in the segment of ratchet limit. A concave ratchet limit for alloy 617 can be observed due to a sharp decrease in yield stress when the temperature is low. The parametric study with different materials has been dramatically simplified by the implementation of UCRE in the LMM framework. Instead of inputting the temperature-dependent rupture

stress manually, the rupture behaviour can be readily described by entering several material constants.

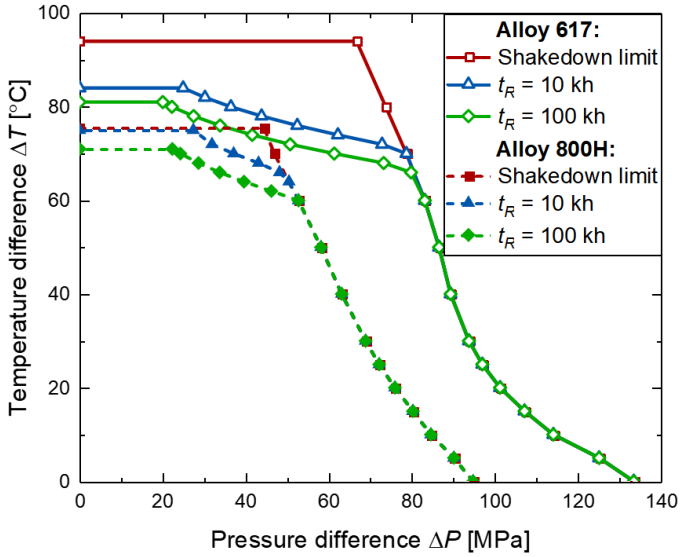

Figure 4.10: Comparisons of the shakedown and creep rupture limit of the PCHE core manufactured of alloy 617 and alloy 800H

4.5.3 Effect of changing channel shapes

It has been reported that the shape of channels may be distorted to semielliptical after the process of diffusion bonding [123]. Therefore, a PCHE core with semielliptical channels with corner radius $r = 6\%R$ has been modelled as shown in Figure 4.11(a). The shakedown and creep rupture analyses have been performed considering $t_R = 100000\,\mathrm{h}$, as shown in Figure 4.11(b). The results have been compared with the shakedown and creep rupture boundaries of the PCHE core with semicircular channels considering identical corner radius and rupture time. It can be observed that the limit load and the ratchet limit of the PCHE core with semielliptical channels are slightly smaller than the one with semicircular channels. However, the reverse plasticity parts of the boundaries are unaffected by the change of channel shape. The reason is that the change of reverse plasticity parts of the boundaries mainly depends on the corner angle. In contrast, the change of ratchet parts of the boundaries mostly depends on the thickness of the material. In this case, both semicircular and semielliptical channels share the same corner radius, but the obtuse angle of semielliptical channels at the bottom corner causes a loss of material, which slightly reduces the thickness of structure at that location. Therefore, it can be concluded that the change of channel shape has a limited influence on the shakedown and creep rupture limits.

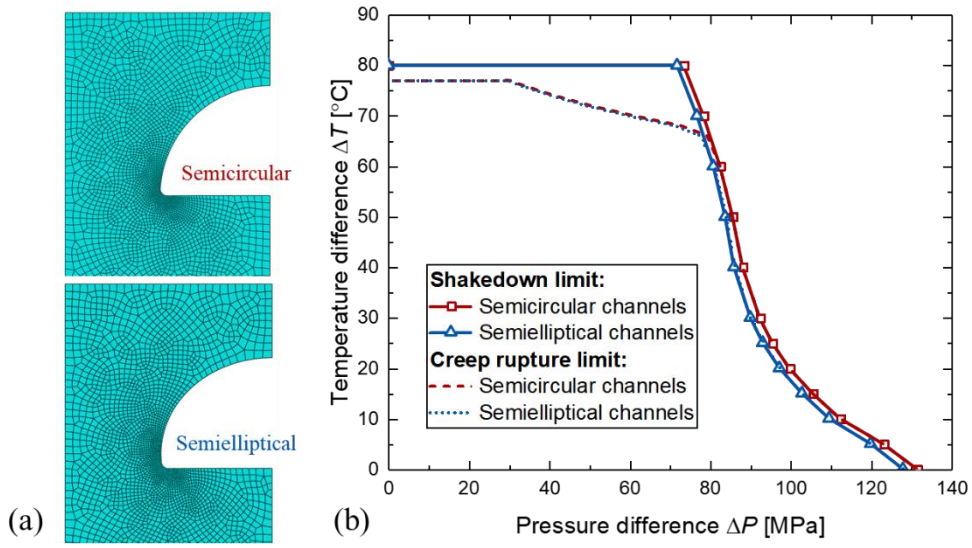

Figure 4.11: (a) The geometry and mesh of the PCHE core with semicircular and semielliptical channels (b) Comparisons of the shakedown and creep rupture limit of the PCHE core with different channel shapes

4.5.4 Effect of changing channel dimensions

Since a PCHE core can be designed in various scales and dimensions depending on its working condition, an investigation of the effect of changing channel dimensions becomes highly significant. The shakedown and creep rupture limit of the PCHE core with various channel radius *R*, and corner radius *r* have been evaluated and presented in Figure 4.12, where *R* [mm] is taken as 0.65, 0.75, 0.9, and 1; *r* is taken as 1%, 3%, 6%, and 10% of the channel radius *R*. For parametric studies, *r* remains constant at 10%*R* when *R* is variable; *R* is kept constant at 0.75 mm when *r* is variable. The shape of the channels is semicircular, and the material adopted is alloy 617. The reverse plasticity limit and limit load have been extracted from the curves and plotted in Figure 4.13 for further comparison. For the shakedown boundaries considering various channel radius *R* in Figure 4.12(a) and Figure 4.13(a), the limit load reduces significantly with increasing *R* due to the loss of material in the component. The reverse plasticity limit, on the other hand, increases with increasing *R*. The reason is that in this case, the ratio of corner radius *r* to the channel radius *R* is fixed at 10%. Thus an increase of *R* also results in a growth of *r*. Since low cycle fatigue is highly related to the stress concentration in the local region, the reverse plasticity limit would increase correspondingly with an increasing *r*. A similar trend can be observed in the creep rupture limits when the temperature reaches around 650 °C and the creep rupture boundaries begin to separate from the shakedown boundaries. As presented

in Figure 4.12(b) and Figure 4.13(b), the effect of changing the corner radius *r* is also considered for the shakedown. The limit load is barely affected in this case, but the reverse plasticity limit significantly increases with increasing *r* due to a lower stress concentration at the corner of channels. In terms of the creep rupture limit, the effect of global creep rupture becomes notable when the temperature is higher than 650 °C, making the creep rupture boundaries shrink towards the Y-axis. It is worth mentioning that for the case $r = 1\%R$, the temperature at the reverse plasticity limit is lower than 650 °C. In this case, the creep effect is negligible and the creep rupture limit becomes identical to the shakedown limit.

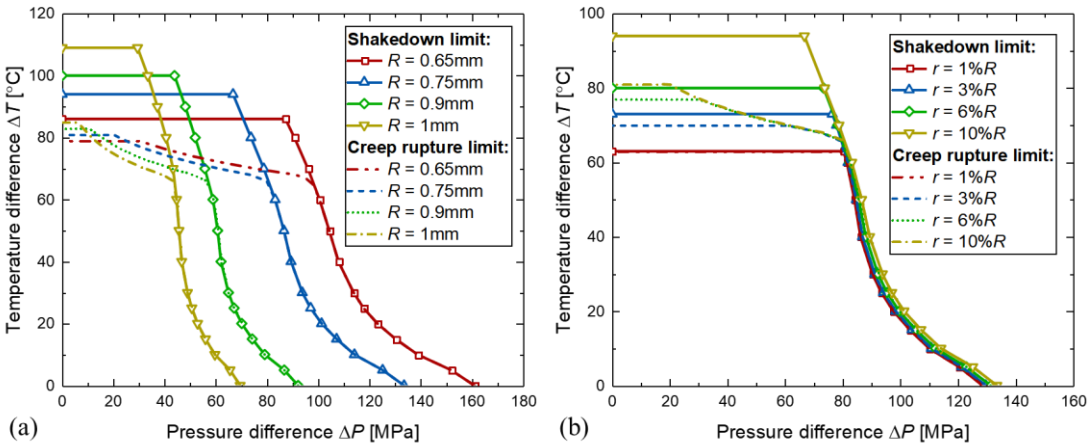

Figure 4.12: Comparisons of the shakedown and creep rupture limit of the PCHE core with (a) various channel radius *R* (b) various corner radius *r*

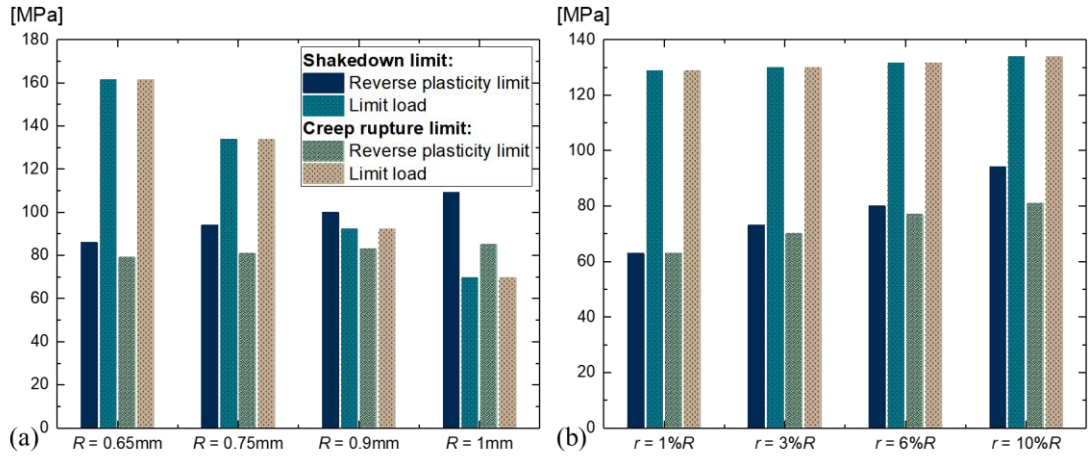

Figure 4.13: Comparisons of the reverse plasticity limit and limit load from the shakedown and creep rupture limits

4.6 Summary

In this chapter, a Unified Creep Rupture Equation (UCRE) has been developed to describe the creep rupture curve for a broader range of steel types. A Python code has also been developed to facilitate the fitting process and generate a database for material parameters storage. Furthermore, a modification has been made in the current LMM framework to include the proposed equations for creep rupture analysis as part of structural integrity assessment.

The UCRE has been comprehensively compared with two other numerical schemes: linear interpolation/extrapolation and Larson-Miller parameter. The UCRE shows better accuracy than the other two techniques when predicting the creep rupture curves for 5CrMo with insufficient data points. The UCRE has also been adopted to fit the rupture strength for four other types of benchmark steel and agrees well with the results from several individual models shortlisted by the ECCC. Further validation of the proposed method has been performed by comparing predicted creep rupture stress using UCRE with the observed rupture stress from ECCC data sheets for more than 40 different steels. For most steels, the predicted rupture strengths are either identical or slightly more conservative than the observed ones within the deviation factor of 0.55, proving the reliability of the proposed technique.

To illustrate the utility of the proposed approach, a creep rupture analysis has been performed on a typical PCHE core. The UCRE has been adopted to generate the temperature-dependent revised yield stress in the structure. The shakedown and creep rupture boundaries have been presented considering cyclic thermal-mechanical loading conditions. Three different failure mechanisms have been observed in the creep rupture boundary: local creep rupture, global creep rupture and global plastic rupture. A series of parametric studies have also been conducted considering various materials and geometries. Compared to alloy 800H, alloy 617 is more suitable for PCHE cores considering the load-bearing capacity at high temperatures. The shape of PCHE channels has a limited effect on the creep rupture boundary, while the channel dimension has a great influence on the rupture limits. Therefore, by comparing the creep rupture curves fitted using UCRE and other numerical models from literature, the UCRE has shown good accuracy and reliability for the interpolation of material parameters for various materials. With a numerical example of a PCHE core, the UCRE has shown good applicability for engineering cases. In addition, the Bree-like diagram is further extended by considering the creep rupture curves.

5. The evaluation of the structural constant fatigue life diagram and ratchet limit

5.1 Introduction

For the evaluation and extension of the lifespan of large-scale pressure vessels in various industries, it has become essential to conduct a structural integrity assessment during the design and assessment procedures [137-139]. Having been investigated by many researchers [140-145], fatigue and ratchetting are two critical problems during the structural integrity assessment. Although these two problems are both caused by cyclic loading conditions, there are still some distinctions between them. Low cycle fatigue usually induces local crack initiation, while ratchetting would lead to incremental collapse, which is a global behaviour.

For the assessment of structural ratchetting, the Bree diagram has been proposed [12] as the foundation of NB-3222.5 in ASME III [146]. The classic Bree problem considers a thin cylindrical pipe subjected to constant internal pressure and cyclic thermal stress. Different ratio of thermal and mechanical loads is considered and the loads are scaled proportionally to form the Bree diagram. For arbitrary thermal-mechanical loading conditions, the modified Bree problem is proposed [24, 147], considering cyclic thermal stress and cyclic mechanical stress. Several numerical methods have been proposed for Bree-like problems, including analytical solution [12, 147], incremental Finite Element (FE) analysis, Direct Cycle Analysis (DCA) [148-150], Noncyclic Method [151, 152], and several direct methods [14, 81-85, 87-90]. As one of the direct methods, the Linear Matching Method (LMM) framework features high accuracy and computational efficiency compared to other approaches.

As another crucial part of structural integrity assessment, fatigue problems are split into two categories, high cycle fatigue (HCF) and low cycle fatigue (LCF) [153, 154]. For HCF problems, the structure typically operates in the elastic region, and the typical number of cycles to failure is higher than 5×10^4. The HCF life is calculated using the material's stress-life (S-N) curves based on the alternating stress [155]. For LCF problems, plasticity may be observed in the structure, and the typical number of cycles to failure is lower than 5×10^4 [11]. The LCF life can be evaluated using the material's strain-life (E-N) curves based on the total strain range or plastic strain range.

Numerical formulae have also been proposed for LCF life prediction, including the Coffin and Manson Law [27, 28]. At the material level, the constant life diagram has been introduced for LCF design, where the constant amplitude cyclic loading is depicted for constant fatigue life [156]. The constant life diagram is often plotted with alternating stress versus mean stress [157]. In this work, the concept of constant life diagrams is extended from the material level to the structure level. The LCF life boundary is plotted with the thermal load versus the mechanical load, where the number of cycles to failure is constant for any load combinations on the LCF life boundaries. The fatigue life can then be rapidly determined for arbitrary loading conditions in structural design.

Several numerical approaches have been proposed for the evaluation of strain range, including Neuber's rule [158-160], the elastic-plastic method in ASME VIII-2 [161], and the Direct Steady Cycle Analysis (DSCA) method [20, 90] in the Linear Matching Method (LMM) framework. Neuber's rule uses linear elastic analysis to estimate the plastic strain range in areas with stress concentration. This method is considered safe and efficient, but it is restricted to local geometry and can be over-conservative for cases with sharp notches [162]. The elastic-plastic method is based on cycle-by-cycle analyses in Finite Element (FE) software using nonlinear constitutive models. Therefore, this method is usually accurate but highly time-consuming. On the other hand, the DSCA method is a direct method with both high accuracy and efficiency. Several linear elastic equations are introduced to evaluate the residual stress and the plastic strain range iteratively. The stress and strain at steady state is calculated directly for the plotting of saturated hysteresis loops and the evaluation of fatigue damage.

A generalised method [23, 24] has been previously proposed for the evaluation of the ratchet limits of structures subjected to arbitrary thermal-mechanical load histories. To further evaluate the LCF life boundaries effectively, a Unified Procedure for Fatigue and Ratchet Analysis (UPFRA) [163] is proposed in this work as a one-stop solution for the ratchet and fatigue analysis considering arbitrary thermal-mechanical load conditions. Based on a bisection scheme, the DSCA subroutine is called iteratively for the evaluation of structural ratchet limit and LCF life boundaries considering different target LCF lives. The boundaries are then combined with the shakedown limit to form a complete interaction diagram. Temperature-dependent material properties

are also considered and implemented in the procedure for better accuracy and usability.

In this study, the Bree-like diagram is extended by including the constant fatigue life curves. The numerical methods for ratchet and fatigue analysis are extensively introduced in Section 5.2, including the introduction of DSCA in Section 5.2.1, the current LMM algorithm for ratchet analysis in Section 5.2.2, and the UPFRA in Section 5.2.3. Then two numerical examples are presented to show the advantages of the UPFRA for practical engineering problems in Section 5.3.

5.2 Numerical procedures for ratchet and fatigue analysis

For Bree-like problems, the load condition considered is usually composed of cyclic thermal loads and constant mechanical loads. In the LMM framework, the DSCA [164, 165] and Koiter's kinematic shakedown theorem [166] are adopted together to evaluate the structural ratchet limit. A two-stage procedure has been proposed, where the fixed cyclic load amplitude is firstly considered using the DSCA algorithm before the constant load history is scaled using the shakedown algorithm to reach the ratchet boundary.

For modified Bree problems or engineering problems concerning arbitrary thermal-mechanical load histories, a three-stage procedure has been proposed, which is included in the UPFRA [163]. The load ratio between two types of loads is first selected before the loadings are scaled proportionately to reach the ratchet boundary or the fatigue boundary. The load ratio can then be adjusted to achieve different points on the diagram.

5.2.1 The current DSCA algorithm

A body of volume V and surface S is considered, with cyclic temperatures $\theta(x,t)$ applied in V and cyclic surface loads $P(x,t)$ on the part of the body surface S_T. The displacement rate $\dot{u} = 0$ on the other part of the body surface S_U. Considering time cycle $0 \leq t \leq \Delta t$, the load history is decomposed into the thermal and surface load by:

$$F(x,t) = \theta(x,t) + P(x,t) \tag{5.1}$$

where $\theta(x,t)$ is the thermal load history, and $P(x,t)$ is the mechanical load history. The linear stress history is then calculated by:

$$\hat{\sigma}_{ij}(x,t) = \hat{\sigma}^{\theta}_{ij}(x,t) + \hat{\sigma}^{P}_{ij}(x,t) \tag{5.2}$$

where $\hat{\sigma}^{\theta}_{ij}(x,t)$ and $\hat{\sigma}^{P}_{ij}(x,t)$ are linear stress fields calculated from the linear elastic analyses with $\theta(x,t)$ and $P(x,t)$, respectively. The cyclic steady state is reached after a few cycles, so that:

$$\sigma_{ij}(x,t) = \sigma_{ij}(x,t+\Delta t) \text{ and } \dot{\varepsilon}_{ij}(x,t) = \dot{\varepsilon}_{ij}(x,t+\Delta t) \tag{5.3}$$

The cyclic solution at steady-state is composed of three components:

$$\sigma_{ij}(x,t) = \hat{\sigma}_{ij}(x,t) + \bar{\rho}_{ij}(x) + \rho^{r}_{ij}(x,t) \tag{5.4}$$

where $\bar{\rho}_{ij}(x)$ is a constant residual stress field with the satisfaction of zero surface traction on S_T. $\rho^{r}_{ij}(x,t)$ is a varying residual stress field with the satisfaction of $\rho^{r}_{ij}(x,0) = \rho^{r}_{ij}(x,\Delta t) = 0$. The von Mises yield function $f(\sigma_{ij}) \leq 0$ indicates a convex yield surface. Based on the flow rule:

$$\dot{\varepsilon}^{p}_{ij} = \dot{\alpha}\frac{\partial f}{\partial \sigma_{ij}}, \quad f = 0 \tag{5.5}$$

where $\dot{\alpha}$ denotes a plastic multiplier. According to the maximum work principle:

$$(\sigma^{c}_{ij} - \sigma^{*}_{ij})\dot{\varepsilon}^{c}_{ij} \geq 0 \tag{5.6}$$

where $f(\sigma^{c}_{ij}) = 0$ and $f(\sigma^{*}_{ij}) \leq 0$. σ^{c}_{ij} denotes the stress at yield while σ^{*}_{ij} the stress state with the satisfaction of the yield condition. The function I is defined by:

$$I(\dot{\varepsilon}^{c}_{ij}) = \int_V \int_0^{\Delta t} \{\sigma^{c}_{ij}\dot{\varepsilon}^{c}_{ij} - (\hat{\sigma}_{ij}(x,t) + \rho_{ij}(t))\dot{\varepsilon}^{c}_{ij}\} dt dV \tag{5.7}$$

where $\dot{\varepsilon}^{c}_{ij}$ denotes the kinematically admissible strain rate at yield and $\rho_{ij}(t) = \bar{\rho}_{ij} + \rho^{r}_{ij}$. For the sake of simplicity, the time integrations are replaced by the sum of values at N time instants: $t_1, t_2, t_3, \ldots, t_N$. The cyclic history is discretized into several time instants t_n and plastic strain is only observed at the vertices of stress history. The function I is then simplified by:

$$I(\dot{\varepsilon}^{c}_{ij}) = \sum_{n=1}^{N} I^{n} \tag{5.8}$$

$$\Delta\varepsilon^{c}_{ij} = \sum_{n=1}^{N} \Delta\varepsilon^{n}_{ij} \tag{5.9}$$

$$I^n\left(\Delta\varepsilon_{ij}^n, \rho_{ij}(t_n)\right) = \int_V \{\sigma_{ij}^n \Delta\varepsilon_{ij}^n - \left(\hat{\sigma}_{ij}(t_n) + \rho_{ij}(t_n)\right)\Delta\varepsilon_{ij}^n\} dV \tag{5.10}$$

$$\rho_{ij}(t_n) = \bar{\rho}_{ij} + \sum_{l=1}^{n} \Delta\rho_{ij}^l \tag{5.11}$$

$$\Delta\varepsilon_{ij}^{Tn} = C\Delta\rho_{ij}^n + \Delta\varepsilon_{ij}^n \tag{5.12}$$

where $\Delta\rho_{ij}^n$ satisfies equilibrium condition and $\Delta\varepsilon_{ij}^{Tn}$ is compatible. The minimization procedure of functions I^n is then introduced. Assuming $\Delta\varepsilon_{ij}^n = \Delta\varepsilon_{ij}^{ni}$, the shear modulus is given by:

$$\sigma_y = 2\bar{\mu}_{ui}\bar{\varepsilon}\left(\Delta\varepsilon_{ij}^{ni}\right) \tag{5.13}$$

where σ_y denotes the yield strength. A linear problem is then proposed by:

$$\Delta\varepsilon_{ij}^{Tf'} = \frac{1}{2\mu}\Delta\rho_{ij}^{nf'} + \Delta\varepsilon_{ij}^{nf'} \tag{5.14}$$

$$\Delta\varepsilon_{kk}^{Tf} = \frac{1}{3K}\Delta\rho_{kk}^{nf} \tag{5.15}$$

$$\Delta\varepsilon_{ij}^{nf'} = \frac{1}{2\bar{\mu}_{ui}}\left\{\hat{\sigma}_{ij}(t_n) + \rho_{ij}(t_{n-1}) + \Delta\rho_{ij}^{nf}\right\}' \tag{5.16}$$

where

$$\rho_{ij}(t_{n-1}) = \rho_{ij}(t_0) + \Delta\rho_{ij}^1 + \Delta\rho_{ij}^2 + \Delta\rho_{ij}^3 + \cdots + \Delta\rho_{ij}^{n-1}, \rho_{ij}(t_0) = \bar{\rho}_{ij} \tag{5.17}$$

To solve the linear problem, the varying residual stress $\Delta\rho_{ij_m}^n$ is evaluated at load instance n and iteration number m, where $n = 1,2,3,\ldots,N$ and $m = 1,2,3,\ldots,M$. The convergence criterion $\sum_{n=1}^{N}\Delta\rho_{ij_M}^n = 0$ is met at Mth iteration, where the constant residual stress is given by:

$$\bar{\rho}_{ij} = \sum_{n=1}^{N}\Delta\rho_{ij_1}^n + \sum_{n=1}^{N}\Delta\rho_{ij_2}^n + \sum_{n=1}^{N}\Delta\rho_{ij_3}^n + \cdots + \sum_{n=1}^{N}\Delta\rho_{ij_M}^n \tag{5.18}$$

The plastic strain amplitude at t_n is given by:

$$\Delta\varepsilon_{ij}^P(t_n) = \frac{1}{2\bar{\mu}_n}\left(\hat{\sigma}_{ij}'(t_n) + \rho_{ij}'(t_n)\right) \tag{5.19}$$

The equivalent ratchet strain over the cycle is calculated by:

$$\bar{\varepsilon}^R = \bar{\varepsilon}\left(\sum_{n=1}^{N} \Delta\, \varepsilon_{ij}^P(t_n)\right) \tag{5.20}$$

The total strain range $\Delta\bar{\varepsilon}$ over the cycle can also be evaluated by:

$$\Delta\bar{\varepsilon} = \max\left(\bar{\varepsilon}(t_a) - \bar{\varepsilon}(t_b)\right), \quad \forall a \in [1, N], \ \forall b \in [1, N] \tag{5.21}$$

5.2.2 The current approach for the evaluation of ratchet boundary

For Bree-like problems where the mechanical load is constant, a procedure with two stages has been given in [16]:

- Stage 1: the varying residual stress field caused by fixed cyclic loads is evaluated with the DSCA algorithm.
- Stage 2: the constant residual stress field is evaluated by scaling the constant loads to the ratchet limit with Koiter's kinematic shakedown algorithm.

Koiter's shakedown theorem [166] is given by:

$$\int_0^{\Delta t}\int_V \ \hat{\sigma}_{ij}\varepsilon_{ij}^c dtdV = \int_0^{\Delta t}\int_V \ \sigma_{ij}^c\varepsilon_{ij}^c dtdV \tag{5.22}$$

where

$$\hat{\sigma}_{ij} = \lambda\hat{\sigma}_{ij}^{\bar{F}} + \hat{\sigma}_{ij}^{\Delta}(x,t) + \rho_{ij}(x,t) \tag{5.23}$$

where λ denotes the load multiplier, $\hat{\sigma}_{ij}^{\bar{F}}$ denotes the constant stress field, $\hat{\sigma}_{ij}^{\Delta}(x,t)$ denotes the cyclic stress field, $\rho_{ij}(x,t)$ denotes the total residual stress field from Equation (5.11). Based on the flow rule and time discretization:

$$\int_0^{\Delta t}\int_V \ \sigma_{ij}^c\varepsilon_{ij}^c dtdV = \int_V \ \sum_{n=1}^{N}\sigma_{ij}^{c^n}\Delta\varepsilon_{ij}^n dV = \int_V \ \sum_{n=1}^{N}\sigma_y\,\bar{\varepsilon}(\Delta\varepsilon_{ij}^n)dV \tag{5.24}$$

where

$$\bar{\varepsilon}\left(\Delta\varepsilon_{ij}^n\right) = \sqrt{\frac{2}{3}\Delta\varepsilon_{ij}^n\Delta\varepsilon_{ij}^n} \tag{5.25}$$

The upper bound ratchet limit multiplier is then calculated by:

$$\lambda = \frac{\int_V \ \sum_{n=1}^{N}\sigma_y\bar{\varepsilon}\left(\Delta\varepsilon_{ij}^n\right)dV - \int_V \ \sum_{n=1}^{N}\left(\hat{\sigma}_{\mathrm{ij}}^{\Delta}(t_n)+\rho_{ij}(t_n)\right)\Delta\varepsilon_{ij}^n dV}{\int_V \ \hat{\sigma}_{\mathrm{ij}}^{\bar{F}}(\sum_{n=1}^{N}\Delta\varepsilon_{ij}^n)dV} \tag{5.26}$$

The difference between the ratchet and shakedown analyses in the LMM framework is that ratchet analysis includes a varying residual stress field calculated in Stage 1 as the input condition for Stage 2.

5.2.3 The Unified Procedure for Fatigue and Ratchet Analysis (UPFRA)

For modified Bree problems, cyclic thermal load and cyclic mechanical load are subjected to a component, where no phase shift is defined between both loads. An illustration of the typical shakedown limit, ratchet limit and constant fatigue life curve for modified Bree problems has been presented in Figure 5.1. The cyclic mechanical load P is normalised by the limit load P_{lim} and the cyclic thermal load σ_T is normalised by the yield stress σ_Y. The shakedown limit intersects with X-axis at the limit load and with Y-axis at twice the yield stress. An example constant low cycle fatigue life curve is also given, on which the load points would yield identical the target number cycles to failure N_T. For load points above, the number of cycles $N < N_T$; while for load points below, $N > N_T$. The failure mechanisms in different regions are also shown in Figure 5.1, which are separated by the plotted boundaries. The evaluation of shakedown boundary and limit load has already been considered in the existing LMM framework. To calculate the ratchet limit and fatigue boundaries for arbitrary thermal-mechanical loading conditions, a Unified Procedure for Fatigue and Ratchet Analysis (UPFRA) has been proposed in this work.

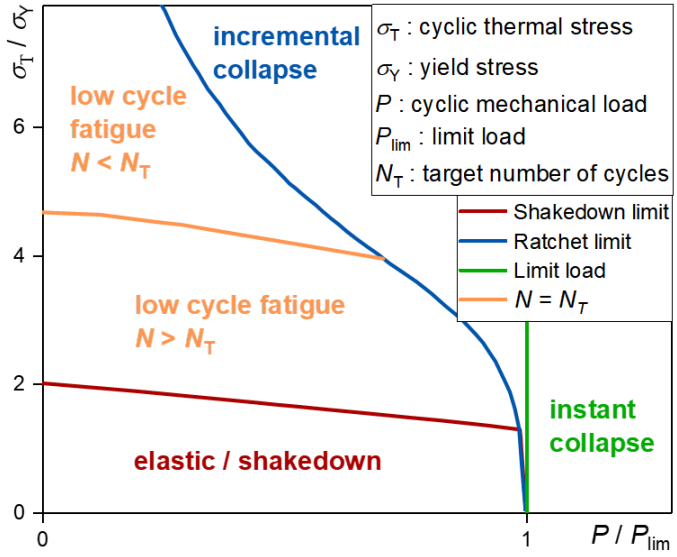

Figure 5.1: An illustration of typical shakedown limit, ratchet limit and constant fatigue life curve for modified Bree problems

It can be postulated that ratchet limit and fatigue boundaries always lie between the limit load and shakedown limit. Thus, a general procedure with three stages is proposed for faster calculation:

- Stage 1: the shakedown limit is evaluated for load ratio R using the LMM shakedown module.
- Stage 2: the limit load is evaluated using a special case in the LMM shakedown module.
- Stage 3: the ratchet limit or the constant life load multiplier is evaluated using the UPFRA.

A flowchart of key procedures in the UPFRA is given in Figure 5.2. The DSCA module has been modified to include damage models, and Python scripts have been developed to implement the numerical procedures in the UPFRA. Several input parameters are required for the procedure, including the load ratio *R*, convergence parameters *CONV*1, *CONV*2, lower bound multiplier λ_1^{LB} and upper bound multiplier λ_1^{UB} at first iteration. Here λ_1^{LB} is the shakedown multiplier from Stage 1; while λ_1^{UB} is the limit load multiplier from Stage 2.

The analysis mode can be chosen at the start of the script. For fatigue analysis, it is required to input a target number of cycles to failure N_T. The bisection numerical scheme is then used to call the DSCA repeatedly until the convergence condition is met. For the first iteration, the load multiplier $\lambda_1 = (\lambda_1^{LB1} + \lambda_1^{UB1})/2$. For the ith iteration, the load multiplier λ_i^F is computed by:

$$\lambda_i^{LB1} = \begin{cases} \lambda_{i-2}, & N_{i-2} > N_T \\ \lambda_{i-1}^{LB1}, & N_{i-2} \leq N_T \end{cases} \tag{5.27}$$

$$\lambda_i^{UB1} = \begin{cases} \lambda_{i-1}^{UB1}, & N_{i-2} > N_T \\ \lambda_{i-2}, & N_{i-2} \leq N_T \end{cases} \tag{5.28}$$

$$\lambda_i^F = \begin{cases} \frac{\lambda_{i-1}+\lambda_i^{UB1}}{2}, & N_{i-1} > N_T \\ \frac{\lambda_{i-1}+\lambda_i^{LB1}}{2}, & N_{i-1} \leq N_T \end{cases} \tag{5.29}$$

where λ_i^{LB1} and λ_i^{UB1} denote the lower and upper bound load multiplier at the ith iteration. The structural loads applied are then scaled by the multiplier λ_i^F and substituted into the DSCA subroutine. When the DSCA calculation is completed, the

minimum number of cycles to failure N_i within the component can be evaluated at the post-processing stage. Finally, N_i is compared with the target life N_T to determine the convergence of UPFRA. The whole procedure is repeated several times until the difference between N_i and N_T satisfies the convergence criterion.

For ratchet analysis, it is required to provide a target equivalent ratchet strain ε_T^R. Considering acceptable numerical errors for direct methods, ε_T^R can be taken as 0.02%/cycle [24]. For the first iteration, the load multiplier $\lambda_1 = (\lambda_1^{LB2} + \lambda_1^{UB2})/2$. For the ith iteration, the load multiplier λ_i^R is computed by:

$$\lambda_i^{LB2} = \begin{cases} \lambda_{i-2}, & \varepsilon_{i-2}^R < \varepsilon_T^R \\ \lambda_{i-1}^{LB2}, & \varepsilon_{i-2}^R \geq \varepsilon_T^R \end{cases} \tag{5.30}$$

$$\lambda_i^{UB2} = \begin{cases} \lambda_{i-1}^{UB2}, & \varepsilon_{i-2}^R < \varepsilon_T^R \\ \lambda_{i-2}, & \varepsilon_{i-2}^R \geq \varepsilon_T^R \end{cases} \tag{5.31}$$

$$\lambda_i^R = \begin{cases} \frac{\lambda_{i-1}+\lambda_i^{UB2}}{2}, & \varepsilon_{i-1}^R < \varepsilon_T^R \\ \frac{\lambda_{i-1}+\lambda_i^{LB2}}{2}, & \varepsilon_{i-1}^R \geq \varepsilon_T^R \end{cases} \tag{5.32}$$

where λ_i^{LB2} and λ_i^{UB2} denote the lower and upper bound load multiplier at the ith iteration. Unlike fatigue analysis, the maximum equivalent ratchet strain ε_i^R is evaluated and compared to ε_T^R to check convergence status. The UPFRA script has been fully optimised so that a number of different load ratios can be specified at the beginning, and a result CSV file is automatically generated at the end.

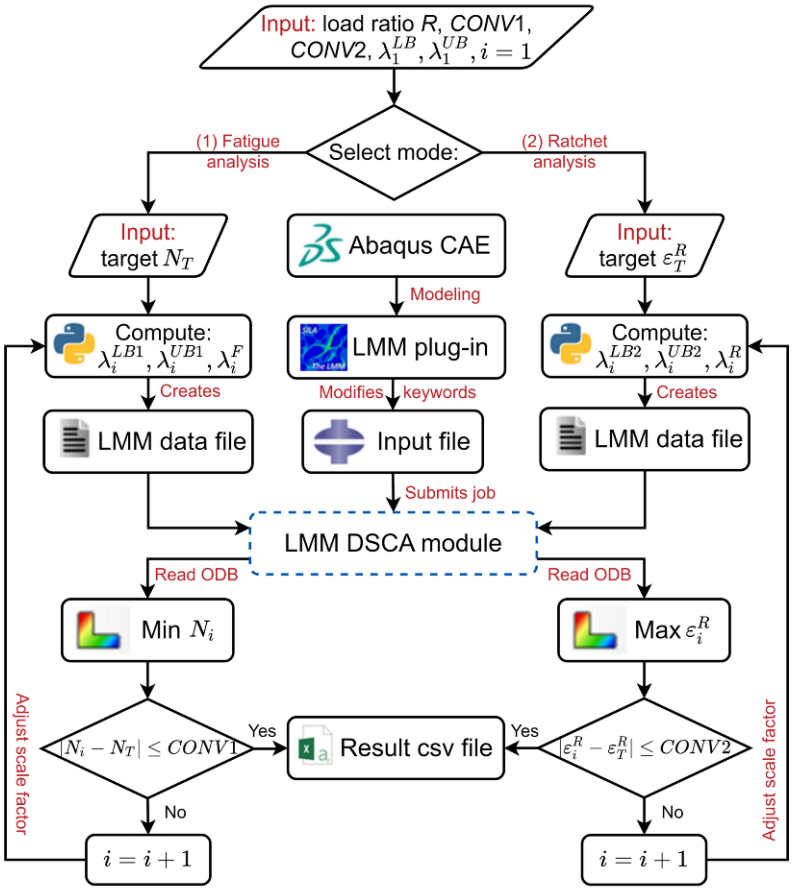

Figure 5.2: Simplified flowchart of the UPFRA

5.3 Numerical examples

5.3.1 A holed plate

5.3.1.1 FE model and material parameters

The holed plate has become a simplified but effective model to simulate the tubesheet in a heat exchanger [96]. As shown in Figure 5.3(a), the dimensionless geometry of the holed plate is taken from [24], where $D/L = 0.2$ and $d/L = 0.05$. The full plate is further simplified with a quarter model by applying symmetry boundary conditions. An axial pressure σ_P and a temperature gradient $\Delta T = T - T_0$ is also applied in the model. The model is meshed into 642 quadratic hexahedral elements of type C3D20R, followed by a steady-state thermal analysis to compute the thermal field at loading stage, as shown in Figure 5.3(b).

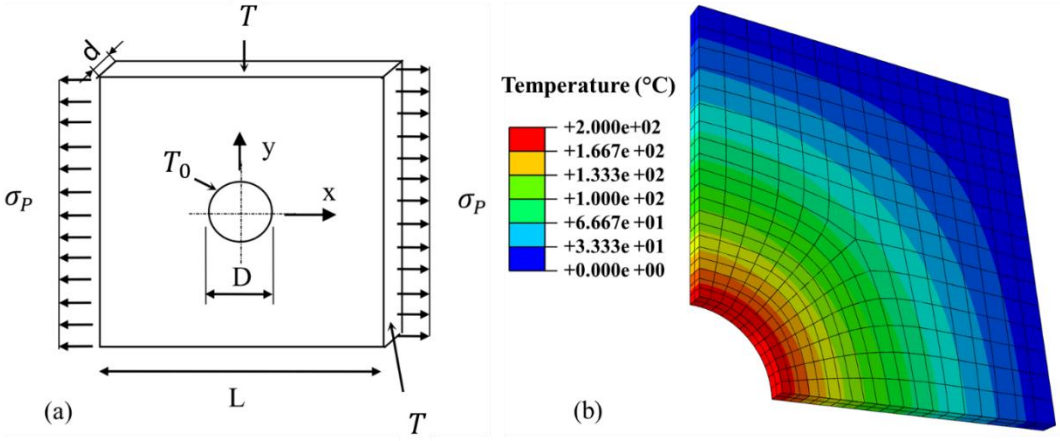

Figure 5.3: (a) The geometry of a holed plate [24] (b) The temperature distribution and FE mesh

The ratchet analysis on the holed plate subjected to arbitrary thermal-mechanical load histories has been introduced in [24]. Based on that work, the fatigue analysis and non-isothermal effect are further considered in this work. The X2CrNiMo17-12-2 steel is considered here, with its temperature-dependent material parameters for the EPP model given in Table 5.1. Ramberg-Osgood (R-O) model has also been adopted to describe the cyclic stress-strain behaviour, where the steady-state total strain ranges are given by:

$$\frac{\Delta\bar{\varepsilon}_t}{2} = \frac{\Delta\bar{\sigma}}{2E} + \left(\frac{\Delta\bar{\sigma}}{2A(T)}\right)^{\frac{1}{\beta(T)}} \tag{5.33}$$

The temperature-dependent material parameters for the R-O model are given in Table 5.2. As shown in Figure 5.4(a), the yield stress in the EPP model is taken as the 0.2% proof stress from the R-O curves. The effective Young's modulus $\bar{E}$ used in EPP model is derived from the elastic modulus E in R-O model by:

$$\bar{E} = \frac{3E}{2(1+\nu)} \tag{5.34}$$

where the Poisson's ratio $\nu = 0.3$. Linear interpolation and extrapolation techniques have been adopted to calculate values based on the local temperature in the structure. It should be mentioned that all the material parameters considered here are from [165].

The fatigue curves of X2CrNiMo17-12-2 steel at various temperatures have been given in Figure 5.4(b) for fatigue damage evaluation. A bilinear interpolation technique has been employed to compute the number of cycles to failure N based on local temperature T and total strain range $\Delta\varepsilon_t$. Then the lowest N in the structure is derived

and compared with the target fatigue life N_T for the plot of constant fatigue life diagrams.

Table 5.1: Temperature-dependent material parameters of X2CrNiMo17-12-2 steel considering the EPP model

Temperature, T [ºC]	Heat capacity, $C_p(T)$ [J/(kg·ºC)]	Conductivity, $\lambda(T)$ [W/(m·ºC)]	Thermal expansion, $\alpha(T)$ [10^{-5}/ºC]	$R_{p0.2}(T)$ [MPa]	$\bar{E}$ [MPa]
20	472	14.28	1.53	258	
100	501	15.48	1.59	252	
200	522	16.98	1.66	248	2.17×10^5
300	538	18.49	1.72	240	
400	556	19.99	1.78	240	

Table 5.2: Temperature-dependent material parameters for considering the R-O model

Temperature, T [ºC]	$A(T)$ [MPa]	$\beta(T)$
20	2286	0.351
100	2082	0.339
200	1860	0.325
300	1650	0.31
400	1650	0.31

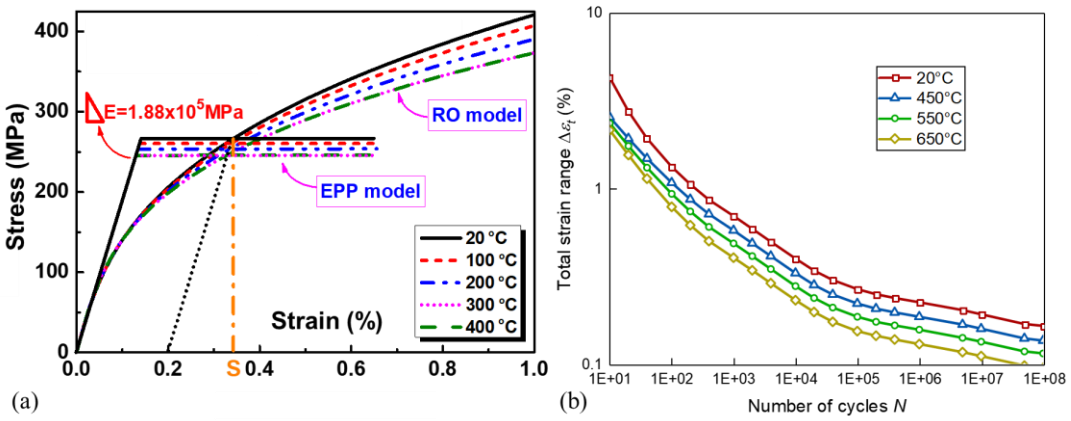

Figure 5.4: (a) Cyclic steady-state stress-strain curves described with the EPP model and the R-O model [167] (b) Fatigue curves of X2CrNiMo17-12-2 steel at various temperatures [6]

Two different load cases are considered here, as shown in Figure 5.5. For load case I, both the axial load and the thermal load are cyclic with two load vertices in the loading domain: $(P, \Delta T)$ and $(0, 0)$. For load case II, the axial load is constant while the thermal load is cyclic with two load vertices in the loading domain: $(P, \Delta T)$ and $(P, 0)$.

Using the shakedown module in the LMM framework, the limit load $P_0 = 225.5\ \mathrm{MPa}$ and the reverse plasticity limit $\Delta T_0 = 200\ ^\circ\mathrm{C}$ has been evaluated for future normalization. As shown in Figure 5.6, the elastic analysis has been performed on the

component subjected to pure axial pressure P_0 or pure thermal load ΔT_0. Both thermal and mechanical loads would induce stress concentration at the inner edge of the holed plate.

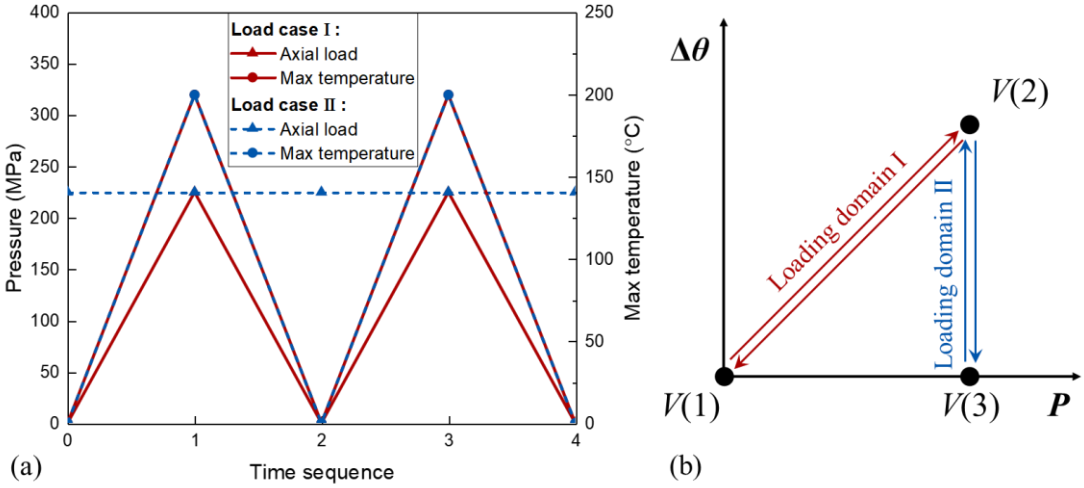

Figure 5.5: (a) Two simplified load cases (b) The corresponding loading domains

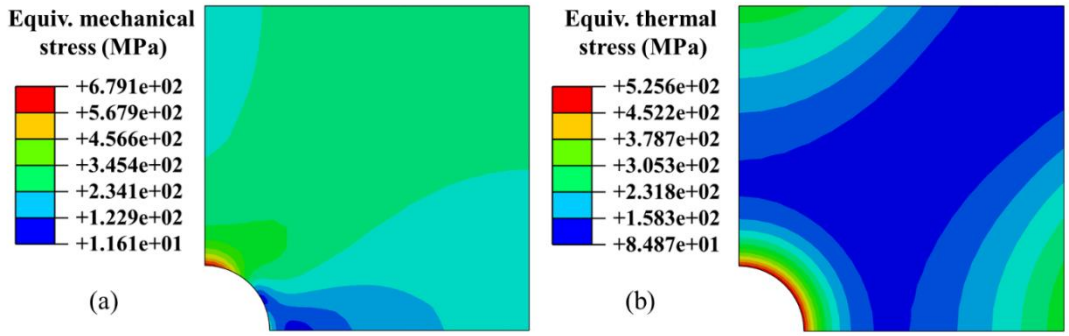

Figure 5.6: Elastic analysis contours of (a) the mechanical von Mises stress (b) the thermal von Mises stress during the loading stage

5.3.1.2 Results and discussions

For load case I, the shakedown limit, ratchet limit and constant fatigue life curves have been computed and presented in Figure 5.7(a). The EPP model is firstly considered for simplicity. The axial pressure P and the temperature difference ΔT have been normalised by P_0 and ΔT_0, respectively. In the reverse plasticity region, a series of fatigue boundaries are plotted, on which the number of cycles to fatigue failure is identical. These curves would greatly benefit the design and check procedure so that the expected fatigue life can be quickly determined from arbitrary loading combinations. It can be observed that the fatigue boundaries are mostly parallel to

the reverse plasticity limit. The lower the number of cycles to failure, the distance between the fatigue boundary and the reverse plasticity limit becomes larger. Due to the application of cyclic mechanical loads, a downward slope is found in the reverse plasticity limit. The other part of the shakedown boundary is shared with the lower part of the ratchet boundary, which is not vertical, as shown in [24]. The slight shrink of the lower part of the ratchet boundary is caused by the decrease of yield stress with increasing temperature. The upper part of the ratchet limit would approach the Y-axis rapidly when the thermal load increases.

For load case II, the shakedown limit, ratchet limit and constant fatigue life curves of the holed plate are presented in Figure 5.7(b). Since the mechanical load is constant, a Bree-like diagram is observed with a horizontal reverse plasticity limit. The fatigue boundaries are also parallel to the reverse plasticity limit and horizontal. The low cycle fatigue life is not affected by the increase of mechanical load as the thermal load dominates within the reverse plasticity region. Therefore, the plotting of a fatigue boundary may be simplified by only calculating the load point with pure thermal load and drawing the line parallel to the reverse plasticity limit.

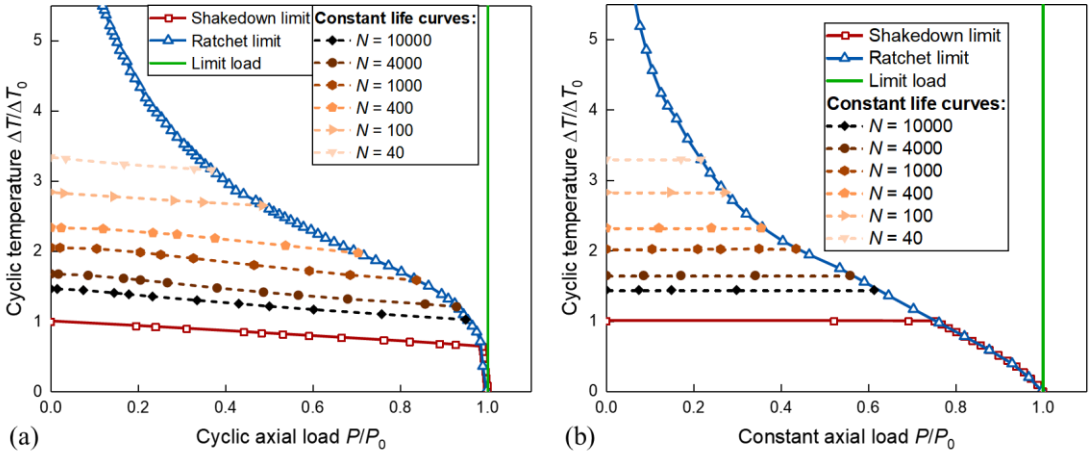

Figure 5.7: Shakedown limit, ratchet limit and constant fatigue life curves of the holed plate with EPP model subjected to (a) load case I (b) load case II

For materials with a significant hardening effect, the R-O model is further considered for the problem. The shakedown limit, ratchet limit and constant fatigue life curves of the holed plate obtained with the R-O model are shown in Figure 5.8. The fatigue boundaries obtained with the EPP model are also presented for comparison. It can be observed that the fatigue boundaries obtained with the R-O model still follow the slope of the reverse plasticity limit but are greatly influenced by the stress level in the

component. For both load cases, a transition point can be found in the fatigue boundary, after which the curve travels upward due to the hardening effect with increasing mechanical loads. Also, for higher temperatures, the fatigue boundaries obtained with the R-O model also move away from the ones obtained with the EPP model due to the hardening effect with a larger thermal load.

Two load points have been chosen in Figure 5.8(a) to further illustrate the difference induced by using different numerical models. The comparisons of the hysteresis loop obtained with R-O and EPP models have been presented in Figure 5.9. For load point (A), the hardening effect is minor, and the stress calculated by the R-O equation is lower than the yield stress of the EPP model. Thus the R-O model produces lower stress and a larger total strain range in the hysteresis loop. For load point (B), the hardening effect becomes significant, and the R-O model becomes more conservative, which results in a smaller total strain range and a higher fatigue life compared to the EPP model.

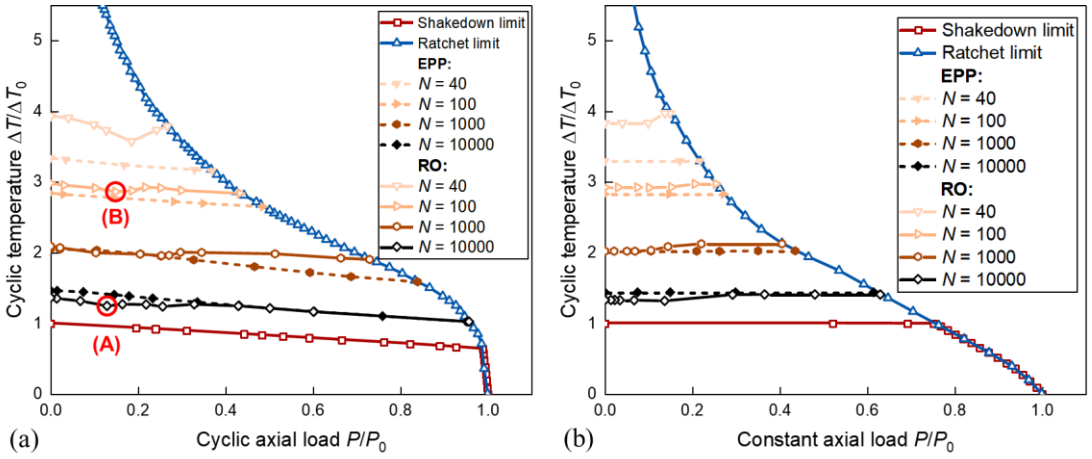

Figure 5.8: Shakedown limit, ratchet limit and constant fatigue life curves of the holed plate with R-O model subjected to (a) load case I (b) load case II

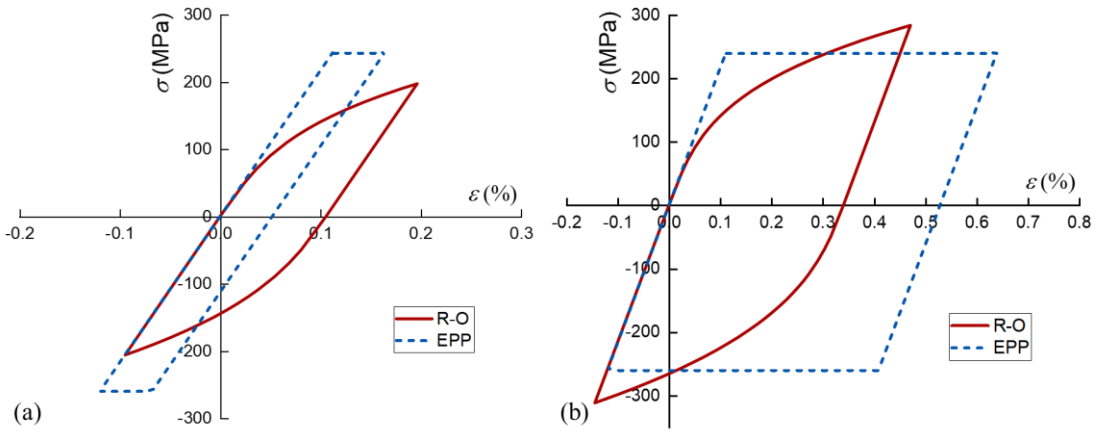

Figure 5.9: The comparisons of hysteresis loops obtained with R-O and EPP models for (a) load point (A) (b) load point (B)

Three different scale paths are shown in Figure 5.10(a). In the UPFRA, a fixed load ratio is firstly decided, and the loads are scaled proportionally to reach the specified target value. The target $\varepsilon_R = 0.04\%$ for ratchet analysis, as given in [23]. The target $N = 1000$ for fatigue analysis in this example. By selecting different load ratio, various scale paths are specified to obtain different load points on the boundary. The convergence histories of the maximum equivalent ratchet strain and the minimum number of cycles to failure for three scale paths are shown in Figure 5.10(b). By adopting the bisection scheme, both ε_R and N converge within five successive sub-cycles. For the same geometry considering load case I, a generalised numerical scheme has also been proposed in [24], which requires 10-15 sub-cycles for the convergence of ε_R. Therefore, the bisection scheme proposed in this work is considered more efficient than the generalised method from the previous work.

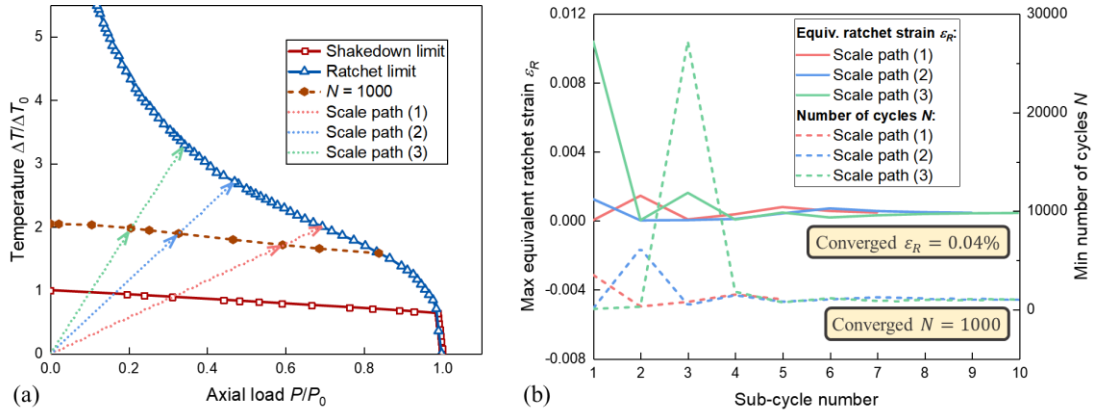

Figure 5.10: (a) Three scale paths used to plot ratchet limit and constant fatigue life curves (b) The convergence histories of the maximum equivalent ratchet strain and the minimum number of cycles to failure for three scale paths

5.3.1.3 Verification of results

The shakedown and ratchet boundaries obtained with the EPP model are further compared in Figure 5.11(a). It can be observed that the shakedown boundaries intercept with both axes at the same points, but the slope of reverse plasticity limits are different. The consideration of cyclic mechanical load would also significantly influence the shape of the ratchet limit by expanding its coverage area. To justify the accuracy of shakedown and ratchet boundaries of the holed plated subjected to load case I, several load points have been chosen for step-by-step (SBS) calculation, as shown in Figure 5.11(a). A total of 100 steps are created in ABAQUS to achieve the saturate stress-strain state. The evolution of the maximum plastic strain magnitude (PEMAG) in the structure subjected to load points (3), (7) and (8) has been plotted, as given in Figure 5.11(b). Load point (3) locates in the reverse plasticity region, and its PEMAG fluctuate around a particular value during steady-state. Load point (7) is in the shakedown region, and the corresponding PEMAG remains constant after a few cycles. Load point (8) is outside the ratchet limit, and its PEMAG keeps growing indefinitely with increasing time increment. Therefore, the behaviours of interesting load points have been justified by the evolution of PEMAG, proving the accuracy of the shakedown and ratchet limit calculated by the UPFRA.

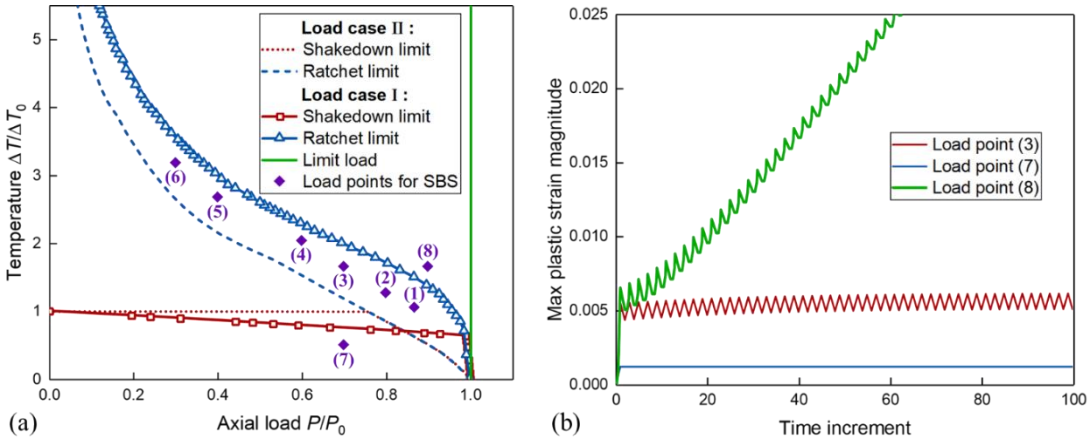

Figure 5.11: (a) Comparison of boundaries of the holed plate subjected to two load cases, and load points considered for SBS analysis (b) The evolution of the maximum plastic strain magnitude of the holed plate obtained with SBS analysis

To validate the constant fatigue life diagram, the load point (3) has been chosen from one of the constant life curves $N = 1000$. The failure mechanism is demonstrated by the equivalent ratchet strain ε_R, as shown in Figure 5.12(a). It can be observed that

the structure would first fail at the upper edge of the hole and the upper left corner simultaneously. Then the plastic zone would expand across the left side and connect both failure locations. The largest ε_R is found to be 0.01013%, which is less than the target $\varepsilon_R = 0.04\%$ as the load point (3) is situated within the ratchet limit. The total strain range $\Delta\varepsilon_t$ has been evaluated to calculate the fatigue life, as displayed in Figure 5.12(b). The largest $\Delta\varepsilon_t$ is found at the lower edge of the hole, where the largest fatigue damage is also determined. By looking up the $\Delta\varepsilon_t$ and local temperature into the Figure 5.4, the number of cycles to failure N can be evaluated using a bilinear interpolation scheme, as given in Figure 5.12(c). The lowest N is found to be 1000, proving the accuracy of the constant fatigue life curves computed by the UPFRA.

A series of SBS analyses have also been performed on the holed plate subjected to load point (3). Some contours obtained with SBS and DSCA have been presented and compared in Figure 5.13. The von Mises stress value and distribution during loading and unloading stages from SBS and DSCA are highly comparable, which indicates the reliability of DSCA. The equivalent plastic strain range $\Delta\varepsilon_P$ from DSCA and SBS have also been extracted and compared. The $\Delta\varepsilon_P$ from DSCA is slightly less conservative due to the different post-processing procedures, as discussed in Section 5.3.1. The maximum $\Delta\varepsilon_P$ is found at the lower edge of the hole, where an interesting integration point is selected for the further investigation of the stress-strain behaviour.

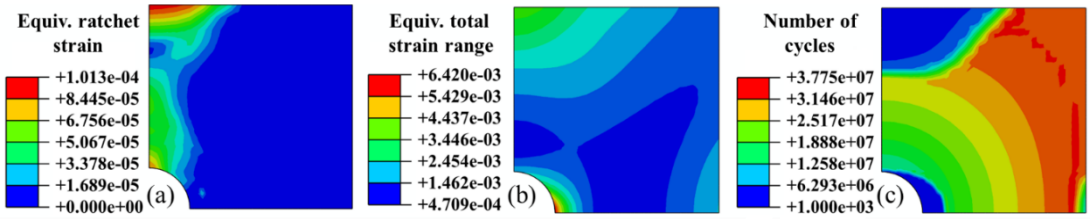

Figure 5.12: DSCA contours for load point (3) of (a) equivalent ratchet strain (b) equivalent total strain range (c) number of cycles to failure

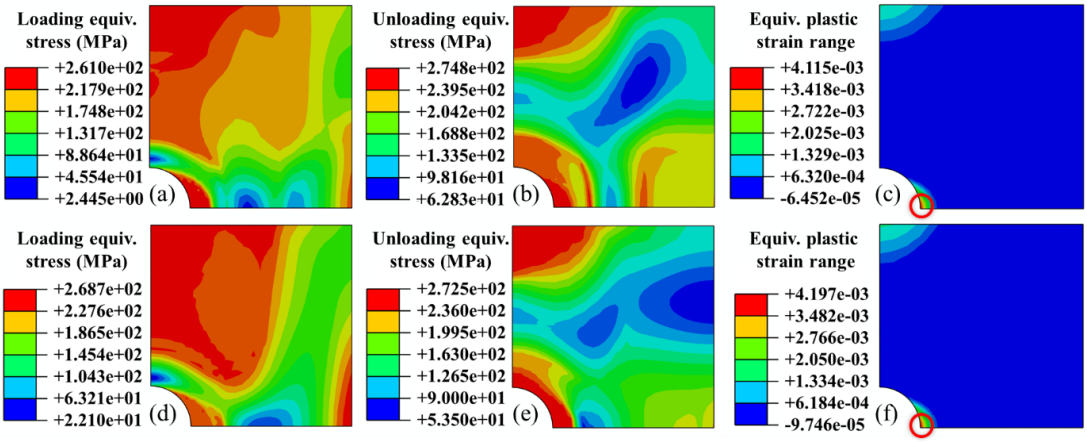

Figure 5.13: Comparison of contours for load point (3) of (a) von Mises steady-state stress during loading process obtained with DSCA (b) von Mises steady-state stress during unloading process obtained with DSCA (c) $\Delta\varepsilon_p$ obtained with DSCA and the location of maximum $\Delta\varepsilon_p$ (d) von Mises steady-state stress during loading process obtained with SBS (e) von Mises steady-state stress during the unloading process obtained with SBS (f) $\Delta\varepsilon_p$ obtained with SBS and the location of maximum $\Delta\varepsilon_p$

The saturated hysteresis loops at the location of the largest $\Delta\varepsilon_P$ for the holed plate considering various load points have been evaluated with DSCA and SBS, as shown in Figure 5.14(a). Due to the nature of the EPP model, the von Mises stress could not exceed the temperature-dependent yield stress. The largest effective tensile stress is controlled by the highest local temperature, while the largest effective compressive stress equals the yield stress at $T = 0$ °C. For load points chosen from Figure 5.11(a), load point (1) represents higher axial load and lower temperature, while load point (3) represents lower axial load and higher temperature. It can be observed in Figure 5.14(a) that the hysteresis loop for load point (1) has a lower total strain range than load point (3). The reason is that the failure mechanisms for these load points are low cycle fatigue and are thermal load dominant.

The maximum total strain range $\Delta\varepsilon_p$ in the structure subjected to 6 different load points is further compared in Figure 5.14(b). As discussed in Section 5.3.1, the $\Delta\varepsilon_p$ calculated by the DSCA is slightly smaller than the $\Delta\varepsilon_p$ from SBS because of the different sequence during the post-processing of effective values. In DSCA, the strain tensors at the loading and unloading stages are first subtracted before calculating the effective values. In SBS, the effective values are first calculated before the subtraction in a user-defined field. An average error of 2.96% between results obtained with DSCA and SBS is found for load points (1) – (6), proving the precision and reliability of the proposed method.

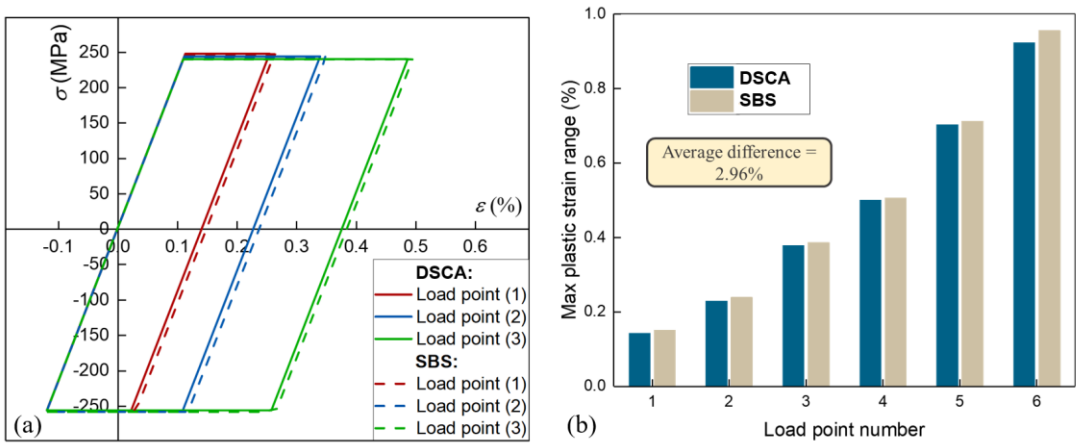

Figure 5.14: Comparison of (a) saturated hysteresis loops obtained with DSCA and SBS (b) maximum plastic strain range obtained with DSCA and SBS

5.3.2 A heat exchanger in aero-engine

5.3.2.1 FE model and material parameters

For typical aero-engines, lubricating oil is circulated within the rotating components to reduce friction. With the increase of ambient temperature and influence of friction force, the temperature of the turbine oil would also rise. In this way, the performance of the turbine oil would be significantly reduced due to the decrease in viscosity and oxidation stability [168]. Therefore, it is essential to employ a heat exchanger to cool down the lubricating oil. The geometry of an assembled shell-and-tube heat exchanger is shown in Figure 5.15. Because of the limited available space in the aero-engine, a small-scaled heat exchanger has been designed for this study. In addition, instead of using a thick and walled tubesheet [161], a thin and flexible tubesheet has been designed to be welded to the outer shell so that the total weight of the heat exchanger can be further reduced.

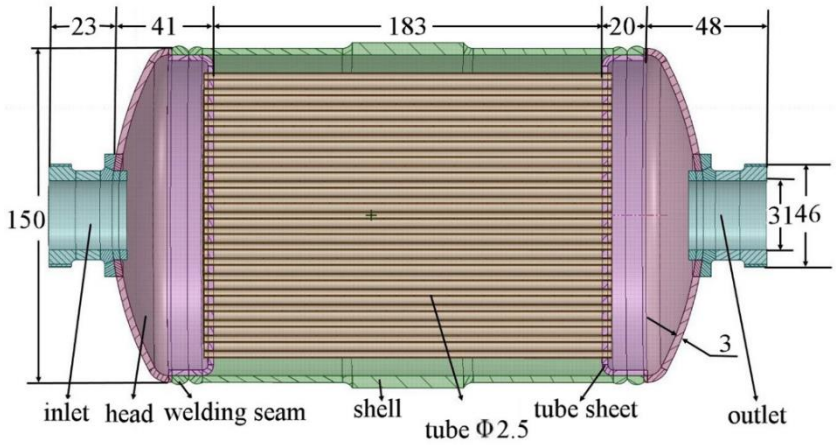

Figure 5.15: The geometry of an assembled shell-and-tube heat exchanger (dimensions in millimetres)

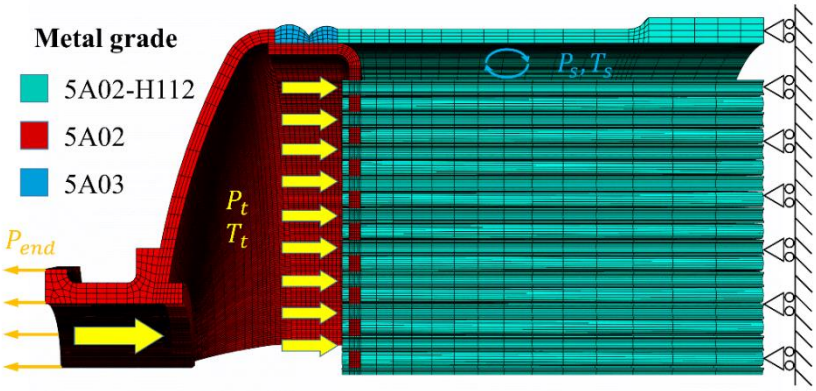

Figure 5.16: The FE mesh, material designation and a typical operating condition

A 1/8 FE model has been created in ABAQUS/CAE [21] for simplification, as shown in Figure 5.16. Some features such as the traverse baffles between tubes have also been ignored to improve efficiency. The FE model has been meshed into 245534 linear hexahedral elements of type C3D8 and 1968 linear wedge elements of type C3D6. The mesh on the tubesheet has been further refined due to stress concentration in the region. During the typical working condition, the turbine oil with pressure P_t and temperature T_t enters through the inlet and flow inside the thin tubes. Meanwhile, the coolant water with pressure P_s and temperature T_s is circulated between the tubes with the shell. An equivalent pressure P_{end} is applied to the inlet surface due to the closed end effect. Symmetry boundary conditions have also been applied on symmetric surfaces to simulate the whole body.

As shown in Figure 5.16, three different metal grades of aluminium have been adopted and assigned in different parts. The temperature-independent material

parameters are presented in Table 5.3. Since the highest temperature of turbine oil is found to be 150 ºC, the material parameters of aluminium at 150 ºC have been chosen for conservative results. Due to the complexity of the geometry, the use of temperature-independent properties could avoid convergence problems and improve computational efficiency. The justification for adopting temperature-dependent and temperature-independent material properties has been given in [120, 165].

Table 5.3: Material parameters for specified metal grades of aluminium at 150 ºC

Metal grade	5A02-H112	5A02	5A03
Conductivity, k [W/(m·ºC)]	168	168	175
Density, ρ [g/cm^3]	2.68	2.68	2.77
Young's modulus, E [GPa]	70	70	65
Poisson's ratio, v	0.3	0.3	0.3
Thermal expansion coefficient, α [10^{-5}/ºC]	2.57	2.57	4
Specific heat capacity, c [J/(kg·ºC)]	825	825	875
Yield stress, σ_s [MPa]	186	78	202

Two simplified load cases are chosen for this problem, as shown in Figure 5.17. The general cyclic loading condition of start-up and shut-down is considered, and the creep effect is neglected. For typical operating conditions, the temperature of the inlet turbine oil $T_t = 150$ ℃ and the tube pressure $P_t = 3$ MPa. The shell pressure caused by the coolant water $P_s = 1$ MPa. A Bree-like problem with constant inner pressure and cyclic temperature has been considered, as shown in Figure 5.17(a). A modified Bree problem with cyclic inner pressure and cyclic temperature has also been considered, as shown in Figure 5.17(b).

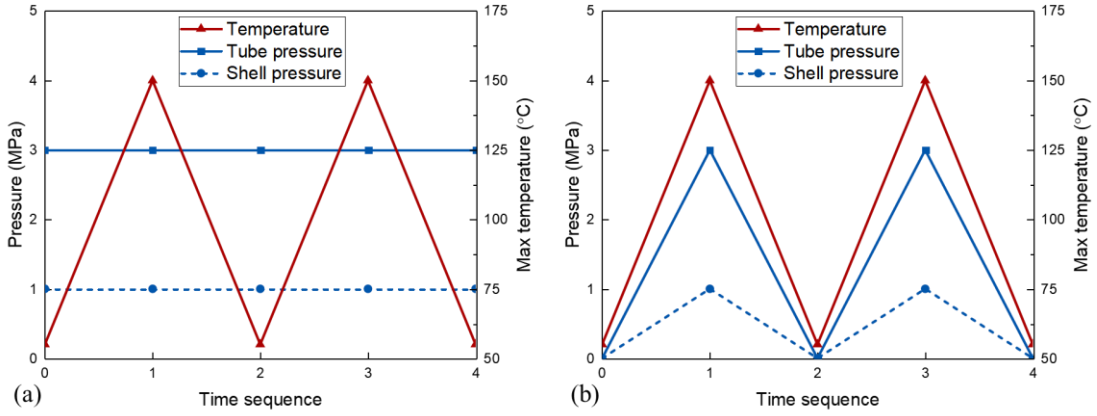

Figure 5.17: Simplified load cases with (a) constant inner pressure and cyclic temperature (b) cyclic inner pressure and cyclic temperature

5.3.2.2 Results and discussions

A steady-state thermal analysis has been performed to evaluate the temperature field, as given in Figure 5.18(a). Since the transient thermal effect is not considered in this case, the loading and unloading time is ignored. The inlet temperature of turbine oil is 150 ºC, and the shell temperature of coolant water is 55 ºC. A significant temperature gradient is then created around the tubesheet area. After that, linear elastic analysis has been conducted to generate the stress field for later use. The mechanical con Mises stress is shown in Figure 5.18(b), and the thermal von Mises stress at the tubesheet is given in Figure 5.18(c). Besides the tubesheet, the other part of the heat exchanger is subjected to relatively low thermal stress, so the stress distribution on the other part is not presented. It is worth mentioning that for traditional thick and walled tubesheet design, the concentration of thermal stress is usually found at the connection weldment between the tubesheet and outer shell. In this case, the use of a thin and flexible tubesheet translates the thermal stress concentration area to the corner of the tubesheet, away from the weldment part. The largest stress caused by the internal pressure is found at the vessel head with the largest diameter and smallest thickness.

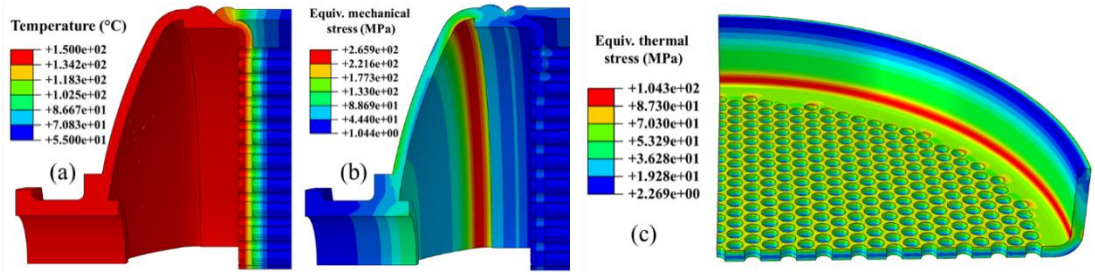

Figure 5.18: Contours during loading stage showing (a) the temperature distribution (b) the mechanical von Mises stress (c) thermal von Mises stress at the tubesheet

For this case, only the ratchet analysis has been conducted because of limited computation resources and the requirement of structural design. The shakedown and ratchet limit of the aero-engine heat exchanger undergoing constant mechanical load and cyclic thermal load is presented in Figure 5.19(a). The characteristic of a Bree-like diagram is observed, including a horizontal reverse plasticity limit and a ratchet limit approaching the Y-axis. Several regions can then be determined, which are separated by the shakedown and ratchet boundaries. Load points located within the shakedown envelope would experience elastic shakedown, which is considered safe for structural design. For load points located above the shakedown boundary but

within the ratchet boundary, the structure behaviour would be plastic shakedown where a closed hysteresis loop would form. In this case, the failure mechanism would be low cycle fatigue leading to crack initiation. For load points located outside the ratchet boundary, the structural behaviour becomes ratchetting leading to incremental collapse. The vertical green line in Figure 5.19(a) denotes the limit load. The structure would collapse instantaneously when the pressure reaches the limit load. Both axes of the diagram have been normalised for better clarification and comparison. The inner pressure is normalised by the limit load $P_0 = 2.939\,\mathrm{MPa}$ and the cyclic temperature is normalised by the reverse plasticity limit $\Delta T_0 = 229.2\,^{\circ}\mathrm{C}$.

As described in Section 5.2.2, a two-stage procedure is employed for ratchet limit evaluation. The procedure sequence is visually displayed in Figure 5.19(a) for a load point (0.657, 2.356) on the ratchet boundary. Stage I only considers the cyclic thermal load by using the DSCA module. The saturated loading and unloading stress state is shown in Figure 5.20(a-b) by the end of stage I. The highest stress is found in the tubesheet, which would yield local fatigue damage. The failure mechanism at stage II is also presented in Figure 5.20(c) with the form of the equivalent strain increment $\Delta\varepsilon_{eq}^{c}$. It can be observed that the critical failure location translates to the vessel head which is caused by dominant constant inner pressure at ratchetting state.

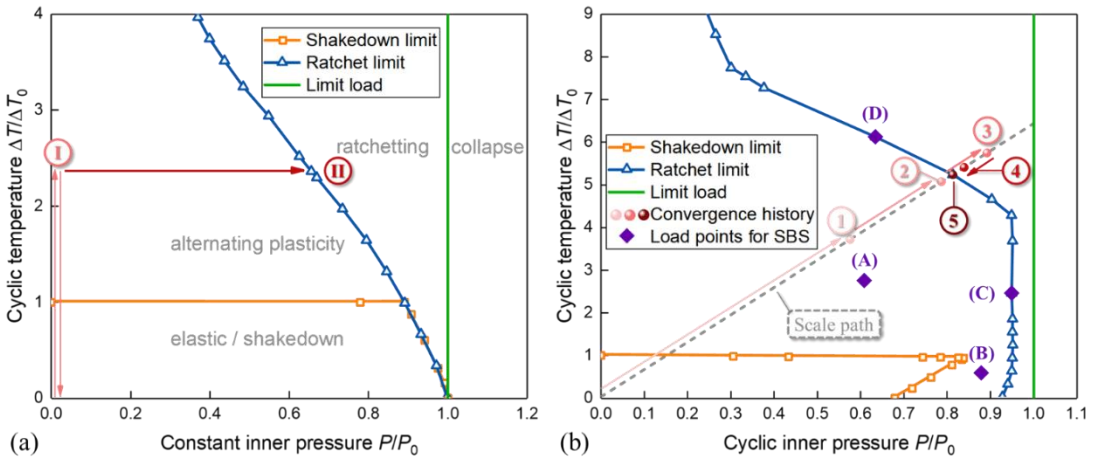

Figure 5.19: Shakedown and ratchet limit of the aero-engine heat exchanger subjected to (a) constant mechanical load and cyclic thermal load (b) cyclic mechanical load and cyclic thermal load

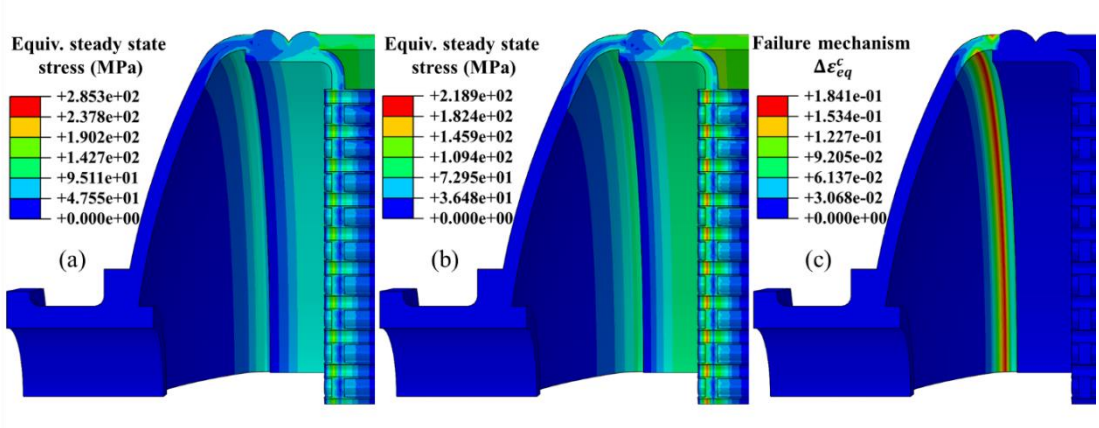

Figure 5.20: Contours obtained with the two-stage ratchet analysis of (a) von Mises steady-state stress for stage I during the loading process (b) von Mises steady-state stress for stage I during the unloading process (c) the failure mechanism for stage II

The modified Bree problem has also been considered here, which involves cyclic thermal load and cyclic inner pressure, as shown in Figure 5.19(b). Both axes have been normalised by P_0 and ΔT_0 from the Bree-like problem. It can be observed that the shakedown boundary intersects with X-axis at 0.679 instead of coinciding with the lower part of the ratchet boundary. The consideration of cyclic mechanical stress introduces the bending stress to the component in addition to the membrane stress caused by constant mechanical stress, which induces a shrink of the lower part of the shakedown boundary. With the increase of temperature, the shakedown envelope expands accordingly, forming a sharp angle at the transition point. It could be caused by the counteract effect between the thermal and mechanical loads in high-stress regions. Therefore, the maximum shakedown multiplier is achieved at load point (0.838, 0.940), where the thermal and mechanical loads are comparable.

For the ratchet boundary of the modified Bree problem, a target ratchet strain $\varepsilon_R = 0.02\%$ is set. The result ratchet limit lies between the limit load and the shakedown limit. It can be observed that the lower part of the ratchet limit follows an identical tendency to the shakedown limit. With the increase of temperature, the ratchet boundary becomes a vertical line before finally approaching the Y-axis. As introduced in Section 5.2.3, several different ratios of $\Delta T/P$ have been specified to obtain the data points on the ratchet boundary. A scale path has been chosen in Figure 5.19(b) for illustration, showing the convergence history of load points for each sub-cycle. The convergence history of the load multiplier λ has also been plotted and presented in Figure 5.21(a). At the first sub-cycle, the lower bound multiplier $\lambda_s = 0.151$ is selected on the shakedown boundary. At the second sub-cycle, the upper bound multiplier

$\lambda_L = 0.979$ is chosen from the limit load. A series of bisection scheme is then conducted repeatedly until the load multiplier converges at the fifth sub-cycle: $\lambda_5 = 0.798$.

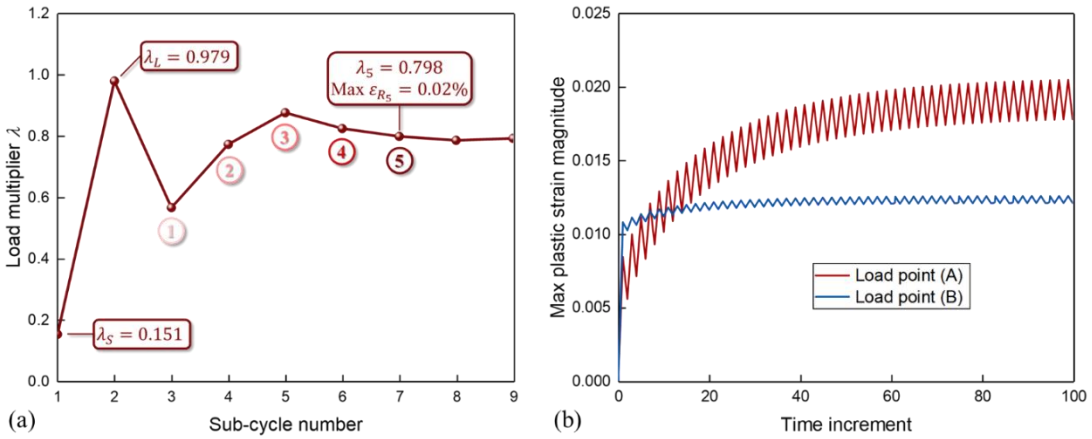

Figure 5.21: (a) Convergence history of the load multiplier λ for a specific scale path (b) evolution of the maximum plastic strain magnitude of the aero-engine heat exchanger obtained with SBS analysis

5.3.2.3 Verification of results

To validate the results, the inelastic SBS analysis has been performed in ABAQUS. To ensure the achievement of steady-state stress-strain behaviour, a total of 100 static steps have been created with the help of a Python script. All the material parameters and boundary conditions considered are the same as the settings in the LMM framework. It usually takes several increments for each step to converge, so SBS analysis is considered accurate but highly time-consuming. The SBS analysis has been widely adopted as an effective validation tool in several existing works [169, 170].

Four different load points have been selected in Figure 5.19(b) for SBS verification. Load points (A) and (B) are located in the reverse plasticity region. The evolution of PEMAG in the structure has been evaluated and plotted in Figure 5.21(b). For both load points, the PEMAG remains at a steady level after a few cycles, showing the characteristic of reverse plasticity behaviour. Therefore, the accuracy of the ratchet boundary produced by the UPFRA has been proved. To evaluate the plastic strain range $\Delta\varepsilon_p$ at the final cycle, the equivalent plastic strain (PEEQ) at the last step is subtracted by the PEEQ at the step before the last step. As shown in Figure 5.22, the $\Delta\varepsilon_p$ obtained with SBS and DSCA for both load points are compared. For load point

(A), the thermal stress dominates and the largest $\Delta\varepsilon_p$ appears at the tubesheet. For load point (B), the mechanical stress dominant and the largest $\Delta\varepsilon_p$ is found on the vessel head. It can be seen that the results obtained with SBS and DSCA are highly compatible, proving the accuracy of the proposed method.

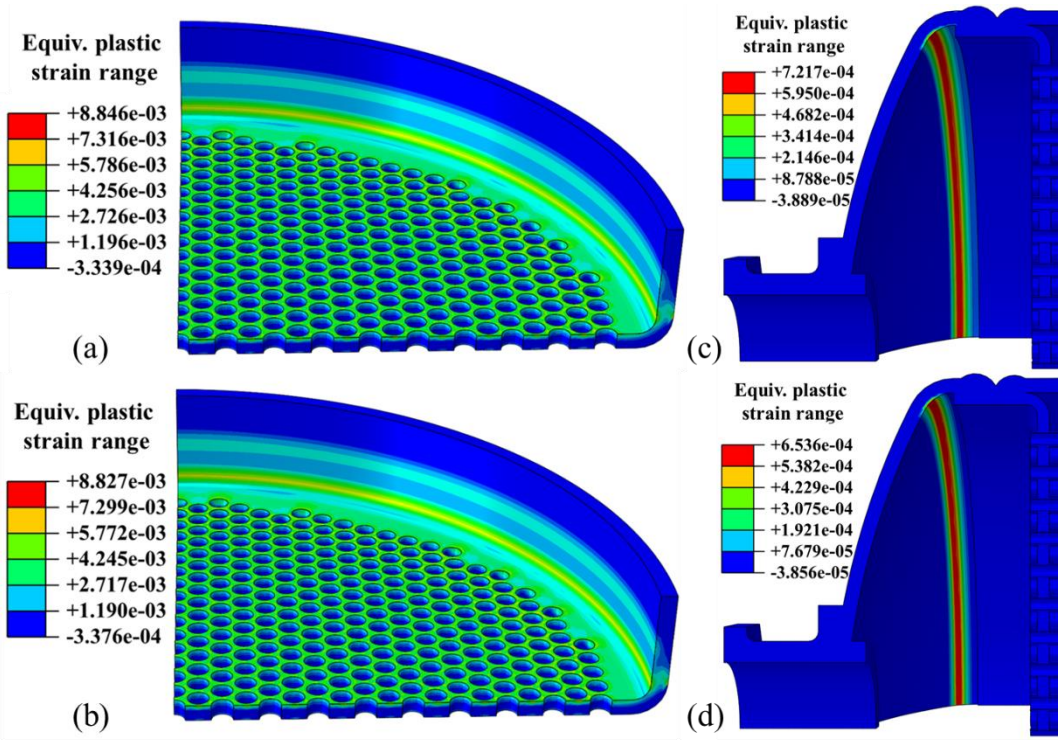

Figure 5.22: Contours of the equivalent plastic strain range $\Delta\varepsilon_p$ for (a) load point (A) obtained with DSCA (b) load point (A) obtained with SBS (c) load point (B) obtained with DSCA (d) load point (B) obtained with SBS

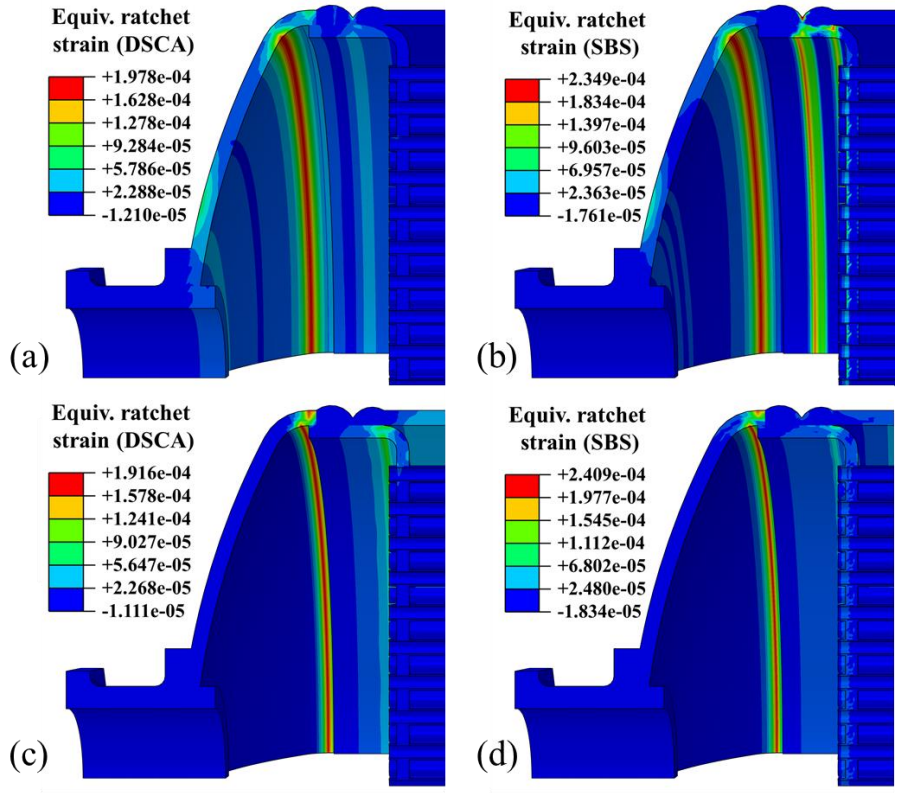

Figure 5.23: Contours of the equivalent ratchet strain ε_R for (a) load point (C) obtained with DSCA (b) load point (C) obtained with SBS (c) load point (D) obtained with DSCA (d) load point (D) obtained with SBS

On the ratchet boundary, load points (C) and (D) have been chosen from Figure 5.19(b) for SBS validation. The contours of equivalent ratchet strain ε_R from the SBS and DSCA are compared in Figure 5.23. The maximum ε_R is found to be around to be 0.02%, identical to the target settings in the UPFRA. It can be observed that the distribution of ε_R are comparable for both methods, but the SBS produces overall higher values of ε_R than the results from DSCA. The difference is mainly caused by the post-processing procedures used to obtain ε_R. For SBS, ε_R is evaluated by subtracting the PEEQ accumulated during the unloading stage by the PEEQ at the loading stage. For DSCA, the plastic strain component during the unloading and loading stages are subtracted first before calculating the equivalent value of ε_R. In this case, the ε_R from DSCA is proved to be more precise than the one from SBS.

The total CPU time required for each load point using the DSCA and SBS has been compared in Table 5.4. It can be found that for all the load points, the DSCA requires less time than SBS, with a speed advantage of up to 73.1%. The reason is that inelastic analysis in SBS usually takes several iterations for each increment to

converge, while the DSCA aims directly at the final cycle by solving a series of linear equations. Therefore, the DSCA has been proved to offer better efficiency without potential convergence issues.

Table 5.4: Comparisons of total CPU time using the DSCA and SBS

	Load point (A)	Load point (B)	Load point (C)	Load point (D)
CPU time (SBS) [sec]	45711	40672	62136	76529
CPU time (DSCA) [sec]	20426	20358	20404	20602
Speed improvement	55.3%	49.9%	67.2%	73.1%

5.4 Summary

In this chapter, the differences between material and structural ratchetting have been discussed. The constant life diagram has been extended from the material level to the structure level. For the evaluation of ratchet boundary and fatigue boundary for structures subjected to arbitrary cyclic thermal-mechanical load histories, a Unified Procedure for Fatigue and Ratchet Analysis (UPFRA) has been proposed as part of the LMM framework. The R-O model has also been introduced to consider the cyclic hardening effect. Two case studies have been conducted using the UPFRA to show the usability of the proposed method.

It has been discovered that material ratchetting is usually considered with a homogeneous stress field and no residual stress. In contrast, structural ratchetting is considered with an inhomogeneous stress field and sophisticated residual stress field. For Bree-like problems, an existing two-stage procedure has been introduced based on the DSCA subroutine and Koiter's shakedown algorithm, while for modified Bree problems, a three-stage procedure is proposed based on the LMM shakedown module and the UPFRA. A series of DSCA subroutine is called iteratively by the bisection scheme in the UPFRA, which is capable of computing the ratchet and fatigue boundaries for complex engineering structures considering temperature-dependent material properties. The validation of the proposed method is performed by comparing the results with the ones obtained with the SBS analysis. The stress-strain contours and saturated hysteresis loops from the UPFRA agree well with those from the SBS. Therefore, in the benchmark case of a holed plate, the support for R-O model is illustrated and the constant LCF life diagram is verified by the SBS analysis. In the

engineering case of a heat exchanger in aero-engine, complex FE model and material parameters are considered and the UPFRA is proved to be more efficient than the SBS analysis. In addition, the Bree-like diagram is further extended by including the constant LCF life curves.

6. The evaluation of the structural constant creep-fatigue life diagram

6.1 Introduction

During the process of structural integrity assessment for components subjected to cyclic loads in a high-temperature environment, one of the most critical problems is the prediction of the number of cycles to crack initiation. The creep effect also becomes significant due to the degeneration of material performance and stress relaxation during creep dwell. The inclusion of creep strain may cause the creep ratchetting mechanism where the open hysteresis loop is formed. Creep and fatigue could also interact with each other in various ways and induce phenomena such as “cyclically enhanced creep” and “creep enhanced plasticity”, as introduced in [47]. The accurate estimation of structural life would greatly benefit the optimization of operation routine and prevent system failure. In addition, the structural location with the largest potential creep-fatigue damage can also be discovered for reinforcement and periodic maintenance.

Among industries, two approaches are usually adopted for creep-fatigue design and assessment, including the rule-based and analysis-based methods. Rule-based approaches introduced in the R5 procedure [7] and ASME NH [5] are simple to apply but often considered over-conservative and inaccurate. Analysis-based approaches include inelastic cycle-by-cycle FE analysis and direct methods. The cycle-by-cycle analysis considers sophisticated constitutive models which can be highly precise but time-consuming. Direct methods utilise specific hypotheses to simplify the material models and aim at solving the stress-strain relationship at the steady-state cycles directly. Thus the time efficiency is greatly improved with potential convergence issues avoided. As part of the Linear Matching Method (LMM) framework, the extended Direct Steady Cycle Analysis (eDSCA) has been proposed by previous researchers for creep-fatigue assessment and applied to various types of engineering problems [171-175]. The eDSCA has also been widely validated with ABAQUS step-by-step analysis and proved to be an efficient, robust and easy-to-use engineering tool.

A number of numerical approaches to evaluate the creep damage have also been implemented in the existing eDSCA subroutine, including the Time Fraction rule (TF), Ductility Exhaustion method (DE), Stress Modified Ductility Exhaustion method (SMDE) [176] and Strain Energy Ductility Exhaustion method (SEDE) [175]. The fatigue damage can also be calculated with a fitted equation using the Modified Universal Slope Method (MUSM) [175] or the bilinear interpolation technique using the fatigue life curves [163]. Since the fatigue damage is determined by the total strain range, the creep strain accumulated during creep dwell could result in an increase of strain range and fatigue damage. The total damage is then calculated by combining the creep and fatigue damage using the Linear Damage Summation (LDS) method, the bilinear method introduced in ASME NH [5], and the combined damage rules [177]. For the simplicity and conservativeness of this work, the TF rule and the bilinear interpolation technique have been selected for creep and fatigue damage evaluation.

Considering the effect of creep at high temperatures, the concept of constant life diagrams is further extended to the structural level as constant creep-fatigue life curves. Different combinations of thermal-mechanical loads with identical total creep-fatigue life are plotted in a diagram, considering the effect of creep dwell time. It is challenging to solve engineering problems with creep-fatigue interaction using traditional inelastic step-by-step (SBS) analysis even for a single load combination, as the SBS method can be highly time-consuming and difficult to converge. Thanks to the development of direct methods, it becomes possible to efficiently plot the constant creep-fatigue life curves containing a large number of data points. To evaluate the constant fatigue life boundaries for engineering structures, the Unified Procedure for Fatigue and Ratchet Analysis (UPFRA) [163] has been introduced comprehensively in Section 5. In this work, a post-processing module for creep-fatigue damage evaluation has been implemented in eDSCA. The UPFRA algorithm is also extended and improved to call the eDSCA iteratively for the computation of creep-fatigue interaction and total damage. The constant creep-fatigue life curves are then combined with the shakedown and ratchet boundary to describe the structural behaviour for arbitrary loading combinations. The newly developed Python script contains the UPFRA and extended UPFRA, providing a one-stop solution for structural ratchetting, fatigue and creep-fatigue analyses.

In this study, the Bree-like diagram is extended by including the constant creep-fatigue life curves. The numerical methods for creep-fatigue analysis are extensively

introduced in Section 6.2, including the introduction of the current eDSCA in Section 6.2.1, the adopted creep and fatigue damage rules in Section 6.2.2, and the extended UPFRA in Section 6.2.3. Then two numerical examples are presented to show the advantages of the extended UPFRA for practical engineering problems in Section 6.3.

6.2 Numerical procedures for creep-fatigue analysis

6.2.1 The current eDSCA algorithm

Consider a body subjected to cyclic temperature $\theta(x,t)$ within the volume V and cyclic load $P(x,t)$ on the part of the surface S_T over the cycle $0 \le t \le \Delta t$. The displacement $u = 0$ on the rest of the surface S_u. The linear elastic stress history is calculated by:

$$\hat{\sigma}_{ij}(x,t) = \hat{\sigma}_{ij}^{\theta}(x,t) + \hat{\sigma}_{ij}^{P}(x,t) \tag{6.1}$$

where $\hat{\sigma}_{ij}^{\theta}(x,t)$ and $\hat{\sigma}_{ij}^{P}(x,t)$ are elastic solutions derived with $\theta(x,t)$ and $P(x,t)$, respectively. The stress state at steady-state is then given by:

$$\sigma_{ij}(x,t) = \hat{\sigma}_{ij}(x,t) + \bar{\rho}_{ij}(x) + \rho_{ij}^{r}(x,t) \tag{6.2}$$

where $\bar{\rho}_{ij}(x)$ is a constant residual stress field in which the surface traction is zero on S_T. $\rho_{ij}^{r}(x,t)$ denotes varying residual stress which meets the condition:

$$\rho_{ij}^{r}(x,0) = \rho_{ij}^{r}(x,\Delta t) \tag{6.3}$$

The similar minimization process adopted here has been described in Section 5.2.1. Considering a series of time instant t_n to replace integration computation, the minimization function is given by:

$$I^{n}\left(\Delta\varepsilon_{ij}^{n}\right) = \int_{V} \left\{\sigma_{ij}^{n}\Delta\varepsilon_{ij}^{n} - \left[\hat{\sigma}_{ij}(x,t_n) + \rho_{ij}^{r}(x,t_n)\right]\Delta\varepsilon_{ij}^{n}\right\} dV \tag{6.4}$$

A total number of load instance N and a total number of cycles M are considered before convergence. The accumulated residual stress $\rho_{ij}^{r}(x,t_n)$ is then given by:

$$\rho_{ij}^{r}(x,t_n)_m = \sum_{k=1}^{m-1}\sum_{n=1}^{N}\Delta\,\rho_{ij}^{r}(x,t_n)_k + \sum_{k=1}^{n}\Delta\rho_{ij}^{r}(x,t_k)_m \tag{6.5}$$

For load instances t_n with no creep dwell, the plastic strain amplitude is calculated by:

$$\Delta\varepsilon_{ij}^{p}(x,t_n)=\frac{1}{2\bar{\mu}(x,t_n)}\left\{\hat{\sigma}_{ij}(x,t_n)+\rho_{ij}^{r}(x,t_n)\right\}' \tag{6.6}$$

where $\bar{\mu}(x,t_n)$ denotes an iterative shear modulus.

For load instances t_n with creep dwell, the creep strain is calculated with a time hardening power law:

$$\dot{\bar{\varepsilon}}^{c}=A\bar{\sigma}^{n}t^{m} \tag{6.7}$$

where $\dot{\bar{\varepsilon}}^{c}$ denotes the effective creep strain rate, $\bar{\sigma}$ denotes the effective von-Mises stress, t denotes the dwell time, and A, n, and m are power-law parameters. Considering the non-isothermal effect, creep parameter A is temperature-dependent with the application of the Arrhenius law:

$$A=A^{*}\exp\left(-\frac{Q}{RT}\right) \tag{6.8}$$

where A^{*} denotes the frequency factor, Q denotes the activation energy, R is the global gas constant, and T denotes the local temperature. The effective creep strain increment during creep dwell is computed by:

$$\Delta\bar{\varepsilon}^{c}=\frac{A(n-1)\Delta t^{m+1}(\bar{\sigma}_s-\bar{\sigma}_c)}{(\bar{\sigma}_c^{1-n}-\bar{\sigma}_s^{1-n})(m+1)} \tag{6.9}$$

where $\bar{\sigma}_s$ denotes the effective stress at the start of creep dwell and $\bar{\sigma}_c$ denotes the effective stress at the end of creep dwell (creep flow stress). For pure creep conditions when $\bar{\sigma}_s=\bar{\sigma}_c$, the effective creep strain becomes:

$$\Delta\bar{\varepsilon}^{c}=\frac{A\bar{\sigma}_s^{n}\Delta t^{m+1}}{m+1} \tag{6.10}$$

The creep strain rate at the end of dwell is given by:

$$\dot{\bar{\varepsilon}}^{f}=\frac{\Delta\bar{\varepsilon}^{c}(m+1)\bar{\sigma}_c^{n}}{(n-1)(\bar{\sigma}_s-\bar{\sigma}_c)\Delta t}(\bar{\sigma}_c^{1-n}-\bar{\sigma}_s^{1-n}) \tag{6.11}$$

For pure creep condition, the creep strain rate becomes:

$$\dot{\bar{\varepsilon}}^{f}=A\bar{\sigma}_s^{n}\Delta t^{m} \tag{6.12}$$

During the iteration procedure, the estimated values of $\bar{\sigma}_c^{i}$ and $\bar{\sigma}_s^{i}$ are used to compute the final creep flow stress as the new creep flow stress $\bar{\sigma}_c=\bar{\sigma}_c^{f}$:

$$\bar{\sigma}_c = \left(\frac{\dot{\bar{\varepsilon}}^f}{A\Delta t^m}\right)^{\frac{1}{n}} \tag{6.13}$$

The iterative shear modulus $\bar{\mu}_m(x, t_n)$ is updated for every integration point at the end of each cycle m using the linear matching equation:

$$\bar{\mu}_{m+1}(x, t_n) = \frac{\bar{\mu}_m(x,t_n)\sigma_y^R(x,t_n)_m}{\bar{\sigma}\left(\hat{\sigma}_{ij}(x,t_n)+\rho_{ij}^r(x,t_n)_m\right)} \tag{6.14}$$

where $\sigma_y^R(x, t_n)_m$ denotes revised yield stress. For load instances without creep dwell, the revised yield stress equal to the yield stress of the material $\sigma_y^R = \sigma_y$; for load instances with creep dwell, the revised yield stress is replaced by the creep flow stress $\sigma_y^R = \bar{\sigma}_c$. The convergence check is performed at the end of each cycle. The whole process is repeated until the convergence criterion is satisfied. The detailed introduction of the eDSCA procedure can be further found in [19].

6.2.2 The evaluation of creep-fatigue damage

Based on the results from the eDSCA subroutine, a series of post-processing subroutines have been developed and implemented in the LMM plug-in to evaluate the creep-fatigue damage. The elastic follow up factor Z is given by:

$$Z = \frac{\bar{E}\Delta\bar{\varepsilon}^c}{\bar{\sigma}_s - \bar{\sigma}_c} \tag{6.15}$$

where the effective elastic modulus $\bar{E} = \frac{3E}{2(1+\nu)}$.

Assuming a constant elastic follow up factor during the creep dwell, the stress during the creep can be calculated using the power-law equation:

$$\bar{\sigma}(t, Z, \bar{\sigma}_s) = \left[\bar{\sigma}_s^{1-n} - \frac{\bar{E}A(1-n)t^{m+1}}{Z(m+1)}\right]^{\frac{1}{1-n}} \tag{6.16}$$

The effective creep strain at steady-state is therefore given by:

$$\bar{\varepsilon}^c = \frac{[\bar{\sigma}_s - \bar{\sigma}(t,Z,\bar{\sigma}_s)]Z}{\bar{E}} \tag{6.17}$$

The average creep stress $\bar{\sigma}_{ac}$ can then be evaluated by integrating (6.16) over total dwell time Δt:

$$\bar{\sigma}_{ac} = \frac{1}{\Delta t}\int_0^{\Delta t} \bar{\sigma}(t, Z, \bar{\sigma}_s)dt \tag{6.18}$$

The integration is not directly applicable in the FORTRAN subroutine, so the dwell time Δt is split into a number of small segments and substituted into (6.16) before summation. For the evaluation of creep damage, the Time Fraction rule has been implemented as part of the subroutine. The time to creep rupture $t^*(\bar{\sigma}_{ac}, T)$ is firstly determined by local temperature and average creep stress based on the rupture curves from creep experiments. The creep damage accumulated per cycle ω_C is then given by:

$$\omega_C = \frac{\Delta t}{t^*(\bar{\sigma}_{ac}, T)} \tag{6.19}$$

The total strain range $\Delta\bar{\varepsilon}$ can also be calculated considering the influence of creep strain:

$$\Delta\bar{\varepsilon} = \max\left(\bar{\varepsilon}(t_a) - \bar{\varepsilon}(t_b)\right), \quad \forall a \in [1, N], \ \forall b \in [1, N] \tag{6.20}$$

The number of cycles to failure $N^*(\Delta\bar{\varepsilon}, T)$ is then determined by the total strain range and local temperature based on the fatigue curves. The fatigue damage accumulated per cycle ω_F is given by:

$$\omega_F = \frac{1}{N^*(\Delta\bar{\varepsilon}, T)} \tag{6.21}$$

Considering a bilinear creep-fatigue interaction envelope, the intersection coordinate of two lines is (c, f) where c, f are material parameters and $0 < c < 0.5, 0 < f < 0.5$. The total number of cycles to failure N_{tot} is finally given by:

$$N_{tot} = \begin{cases} \left(\omega_F + \frac{\omega_C(1-f)}{c}\right)^{-1}, & \omega_C < \omega_F \\ \left(\omega_C + \frac{\omega_F(1-c)}{f}\right)^{-1}, & \omega_C \geq \omega_F \end{cases} \tag{6.22}$$

6.2.3 The extended UPFRA

One of the UPFRA modules for fatigue analysis described in Section 5.2.3 has been adopted and extended here for the evaluation of constant creep-fatigue life diagrams. Due to the limitation of direct methods, the creep effect on the shakedown and ratchet

boundaries is not considered in the LMM. A three-stage procedure is then proposed for faster computation:

- Stage 1: the shakedown limit is evaluated for load ratio R using the LMM shakedown module for load cycle without creep.
- Stage 2: the limit load is evaluated using a special case in the LMM shakedown module.
- Stage 3: the constant creep-fatigue life load multiplier is evaluated using the extended UPFRA.

A simplified flowchart of the extended UPFRA is shown in Figure 6.1. The eDSCA module in the LMM plug-in has been further modified for the implementation of damage models introduced in Section 6.2.2. The modified eDSCA is iteratively called under the control of the extended UPFRA using Python script. As input parameters, the load ratio *R*, convergence parameter *CONV*, the target number of cycles to creep-fatigue failure N_T, lower bound multiplier λ_1^{LB} and upper bound multiplier λ_1^{UB} at first iteration are firstly determined by the user, where λ_1^{LB} and λ_1^{UB} can be defined as the shakedown multiplier from Stage 1 and the limit load multiplier from Stage 2, respectively. The Abaqus model is pre-processed by the LMM plug-in to create UMAT parameters and steps for LMM analysis. The LMM data file configures the load multipliers which is modified by the extended UPFRA at the start of every iteration and transferred to eDSCA. Controlled by a bisection scheme, the load multipliers are scaled proportionally so that the total creep-fatigue life would converge to N_T. At the first iteration, the load multiplier $\lambda_1 = (\lambda_1^{LB} + \lambda_1^{UB})/2$. At the ith iteration, the load multiplier λ_i is computed by:

$$\lambda_i^{LB} = \begin{cases} \lambda_{i-2}, & N_{i-2} > N_T \\ \lambda_{i-1}^{LB}, & N_{i-2} \leq N_T \end{cases} \tag{6.23}$$

$$\lambda_i^{UB} = \begin{cases} \lambda_{i-1}^{UB}, & N_{i-2} > N_T \\ \lambda_{i-2}, & N_{i-2} \leq N_T \end{cases} \tag{6.24}$$

$$\lambda_i = \begin{cases} \frac{\lambda_{i-1}+\lambda_i^{UB}}{2}, & N_{i-1} > N_T \\ \frac{\lambda_{i-1}+\lambda_i^{LB}}{2}, & N_{i-1} \leq N_T \end{cases} \tag{6.25}$$

where λ_i^{LB} and λ_i^{UB} denote the lower and upper bound load multiplier at the ith iteration. After computing the stress-strain behaviour considering the creep-fatigue

interaction effect at steady-state by the eDSCA subroutine, a series of post-processing procedures are taken to calculate the creep-fatigue damage. The creep and fatigue damage is first evaluated separately based on the TF rule and total strain range, respectively. Then the total damage is evaluated based on the bilinear creep-fatigue interaction lotus. After that, the minimum number of cycles to failure N_i in the structure is read from the Abaqus output database file to compare with the target life N_T. If not converged, the load multiplier λ_i is adjusted by equations (6.23)-(6.25) before submitting the eDSCA job again with the updated loads applied. When the divergence between N_i and N_T meets the convergence criterion, the iteration stops, and a result CSV file is created as the output. The extended UPFRA also support the input of multiple load ratio R to generate a full constant life curve consisting of several data points efficiently. The unified procedures containing the UPFRA and extended UPFRA Python codes for ratchet, fatigue and creep-fatigue analyses have been combined together for better usability, as presented in Appendix B.

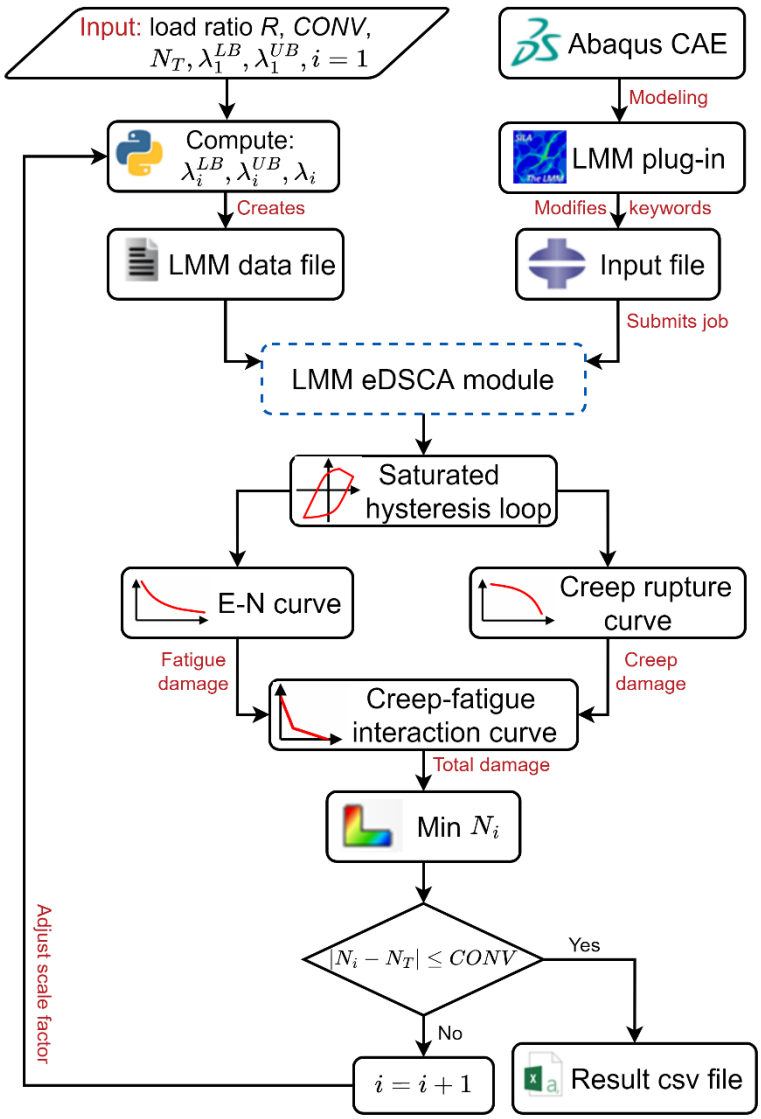

Figure 6.1: Simplified flowchart of the numerical procedure for the evaluation of constant creep-fatigue life diagram

6.3 Numerical examples

6.3.1 A holed plate

6.3.1.1 FE model and material parameters

The geometry of a holed plate has been shown in Figure 6.2(a), which is identical to the one given in Section 5.3.1. The dimensionless geometry with $D/L = 0.2$ and $d/L = 0.05$ has also been used in [24]. An axial pressure σ_P is applied at the edge surface and a temperature gradient $\Delta T = T - T_0$ is caused by the temperature difference between inner and outer surfaces. A steady-state thermal analysis is firstly

performed on a quarter FE model, as shown in Figure 6.2(b). It is worth mentioning that the temperature field adopted here has a higher base temperature and a lower temperature difference compared to the one in Section 5.3.1. It is intended to produce a much higher scaled temperature at the inner surface, and the creep effect becomes much more significant.

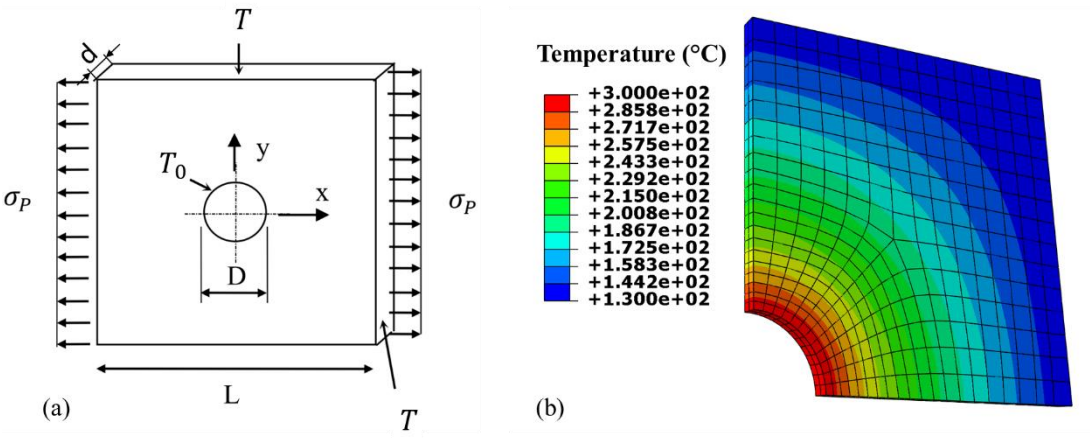

Figure 6.2: (a) The geometry of a holed plate [24] (b) The temperature distribution and FE mesh

The material used for the holed plate is X2CrNiMo17-12-2 steel, which is also identical to the material in Section 5.3.1. Only the EPP model is considered here due to the complexity of creep-fatigue problems. The temperature-dependent yield stress is taken as 0.2% proof stress from the cyclic steady-state stress-strain curves, as given in Table 6.1. Linear interpolation and extrapolation techniques are also adopted to evaluate the yield stress at an arbitrary temperature in local regions.

For creep behaviour, a Norton law has been adopted to describe the secondary creep regime. The Arrhenius law is also used to consider the non-isothermal effect, as given in Equations (6.7) and (6.8). The corresponding creep parameters are taken from [175], as listed in Table 6.2.

Table 6.1: Temperature-dependent yield strength of X2CrNiMo17-12-2 steel

Temperature, T [ºC]	20	100	200	300	400
$R_{p0.2}(T)$ [MPa]	258	252	248	240	240

Table 6.2: Creep parameters for the Norton law

A^*	Q [J/mol]	R [J/(mol•K)]	n
46333.8	330000	8.314	6.1

For fatigue damage, the total strain range is first evaluated with Equation (6.20) and then substituted into the fatigue damage curves from [6], as given in Figure 6.3(a). A bilinear interpolation technique has been developed to compute the number of cycles to fatigue failure in a local region with arbitrary temperature. After that, the fatigue damage accumulated per cycle ω_F can be calculated using Equation (6.21).

For creep damage, although the TF rule is often considered less accurate compared to other damage models such as DE and SMDE, we still use the TF rule here due to its simplicity and usability. Other damage models have also been implemented in the LMM subroutine and can be adopted for creep-fatigue assessment if required. In the TF model, the average creep stress $\bar{\sigma}_{ac}$ during the creep dwell stage is firstly calculated with Equation (6.18). Then the time to creep rupture $t^*(\bar{\sigma}_{ac}, T)$ is evaluated using the creep rupture curves from [49], as shown in Figure 6.3(b). A master equation has also been fitted to describe the rupture curves considering various temperatures and rupture times:

$$\ln(t^*) = -672.826 + 185.925\lg(T) - \frac{8250.515\lg(\bar{\sigma}_{ac})}{T} + \frac{139204.547}{T} - \frac{19.972\bar{\sigma}_{ac}}{T} \quad (6.26)$$

where T is the absolute temperature and t^* is the rupture failure time in hours. Considering the creep dwell time in the load cycle, the creep damage accumulated per cycle ω_C can be finally calculated with Equation (6.19).

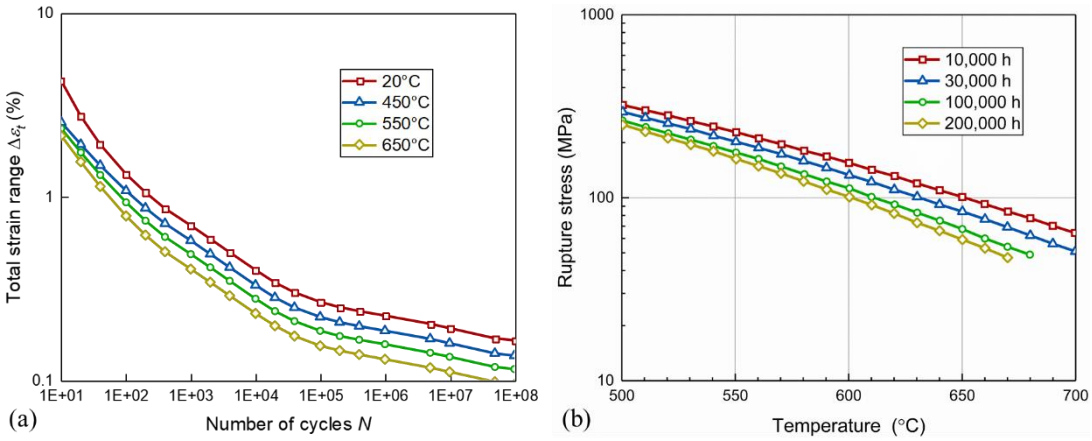

Figure 6.3: (a) Fatigue curves at various temperatures [6] (b) Creep rupture stress at various temperatures and rupture times [49]

After the separate computation of creep and fatigue damage, the total damage is evaluated using a bilinear creep-fatigue interaction diagram from [5], as shown in Figure 6.4. The X-axis is defined as the fatigue damage, and the Y-axis is defined as

the creep damage. An intersection point can be observed between two lines with the coordinate of (c, f). The value of c and f are dependent on the choose of material and the intensity of creep-fatigue interaction. For X2CrNiMo17-12-2 steel, $c = 0.3$ and $f = 0.3$. The total life N_{tot} can then be evaluated with Equation (6.22) for the further computation of constant creep-fatigue life diagram.

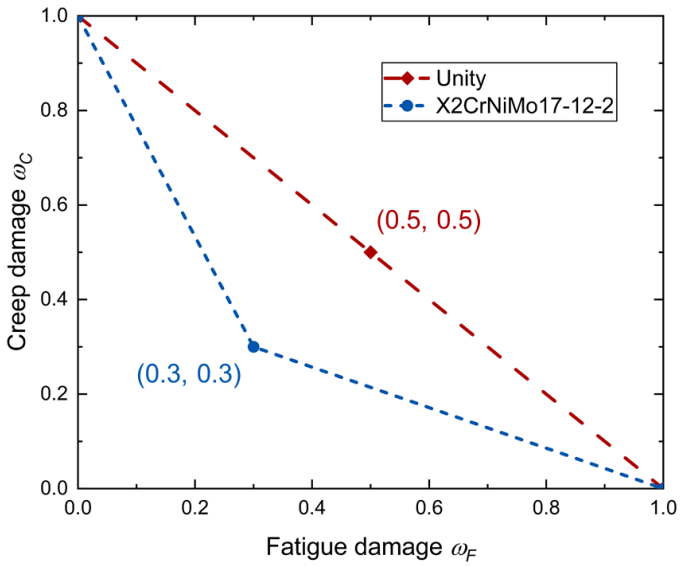

Figure 6.4: Creep-fatigue damage envelope for X2CrNiMo17-12-2 steel [5]

Two different simplified load cases are presented in Figure 6.5. Load case (A) represents a constant axial pressure and cyclic temperature field, while for load case (B), both thermal and mechanical loads are cyclic. Unlike previous examples, the influence of time and creep effect has been considered here. The start-up and cool-down stages are still considered instant, but the creep dwell time Δt has been included between both stages. During the creep dwell stage, both thermal and mechanical loads remain constant. The shakedown analysis is firstly conducted to determine the limit load P_0 and reverse plasticity limit ΔT_0 for normalization. Using the shakedown module in the LMM framework, it has been calculated that $P_0 = 225.5\ \mathrm{MPa}$ and $\Delta T_0 = 204\ °\mathrm{C}$. Meanwhile, at the reverse plasticity state when pressure is zero, the inner temperature is 360 °C, and the outer temperature is 156 °C.

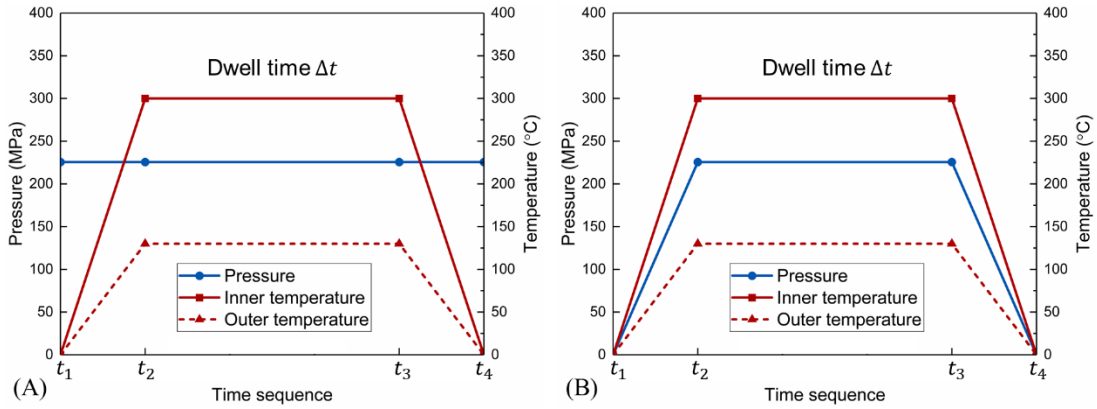

Figure 6.5: Simplified load cases with (A) constant pressure and cyclic temperature (B) cyclic pressure and cyclic temperature

6.3.1.2 Results and discussions

For load case (A), the shakedown limit, ratchet limit and constant creep-fatigue life curves have been calculated and shown in Figure 6.6(a). The axial pressure P and the temperature difference ΔT have been normalised by P_0 and ΔT_0, respectively. The shakedown and ratchet limits are evaluated using the original LMM plug-in, and the constant life curves are evaluated using the extended UPFRA. The creep dwell time is fixed at $t = 100\,\mathrm{h}$. Three different target numbers of cycles ($N = 10, 40, 100$) are considered for the constant life curves located within the reverse plasticity region. Since the mechanical load is constant for this case, the reverse plasticity limit is horizontal as part of the shakedown boundary. The constant life curve $N = 100$ is also mainly horizontal because for lower temperatures, the value of creep damage is minimal considering the magnitude of fatigue damage. However, a slight ascension can be observed when the curve approaches the Y-axis, indicating a change of mechanism. Compared with load points with larger constant pressure, the creep strain for load points near the Y-axis is smaller due to the decrease of mechanical load. The fatigue damage is thus more minor and comparable to the creep damage. The lower the target number of cycles to failure, the further the constant life curve moves away from the reverse plasticity limit. A large curvature can be found in the curve $N = 10$ while the temperature is very high. The creep and fatigue damage are highly comparable and interact with each other. The lower the magnitude of constant pressure, the lower the fatigue damage, allowing for higher creep damage to reach specified total damage. The constant creep-fatigue life curve thus gradually approaches the Y-axis with increasing temperature. It should be noted that the temperature is capped at 650 °C when computing fatigue damage using fatigue

curves from Figure 6.3(a). The example is primarily an illustration of the numerical method, so the constant life curves may not climb up indefinitely for other engineering cases. Four different load points have been selected and highlighted in Figure 6.6(a) for further investigation.

For load case (B), the shakedown limit, ratchet limit and constant creep-fatigue life curves have been computed and shown in Figure 6.6(b). The shakedown limit is evaluated using the original LMM plug-in; the ratchet limit is evaluated using the UPFRA, while the constant life curves are evaluated using the extended UPFRA. The computation process of the shakedown and ratchet limit has been extensively discussed in Section 5.3.1. For a larger number of cycles to failure, the constant creep-fatigue life curves are nearly parallel to the reverse plasticity limit due to the lower temperature. For a lower number of cycles to failure, the constant life curves consist of two parts. For the part with higher cyclic pressure, the curves mostly follow the same slope as the reverse plasticity limit due to the dominance of fatigue damage; for the part with lower cyclic pressure, the curves become steeper and gradually approach the Y-axis due to the creep-fatigue interaction.

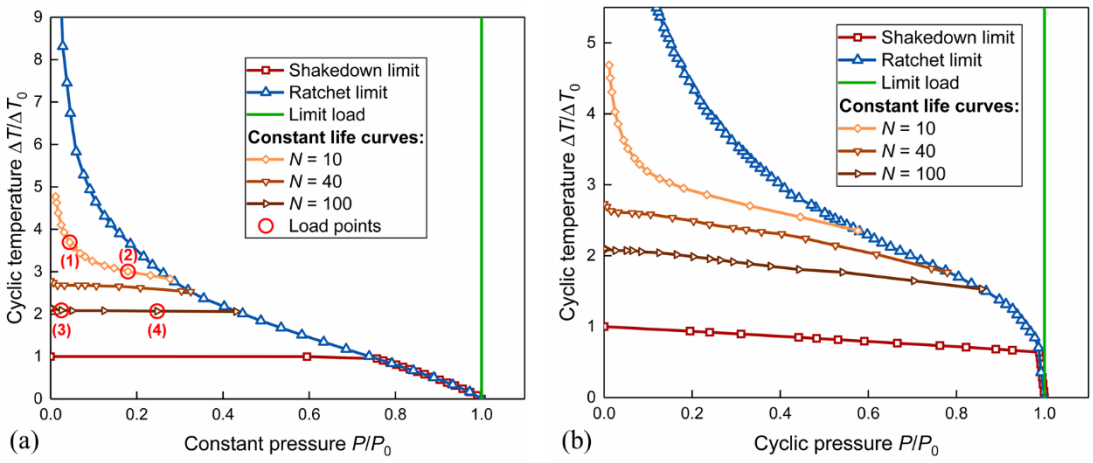

Figure 6.6: The shakedown, ratchet and fatigue limit of the holed plate subjected to (a) load case (A) (b) load case (B)

For a better understanding of the effect of dwell time, the load case (A) with cyclic thermal load and constant mechanical load has been chosen for a series of parametric studies. The constant creep-fatigue life diagram considering various creep dwell times ($t = 10\ \mathrm{h}, 100\ \mathrm{h}, 1000\ \mathrm{h}$) with fixed target life $N = 10$ has been presented in Figure 6.7(a). Other target numbers of cycles to failure are not considered because of the dominance of fatigue damage in those cases. It can be observed that the curvature

of the curves follows a similar trend for various dwell times because of the same creep-fatigue failure mechanism. The longer the dwell time, the larger the creep strain and creep damage, resulting in a shrink of the constant life curve. Load cycles without creep dwell have also been considered and compared with load cycles with dwell time $t = 100\ \mathrm{h}$, as shown in Figure 6.7(b). Although the constant life curves for $N = 40$ and $N = 100$ are dominant by fatigue damage, they are still different from the constant fatigue life curves without creep dwell. The reason is that the creep strain would increase the total strain range, which induces larger fatigue damage. Hence for the same number of cycles to failure, the constant creep-fatigue life curves are much closer to the reverse plasticity limit than the constant fatigue life curves without creep dwell. It can also be observed that the constant creep-fatigue life curve for $N = 40$ is not completely horizontal compared to the constant fatigue life curve. When the constant pressure increases, the primary stress also increases in the structure, which is not affected by stress relaxation during creep dwell. In this case, the average stress would also increase which induces larger creep damage and a shrink of the constant creep-fatigue life curve. Therefore, the inclusion of creep dwell in the load cycle has a significant influence on the shape and size of the constant life diagram.

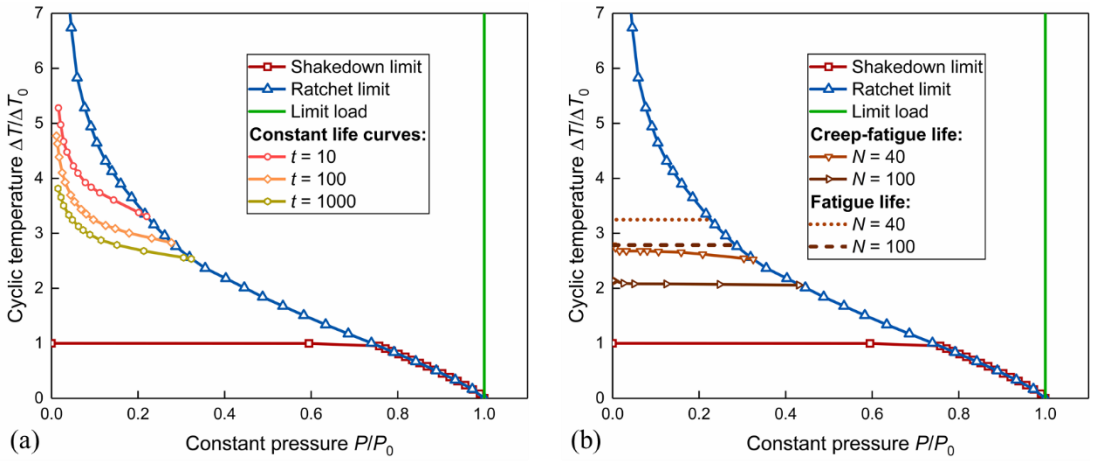

Figure 6.7: The constant life diagram of the holed plate subjected to load case (A) considering (a) various dwell times (b) no dwell time

To plot the hysteresis loop, the contours of equivalent steady-state stress at the end of each load stage for load points (1) and (4) have been presented in Figure 6.8. Load point (1) represents higher thermal load and lower mechanical load. Thus the stress fields at the loading and unloading stages are nearly symmetric along the diagonal. A more considerable amount of stress relaxation is also noticed at the end of creep dwell due to the high composition of secondary stress. Load point (4) is composed of

lower thermal load and higher mechanical load. So the stress fields at the loading and unloading stages are not symmetric due to the additional axial pressure. Due to the higher composition of primary stress, the amount of stress relaxation at the end of creep dwell is smaller. During the creep dwell, the elastic strain turns into creep strain which causes a significant stress reduction in the high-stress region near the hole. A stress redistribution is also observed at the end of the creep dwell. The high-stress area grows at the corners of the holed plate whereas the low-stress region expands near the hole.

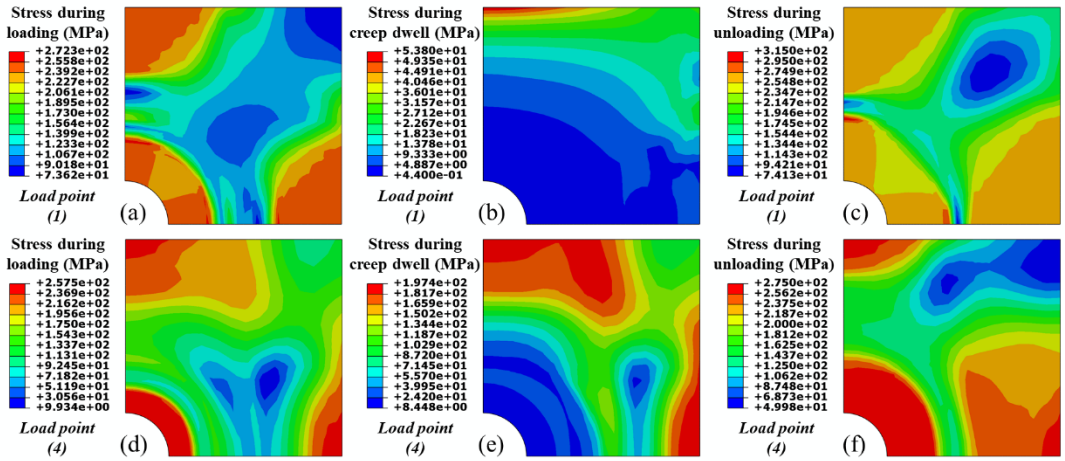

Figure 6.8: The equivalent steady-state stress at the end of each load stage for load points (1) and (4)

The contours of total strain range, creep strain, and creep/fatigue dominance for different load points have been shown in Figure 6.9. The total strain range is used for fatigue damage evaluation, and the creep strain is used for the plotting of hysteresis loops. Since creep strain is considered part of the total strain range, the larger creep strain in load point (2) leads to a more extensive total strain range compared to load point (1), as shown in Figure 6.9(a)(b). Although the temperature is lower for load point (2), the overall stress level is higher due to the additional constant pressure than load case (1). According to Equation (6.9), the higher initial stress value would induce a larger creep strain, as shown in Figure 6.9(d)(e). For load points (4), the distribution of the total strain range and the creep strain shows a different pattern due to the different composition of thermal and mechanical stress, as shown in Figure 6.9(c)(f). The overall magnitude of strain for load point (4) is lower than the one for load points (1) and (2) because of the different target numbers of cycles to creep-fatigue failure. The creep damage ω_C and fatigue damage ω_F for each load point has been evaluated and compared. According to Equation (6.22), for $\omega_C \geq \omega_F$ in local area of

the holed plate, it is considered to be dominated by creep; for $\omega_C < \omega_F$, it is determined as fatigue-dominant. For load points (1) and (2), the high-stress region near the hole experience significant stress relaxation during creep dwell, which induces lower average stress based on Equation (6.18). In this case, the creep damage near the hole also decreases and is overwhelmed by the fatigue damage. As shown in Figure 6.9(g)(h), the creep damage dominates at the centre area of the holed plate and the area of creep-dominance is larger for load point (1) due to the higher local temperature compared to load point (2). As shown in Figure 6.9(i), the fatigue damage is dominant across the whole body because of the relatively lower temperature for load point (4). Based on the creep rupture curve in Figure 6.3(b), the creep damage is thus much lower and unable to compete with the fatigue damage.

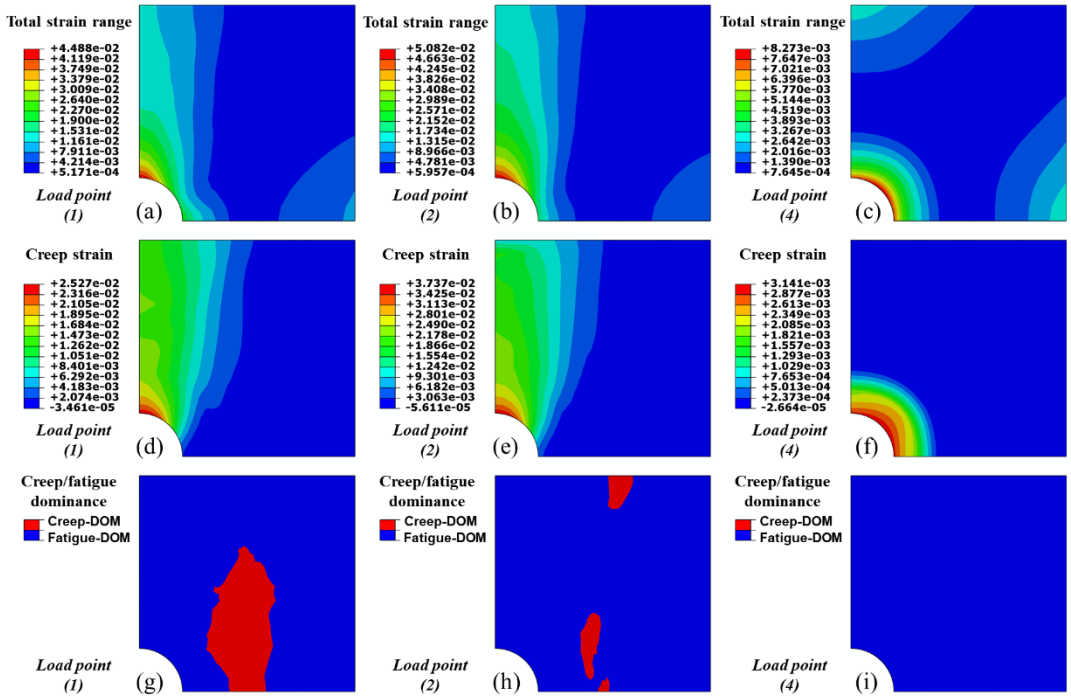

Figure 6.9: Comparison of contours of total strain range, creep strain and creep/fatigue dominance between different load points

Based on the results from the eDSCA, a series of post-processing user subroutines have been developed to evaluate the creep-fatigue damage. The creep, fatigue and total damage contours for various load points have been given in Figure 6.10. The critical location with the largest total damage has been chosen for stress-strain behaviour investigation. The saturated hysteresis loops at the same critical location for different load points are also plotted and compared in Figure 6.11. The most considerable creep damage for all load points can be found around the corner of the

hole because of the high local temperature. The creep damage not only depends on the local temperature but also depends on the average stress during the creep dwell. The largest fatigue damage is also located around the hole near the left edge of the body. As shown in Figure 6.11(a), load point (2) induces a larger creep strain and a larger total strain range compared to load point (1) due to the introduction of an additional mechanical load. More stress relaxation can also be observed for load point (1), which causes larger residual stress and thus more reverse plasticity during the unloading stage. The creep ratchetting behaviour in the open steady-state hysteresis loop is driven by the “cyclically enhanced creep” mechanism. The creep strain is enhanced by the cyclic stress at the start of dwell, and the accumulation of creep strain induces the ratcheting response simultaneously. As shown in Figure 6.10(a)(b)(d)(e), compared to load point (2), the affected area of great creep damage is larger, but the large fatigue damage region is smaller for load point (1). As shown in Figure 6.10(g)(h), with creep and fatigue damage combined, balanced total damage contours are created for both load points, and the lowest creep-fatigue life in the structure is also identical on a constant life curve of $N = 10$.

For load point (4), a different distribution of creep and fatigue damage is found around the hole due to the different load compositions. As shown in Figure 6.11(b), significant stress relaxation is also observed because both load cases are selected in the reverse plasticity region controlled by dominant secondary stress and peak stress caused by stress concentration at the corner of the edge. Significant stress relaxation enhances reverse plasticity at the unloading stage so that a closed saturated hysteresis loop appears, which is driven by the mechanism of “creep enhanced plasticity”. The creep and fatigue damage contours for load point (3) are not shown here because they are similar to load point (4). As shown in Figure 6.10(c)(f)(i), the magnitude of creep damage is much less than the fatigue damage due to the relatively low temperature. Hence the total damage is mainly determined by the fatigue damage, and the lowest creep-fatigue life in the structure is found to be $N = 100$. Therefore, with the presentation of damage contours for several load points, the accuracy and reliability of the proposed constant life diagrams have been validated.

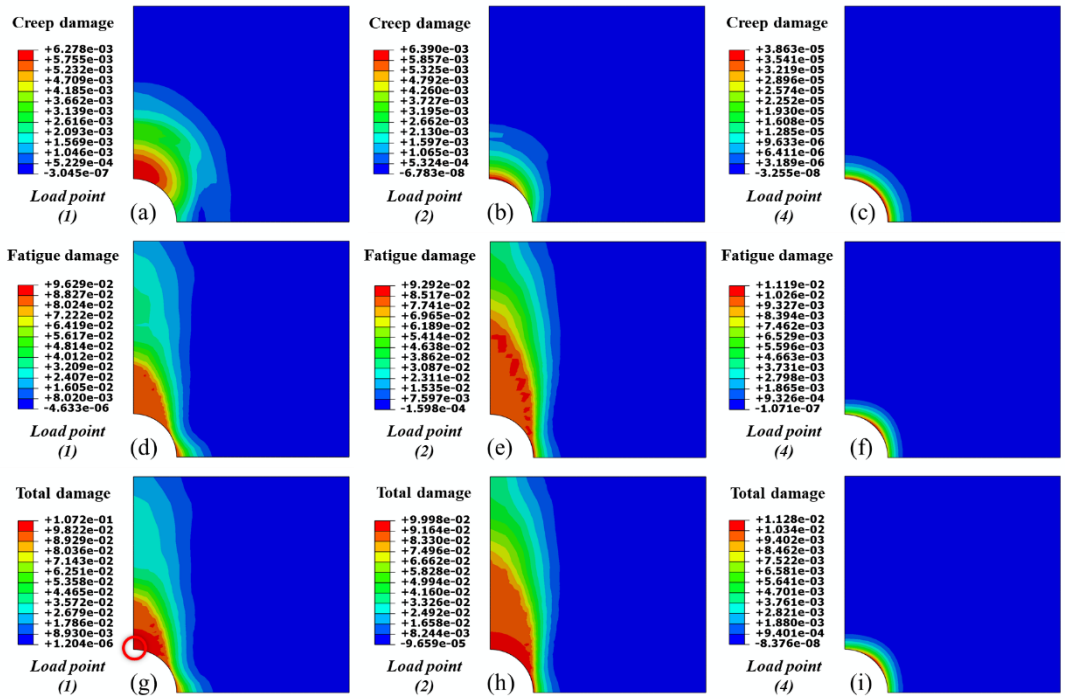

Figure 6.10: Comparison of damage contours between different load points

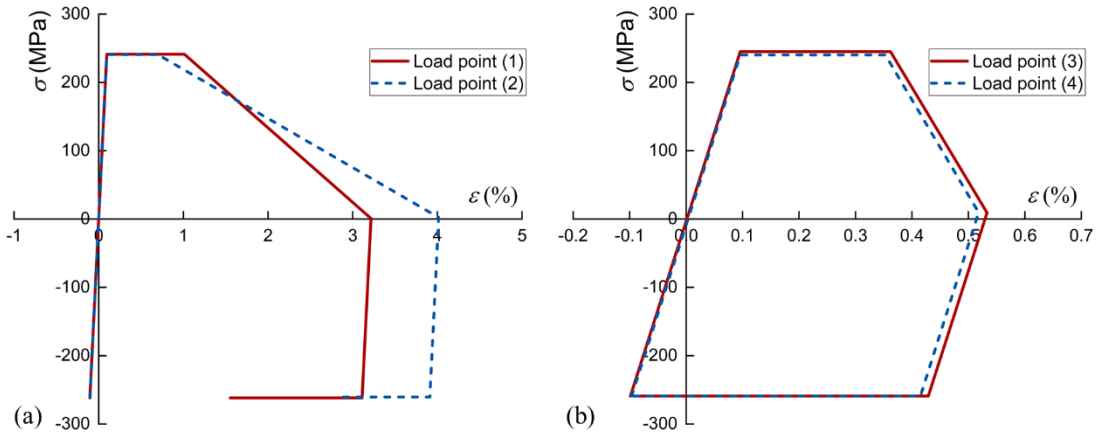

Figure 6.11: Saturated hysteresis loops at the critical location for different load points

6.3.2 A hydrogenation reactor

6.3.2.1 FE model and material parameters

In the field of petrochemical engineering, hydrogenation reactors are used in various industrial processes including hydrocracking and hydrodesulphurization. Being one of the most critical pressure vessels, they require complete creep-fatigue assessment due to the extreme operating environment with hydrogen, high temperature and large pressure involved. The damage caused by creep-fatigue interaction has been

confirmed to have a major impact on the design life of hydro-processing equipment [178]. For the design and assessment of hydrogenation reactors operating at temperatures between 371 °C and 500 °C, Code Case 2605 [179] of ASME BPV VIII-2 has provided a series of simplified procedures including shakedown analysis, creep damage evaluation and creep-fatigue damage interaction. However, for complicated industrial cases where the simplified procedures are not applicable, it is suggested to perform cycle-by-cycle inelastic analysis which is often considered computational consuming. Therefore, based on a series of direct methods, the extended UPFRA has been utilised for the complete creep-fatigue assessment of a typical hydrogenation reactor shell.

A hydrogenation reactor has been modelled in Abaqus, as shown in Figure 6.12(a). With relatively large strength at elevated temperatures and good resistance to creep and hydrogen corrosion, 2.25Cro1Mo steel has been adopted for the manufacture of hydrogenation reactors. The FE model is composed of several components, including the inlet nozzle, the reactor head, the cylindrical shell and the flange. The thickness of the reactor varies from 38 mm to 48 mm. To further simplify the model, the flange bores on the flange are neglected and an axisymmetric 2D model is created. The axial displacement is restricted at the bottom, the inner pressure is applied on the internal surface, and the corresponding pressure is applied at the top end to simulate the closed-end boundary condition. A steady-state thermal analysis has been performed to generate the temperature field for normal operating conditions, as shown in Figure 6.12(b). Since the solid catalyst used during the hydrogenation process has a limited lifetime, it must be replaced periodically to remain active. During the replacement procedure of the catalyst, the inner pressure is released while the inner temperature drops due to the absence of the catalyst. The temperature field during the unloading stage is shown in Figure 6.12(c). The model is then meshed into 755 quadratic DCAX8 elements, as shown in Figure 6.12(b)(c). A denser mesh is configured at the transition area between the nozzle and head due to the presence of geometric discontinuities.

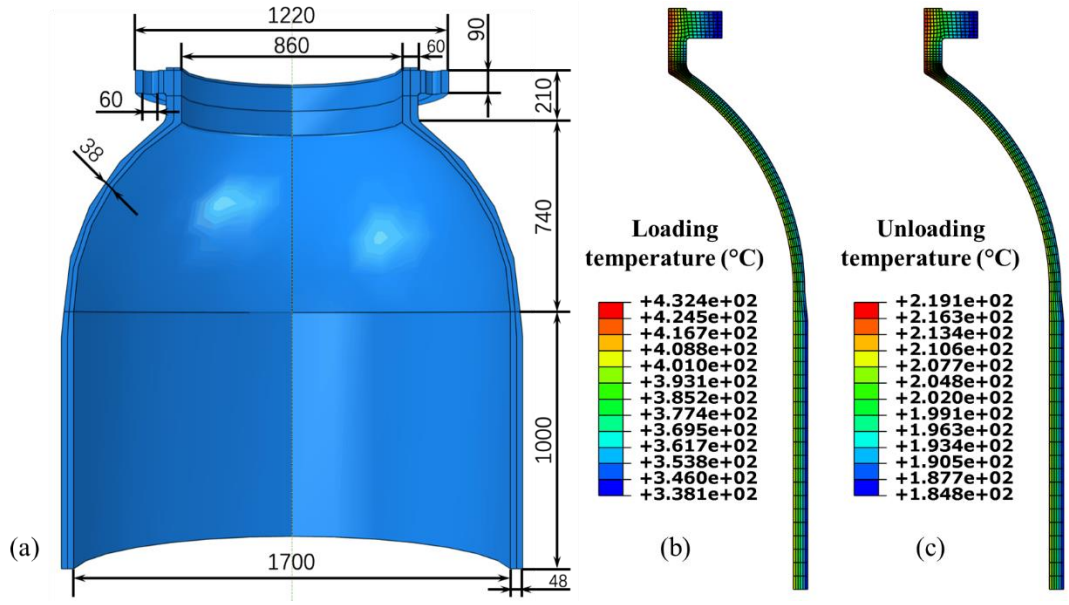

Figure 6.12: (a) The geometry of a hydrogenation reactor (b) The temperature distribution at the loading stage (c) The temperature distribution at the unloading stage

The temperature-dependent parameters of 2.25Cr1Mo used for the LMM analysis are provided by [180], as shown in Table 6.3. The temperature-independent parameters of 2.25Cr1Mo at 600°C are used to achieve conservative results, as shown in Table 6.5. The Norton law has been adopted to simulate the secondary stage of the creep behaviour:

$$\dot{\varepsilon}^c = A\sigma^n \tag{6.27}$$

where $\dot{\varepsilon}^c$ denotes the creep strain rate, material constants A and n are temperature-dependent, as provided in [181]. The Norton parameters are listed in Table 6.4 and implemented in the eDSCA using piecewise functions.

Table 6.3: Temperature-dependent material parameters of 2.25Cr1Mo

Temperature, T [ºC]	Thermal expansion, $\alpha(T)$ [10^{-5}/ºC]	Yield stress, $\sigma_Y(T)$ [MPa]
20	1.2	300
100	1.2	280
200	1.2	270
300	1.21	250
400	1.25	223
500	1.32	207
600	1.36	180
700	1.38	111
800	1.4	40

Table 6.4: Temperature-dependent Norton parameters of 2.25Cr1Mo

Temperature, T [ºC]	A	n
450	8.334×10^{-38}	12.430
475	6.665×10^{-33}	10.880
500	1.246×10^{-33}	11.420
525	3.286×10^{-28}	9.493
550	1.240×10^{-18}	5.651

Table 6.5: Temperature-independent material parameters of 2.25Cr1Mo at 600°C

Young's modulus, $\bar{E}(T)$ [MPa]	1.75×10^5
Poisson ratio	0.3
Conductivity, $\lambda(T)$ [W/(m·ºC)]	35.6
Heat capacity, $C_P(T)$ [J/(kg·ºC)]	723

The damage models used in this case are identical to the ones used in Section 6.3.1. For the evaluation of low cycle fatigue damage, the total strain range is used to compute the number of cycles to failure using the fatigue damage curves from [182], as shown in Figure 6.13(a). The fatigue damage curves have been fitted to be implemented in the extended DSCA using the polynomial function. For the evaluation of creep damage during creep dwell, the time fraction method is adopted where the creep rupture curves are used to acquire the time to rupture based on the average stress during creep dwell. As shown in Figure 6.13(b), the creep rupture curves at various temperatures from [183] have been modified by the Manson-Haferd parameter P_{MH} [52] to achieve a master curve:

$$P_{MH} = \frac{\log(t_R) - 16.053}{T_K - 380} \tag{6.28}$$

where t_R denotes time to creep rupture and T_K denotes temperature in Kelvin. The master rupture curve is then implemented in the extended DSCA using the polynomial function. For the evaluation of creep-fatigue damage, a bilinear creep-fatigue interaction diagram from [5] has been adopted, as shown in Figure 6.14. For 2.25Cr1Mo steel, two line segments of creep and fatigue envelope intersect at the coordinate $(0.1, 0.1)$.

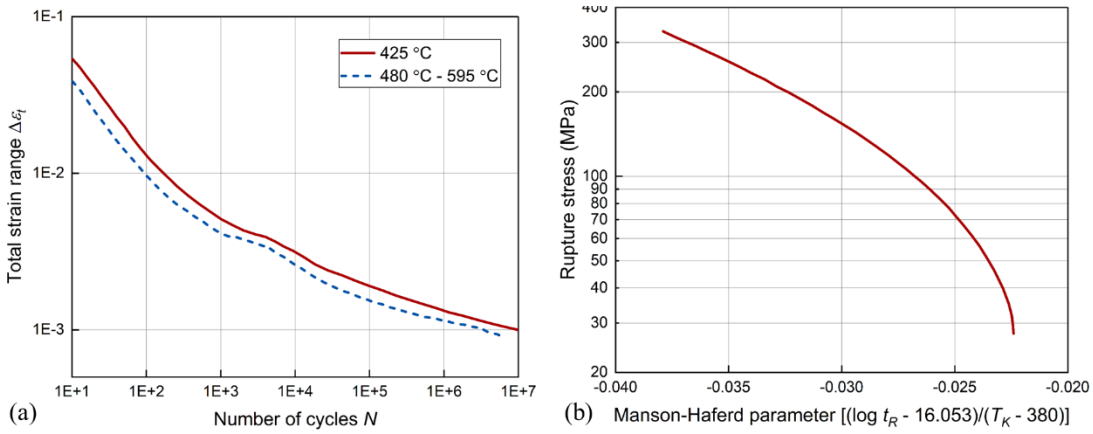

Figure 6.13: (a) Fatigue curves at various temperatures (b) The master creep rupture curve obtained with the Manson-Haferd parameter method

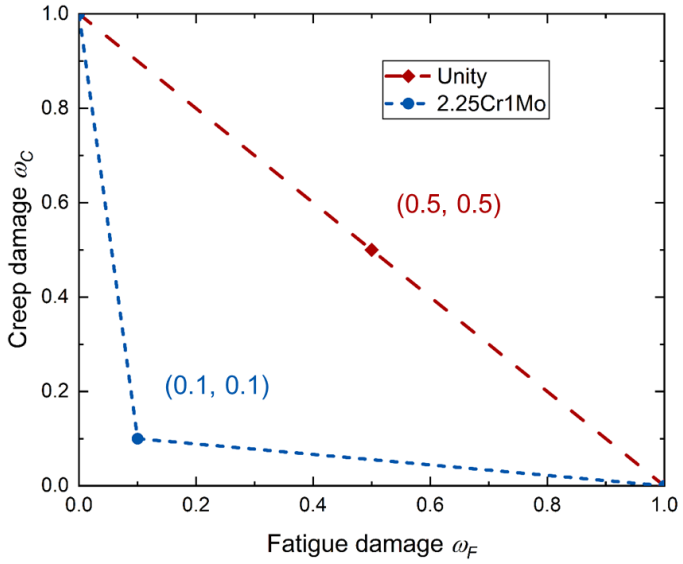

Figure 6.14: Creep-fatigue damage envelope for 2.25Cr1Mo

The simplified loading history for a typical hydrogenation operation cycle is presented in Figure 6.15. As mentioned before, the replacement of catalyst is required to ensure the normal operation process. Hence a load cycle is formed as the catalyst is removed and replaced periodically. At time sequence t_2, the high-temperature mixture of oil and hydrogen is first transferred into the reactor while the temperature of the inner surface rises to 432.4°C. Considering the room temperature and the insulation layer outside the reactor, a temperature gradient is observed across the thickness direction, as shown in Figure 6.12(b). At time sequence t_3, the replaced catalyst is put into the reactor to activate the hydrogenation reaction. At this stage, the inner pressure rises to 10 MPa and the corresponding pressure at the end surface is 33.49 MPa. Typical catalyst requires replacement after 10000 hours of the operation time, causing a creep

dwell time $\Delta T = 10000\,\mathrm{h}$. The influence of operation time is discussed in this work to consider the use of inferior catalysts with a shorter lifespan. At time sequence t_5, the performance limit of catalyst is reached and the pressure is released from the reactor to remove the catalyst. At time sequence t_6, the temperature drops to idle state and the whole load cycle is completed. The temperature distribution at the unloading stage is shown in Figure 6.12(c). It is important to ensure that the pressure elevates after the operation temperature is reached so that the temper embrittlement behaviour of 2.25Cr1Mo is prevented. A similar operation procedure is applied during the unloading stage while the pressure is released before the drop of temperature.

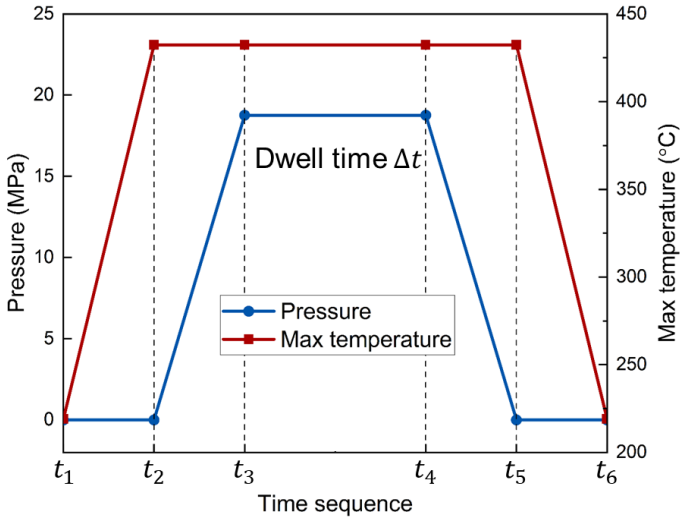

Figure 6.15: Simplified loading history for a typical hydrogenation operation cycle

6.3.2.2 Results and discussions

The creep-fatigue limit is bounded by several factors including the ratchet limit, the interaction between thermal and mechanical stress, the damage models and the dominance of creep and fatigue damage. Therefore, the shape of a structural constant creep-fatigue life curve is highly unpredictable and is greatly affected by the choice of material properties, unlike the constant low-cycle-fatigue damage curves which are mostly parallel to the reverse plasticity limit. The constant creep-fatigue life diagram considering various numbers of cycles to failure and various dwell times is presented in Figure 6.16. Due to the complexity of the geometry and loading spectrum, the constant creep-fatigue life curves are directly calculated without the aid of shakedown and ratchet boundaries. The diagram provides a series of design limits for various combinations of pressure and loading temperature at the inner surface of the reactor. In Figure 6.16(a), the dwell time is fixed at $\Delta t = 10000\,\mathrm{h}$ and five different target

numbers of cycles ($N = 20, 40, 60, 80, 100$) are considered. In this scenario, the design life of the reactor varies accordingly, ranging from 22 to 114 years. It can be seen that the higher the target N, the more the constant life curve shrinks, while the difference between the curves across various N is relatively small. Some discontinuities can be observed along the curves which are caused by the change of the failure mechanism. A bulge can also be found in the middle part of the diagram where the thermal and mechanical loads counteract with each other. When the temperature is high, the creep behaviour becomes prominent and horizontal creep-fatigue life limits are found near the Y-axis. This phenomenon is distinct from the one observed in Figure 6.6 due to the use of the temperature-independent Norton creep law. Also, the fatigue damage is calculated conservatively without the use of bilinear interpolation. In Figure 6.16(b), the target numbers of cycles are fixed at $N = 20$ and five different creep dwell times ($\Delta t = 10000, 8000, 6000, 4000, 2000$ h) are considered. In this scenario, the performance of catalyst is considered with various hours between maintenances. A similar trend can be observed that the higher the creep dwell time, the more the constant life curve shrinks. The alteration of dwell time greatly affects the creep strain and creep damage accumulated during a load cycle. Therefore, the lower part of the diagram is unaffected by the change of dwell time because the creep damage is minimal at lower temperatures.

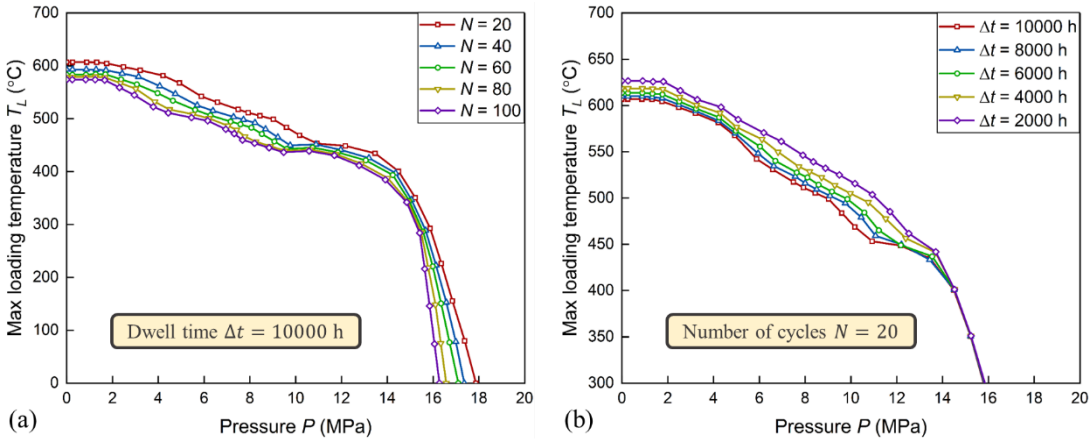

Figure 6.16: The constant creep-fatigue life diagram considering (a) various numbers of cycles to failure (b) various dwell times

It is worth mentioning that the constant creep-fatigue life curves are quite smooth when the body temperature is relatively low. But when the max loading temperature reaches a certain level, the curves become slightly irregular with some fluctuations. This phenomenon could be caused by several factors considering the complexity of

creep-fatigue interaction. Firstly, the main reason could be the discontinuity of material parameters for different temperatures. Due to the limited number of experimental data points obtained from literature, the curves of certain material parameters may not be smooth and there could be a lack of parameters at a certain temperature. For instance, in Figure 6.13, there is a slight fluctuation in fatigue curves between $N = 1000$ and $N = 10000$. Also, since there are only two fatigue curves for two different temperature intervals, the interpolation and extrapolation of material parameters for additional temperatures could be highly inaccurate. Hence for body temperature over 425 °C, the fatigue curve for 480 °C - 595 °C is used; for body temperature below 425 °C, the fatigue curve for 425 °C is used for conservative results. Secondly, the fluctuations in constant creep-fatigue life curves could be caused by the displacement of critical locations in the structure. The total creep-fatigue life of the structure is determined by the integration point with the largest creep-fatigue damage which is also known as the critical point. The critical point may not be consistent with various combinations of thermal and mechanical loads applied, inducing inconsistency and discontinuity in the calculation of total damage. For example, in Figure 6.18, the critical locations of the largest total damage are identical for load points (1) and (3). But for load point (2), the critical location shifts to the internal surface of the reactor head, causing a fluctuation in the constant life curves around load point (2). Thirdly, the fluctuations could also be caused by the difference in convergence performance with the transformation of failure mechanisms. Although several techniques have been utilised to ensure the satisfaction of the convergence criterion for various load combinations, the interaction of creep-fatigue failure mechanisms has a great impact on the convergence rate of eDSCA and extended UPFRA. Based on previous experience, the number of increments required for final convergence could cause slight deviations of stress-strain results and consequent fluctuations in constant creep-fatigue life curves.

A benchmark operation case ($N = 20, \Delta t = 10000\,\mathrm{h}$) has been selected to further study the interaction between creep and fatigue behaviour, as shown in Figure 6.17. Three load points have been chosen and numbered along the constant creep-fatigue life curve. The dominance of creep or fatigue is determined by comparing the creep and fatigue damage at each integration point and presented in form of contours. It can be observed that for load point (1), at high temperature, the entire body is mostly creep-dominant due to the large overall creep damage. For load point (2), with the decrease of temperature, fatigue-dominance is observed at the transition part of the

body. Geometric discontinuity is found in that region that causes the stress concentration and large strain range. Thus the fatigue damage exceeds the creep damage and contributes more to the total damage. For load point (3), the dominance of fatigue gradually spread from the transition area to the whole body. It is caused by the decrease of temperature and increase of mechanical load in the body. Therefore, the evolution of creep and fatigue dominance is explicitly illustrated and discussed with the aid of several contours.

The creep, fatigue and total damage contours for different load points are presented and compared in Figure 6.18. The failure mechanisms caused by creep and fatigue are highly different and the distribution of total damage contours is identical to the dominant creep/fatigue damage contour. Large creep damage is observed at the inner surface of the reactor due to the effect of high temperature, while large fatigue damage is observed at the transition area between the reactor head and the cylindrical shell due to the presence of stress concentration. For load points (1) and (2), the overall creep damage is larger than the fatigue damage. It can be seen that the creep damage contours are not smooth as the fatigue damage. It could be caused by the mismatch between the use of time fraction law and the interpolation post-processing algorithm of Abaqus. For load point (3), the overall fatigue damage is larger than the creep damage. It is worth noting that for all the load points on the same constant creep-fatigue life curve, the largest total damage in the structure is around 0.05, resulting in the same number of cycles to failure at $N = 20$.

To further investigate the stress-strain behaviour considering various load combinations and creep dwell times, the hysteresis loops for load point (1) and load point (3) have been presented in Figure 6.19. The results are calculated with the LMM eDSCA subroutine. The integration point for the plotting of hysteresis loops is chosen based on the location of the largest total damage, as shown in Figure 6.18(c)(i). For the sake of consistency, the same integration point is considered for the additional illustration of the saturated stress-strain relationship for other load points. Two different creep dwell times are also considered for each load point to show the influence of dwell time.

It can be observed in Figure 6.19 that the stress-strain behaviour of load point (1) is distinct from load point (3) due to the dominance of creep or fatigue behaviour. Load point (1) is creep dominant, with higher thermal stress and lower mechanical stress.

During the creep dwell stage, a large amount of stress relaxation is observed due to the presence of large secondary loads. The elastic follow up factor Z is assumed constant during creep dwell because of the limitations of the eDSCA. With the decreasing creep dwell time, the creep strain and Z become smaller accordingly. Unlike the example in Section 6.3.1, the range of the creep dwell time considered for this case is quite small, ranging from 2000 hours to 10000 hours. Therefore, the effect of dwell time on the creep-fatigue is relatively insignificant considering the better anti-creep performance of 2.25Cr1Mo. Load point (3) is fatigue dominant, with higher mechanical stress and lower thermal stress. Compared to load point (1), the yield stress at the loading stage is larger and creep strain is smaller for load point (3) due to the lower maximum temperature in the structure. During the creep dwell stage, $Z \rightarrow \infty$ since the load applied is mostly primary load. The large mechanical stress also induces large plastic strain and total strain range, resulting in significant fatigue damage, as shown in Figure 6.18(h). It is worth mentioning that the creep ratchetting behaviour is also observed in the hysteresis loops of load point (3), especially when the creep dwell time is large. The reason is that the small stress relaxation and residual stress field during the creep dwell has little contribution to the reverse plasticity at unloading stage. Therefore, the additional creep strain is not fully covered during unloading and a open hysteresis loop is observed.

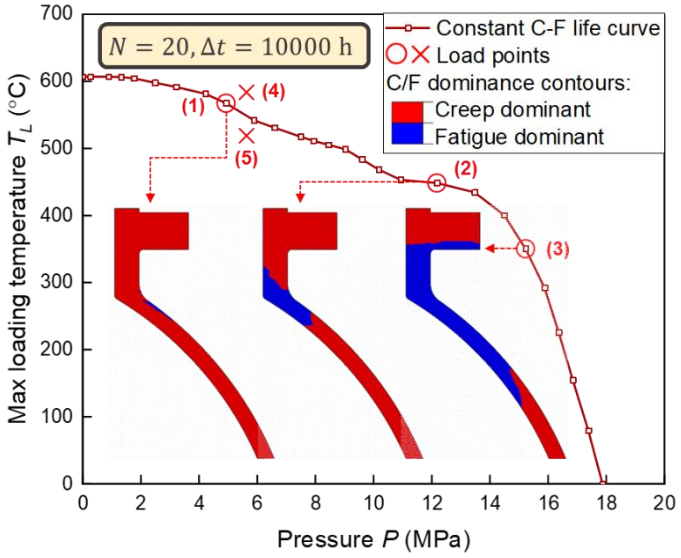

Figure 6.17: The evolution of creep/fatigue dominance along the constant creep-fatigue life curve

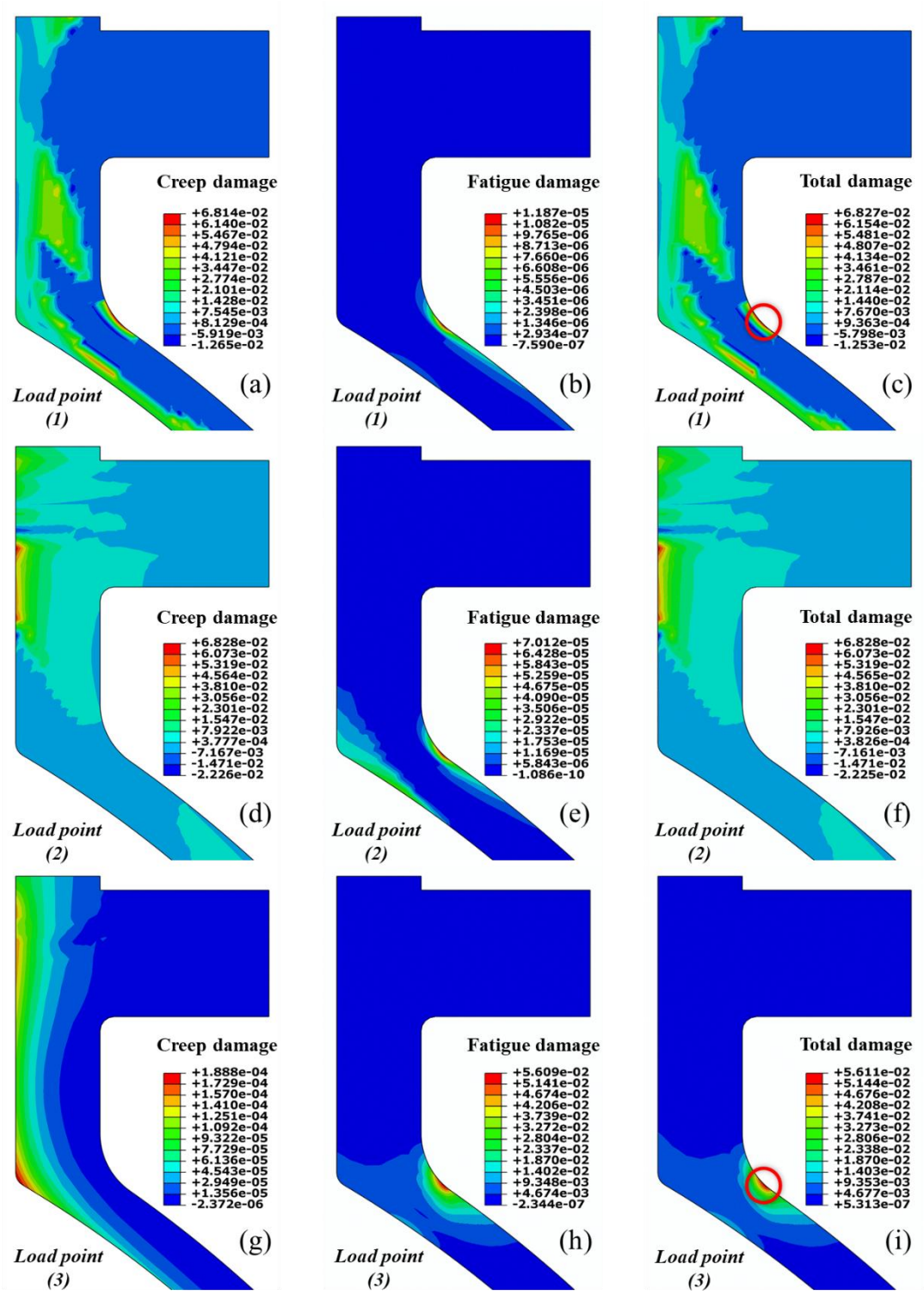

Figure 6.18: Comparison of damage contours between different load points

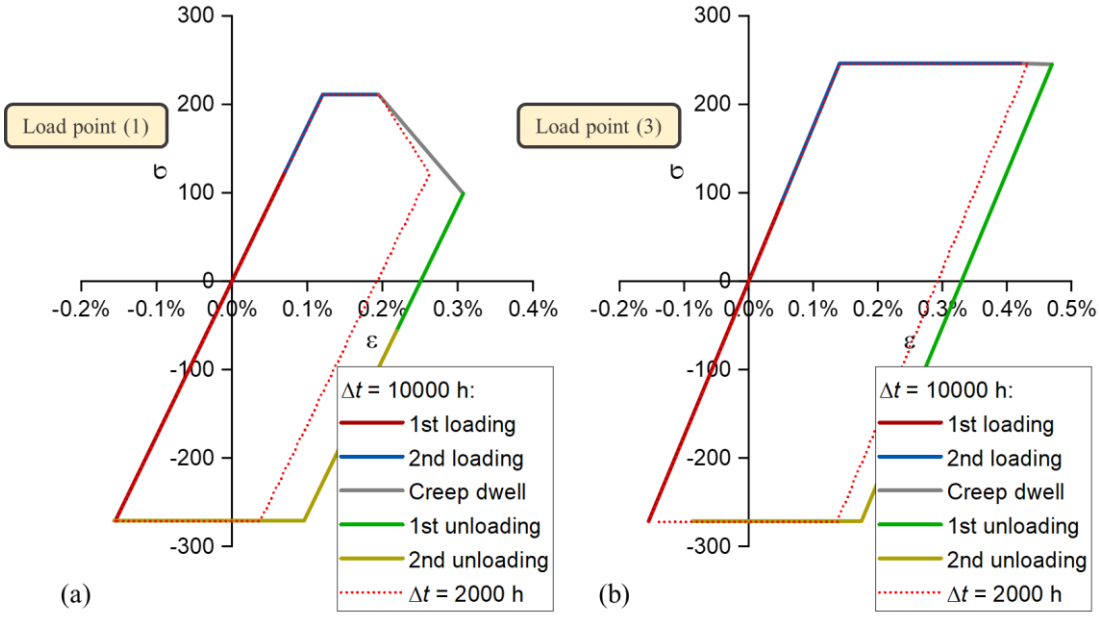

Figure 6.19: Hysteresis loops obtained with eDSCA considering effect of different dwell times for two different load points

6.3.2.3 Verification of results

To verify the accuracy of the proposed method, two load points have been selected from the constant creep-fatigue life curve of $N = 20, \Delta t = 10000$ h for inelastic SBS analysis, as shown in Figure 6.17. Load point (4) is slightly above the benchmark curve and load point (5) is slightly below the benchmark curve. The creep-fatigue damage for both load points is evaluated and compared with the target number of cycles to failure $N = 20$. The material properties adopted for the SBS analysis are identical to the ones used in the eDSCA. In addition, the time-hardening creep constitutive relationship is considered and 40 load cycles are established to ensure the steady-state is reached. Each cycle contains 5 steps and the corresponding load spectrum is shown in Figure 6.15. The creep FORTRAN subroutine implementing the temperature-dependent Norton law is given in Appendix C.

The SBS contours of von Mises steady-state stress and creep strain during creep dwell are presented in Figure 6.20. Stress concentration is observed at the transition area between the reactor head and nozzle due to the geometric discontinuity. During the creep dwell, a significant drop in stress and stress redistribution behaviour is observed due to the relaxation of thermal stress. Since the temperature at load point (4) is higher than the temperature at load point (5), the largest yield stress in the structure is higher for load point (5). A larger creep strain is also observed for load

point (4) because of the higher temperature. The integration point for the largest creep strain has been selected from Figure 6.20(c)(d) for the evaluation of hysteresis loops, as plotted in Figure 6.21. Different stages of loading have been marked with various colours. The stress-strain behaviour at the first loading and unloading stages is mostly elastic and a drop in stress level can be seen during the creep dwell stage. The steady-state hysteresis loops are both closed, hence the creep ratchetting behaviour is not detected. It is also noticed that compared to load point (5), the total strain range for load point (4) is greater due to the larger thermal load. Therefore, the structural creep-fatigue damage is also different for both load points. For load point (4), the number of cycles to creep-fatigue failure $N = 12 < 20$; for load point (5), the number of cycles to creep-fatigue failure $N = 49 > 20$. Since both load points are selected from the inside and outside of the constant creep-fatigue life boundary of $N = 20$, the SBS results agree well with the constant life diagram calculated with the extended UPFRA. The accuracy and robustness of the proposed method are thus proved, with further advantages of great computational efficiency and convergence performance compared to the conventional SBS method as stated below.

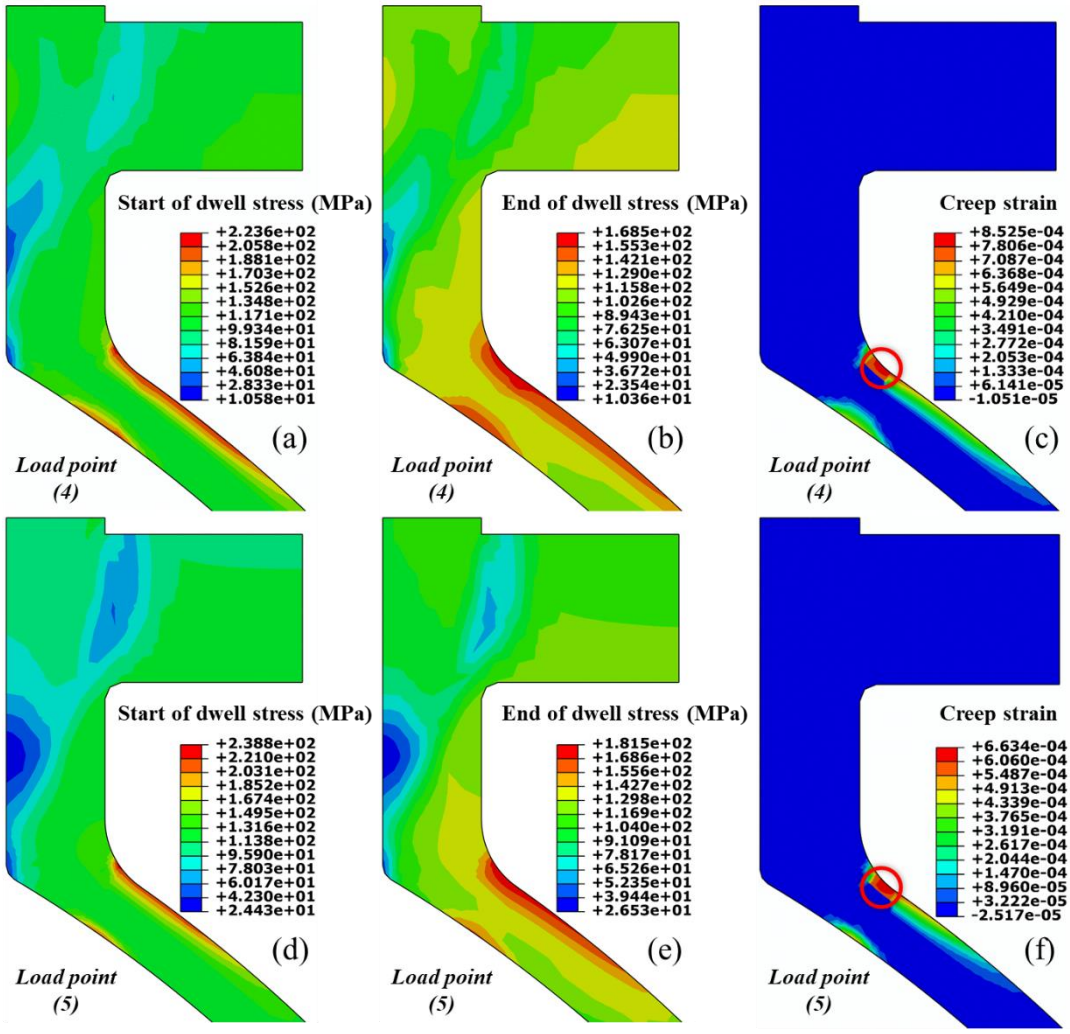

Figure 6.20: Stress and creep strain contours for SBS validation

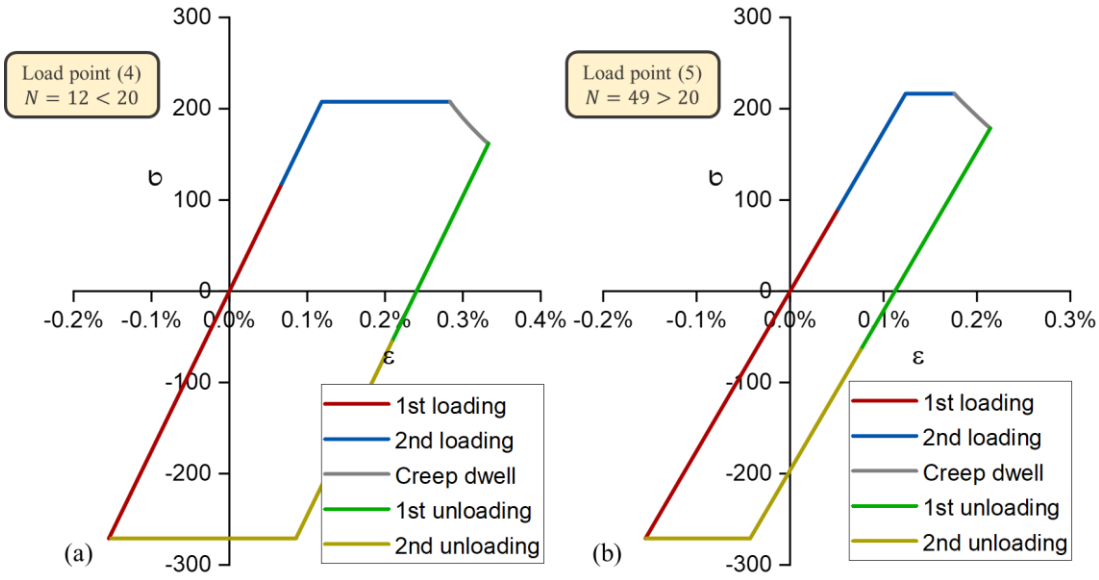

Figure 6.21: Hysteresis loops for load points near the constant creep-fatigue life curve of N = 20, Δt = 10000h obtained with SBS analysis

To further validate the eDSCA subroutine which is the basis of the extended UPFRA, SBS analysis has also been conducted for load points (1) and (3) located on the constant creep-fatigue life curve of $N = 20$, as shown in Figure 6.22. The hysteresis loops obtained with SBS are plotted for the integration point highlighted in Figure 6.18 and compared with the results obtained with eDSCA from Figure 6.19. Considering identical loading conditions and material parameters, it can be noticed that the hysteresis loops obtained with SBS and eDSCA agree well with each other. The numbers of cycles to creep-fatigue failure calculated with SBS are slightly smaller than the ones computed with eDSCA. In this case, the results obtained with eDSCA are less conservative because of the numerical errors and differences in creep evaluation techniques during the creep dwell stage. For load point (1), the stress relaxation predicted by SBS is smaller than eDSCA, causing an increase in average stress and creep damage. For load point (2), the creep strain predicted by SBS is larger than eDSCA, inducing an increase in total strain range and fatigue damage.

The CPU time required for eDSCA and SBS for both load points is listed and compared in Table 6.6. As one of the direct methods, eDSCA has a large advantage in calculation speed with an improvement of more than 50% over SBS. In addition, to plot a constant creep-fatigue life diagram, the use of SBS analysis requires a large amount of trial and error to find the load points with a designated number of cycles to failure. SBS calculation of different load points and dwell times also requires the renewal of boundary conditions, material properties and step configurations in the FE model. The whole process can thus be highly time-consuming and inefficient, with possibilities of potential convergence issues at steps of creep dwell. On the other hand, eDSCA utilises a series of linear equations for creep-fatigue computation to deliver accurate results and improve convergence performance significantly. Therefore, based on eDSCA and creep-fatigue damage models, the extended UPFRA provides an effective and reliable solution to the evaluation of the constant creep-fatigue life diagram.

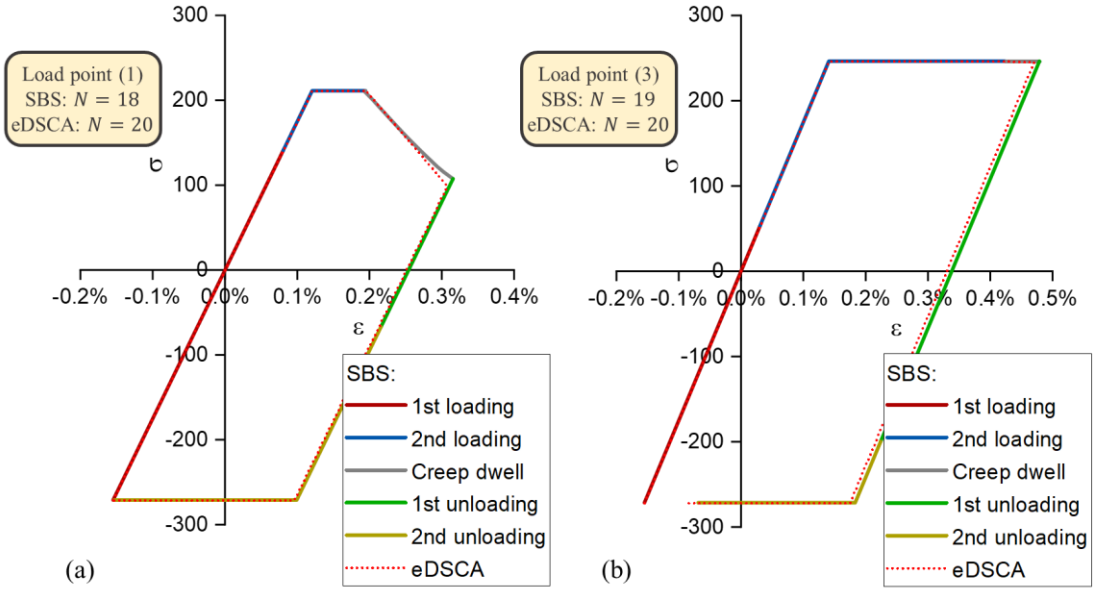

Figure 6.22: Comparisons of hysteresis loops for load points on the constant creep-fatigue life curve of $N = 20$, $\Delta t = 10000$h obtained with SBS and eDSCA

Table 6.6: Comparisons of total CPU time using the eDSCA and SBS

	Load point (1)	Load point (3)
CPU time (SBS) [sec]	332.9	202.7
CPU time (eDSCA) [sec]	135.9	98.9
Speed improvement	59.2%	51.2%

6.3.2.4 A 3D constant creep-fatigue life diagram

A 3D constant creep-fatigue life diagram considering various numbers of cycles to failure and various dwell times has been plotted, as shown in Figure 6.23. For $N = 20$, the 2D curves from Figure 6.16 have been combined into a surface in the 3D space. A number of extended UPFRA analyses have been conducted considering various numbers of cycles to failure to generate enough data points for a whole 3D diagram. The 2D constant creep-fatigue life curves have been marked out with black lines on the 3D surface. The influence of thermal load, mechanical load and dwell time can be readily observed in the 3D diagram. At low temperatures, the difference between the surfaces is minimal and the intersection line between the constant life surfaces and the X-Y plane is parallel to the Y-axis. This part of the diagram is mainly controlled by fatigue damage and is not affected by creep dwell time. With the increase of temperature, a transition point is observed in the constant life diagram and a bending

edge is shown on the 3D surface, indicating a change of the failure mechanism. At high temperatures, the difference between the surfaces becomes larger and the intersection line between the constant life surfaces and the Y-Z plane inclines toward the X-axis with the increase of dwell time. The reason is that the creep damage takes dominance at this stage and the constant life surfaces are greatly affected by the temperature and creep dwell time. As mentioned before, the range of the dwell time considered for this case is relatively small. Thus the influence of dwell time is not significantly shown in Figure 6.23. The constant creep-fatigue life surfaces have provided an intuitive and convenient way for the design and assessment of hydrogenation reactors. The extended UPFRA has also been proved to be a robust and efficient tool for practical engineering cases.

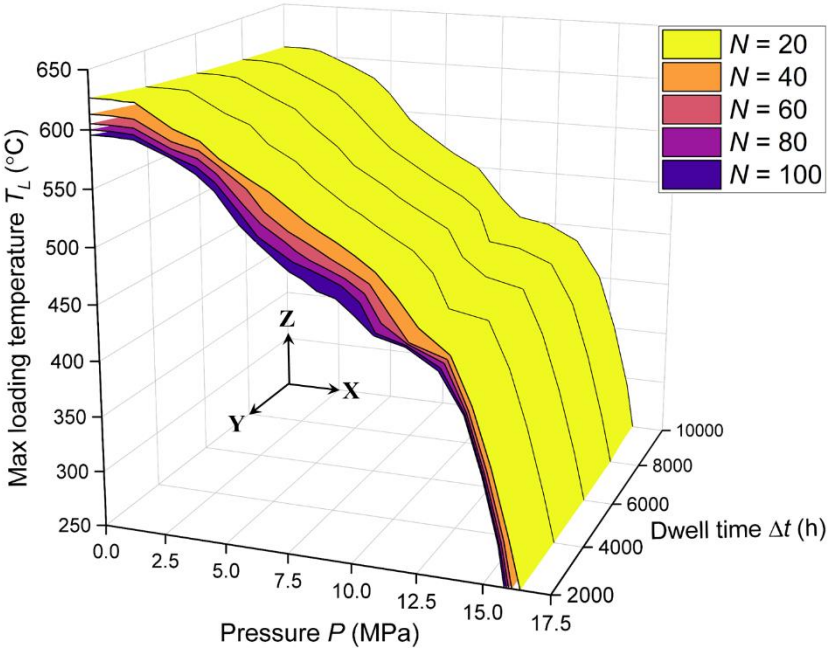

Figure 6.23: A 3D constant creep-fatigue life diagram considering various numbers of cycles to failure and various dwell times

6.4 Summary

In this chapter, the concept of the structural constant life diagram has been extended to consider the effect of creep-fatigue interaction. The user subroutines for creep-fatigue damage calculation have been implemented in the existing LMM plug-in for better usability. The Unified Procedure for Fatigue and Ratchet Analysis (UPFRA) has also been extended by calling the eDSCA module iteratively in the LMM framework. A three-stage process has been further proposed to evaluate the constant creep-

fatigue life diagrams for engineering components subjected to arbitrary thermal-mechanical loads.

A numerical example of a holed plate is given to demonstrate and validate the proposed method. In this example, temperature-dependent material properties are adopted to consider the non-isothermal effect and typical creep-fatigue damage models are adopted. The constant creep-fatigue life curves of the holed plate subjected to different load cases considering various target numbers of cycles to failure have been evaluated, and the influence of dwell time is also investigated. In addition, the failure mechanisms induced by creep and fatigue damage have been discussed, and a series of hysteresis loops have been plotted. The creep ratchetting behaviour is found as the result of creep-fatigue interaction, which is driven by “cyclically enhanced creep” and “creep enhanced plasticity” mechanisms. Another industrial numerical example of a hydrogenation reactor is given to demonstrate the viability of the proposed method for practical engineering problems. A different type of steel and thermal-mechanical loading history is considered for this problem. A 3D constant creep-fatigue life diagram is plotted for design and assessment purposes. The interaction and dominance of creep and fatigue damage have been further discussed for various load points from the diagram. The accuracy of the results has been further verified by a series of SBS analyses. Therefore, the benchmark case of a holed plate from Section 5.3.1 is further extended in this section to show the versatility of proposed procedure. The creep effect is illustrated by comparing the constant LCF life curves and the constant creep-fatigue life curves. In the engineering case of a hydrogenation reactor, the effect of creep dwell time is investigated by plotting a 3D constant creep-fatigue life diagram. The accuracy and efficiency of the extended UPFRA is illustrated by comparing the results with SBS analysis. In addition, the Bree-like diagram is further extended by including the constant creep-fatigue life curves.

7. Conclusions

7.1 Summary of the thesis

In this thesis, the capability and functionality of the existing LMM framework have been enhanced by implementing multiple numerical procedures for different aspects of high-temperature structural integrity assessment. The Bree-like diagrams have been developed in various ways for high-temperature design and assessment. The primary outcomes of the research are summarised as follows:

1) A literature review of high-temperature structural cyclic response, current numerical methods, and international design codes has been presented.
2) A limited kinematic hardening algorithm for shakedown analysis and a corresponding two-stage numerical procedure has been implemented in the LMM shakedown analysis module.
3) A numerical scheme for the prediction of creep rupture stress has been developed which has been implemented in the LMM creep rupture analysis module.
4) The evaluation of structural ratchet limit and constant fatigue life curves considering arbitrary thermal-mechanical loading histories for the extended Bree-like diagram has been proposed by a numerical procedure, which is based on the existing LMM DSCA module.
5) The evaluation of structural constant creep-fatigue life curves considering creep-fatigue interaction for the extended Bree-like diagram has been proposed by a numerical procedure, which is based on the existing LMM eDSCA module.

The main findings of this work are concluded below.

7.2 Key achievements, justification and scientific impacts

With decades of development, the LMM plug-in has become one of the most advanced software tools to perform the LMM direct methods for structural integrity assessment. This work focuses on the novel application of these direct methods for extending the Bree-like diagram in four stages.

For the first stage, the Bree-like diagram is extended by including the shakedown limit considering kinematic hardening materials. The structural shakedown boundaries could be greatly affected by the kinematic hardening behaviour which is difficult to consider in direct methods. Temperature-dependent material properties are fully supported so that the accuracy of the shakedown boundaries is greatly improved. A shakedown algorithm considering limited kinematic hardening material has been implemented in the current LMM framework based on a two-surface hardening model. An overall deviation factor of 0.07 is achieved when comparing the results from the extended LMM shakedown module with the ones from other researchers.

For the second stage, the Bree-like diagram is extended by including the creep rupture limit. The creep rupture limit determines the load-bearing capacity for high-temperature components subjected to cyclic loading conditions. The UCRE has been proposed to predict the creep rupture strength and it is capable of fitting the rupture curves for more than 40 different types of steel with satisfactory accuracy. A deviation factor of 0.55 is observed when comparing the predicted rupture strengths with experimental data points. The UCRE has then been implemented in the LMM framework for the derivation of the temperature-dependent revised yield stress.

For the third stage, the Bree-like diagram is extended by including the constant LCF life curves. The constant life diagram provides a convenient way of determining the structural life based on any combination of thermal-mechanical loads. The UPFRA has been proposed to use the LMM DSCA subroutine for the evaluation of the constant fatigue life diagram and ratchet boundary. The R-O model has also been utilised in the fatigue analysis to describe the saturated stress-strain relationship considering the hardening effect. The R-O model produces more conservative results than the EPP model when the hardening effect is significant at a high load level. The numerical procedure is validated by a series of SBS analyses for various load points along the boundaries.

For the fourth stage, the Bree-like diagram is extended by including the constant creep-fatigue life curves. The consideration of creep-fatigue interaction damage is crucial for high-temperature structures. Creep dwell time also has an enormous impact on the constant life curves. The extended UPFRA has been proposed to use the LMM eDSCA subroutine for the evaluation of the constant creep-fatigue life

diagram. SBS analyses have also been performed on several load points to show the accuracy and efficiency of the proposed method.

Therefore, several contributions have been made to the development of computational tools for the evaluation of cyclic plasticity and creep behaviours of high-temperature structures. With the implementation of the proposed numerical methods, the LMM framework has become a more powerful engineering tool for high-temperature structural integrity assessment with better accuracy, efficiency, and versatility.

7.3 Future work

Although the LMM framework has become one of the most advanced numerical methods in the field of direct methods, it can still be further improved in various ways as given below:

1) In Chapter 3, Melan's static shakedown theorem has been extended to consider limited kinematic hardening material. The extended shakedown theorem is proposed using a general nonlinear kinematic hardening model bounded by the ultimate stress and unlimited hardening behaviour. For a more accurate estimation of the kinematic hardening behaviour, it could be possible to implement specific hardening rules such as Prager linear hardening rule [44] and Chaboche constitutive models [38] in the shakedown algorithm. Furthermore, isotropic hardening rules or combined hardening rules could be included for further development in the LMM shakedown analysis module.
2) In Chapter 6, a numerical procedure for the evaluation of the constant creep-fatigue life diagram has been proposed. For better clarification of the proposed method, the numerical example only considers EPP constitutive model and basic creep-fatigue damage models. For complicated engineering problems, the R-O model can be used to describe the steady-state stress-strain relationship to consider the hardening effect. Also, complex damage models such as the DE method, SMDE method and nonlinear creep-fatigue damage interaction envelope may be adopted for creep-fatigue damage calculation. In addition, multiple creep dwell stages can be considered in the load cycle based on industrial loading spectrums.

3) Since this research work primarily focuses on FE simulations and numerical algorithms, there is a lack of physical characterization and experiments to support and validate the proposed methods. Material experiments could be performed to determine the realistic material parameters, especially for the two-surface kinematic hardening model. Physical characterization could be conducted to investigate the mechanics of creep rupture and provide physical meanings to the UCRE. Structural experiments could also be performed to validate the accuracy of constant life diagrams calculated by the UPFRA or extended UPFRA.
4) As an engineering tool for the general structural integrity assessment, the LMM plug-in could be further developed in various ways. A post-processing module could be developed which directly shows the user-specified contours instead of displaying SDV values. The shakedown limit, ratchet limit and the hysteresis loop can also be plotted automatically with the post-processing module. A “design by rule” module could also be implemented in the LMM framework, including numerical equations from international design codes such as ASME and R5. Additionally, a material database could be built containing the essential parameters of commonly used materials for the LMM analysis. The UPFRA and extended UPFRA could be further implemented in the LMM plug-in in the form of GUI for improved usability and efficiency.

References

1. Buckthorpe, D., *Introduction to Generation IV nuclear reactors*, in *Structural Materials for Generation IV Nuclear Reactors*. 2017, Elsevier. p. 1-22.
2. Sabharwall, P., S.M. Bragg-Sitton, and C. Stoots, *Challenges in the development of high temperature reactors.* Energy conversion and management, 2013. **74**: p. 574-581.
3. Li, M., et al., *Cyclic plasticity of welded P91 material for simple and complex power plant connections.* International Journal of Fatigue, 2016. **87**: p. 391-404.
4. Thielen, H., *The Fukushima Daiichi nuclear accident—an overview.* Health physics, 2012. **103**(2): p. 169-174.
5. ASME Boiler and Pressure Vessel Code, *Section III, Division 1—Subsection NH*. 2013, The American Society of Mechanical Engineers: New York.
6. RCC-MRx Code, *Design and Construction rules for Nuclear Power Generating Stations.* AFCEN, France, 2015.
7. Ainsworth, R.A., *R5: Assessment Procedure for the High Temperature Response of Structures*. 2003, British Energy Generation Ltd.
8. Viswanathan, R., *An Overview of Failure Mechanisms in High Temperature Componentd in Power Plants.* Electric Power Research Institute, 2000. **122**: p. 246-255.
9. Vardar, N. and A. Ekerim, *Failure analysis of gas turbine blades in a thermal power plant.* Engineering Failure Analysis, 2007. **14**(4): p. 743-749.
10. Viswanathan, R. and J. Stringer, *Failure mechanisms of high temperature components in power plants.* J. Eng. Mater. Technol., 2000. **122**(3): p. 246-255.
11. Sonsino, C., *Fatigue design for powder metallurgy.* Powder Metallurgy, 1990. **33**(3): p. 235-245.
12. Bree, J., *Elastic-plastic behaviour of thin tubes subjected to internal pressure and intermittent high-heat fluxes with application to fast-nuclear-reactor fuel elements.* Journal of strain analysis, 1967. **2**(3): p. 226-238.
13. Barbera, D., H. Chen, and Y. Liu. *Review and Case Study of the Linear Matching Method Framework for Structure Integrity Assessment*. in *ASME 2016 Pressure Vessels and Piping Conference*. 2016. American Society of Mechanical Engineers Digital Collection.
14. Chen, H. and A.R. Ponter, *Shakedown and limit analyses for 3-D structures using the linear matching method.* International Journal of Pressure Vessels and Piping, 2001. **78**(6): p. 443-451.
15. Chen, H., M. Engelhardt, and A.R. Ponter, *Linear matching method for creep rupture assessment.* International journal of pressure vessels and piping, 2003. **80**(4): p. 213-220.
16. Chen, H. and A.R. Ponter, *A direct method on the evaluation of ratchet limit.* Journal of Pressure Vessel Technology, 2010. **132**(4): p. 041202.
17. Chen, H., J. Ure, and D. Tipping, *Integrated structural analysis tool using the Linear Matching Method part 2–Application and verification.* International Journal of Pressure Vessels and Piping, 2014. **120**: p. 152-161.
18. Ure, J., H. Chen, and D. Tipping, *Integrated structural analysis tool using the linear matching method part 1–Software development.* International Journal of Pressure Vessels and Piping, 2014. **120**: p. 141-151.

19. Chen, H., W. Chen, and J. Ure, *A direct method on the evaluation of cyclic steady state of structures with creep effect.* Journal of Pressure Vessel Technology, 2014. **136**(6): p. 061404.
20. Barbera, D., et al., *Recent developments of the linear matching method framework for structural integrity assessment.* Journal of Pressure Vessel Technology, 2017. **139**(5): p. 051101.
21. Hibbitt, D., B. Karlsson, and P. Sorensen, *Abaqus 6.12. 3 Manual.* Dassault Systèmes Simulia Corp., Providence, RI, 2012.
22. Svensson, N., *Ageing and the Bauschinger Effect in Mild Steel.* Nature, 1966. **211**(5046): p. 290.
23. Lytwyn, M., H. Chen, and M. Martin. *Ratchet analysis of structures under a generalised cyclic load history*. in *ASME 2014 Pressure Vessels and Piping Conference*. 2014. American Society of Mechanical Engineers Digital Collection.
24. Lytwyn, M., H. Chen, and A.R. Ponter, *A generalised method for ratchet analysis of structures undergoing arbitrary thermo‐mechanical load histories.* International Journal for Numerical Methods in Engineering, 2015. **104**(2): p. 104-124.
25. Melan, E., *Theorie statisch unbestimmter Systeme aus ideal-plastischem Baustoff*. 1936: Hölder-Pichler-Tempsky in Komm.
26. Koiter, W.T., *General theorems for elastic plastic solids.* Progress of Solid Mechanics, 1960: p. 167-221.
27. Coffin Jr, L.F., *A study of the effects of cyclic thermal stresses on a ductile metal.* Transactions of the American Society of Mechanical Engineers, New York, 1954. **76**: p. 931-950.
28. Manson, S.S., *Behavior of materials under conditions of thermal stress*. Vol. 2933. 1953: National Advisory Committee for Aeronautics.
29. Jacques, S., et al. *A Coffin-Manson model to predict the TRIAC solder joints fatigue during power cycling*. in *Proceedings of the 2011 14th European Conference on Power Electronics and Applications*. 2011. IEEE.
30. Manson, S., *Fatigue: a complex subject—some simple approximations.* Experimental mechanics, 1965. **5**(4): p. 193-226.
31. Muralidharan, U. and S. Manson, *A modified universal slopes equation for estimation of fatigue characteristics of metals.* 1988.
32. Ong, J., *An improved technique for the prediction of axial fatique life from tensile data.* International journal of fatigue, 1993. **15**(3): p. 213-219.
33. Mitchell, M., *Fundamentals of modern fatigue analysis for design.* 1996.
34. Park, J.-H. and J.-H. Song, *New estimation method of fatigue properties of aluminum alloys.* J. Eng. Mater. Technol., 2003. **125**(2): p. 208-214.
35. BÄUMEL, A.J. and T. Seeger, *Materials data for cyclic loading.* Materials science monographs, 1990. **61**.
36. Meggiolaro, M. and J. Castro, *Statistical evaluation of strain-life fatigue crack initiation predictions.* International Journal of Fatigue, 2004. **26**(5): p. 463-476.
37. Halama, R., M. Fusek, and Z. Poruba, *Influence of mean stress and stress amplitude on uniaxial and biaxial ratcheting of ST52 steel and its prediction by the AbdelKarim–Ohno model.* International Journal of Fatigue, 2016. **91**: p. 313-321.
38. Chaboche, J. and D. Nouailhas, *Constitutive modeling of ratchetting effects—part i: experimental facts and properties of the classical models.* 1989.
39. Kan, Q.H., et al. *An Improved Thermo-Ratcheting Boundary of Pressure Pipeline*. in *Key Engineering Materials*. 2017. Trans Tech Publ.

40. Ponter, A. and M. Megahed, *Creep and plastic ratchetting in cyclically thermally loaded structures*, in *Physical Non-Linearities in Structural Analysis*. 1981, Springer. p. 220-227.
41. Segle, P., G. Eklund, and M. Skog, *A two-rod testing approach for understanding ratcheting in structures.* International Journal of Pressure Vessels and Piping, 2016. **139**: p. 184-193.
42. Dunne, F. and N. Petrinic, *Introduction to computational plasticity*. 2005: Oxford University Press on Demand.
43. Armstrong, P.J. and C. Frederick, *A mathematical representation of the multiaxial Bauschinger effect*. Vol. 731. 1966, Berkeley: Central Electricity Generating Board [and] Berkeley Nuclear Laboratories, Research & Development Department.
44. Prager, W., *The theory of plasticity: a survey of recent achievements.* Proceedings of the Institution of Mechanical Engineers, 1955. **169**(1): p. 41-57.
45. Ziegler, H., *A modification of Prager's hardening rule.* Quarterly of Applied mathematics, 1959. **17**(1): p. 55-65.
46. Weichert, D. and J. Gross-Weege, *The numerical assessment of elastic-plastic sheets under variable mechanical and thermal loads using a simplified two-surface yield condition.* International journal of mechanical sciences, 1988. **30**(10): p. 757-767.
47. Barbera, D., *On the evaluation of high temperature creep-fatigue responses of structures*. 2017, University of Strathclyde.
48. Recommendation, E., *Creep data validation and assessment procedures.* ERA Technology Ltd., UK, 2001.
49. *ECCC Data Sheets, Rupture strength, creep strength and relaxation strength values for carbon manganese, low alloy ferritic, high alloy ferritic and austenitic steels, and high temperature bolting steels/alloys*. 2014, European Creep Collaborative Committee.
50. Larson, F.R. and J. Miller, *A time-temperature relationship for rupture and creep stresses.* Trans. ASME, 1952. **74**: p. 765-775.
51. Pink, E., *Physical significance and reliability of Larson–Miller and Manson–Haferd parameters.* Materials science and technology, 1994. **10**(4): p. 340-346.
52. Manson, S.S. and A.M. Haferd, *A linear time-temperature relation for extrapolation of creep and stress-rupture data*. 1953, Lewis Flight Propulsion Lab., NACA.
53. Orr, R.L., O.D. Sherby, and J.E. Dorn, *Correlations of rupture data for metals at elevated temperatures*. 1953, Institue of Engineering Research, Univ. of Calif., Berkeley.
54. Mendelson, A., E. Roberts Jr, and S. Manson, *Optimization of time-temperature parameters for creep and stress rupture, with application to data from German cooperative long-time creep program*. 1965, NATIONAL AERONAUTICS AND SPACE ADMINISTRATION CLEVELAND OH LEWIS RESEARCH CENTER.
55. Whittaker, M., M. Evans, and B. Wilshire, *Long-term creep data prediction for type 316H stainless steel.* Materials Science and Engineering: A, 2012. **552**: p. 145-150.
56. Peng, H., Y. Liu, and H. Chen, *Numerical schemes based on the stress compensation method framework for creep rupture assessment.* European Journal of Mechanics-A/Solids, 2020: p. 104014.
57. Peng, H., Y. Liu, and H. Chen, *Creep rupture assessment of cyclically heated 3D pressure pipelines with volumetric defects using a direct numerical*

approach. International Journal of Pressure Vessels and Piping, 2021. **192**: p. 104387.
58. Yan, X.-L., et al., *Review of creep–fatigue endurance and life prediction of 316 stainless steels.* International Journal of Pressure Vessels and Piping, 2015. **126**: p. 17-28.
59. Hales, R., *A quantitative metallographic assessment of structural degradation of type 316 stainless steel during creep‐fatigue.* Fatigue & Fracture of Engineering Materials & Structures, 1980. **3**(4): p. 339-356.
60. Plumbridge, W., *Metallography of high temperature fatigue*, in *High Temperature Fatigue*. 1987, Springer. p. 177-228.
61. Meng, L. and W. Chen, *A new thermodynamically based model for creep and cyclic plasticity.* International Journal of Mechanical Sciences, 2022. **214**: p. 106923.
62. Ohno, N., et al., *Ratchetting characteristics of 316FR steel at high temperature, part I: strain-controlled ratchetting experiments and simulations.* International Journal of Plasticity, 1998. **14**(4-5): p. 355-372.
63. Kobayashi, M., N. Ohno, and T. Igari, *Ratchetting characteristics of 316FR steel at high temperature, Part II: analysis of thermal ratchetting induced by spatial variation of temperature.* International Journal of Plasticity, 1998. **14**(4-5): p. 373-390.
64. Robinson, E.L., *Effect of temperature variation on the long-time rupture strength of steels.* Trans. ASME, 1952. **77**.
65. Ding, B., et al., *Accuracy of the predicting for creep-fatigue cyclic life based on parameters in a characteristic cycle.* Engineering Fracture Mechanics, 2021. **255**: p. 107955.
66. Goldhoff, R., *Uniaxial creep-rupture behavior of low-alloy steel under variable loading conditions.* 1965.
67. Kennedy, A.J., *Creep and stress relaxation in metals*. 1965: Oliver & Boyd.
68. Spindler, M., *An improved method for calculation of creep damage during creep–fatigue cycling.* Materials Science and Technology, 2007. **23**(12): p. 1461-1470.
69. Spindler, M., *An improved method to calculate the creep-fatigue endurance of type 316H stainless steel.* Materials for advanced power engineering, 2006.
70. Spindler, M. and W. Payten, *Advanced ductility exhaustion methods for the calculation of creep damage during creep-fatigue cycling.* Creep-Fatigue Interactions: Test Methods and Models, 2011.
71. Takahashi, Y., B. Dogan, and D. Gandy, *Systematic evaluation of creep-fatigue life prediction methods for various alloys.* Journal of Pressure Vessel Technology, 2013. **135**(6).
72. Wong, E.-H., et al., *Creep fatigue models of solder joints: A critical review.* Microelectronics Reliability, 2016. **59**: p. 1-12.
73. Miner, M.A., *Cumulative damage in fatigue.* 1945.
74. Palmgren, A., *Die lebensdauer von kugellargern.* Zeitshrift des Vereines Duetsher Ingenieure, 1924. **68**(4): p. 339.
75. Skelton, R. and D. Gandy, *Creep–fatigue damage accumulation and interaction diagram based on metallographic interpretation of mechanisms.* Materials at High Temperatures, 2008. **25**(1): p. 27-54.
76. Manson, S., G.R. Halford, and M. Hirschbere, *Creep-fatigue analysis by strainrange partitioning.* 1973.
77. Ainsworth, R., M. Ruggles, and Y. Takahashi, *Flaw assessment procedure for high-temperature reactor components.* 1992.

78. Majumdar, S. and P. Maiya, *1976 ASME-MPC Symposium on Creep Fatigue Interaction.* MPC-3, 1976: p. 323.
79. Kachanov, L.M., *Time of the rupture process under creep conditions.* Time of the Rupture Process under Creep Condition, 1958: p. 26-31.
80. Lemaitre, J. and J.-L. Chaboche, *Aspect phénoménologique de la rupture par endommagement.* J Méc Appl, 1978. **2**(3).
81. Zhang, Y.-G., *An iteration algorithm for kinematic shakedown analysis.* Computer methods in applied mechanics and engineering, 1995. **127**(1-4): p. 217-226.
82. Christiansen, E. and K.D. Andersen, *Computation of collapse states with von Mises type yield condition.* International Journal for Numerical Methods in Engineering, 1999. **46**(8): p. 1185-1202.
83. Simon, J.-W. and D. Weichert, *Numerical lower bound shakedown analysis of engineering structures.* Computer Methods in Applied Mechanics and Engineering, 2011. **200**(41-44): p. 2828-2839.
84. Liu, Y., X. Zhang, and Z. Cen, *Lower bound shakedown analysis by the symmetric Galerkin boundary element method.* International Journal of Plasticity, 2005. **21**(1): p. 21-42.
85. Chen, S., Y. Liu, and Z. Cen, *Lower bound shakedown analysis by using the element free Galerkin method and non-linear programming.* Computer Methods in Applied Mechanics and Engineering, 2008. **197**(45-48): p. 3911-3921.
86. Dhalla, A., *A simplified procedure to classify stresses for elevated temperature service.* ASME PVP, 1987.
87. Marriott, D., *Evaluation of deformation or load control of stresses under inelastic conditions using elastic finite element stress analysis.* ASME PVP, 1988. **136**: p. 3-9.
88. Seshadri, R., *Inelastic evaluation of mechanical and structural components using the generalized local stress strain method of analysis.* Nuclear Engineering and Design, 1995. **153**(2-3): p. 287-303.
89. Mackenzie, D., J. Shi, and J. Boyle, *Finite element modelling for limit analysis by the elastic compensation method.* Computers & structures, 1994. **51**(4): p. 403-410.
90. Chen, H. and A.R. Ponter, *A method for the evaluation of a ratchet limit and the amplitude of plastic strain for bodies subjected to cyclic loading.* European Journal of Mechanics-A/Solids, 2001. **20**(4): p. 555-571.
91. Seshadri, R., *The generalized local stress strain (GLOSS) analysis—theory and applications.* 1991.
92. Mackenzie, D., J. Boyle, and R. Hamilton, *The elastic compensation method for limit and shakedown analysis: a review.* The Journal of Strain Analysis for Engineering Design, 2000. **35**(3): p. 171-188.
93. Yang, P., et al., *Limit analysis based on a modified elastic compensation method for nozzle-to-cylinder junctions.* International journal of pressure vessels and piping, 2005. **82**(10): p. 770-776.
94. Muscat, M., R. Hamilton, and J. Boyle, *Shakedown analysis for complex loading using superposition.* The Journal of Strain Analysis for Engineering Design, 2002. **37**(5): p. 399-412.
95. Peng, H., Y. Liu, and H. Chen, *A numerical formulation and algorithm for limit and shakedown analysis of large-scale elastoplastic structures.* Computational Mechanics, 2019. **63**(1): p. 1-22.
96. Peng, H., et al., *Shakedown analysis of engineering structures under multiple variable mechanical and thermal loads using the stress compensation method.* International Journal of Mechanical Sciences, 2018. **140**: p. 361-375.

97. Melan, E., *Zur plastizität des räumlichen kontinuums.* Archive of Applied Mechanics, 1938. **9**(2): p. 116-126.
98. Ponter, A.R. and M. Engelhardt, *Shakedown limits for a general yield condition: implementation and application for a von Mises yield condition.* European Journal of Mechanics-A/Solids, 2000. **19**(3): p. 423-445.
99. Engelhardt, M.J., *Computational modelling of Shakedown*. 1999, University of Leicester.
100. Pham, D.C., *Shakedown theory for elastic plastic kinematic hardening bodies.* International Journal of Plasticity, 2007. **23**(7): p. 1240-1259.
101. Polizzotto, C., *On the conditions to prevent plastic shakedown of structures: Part I—Theory.* Journal of applied mechanics, 1993. **60**(1): p. 15-19.
102. Bouby, C., G. de Saxcé, and J.-B. Tritsch, *Shakedown analysis: comparison between models with the linear unlimited, linear limited and non-linear kinematic hardening.* Mechanics Research Communications, 2009. **36**(5): p. 556-562.
103. Chen, S., et al., *Performance of the MLPG method for static shakedown analysis for bounded kinematic hardening structures.* European Journal of Mechanics-A/Solids, 2011. **30**(2): p. 183-194.
104. Huang, S., et al., *A modified basis reduction method for limited kinematic hardening shakedown analysis under complex loads.* Mechanics Based Design of Structures and Machines, 2018. **46**(1): p. 85-100.
105. Pycko, S. and G. Maier, *Shakedown theorems for some classes of nonassociative hardening elastic-plastic material models.* International Journal of Plasticity, 1995. **11**(4): p. 367-395.
106. Ri, J.-H. and H.-S. Hong, *A basis reduction method using proper orthogonal decomposition for shakedown analysis of kinematic hardening material.* Computational Mechanics, 2018: p. 1-13.
107. Stein, E., G. Zhang, and Y. Huang, *Modeling and computation of shakedown problems for nonlinear hardening materials.* Computer methods in applied mechanics and engineering, 1993. **103**(1-2): p. 247-272.
108. Simon, J.-W., *Direct evaluation of the limit states of engineering structures exhibiting limited, nonlinear kinematical hardening.* International Journal of Plasticity, 2013. **42**: p. 141-167.
109. Heitzer, M., G. Pop, and M. Staat, *Basis reduction for the shakedown problem for bounded kinematic hardening material.* Journal of Global Optimization, 2000. **17**(1-4): p. 185-200.
110. König, J.A., *Shakedown of elastic-plastic structures*. Vol. 7. 2012: Elsevier.
111. Ponter, A., *A general shakedown theorem for elastic/plastic bodies with work hardening.* 1975.
112. Hachemi, A., *Sur les méthodes directes et leurs applications*. 2005, Université des Sciences et Technologies de Lille: France.
113. Mouhtamid, S. and D. Weichert, *Anwendung direkter Methoden zur industriellen Berechnung von Grenzlasten mechanischer Komponenten*, in *Institute of General Mechanics*. 2008, RWTH Aachen University: Germany.
114. Ma, Z., et al., *A direct approach to the evaluation of structural shakedown limit considering limited kinematic hardening and non-isothermal effect.* European Journal of Mechanics-A/Solids, 2020. **79**: p. 103877.
115. Pham, D.C., *Consistent limited kinematic hardening plasticity theory and path-independent shakedown theorems.* International Journal of Mechanical Sciences, 2017. **130**: p. 11-18.
116. Pham, D.C., *On shakedown theory for elastic–plastic materials and extensions.* Journal of the Mechanics and Physics of Solids, 2008. **56**(5): p. 1905-1915.

117. Jin, Y., Y.-h. Hao, and Z.-j. Huang, *Analysis of temperature field and stress field for the twin-web turbine disk of aero engine.* Journal of Zhengzhou University of Light Industry (Natural Science Edition), 2015. **1**: p. 019.
118. Kong, X., et al., *Broaching performance of superalloy GH4169 based on FEM.* Journal of Materials Science & Technology, 2011. **27**(12): p. 1178-1184.
119. Bree, J., *Plastic deformation of a closed tube due to interaction of pressure stresses and cyclic thermal stresses.* International journal of mechanical sciences, 1989. **31**(11-12): p. 865-892.
120. Chen, H., *Lower and upper bound shakedown analysis of structures with temperature-dependent yield stress.* Journal of Pressure Vessel Technology, 2010. **132**(1): p. 011202.
121. Oh, C.H. and E.S. Kim, *Heat Exchanger Design Options and Tritium Transport Study for the VHTR System*. 2008, Idaho National Laboratory (INL).
122. Wright, J., *Next generation nuclear plant steam generator and intermediate heat exchanger materials research and development plan*. 2010, Idaho National Laboratory (INL).
123. Mahajan, H.P., U. Devi, and T. Hassan. *Finite Element Analysis of Printed Circuit Heat Exchanger Core for High Temperature Creep and Burst Responses*. in *Pressure Vessels and Piping Conference*. 2018. American Society of Mechanical Engineers.
124. Mahajan, H.P. and T. Hassan. *Finite Element Analysis of Printed Circuit Heat Exchanger Core for Creep and Creep-Fatigue Responses*. in *Pressure Vessels and Piping Conference*. 2019. American Society of Mechanical Engineers.
125. Zhu, X., et al., *On the creep fatigue and creep rupture behaviours of 9–12% Cr steam turbine rotor.* European Journal of Mechanics-A/Solids, 2019. **76**: p. 263-278.
126. Barbera, D. and H. Chen, *Creep rupture assessment by a robust creep data interpolation using the Linear Matching Method.* European Journal of Mechanics-A/Solids, 2015. **54**: p. 267-279.
127. Chen, H., A.R. Ponter, and R. Ainsworth, *The linear matching method applied to the high temperature life integrity of structures. Part 1. Assessments involving constant residual stress fields.* International Journal of Pressure Vessels and Piping, 2006. **83**(2): p. 123-135.
128. Chen, H., A.R. Ponter, and R. Ainsworth, *The linear matching method applied to the high temperature life integrity of structures. Part 2. Assessments beyond shakedown involving changing residual stress fields.* International Journal of Pressure Vessels and Piping, 2006. **83**(2): p. 136-147.
129. Jackson, G., H. Chen, and D. Tipping, *Shakedown and creep rupture assessment of a header branch pipe using the Linear Matching Method.* Procedia Engineering, 2015. **130**: p. 1705-1718.
130. Spindler, M. and H. Andersson. *ECCC Rupture Data for Austenitic Stainless Steels–Experiences Gained with Demanding Data Analyses*. in *Proc. 5th Intern. Conf. on Advances in Materials Technology for Fossil Power Plants*. 2007.
131. *MATLAB: the language of technical computing. Desktop tools and development environment, version 7*. Vol. 9. 2005: MathWorks, Inc.
132. Spindler, M., et al. *A re-evaluation of the ECCC guidance for the assessment of full size creep rupture datasets*. in *3 rd international ECCC conference on creep and fracture in high temperature components design and life assessment, Rome. INAIL*. 2014.

133. Utgikar, V., et al., *Advanced Reactors-Intermediate Heat Exchanger (IHX) Coupling: Theoretical Modeling and Experimental Validation*. 2016, Battelle Energy Alliance, LLC, Idaho Falls, ID (United States).
134. Natesan, K., A. Moisseytsev, and S. Majumdar, *Preliminary issues associated with the next generation nuclear plant intermediate heat exchanger design.* Journal of nuclear materials, 2009. **392**(2): p. 307-315.
135. SantAnna, R. and N. Zouain, *A direct method for ratchet boundary determination.* European Journal of Mechanics-A/Solids, 2019. **75**: p. 156-168.
136. ASME Boiler and Pressure Vessel Code, *Section II-Materials-Part A-Ferrous Materials Specification*. 2017, American Society of Mechanical Engineers: New York.
137. Toudehdehghan, A. and T.W. Hong. *A critical review and analysis of pressure vessel structures*. in *IOP Conference Series: Materials Science and Engineering*. 2019. IOP Publishing.
138. Patil, A.D. and M.M. Jadhav, *Analysis of Pressure Vessel: A Review.* International Journal for Innovative Research in Science & Technology, ISSN (online): p. 2349-6010.
139. Khattak, M., A. Mukhtar, and K.A. Khan, *Common root causes of pressure vessel failures: a review.* Advanced Research in Applied Mechanics, 2016. **21**(1).
140. Hashemi, Y.M., M. Kadkhodaei, and M.R. Mohammadzadeh, *Fatigue analysis of shape memory alloy helical springs.* International Journal of Mechanical Sciences, 2019. **161**: p. 105059.
141. Moslemi, N., et al., *Uniaxial and biaxial ratcheting behavior of pressurized AISI 316L pipe under cyclic loading: Experiment and simulation.* International Journal of Mechanical Sciences, 2020: p. 105693.
142. Su, H., et al., *Ratcheting behaviour of flash butt welds in heat-treated hypereutectoid steel rails under uniaxial and biaxial cyclic loadings.* International Journal of Mechanical Sciences, 2020. **176**: p. 105539.
143. Kolasangiani, K., et al., *Ratcheting assessment of notched steel samples subjected to asymmetric loading cycles through coupled kinematic hardening-Neuber rules.* International Journal of Mechanical Sciences, 2018. **144**: p. 24-32.
144. Santecchia, E., et al., *A review on fatigue life prediction methods for metals.* Advances in Materials Science and Engineering, 2016. **2016**.
145. Luo, H., et al., *Experimental study on the whole‐life heterogeneous ratchetting and ratchetting‐fatigue interaction of SUS301L stainless steel butt‐welded joint.* Fatigue & Fracture of Engineering Materials & Structures, 2020. **43**(1): p. 36-50.
146. ASME Boiler and Pressure Vessel Code, *Section III, Division 1 – Subsections NB, NC, ND, NCA and Appendices*. 2001, American Society of Mechanical Engineers: New York.
147. Bradford, R., *The Bree problem with primary load cycling in-phase with the secondary load.* International journal of pressure vessels and piping, 2012. **99**: p. 44-50.
148. Pommier, B., *Détermination de la réponse asymptotique d'une structure anélastique soumise à un chargement thermomécanique cyclique*. 2003.
149. D'Angela, D. and M. Ercolino, *Finite element analysis of fatigue response of nickel steel compact tension samples using ABAQUS.* Procedia Structural Integrity, 2018. **13**: p. 939-946.
150. Nečemer, B., J. Kramberger, and S. Glodež. *THE LCF-ANALYSES OF AUXETIC STRUCTURE USING DIRECT CYCLING ALGORITHM*. in *InCell*

2019: Book of Abstracts of the International Conference on Multifunctional Cellular Materials. 2019. UA Editora Universidade de Aveiro.
151. Reinhardt, W., *A noncyclic method for plastic shakedown analysis.* Journal of pressure vessel technology, 2008. **130**(3).
152. Reinhardt, W. and R. Adibi-Asl, *Lower Bound Methods in Elastic-Plastic Shakedown Analysis.* Journal of Pressure Vessel Technology, 2014. **136**(2).
153. Bayati, P., et al., *Toward low and high cycle fatigue behavior of SLM-fabricated NiTi: considering the effect of build orientation and employing a self-heating approach.* International Journal of Mechanical Sciences, 2020: p. 105878.
154. Mozafari, F., et al., *A rate independent inelasticity model with smooth transition for unifying low-cycle to high-cycle fatigue life prediction.* International Journal of Mechanical Sciences, 2019. **159**: p. 325-335.
155. Wöhler, A., *Versucheüber die festiykeit eisenbahnwagenuchsen.* Z Bauwesen, 1860. **10**.
156. Sendeckyj, G., *Constant life diagrams—a historical review.* International journal of fatigue, 2001. **23**(4): p. 347-353.
157. Sarkar, A., et al., *Generation of constant life diagram under elevated temperature ratcheting of 316LN stainless steel.* High Temperature Materials and Processes, 2016. **35**(4): p. 361-368.
158. Topper, T., R. Wetzel, and J. Morrow, *Neuber's rule applied to fatigue of notched specimens*. 1967, Illinois univ at Urbana dept of theoretical and applied mechanics.
159. Kujawski, D. and J.L. Teo, *A generalization of Neuber's rule for numerical applications.* Procedia Structural Integrity, 2017. **5**: p. 883-888.
160. Spring, D.W., et al. *On the Applicability of Neuber's Rule for Low-Cycle Fatigue*. in *Pressure Vessels and Piping Conference*. 2016. American Society of Mechanical Engineers.
161. ASME Boiler and Pressure Vessel Code, *Section VIII, Division 2: Alternative rules, rules for construction of pressure vessels*. 2007, American Society of Mechanical Engineers: New York.
162. Glinka, G., *Energy density approach to calculation of inelastic strain-stress near notches and cracks.* Engineering Fracture Mechanics, 1985. **22**(3): p. 485-508.
163. Ma, Z., et al., *A unified direct method for ratchet and fatigue analysis of structures subjected to arbitrary cyclic thermal-mechanical load histories.* International Journal of Mechanical Sciences, 2021. **194**: p. 106190.
164. Ponter, A.R. and H. Chen, *A minimum theorem for cyclic load in excess of shakedown, with application to the evaluation of a ratchet limit.* European Journal of Mechanics-A/Solids, 2001. **20**(4): p. 539-553.
165. Zheng, X., et al., *A novel fatigue assessment approach by Direct Steady Cycle Analysis (DSCA) considering the temperature-dependent strain hardening effect.* International Journal of Pressure Vessels and Piping, 2019. **170**: p. 66-72.
166. Koiter, W., *Progress in solid mechanics.* vol, 1960. **6**: p. 167-221.
167. Zheng, X.T., et al. *A Novel Fatigue Evaluation Approach with Direct Steady Cycle Analysis (DSCA) Based on the Linear Matching Method (LMM)*. in *Key Engineering Materials*. 2019. Trans Tech Publ.
168. Agarwal, R.K., *Recent Progress in Some Aircraft Technologies*. 2016: BoD–Books on Demand.
169. Chen, H. and A.R. Ponter, *Integrity assessment of a 3D tubeplate using the linear matching method. Part 1. Shakedown, reverse plasticity and ratchetting.* International journal of pressure vessels and piping, 2005. **82**(2): p. 85-94.

170. Chen, H. and A.R. Ponter, *Integrity assessment of a 3D tubeplate using the linear matching method. Part 2: Creep relaxation and reverse plasticity.* International journal of pressure vessels and piping, 2005. **82**(2): p. 95-104.
171. Barbera, D., H.F. Chen, and Y.H. Liu. *Creep Fatigue Life Assessment of a Pipe Intersection with Dissimilar Material Joint by Linear Matching Method*. in *Applied Mechanics and Materials*. 2017. Trans Tech Publ.
172. Barbera, D., H. Chen, and Y. Liu, *On the creep fatigue behavior of metal matrix composites.* Procedia Engineering, 2015. **130**: p. 1121-1136.
173. Chen, Y.G.H., *Creep-fatigue life assessment of high-temperature weldments using the linear matching method.* Poster.
174. Puliyaneth, M. and H. Chen, *Study on the effect of welding residual stress on creep-cyclic plasticity behaviour.* International Journal of Pressure Vessels and Piping, 2021: p. 104444.
175. Cho, N.-K., et al., *Creep-fatigue endurance of a superheater tube plate under non-isothermal loading and multi-dwell condition.* International Journal of Mechanical Sciences, 2019. **161**: p. 105048.
176. Barbera, D., H. Chen, and Y. Liu, *Advances on creep–fatigue damage assessment in notched components.* Fatigue & Fracture of Engineering Materials & Structures, 2017. **40**(11): p. 1854-1867.
177. Barbera, D., H. Chen, and Y. Liu, *On creep fatigue interaction of components at elevated temperature.* Journal of Pressure Vessel Technology, 2016. **138**(4).
178. Wu, X., Z. Zhao, and X. Chen, *A design approach for creep fatigue evaluation of hydrogenation reactor made of 2.25 Cr1MoV steel.* J. Mech. Eng, 2015. **51**(6): p. 51-57.
179. Boiler, A., *Cases of ASME boiler and pressure vessel code, Case 2605.* American Society of Mechanical Engineers, New York, NY, 2017. **1**.
180. Deng, D. and H. Murakawa, *Finite element analysis of temperature field, microstructure and residual stress in multi-pass butt-welded 2.25 Cr–1Mo steel pipes.* Computational materials science, 2008. **43**(4): p. 681-695.
181. *NIMS (former NRIM) Creep Data Sheets, No.36B*. 1991, National Institute for Materials Science: Tsukuba, Japan.
182. Zhao, Z., X. Wu, and X. Chen, *Structural Integrity and Creep-fatigue Assessment by ASME-NH for Hydrogenation Equipment at 454℃.* Procedia Engineering, 2015. **130**: p. 414-422.
183. *NIMS (former NRIM) Creep Data Sheets, No.3B*. 1986, National Institute for Materials Science: Tsukuba, Japan.

Appendix A. The UCRE parameters fitted for materials from the ECCC data sheets [49]

Material	a_1	a_2	a_3	a_4	b_1	b_2	b_3	b_4
Carbon-manganese and low alloy ferritic steels								
P235 (C / CMn)	1.46E-05	-3.10E-02	2.20E+01	-5.25E+03	-1.72E-04	3.69E-01	-2.66E+02	6.45E+04
P355 (CMnNb)	-2.79E-05	6.15E-02	-4.50E+01	1.09E+04	2.88E-04	-6.27E-01	4.51E+02	-1.07E+05
16Mo3 (0.3Mo)	-1.25E-05	3.28E-02	-2.80E+01	7.83E+03	1.64E-04	-4.10E-01	3.35E+02	-8.98E+04
8MoB5-4 (MoB)	-1.09E-04	2.56E-01	-1.99E+02	5.14E+04	1.32E-03	-3.07E+00	2.36E+03	-6.04E+05
25CrMo4 (1CrMo)	-3.30E-05	7.58E-02	-5.77E+01	1.45E+04	3.64E-04	-8.30E-01	6.25E+02	-1.55E+05
12CrMoV6-2-2 (0.5Cr0.5Mo0.25V)	-6.82E-06	1.73E-02	-1.44E+01	3.93E+03	8.15E-05	-1.98E-01	1.57E+02	-4.00E+04
11CrMo9-10 (2.25Cr1Mo)	4.66E-06	-1.24E-02	1.11E+01	-3.30E+03	-7.03E-05	1.88E-01	-1.69E+02	5.10E+04
20CrMoV13-5 (3CrMoV)	-8.49E-05	1.96E-01	-1.50E+02	3.81E+04	8.09E-04	-1.85E+00	1.40E+03	-3.52E+05
X11CrMo5 (5CrMo)	-3.20E-05	7.58E-02	-5.97E+01	1.56E+04	2.44E-04	-5.66E-01	4.34E+02	-1.10E+05
9NiMoCuNb5-6-4 (1NiMoCuNb)	-1.10E-06	3.37E-03	-3.36E+00	1.06E+03	5.13E-05	-1.32E-01	1.09E+02	-2.89E+04
High alloy ferritic steels								
X11CrMo9-1 (9Cr-1Mo)	7.88E-06	-1.89E-02	1.52E+01	-4.09E+03	-8.79E-05	2.16E-01	-1.79E+02	5.03E+04
X10CrMoVNb9-1 (P91/T91)	-2.12E-06	6.01E-03	-5.59E+00	1.69E+03	3.64E-05	-9.50E-02	8.06E+01	-2.19E+04
GX12CrMoVNbN9-1 (Cast Steel 91)	1.15E-05	-2.78E-02	2.24E+01	-6.02E+03	-1.34E-04	3.27E-01	-2.68E+02	7.38E+04
X11CrMoWVNb9-1-1 (E911)	1.15E-05	-2.85E-02	2.34E+01	-6.41E+03	-9.64E-05	2.38E-01	-1.97E+02	5.51E+04
X10CrWMoVNb9-2 (P92/T92)	8.22E-06	-2.07E-02	1.73E+01	-4.85E+03	-7.76E-05	1.97E-01	-1.68E+02	4.83E+04
X20CrMoNiV11-1 (12CrMoV)	1.37E-06	-2.33E-03	1.13E+00	-1.42E+02	-1.33E-05	2.84E-02	-2.24E+01	7.03E+03
Austenitic steels								

X2CrNi18-9 (Type 304L)	9.16E-06	-2.54E-02	2.35E+01	-7.29E+03	-1.06E-04	2.96E-01	-2.76E+02	8.63E+04
X2CrNiN 18-10 (Type 304 LN)	-4.13E-06	1.15E-02	-1.06E+01	3.17E+03	4.09E-05	-1.11E-01	9.83E+01	-2.81E+04
X6CrNi 18-10 (Type 304H)	-2.40E-07	6.74E-04	-5.57E-01	1.14E+02	9.19E-06	-2.24E-02	1.64E+01	-3.06E+03
X2CrNiMo17-12-2 (Type 316L)	-8.60E-07	2.36E-03	-2.08E+00	5.69E+02	6.41E-06	-1.40E-02	7.74E+00	-6.55E+01
X5CrNiMo17-12-2 (Type 316)	-1.07E-06	2.95E-03	-2.63E+00	7.31E+02	6.87E-06	-1.57E-02	9.40E+00	-4.90E+02
X6CrNiMoTi17-12-2 (Type 316Ti)	-7.30E-07	1.97E-03	-1.68E+00	4.24E+02	1.23E-06	8.02E-04	-6.54E+00	4.64E+03
X2CrNiMoN 17-13-3 (Type 316LN)	-6.73E-06	1.94E-02	-1.84E+01	5.75E+03	7.91E-05	-2.23E-01	2.07E+02	-6.25E+04
X2CrNiMo17-12-2 (Type 316L(N))	-2.46E-07	5.19E-04	-2.50E-01	-3.32E+01	-3.43E-06	1.43E-02	-1.95E+01	8.78E+03
X3CrNiMoBN 17-13-3 (Type 316LNB)	-3.01E-06	8.56E-03	-7.96E+00	2.40E+03	2.58E-05	-6.99E-02	6.05E+01	-1.63E+04
X7CrNiTi 18-10 (Type 321H)	4.03E-06	-1.04E-02	8.98E+00	-2.64E+03	-4.28E-05	1.13E-01	-1.02E+02	3.13E+04
X6CrNiNb 18-10 (Type 347)	-3.48E-06	8.89E-03	-7.45E+00	2.02E+03	3.06E-05	-7.43E-02	5.76E+01	-1.36E+04
X8CrNiNb 16-13 (16-13Nb)	-1.93E-06	5.26E-03	-4.69E+00	1.35E+03	2.33E-05	-6.07E-02	5.07E+01	-1.32E+04
X5 NiCrAlTi 31-20 (Alloy 800)	-3.82E-06	9.85E-03	-8.31E+00	2.27E+03	5.92E-05	-1.50E-01	1.23E+02	-3.26E+04
X8NiCrAlTi 32-21 (Alloy 800H)	7.42E-07	-2.51E-03	2.86E+00	-1.10E+03	-1.21E-05	4.10E-02	-4.66E+01	1.79E+04
X6NiCrNbCe32-27 (Type AC 66)	-6.51E-07	1.97E-03	-1.92E+00	5.93E+02	3.95E-06	-9.83E-03	6.65E+00	-6.21E+02
CrNiSiNCe 21-11 (253MA)	6.31E-08	-3.61E-04	5.96E-01	-3.07E+02	-4.02E-06	1.57E-02	-2.03E+01	8.76E+03
X10CrNiMoMnNbVB 15-10-1 (Esshete 1250)	-6.53E-05	1.88E-01	-1.79E+02	5.69E+04	7.65E-04	-2.19E+00	2.08E+03	-6.58E+05
BS1503 310S31 (Type 310)	2.15E-06	-6.76E-03	7.11E+00	-2.50E+03	-3.72E-05	1.17E-01	-1.22E+02	4.29E+04
HR3C	-1.60E-05	4.42E-02	-4.06E+01	1.23E+04	1.53E-04	-4.16E-01	3.75E+02	-1.11E+05
NF709	4.48E-07	-1.65E-03	2.04E+00	-8.53E+02	-1.46E-05	4.95E-02	-5.67E+01	2.20E+04

NF709R	1.35E-06	-4.45E-03	4.96E+00	-1.87E+03	-2.67E-05	8.71E-02	-9.59E+01	3.57E+04
Nickel base alloys								
NiCr23Co12Mo (Alloy 617)	-5.10E-07	1.45E-03	-1.25E+00	2.97E+02	-9.68E-07	7.72E-03	-1.47E+01	8.23E+03
NiCr20TiAl (Nimonic 80A)	8.75E-06	-2.12E-02	1.70E+01	-4.56E+03	-7.39E-05	1.78E-01	-1.44E+02	4.07E+04
High temperature bolting steels								
42CrMo5-6 (Durehete 900)	-4.46E-04	1.03E+00	-7.85E+02	2.00E+05	5.04E-03	-1.16E+01	8.81E+03	-2.24E+06
20CrMoVTiB4-10 (Durehete 1055)	9.37E-05	-2.18E-01	1.68E+02	-4.32E+04	-9.81E-04	2.28E+00	-1.76E+03	4.55E+05
21CrMoV 5-7 (1CrMoV)	5.46E-06	-1.17E-02	8.36E+00	-2.00E+03	-4.26E-05	9.02E-02	-6.54E+01	1.69E+04

Appendix B. The UPFRA Python code for ratchet, fatigue and creep-fatigue analysis

```
from abaqus import *
from abaqusConstants import *
import job
import winsound
import sys
import os
import shutil
import xml.dom.minidom
from odbAccess import *
from abaqusConstants import*
import re
import csv

'''
Note:
Please run LMM Plug-in once for the input file and *_LMM_LC.dat file,
then rename *_LMM_LC.dat to *_LMM_LC.txt, in *_LMM_LC.txt,
substitute scalable pressure for PPP, substitute scalable temperature for TTT.

Result is saved in your working directory as Results.csv,
the file gives effective ratchet strain/number of cycles to failure for each iteration,
as well as converged scaled pressure and temperature.
'''

## User Input:
Mode = 1          # Select mode: ratchet analysis = 0, fatigue analysis = 1, creep-fatigue analysis = 2
Ratio = [0,1]     # Ratio between P and T: Ratio = T/P; Calculate multiple ratios one by one
jobName = 'test'  # Name of input file generated by LMM Plug-in
LowerBound = 0.0# Input first upper bound multiplier of Lambda (normally shakedown limit or zero)
UpperBound = 1.0# Input first lower bound multiplier of Lambda (normally limit load)
Iteration = 12    # Input max number of iteration, suggest 5 or above
Target = 100      # Input target max effective ratchet strain per cycle (normally 0.0002) for ratchet
                  analysis or target number of cycles to failure for fatigue/creep-fatigue analysis
Convergence = 0.01# Input convergence parameter

## Create Results.csv
csvFile = open('Results.csv', 'w')
writer = csv.writer(csvFile,dialect='excel',lineterminator='\n')
fileHeader = ['Ratio']
for j in range(Iteration):
        fileHeader.append('I'+str(j+1))
fileHeader.append('P')
fileHeader.append('T')
writer.writerow(fileHeader)

for R in Ratio:
        ## Initialization
        LB = [0.0] * Iteration
        UB = [0.0] * Iteration
        Lambda = [0.0] * Iteration
        P = [0.0] * Iteration
        T = [0.0] * Iteration
        maxODB = [0.0] * Iteration
        maxODB1 = [0.0] * Iteration
        LB[0] = LowerBound
        UB[0] = UpperBound
        flag = -1
        ## Bisection scheme
        for i in range(Iteration):
```

```
if Mode == 1 or Mode == 2:
	if i == 0:
		Lambda[i] = (LB[i]+UB[i])/2.0
	elif i == 1:
		LB[i] = LB[i-1]
		UB[i] = UB[i-1]
		if maxODB[i-1] > Target:
			Lambda[i] = (Lambda[i-1]+UB[i])/2.0
		else:
			Lambda[i] = (Lambda[i-1]+LB[i])/2.0
	else:
		if maxODB[i-2] > Target:
			LB[i] = Lambda[i-2]
			UB[i] = UB[i-1]
		else:
			LB[i] = LB[i-1]
			UB[i] = Lambda[i-2]
		if maxODB[i-1] > Target:
			Lambda[i] = (Lambda[i-1]+UB[i])/2.0
		else:
			Lambda[i] = (Lambda[i-1]+LB[i])/2.0
else:
	if i == 0:
		Lambda[i] = (LB[i]+UB[i])/2.0
	elif i == 1:
		LB[i] = LB[i-1]
		UB[i] = UB[i-1]
		if maxODB[i-1] < Target:
			Lambda[i] = (Lambda[i-1]+UB[i])/2.0
		else:
			Lambda[i] = (Lambda[i-1]+LB[i])/2.0
	else:
		if maxODB[i-2] < Target:
			LB[i] = Lambda[i-2]
			UB[i] = UB[i-1]
		else:
			LB[i] = LB[i-1]
			UB[i] = Lambda[i-2]
		if maxODB[i-1] < Target:
			Lambda[i] = (Lambda[i-1]+UB[i])/2.0
		else:
			Lambda[i] = (Lambda[i-1]+LB[i])/2.0
P[i]=Lambda[i]
T[i]=P[i]*R
## Modify _LMM_LC.dat file
fp3 = open(jobName+'_LMM.txt','r')
fp4 = open(jobName+'_LMM_LC.txt','w')
for s in fp3.readlines():
	if P[i] < 10:
		s0 = s.replace('PPP',format(P[i],'.5f'))
	else:
		s0 = s.replace('PPP',format(P[i],'.4f'))
	if T[i] < 10:
		fp4.write(s0.replace('TTT',format(T[i],'.5f')))
	else:
		fp4.write(s0.replace('TTT',format(T[i],'.4f')))
fp3.close()
fp4.close()
try:
	os.rename(jobName+'_LMM_LC.txt',jobName+'_LMM_LC.dat')
except WindowsError:
	os.remove(jobName+'_LMM_LC.dat')
	os.rename(jobName+'_LMM_LC.txt',jobName+'_LMM_LC.dat')
```

```
                    ## Abaqus job submission
                    if Mode == 0 or Mode == 1:
                            mdb.JobFromInputFile(name=jobName,inputFileName=\
                                    jobName+'.inp',userSubroutine='C:/SIMULIA/Abaqus/LMM/\
                                    LMM_Steady_Cycle_and_RatchetTEST.obj',numCpus=4)
                            mdb.jobs[jobName].submit()
                            mdb.jobs[jobName].waitForCompletion()
                    else:
                            mdb.JobFromInputFile(name=jobName,inputFileName=\
                                    jobName+'.inp',userSubroutine='C:/SIMULIA/Abaqus/LMM/\
                                    LMM_Creep_FatigueTEST.obj',numCpus=4)
                            mdb.jobs[jobName].submit()
                            mdb.jobs[jobName].waitForCompletion()

                    ## Read odb file
                    OdbFilePath = jobName + '.odb'
                    myodb = openOdb(OdbFilePath)
                    if Mode == 0:
                            mySDV = myodb.steps['LMM-Shakedown'].frames[-1].\
                            fieldOutputs['SDV11']
                    elif Mode == 1:
                            mySDV = myodb.steps['LMM-Shakedown'].frames[-1].\
                            fieldOutputs['SDV100']
                    else:
                            mySDV = myodb.steps['LMM-Shakedown'].frames[-1].\
                            fieldOutputs['SDV176']
                    val1 = mySDV.values
                    val1SDV = []
                    for v1 in val1:
                            val1SDV.append(v1.data)
                    if Mode == 1 or Mode == 2:
                            maxODB[i] = min(val1SDV)
                    else:
                            maxODB[i] = max(val1SDV)
                    myodb.close()

                    ## In case DSCA gives NaN results
                    myodb1 = openOdb(OdbFilePath)
                    mySDV1 = myodb1.steps['LMM-Shakedown'].frames[-1].fieldOutputs['SDV10']
                    val11 = mySDV1.values
                    val11SDV = []
                    for v11 in val11:
                            val11SDV.append(v11.data)
                    maxODB1[i] = max(val11SDV)
                    if maxODB1[i] == 0.0:
                            maxODB[i] = 0.0
                    myodb1.close()
                    ## Check convergence
                    if abs((maxODB[i]-Target)/Target) <= Convergence:
                            flag = i
                            break

            ## Write Results.csv
            if flag != -1:
                    for k in range(flag+1, Iteration):
                            maxODB[k] = '-'
                    maxODB.append(P[flag])
                    maxODB.append(T[flag])
            else:
                    maxODB.append(P[Iteration-1])
                    maxODB.append(T[Iteration-1])
            maxODB.insert(0,R)
            writer.writerow(maxODB)
csvFile.close()
```

Appendix C. The creep FORTRAN subroutine for SBS creep-fatigue analysis

```
      SUBROUTINE CREEP(DECRA,DESWA,STATEV,SERD,EC,ESW,P,QTILD,
     1 TEMP,DTEMP,PREDEF,DPRED,TIME,DTIME,CMNAME,LEXIMP,LEND,
     2 COORDS,NSTATV,NOEL,NPT,LAYER,KSPT,KSTEP,KINC)
C
      INCLUDE 'ABA_PARAM.INC'
C
      CHARACTER*80 CMNAME
C
      DIMENSION DECRA(5),DESWA(5),STATEV(*),PREDEF(*),DPRED(*),
     1 TIME(2),COORDS(*),EC(2),ESW(2)
C
      DO 3 KK=1,5
    3 DECRA(KK)=0.D0
      IF(QTILD.LT.100.) GO TO 10
      IF(TEMP.LE.450.0) then
        A=8.334E-38
        XN=12.43
        XM=0.0
      ELSE IF(TEMP.LE.475.0) THEN
        A=6.665E-33
        XN=10.88
        XM=0.0
      ELSE IF(TEMP.LE.500.0) THEN
        A=1.246E-33
        XN=11.42
        XM=0.0
      ELSE IF(TEMP.LE.525.0) THEN
        A=3.286E-28
        XN=9.493
        XM=0.0
      ELSE
        A=1.24E-18
        XN=5.651
        XM=0.0
      END IF
      C1=1./(1.+XM)
C TIME HARDENING
      TERM1=A*QTILD**XN*C1
      DECRA(1)=TERM1*(TIME(1)**(1.+XM)-(TIME(1)-DTIME)**(1.+XM))
      DECRA(5)=DECRA(1)*XN/QTILD
      GO TO 10
    5 CONTINUE
   10 CONTINUE
      RETURN
      END
```